

## Efficient Thermal Modelling and Topology Optimization for Additive Manufacturing

Ranjan, R.

**DOI**

[10.4233/uuid:43ed643d-0934-4f5c-a0e9-16d66b6c6c50](https://doi.org/10.4233/uuid:43ed643d-0934-4f5c-a0e9-16d66b6c6c50)

**Publication date**

2023

**Document Version**

Final published version

**Citation (APA)**

Ranjan, R. (2023). *Efficient Thermal Modelling and Topology Optimization for Additive Manufacturing*. [Dissertation (TU Delft), Delft University of Technology]. <https://doi.org/10.4233/uuid:43ed643d-0934-4f5c-a0e9-16d66b6c6c50>

**Important note**

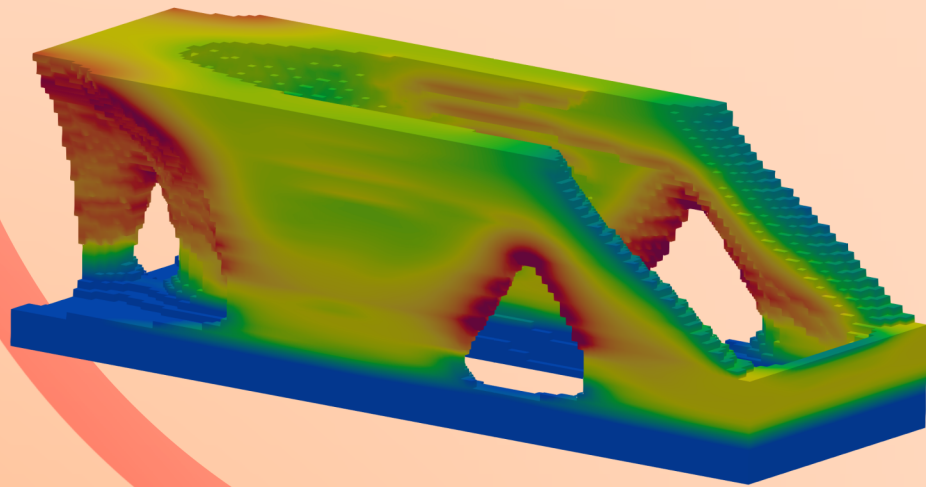
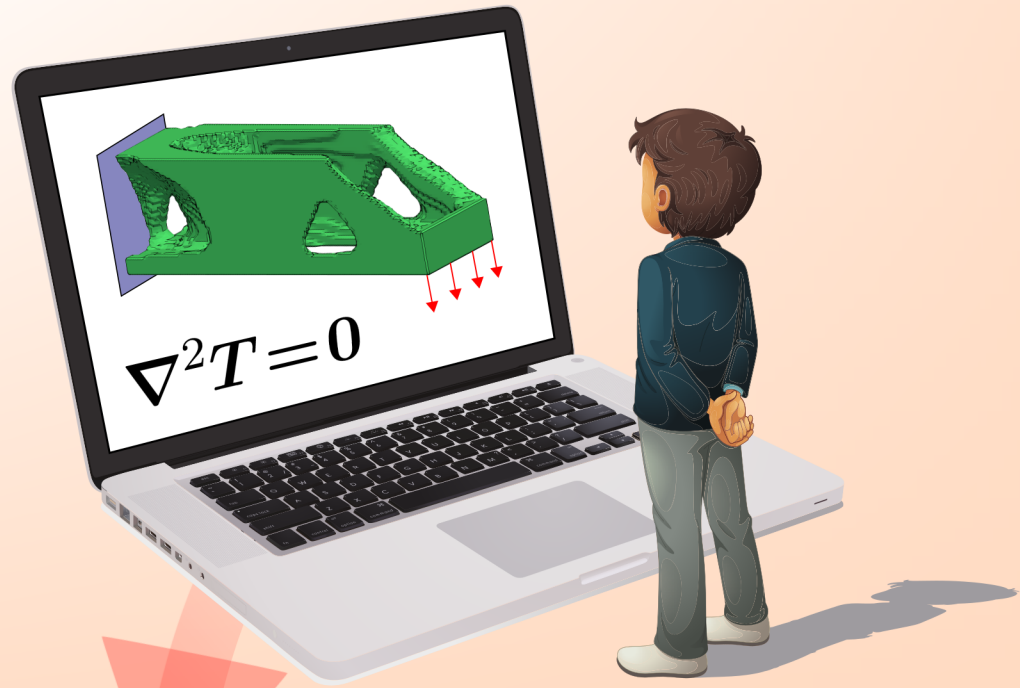
To cite this publication, please use the final published version (if applicable). Please check the document version above.

**Copyright**

Other than for strictly personal use, it is not permitted to download, forward or distribute the text or part of it, without the consent of the author(s) and/or copyright holder(s), unless the work is under an open content license such as Creative Commons.

**Takedown policy**

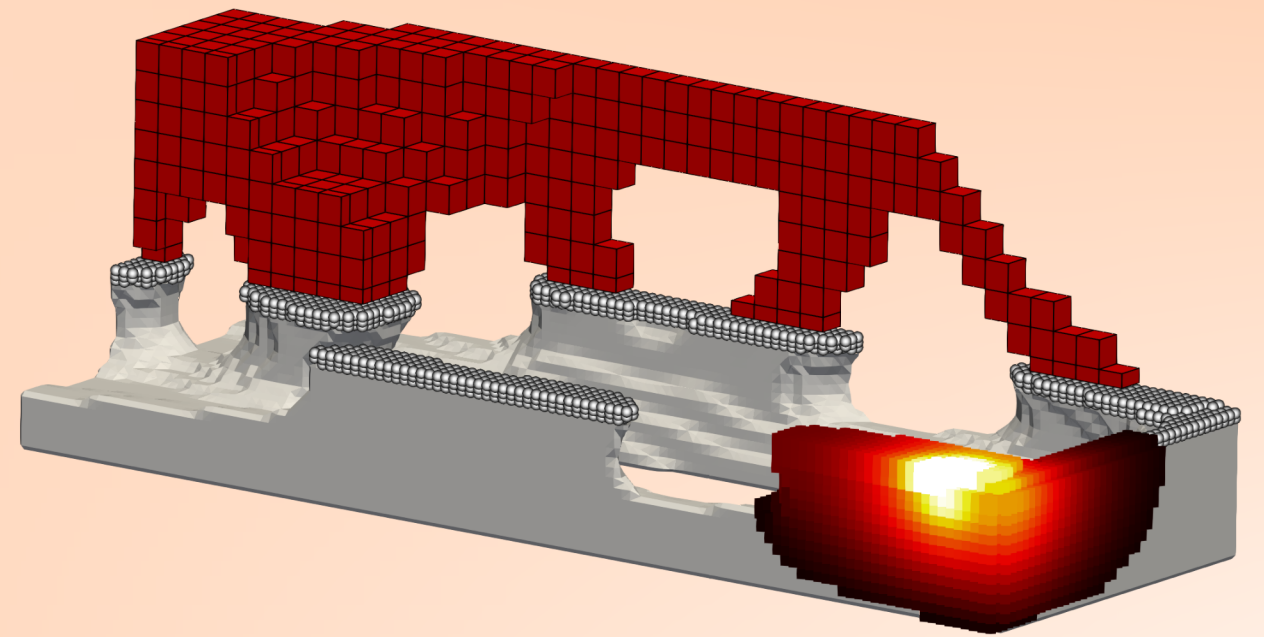
Please contact us and provide details if you believe this document breaches copyrights. We will remove access to the work immediately and investigate your claim.



EFFICIENT THERMAL MODELLING AND TOPOLOGY OPTIMIZATION FOR ADDITIVE MANUFACTURING

Rajit Ranjan

## EFFICIENT THERMAL MODELLING AND TOPOLOGY OPTIMIZATION FOR ADDITIVE MANUFACTURING



Rajit Ranjan

# EFFICIENT THERMAL MODELLING AND TOPOLOGY OPTIMIZATION FOR ADDITIVE MANUFACTURING



# EFFICIENT THERMAL MODELLING AND TOPOLOGY OPTIMIZATION FOR ADDITIVE MANUFACTURING

## **Dissertation**

For the purpose of obtaining the degree of doctor  
at Delft University of Technology,  
by the authority of the Rector Magnificus Prof. dr. ir. T.H.J.J. van der Hagen,  
chair of the board of Doctorates,  
to be defended publicly on  
Monday 27 March 2023 at 10:00 o'clock

by

**Rajit RANJAN**

Master of Science in Mechanical Engineering  
University of Cincinnati, Cincinnati, USA  
born in Sitapur, India.

This dissertation has been approved by the promotor.

Composition of the doctoral committee:

Rector Magnificus,	chairperson
Prof. dr. ir. F. van Keulen,	Delft University of Technology, promotor
Dr. ir. M. Langelaar,	Delft University of Technology, promotor
Dr. C. Ayas,	Delft University of Technology, copromotor

*Independent members:*

Prof. dr. A. A. Zadpoor,	Delft University of Technology
Prof. dr. M. Chiumenti,	Polytechnic University of Catalonia
Prof. dr. G. Allaire,	Ecole Polytechnique
Dr. S. Scholz,	Karlsruhe Institute of Technology
Prof. dr. U. Staufer,	Delft University of Technology, reserve member

This work was performed within PAM<sup>2</sup>, 'Precision Additive Metal Manufacturing', a re-search project funded by The EU Framework Programme for Research and Innovation - Horizon 2020 - Grant Agreement No 721383.



*Keywords:* Topology optimization, Additive manufacturing, overheating, Thermal modelling

*Front & Back:* Rajit Ranjan

Copyright © 2023 by R. Ranjan

ISBN 978-94-6384-428-4

An electronic version of this dissertation is available at  
<http://repository.tudelft.nl/>.

# CONTENTS

<b>Summary</b>	<b>ix</b>
<b>Samenvatting</b>	<b>xi</b>
<b>1 Introduction</b>	<b>1</b>
1.1 Additive manufacturing: background . . . . .	2
1.1.1 Historical perspective . . . . .	2
1.1.2 Working principle . . . . .	4
1.1.3 Enhanced design freedom . . . . .	4
1.2 Motivation . . . . .	5
1.2.1 Overheating in L-PBF . . . . .	5
1.2.2 Need for computational design: Topology optimization . . . . .	6
1.2.3 Challenges: computational times and modelling simplifications . . . . .	9
1.3 Research objective . . . . .	9
1.4 Outline of this thesis . . . . .	10
<b>2 Classification and analysis of common simplifications in part-scale thermal modelling of metal additive manufacturing processes</b>	<b>15</b>
2.1 Introduction . . . . .	16
2.2 Classification of simplifications . . . . .	18
2.3 Model description . . . . .	20
2.4 Numerical experiments . . . . .	21
2.4.1 Mesh considerations . . . . .	22
2.4.2 Influence of in-plane lumping . . . . .	24
2.4.3 Influence of heating time . . . . .	27
2.4.4 Influence of out-of-plane lumping . . . . .	29
2.5 Discussion . . . . .	30
2.6 Recommendations . . . . .	33
2.7 Conclusions . . . . .	36
<b>3 Fast Detection of Heat Accumulation in AM Using Computationally Efficient Thermal Models</b>	<b>43</b>
3.1 Introduction . . . . .	45
3.2 Reference thermal LPBF process model . . . . .	48
3.2.1 Model description . . . . .	48
3.2.2 Finite element analysis and simulation parameter setting . . . . .	50
3.2.3 Identification of overheating zones . . . . .	51

3.3	Thermal modeling simplifications and comparison metrics . . . . .	56
3.3.1	Influence of neglecting convective and radiative heat losses . . . . .	56
3.3.2	Novel simplifications motivated by one-Dimensional heat transfer analysis . . . . .	57
3.3.3	Comparison metrics . . . . .	64
3.4	Numerical results and discussion . . . . .	65
3.4.1	Hotspot Map without considering convective/radiative heat losses . . . . .	65
3.4.2	Hotspot Map without considering temperature-dependent properties . . . . .	66
3.4.3	Hotspot Map with temporal decoupling . . . . .	66
3.4.4	Hotspot Map with spatial decoupling . . . . .	67
3.4.5	Hotspot Map with steady-state analysis . . . . .	67
3.4.6	Comparative analysis . . . . .	67
3.5	Conclusions and future work . . . . .	68
<b>4</b>	<b>Controlling Local Overheating in Topology Optimization for Additive Manufacturing</b>	<b>79</b>
4.1	Introduction . . . . .	80
4.2	Simplified AM model and modifications for TO integration . . . . .	83
4.2.1	Hotspot detection . . . . .	83
4.2.2	Adaptation for TO integration: Normalization . . . . .	85
4.3	Numerical implementation . . . . .	87
4.4	Defining critical temperature using a geometry-temperature relationship . . . . .	90
4.5	Integration with TO . . . . .	92
4.5.1	Problem definition . . . . .	92
4.5.2	Topology optimization . . . . .	94
4.5.3	Robust topology optimization . . . . .	96
4.5.4	Evaluation using high fidelity transient simulation . . . . .	98
4.6	Parameter study . . . . .	98
4.6.1	Influence of hotspot analysis parameters . . . . .	98
4.6.2	Influence of part orientation . . . . .	106
4.7	Comparison with geometry based TO method . . . . .	107
4.8	Extension to 3D . . . . .	109
4.9	Conclusions . . . . .	110
<b>5</b>	<b>A 3D Topology optimization method and experimental validation for controlling local overheating in AM</b>	<b>117</b>
5.1	Introduction . . . . .	119
5.2	Hotspot detection . . . . .	121
5.3	Topology optimization . . . . .	125
5.3.1	Test problem and TO approaches . . . . .	125
5.3.2	Optimized TO designs and hotspot fields . . . . .	128
5.4	Experimental procedures . . . . .	132
5.5	Results . . . . .	134
5.5.1	Data visualization and first impressions . . . . .	135
5.5.2	Influence of short hatches . . . . .	136



5.5.3	Comparison for evaluating overheating behavior . . . . .	137
5.5.4	Correlation with defects . . . . .	138
5.6	Discussion . . . . .	142
5.7	Conclusions. . . . .	146
<b>6</b>	<b>Applications</b>	<b>151</b>
6.1	TO of an injection mould insert . . . . .	152
6.2	TO for support structures for efficient heat evacuation . . . . .	153
6.2.1	Problem formulation. . . . .	157
6.2.2	Support optimization . . . . .	160
6.2.3	2D results . . . . .	161
6.2.4	3D results . . . . .	162
6.3	Conclusions. . . . .	164
<b>7</b>	<b>Conclusions and Recommendations</b>	<b>167</b>
7.1	Conclusions. . . . .	167
7.2	Recommendations . . . . .	169
7.2.1	Thermal modelling of AM . . . . .	169
7.2.2	Mechanical aspects . . . . .	171
7.2.3	Extensions . . . . .	171
<b>A</b>	<b>A numerical study using analytical solution for 1D heat transfer</b>	<b>173</b>
<b>B</b>	<b>Derivation of Analytical Solution for One-Dimensional Heat Eq.</b>	<b>177</b>
<b>C</b>	<b>Appendix: Sensitivity Analysis of the hotspot constraint</b>	<b>181</b>
	<b>List of Publications</b>	<b>183</b>
	<b>Acknowledgements</b>	<b>185</b>
	<b>Curriculum Vitae</b>	<b>187</b>



# SUMMARY

With the advent of Additive Manufacturing (AM) techniques, the design principle of 'form follows function' no longer remains a utopian proposition. The increase in design freedom requires novel design tools which are tailored to capitalize on the form freedom offered by AM. Topology optimization (TO) is such a computational design tool which can find the optimal geometric layout of a part to achieve a pre-defined objective, while satisfying certain constraints. However, AM processes have inherent manufacturing constraints which should be considered at the design stage to ensure manufacturability. The suitability of TO as an ideal design tool is already widely recognized and there have been significant research efforts to integrate AM constraints within TO. In this regard, most AM-oriented TO methods utilize geometry-based constraint where a geometric AM design guideline is integrated within TO. The maturity of research in this direction is evident by the fact that most commercial CAD packages are already equipped with TO plugins including these geometry-based AM constraints. Although beneficial, such geometry-based TO constraint do not guarantee defect-free fabrication since manufacturability is not only a function of geometry, but depends on a range of complex physical interactions during the process. Therefore, a TO method that accounts for more of the physics of the AM process would enhance the likelihood of achieving better quality parts with reduced defects.

This thesis is focused on laser based powder bed fusion (L-PBF) since it is the most widely utilized AM technique for metal parts. However, L-PBF suffers from certain constraints which critically compromise the part quality and inhibit its adoption as a mainstream manufacturing method. Among the constraints, the issue of *local overheating* remains a critical barrier as it leads to poor surface quality, inferior mechanical properties and/or build failures. Moreover, uneven heating/cooling thermal cycles due to overheating could lead to development of undesirable residual stresses and distortions. Typically, overheating is associated with downfacing surfaces called overhangs which led to development of geometry-based design guidelines, for example, avoidance of geometric features with overhangs more acute than a certain threshold. This guideline has been the most common AM constraint to integrate within TO. However, it is evident by a number of numerical and experimental studies in the literature, that the avoidance of overhangs does not guarantee overheating free designs. Therefore, the two aims of this thesis are (1) to thoroughly investigate local overheating during L-PBF process using computational models and (2) to develop a novel TO for generating overheating free AM ready designs. In this regard, the extremely high computational cost of L-PBF models was identified as the biggest challenge for both the objectives *i.e.* quick assessment of overheating-prone features in AM parts and integration of a L-PBF thermal model with TO.

The first half of this thesis deals with a systematic investigation of the simplifications commonly used in the thermal modelling of the heat transfer phenomena during the L-PBF process. With help of numerical experiments, the findings reveal the relationship between spatio-temporal simplifications and their ability to capture certain process attributes. For example, it is found that if peak process temperatures are to be predicted, then short laser exposure times should be specified in the computational domain. On the contrary, if temperatures far away from the topmost layer are analyzed, a simplified model assuming a longer exposure time can capture it. These findings serve as guidelines in making informed choices while setting up an L-PBF thermal model. In addition to this, numerical discretization requirements associated with different simplifications are also provided. Next, a deeper investigation of relevant simplifications for detecting local overheating is presented. Three novel simplifications based on the analytical solution of the heat equation are presented which drastically reduce the computational expense while retaining the ability to identify overheating prone features. The most simplified model in this regard utilizes a localized steady-state analysis which provides maximum computational gain of approximately 600 fold as compared to a high fidelity transient simulation.

The second half of the thesis presents the integration of the aforementioned steady-state L-PBF thermal model with the density- based TO method. This is achieved by formulating a novel constraint which limits the peak temperature predicted by the simplified L-PBF model. This novel physics-based TO method is validated using in-situ optical tomography (OT) measurements. Comparing OT based overheating data across geometry-based and physics-based TO designs, it is revealed that the latter have a lower tendency of overheating. Finally, the usability of the new TO method is demonstrated on an industrial injection mould. Another application of the novel TO is demonstrated by designing support structures for optimal heat evacuation.

Based on the findings presented in thesis, it can be concluded that a physics-based TO method offers significant advantages over a purely geometry-based approach. In particular, it is shown that overheating avoidance cannot be assured just by avoiding acute overhangs. While for overheating detection even a simplification to steady-state analysis was possible, it is expected that for other aspects the full thermal history must be evaluated, which presents a challenge for future work. Apart from development of the novel TO approach, the second major contribution of this thesis are the insights developed regarding modelling simplifications which assist in drastically reducing the computational expenses associated with L-PBF modelling. It is expected that outcomes from this thesis will positively contribute towards development of efficient modelling techniques which will also inherently benefit further advancement of physics-based TO methods.

# SAMENVATTING

Met de opkomst van Additive Manufacturing (AM) technieken, is het ontwerpprincipe 'de vorm volgt de functie' niet langer een utopie. De toegenomen ontwerprijheid vereist nieuwe ontwerptools die erop zijn toegesneden om zoveel mogelijk voordeel te halen uit de vormvrijheid die AM geeft. Topologie optimalisatie (TO) is zo'n ontwerptool dat de optimale geometrische layout van een onderdeel kan vinden om een van te voren gedefinieerd doel te bereiken rekening houdend met bepaalde beperkende voorwaarden. AM processen hebben echter inherente vervaardigingsbeperkingen, waarmee reeds in de ontwerpfase rekening moet worden gehouden om de maakbaarheid te garanderen. De geschiktheid van TO als de ideale ontwerptool wordt al breed erkend en er zijn grote onderzoeksinspanningen verricht om de beperkende voorwaarden van AM te integreren in TO. De meeste AM-georiënteerde TO methoden gebruiken op geometrie gebaseerde restricties om geometrische AM ontwerprichtlijnen op te nemen in de TO. De rijpheid van onderzoek in deze richting wordt geïllustreerd door het feit dat de meeste commerciële CAD pakketten al zijn uitgerust met TO plug-ins die beschikken over deze op geometrie gebaseerde AM restricties. Hoewel dit een stap in de juiste richting is, garanderen dergelijke op geometrie gebaseerde beperkende voorwaarden in TO geen fabricage zonder defecten aangezien maakbaarheid niet alleen een functie is van geometrie, maar afhangt van een scala aan complexe fysische interacties tijdens het maakproces. Een TO methode die beter rekening houdt met de fysica van het AM-proces zou de kans vergroten op onderdelen van betere kwaliteit met minder defecten.

Dit proefschrift richt zich op Laser Based Powder Bed Fusion (L-PBF) omdat dit de meest gebruikte AM-techniek is voor metalen onderdelen. L-PBF heeft echter last van bepaalde restricties die de kwaliteit van de onderdelen ernstig compromitteren en dit belemmert de brede toepassing van deze productiemethode. Onder de restricties is het probleem van lokale oververhitting nog altijd een ernstig obstakel omdat dit leidt tot een slechte oppervlaktekwaliteit, inferieure mechanische eigenschappen en/of productiefouten. Ongelijkmatige thermische cycli voor verwarming/afkoeling door oververhitting kunnen bovendien leiden tot de ontwikkeling van onwenselijke restspanningen en vervormingen. Oververhitting wordt doorgaans geassocieerd met naar beneden gerichte oppervlakken die overhangen worden genoemd, welke hebben geleid tot de ontwikkeling van op geometrie gebaseerde ontwerprichtlijnen, bijvoorbeeld het vermijden van vormen met overhangen voorbij een bepaalde drempelwaarde. Deze richtlijn is de meest voorkomende restrictie in AM die in de TO is geïntegreerd. Een aantal numerieke en experimentele studies in de literatuur hebben echter aangetoond dat het vermijden van overhangen geen garantie is voor het voorkomen van oververhitting. De twee doelstellingen van dit proefschrift zijn derhalve (1) om de lokale oververhitting gedurende het L-PBF proces grondig te onderzoeken, gebruikmakend van computermodellen en (2) om een nieuwe TO methode te ontwikkelen om voor AM geschikte ontwerpen te ge-

nereren zonder oververhittingsrisico. De extreem hoge rekentijd van L-PBF modellen vormt hierbij de grootste uitdaging voor beide doelstellingen, d.w.z. voor een snelle beoordeling van kenmerken in AM onderdelen die vatbaar zijn voor oververhitting en de integratie van een L-PBF thermisch model in TO.

De eerste helft van dit proefschrift richt zich op een systematisch onderzoek naar de vereenvoudigingen die doorgaans gebruikt worden in de thermische modellering van de warmteoverdracht verschijnselen tijdens het L-PBF proces. Aan de hand van numerieke experimenten wordt de relatie onthuld tussen reductie van ruimtelijke en temporele resolutie en het bijbehorende vermogen om bepaalde proceseigenschappen te beschrijven. Er is bijvoorbeeld ontdekt dat als piekprocesemperaturen moeten worden voorspeld, er korte laser belichtingstijden moeten worden gespecificeerd in de berekening. Als er temperaturen worden geanalyseerd ver weg van de bovenlaag, daarentegen, kan dit worden bereikt met een vereenvoudigd model dat een langere belichtingstijd ondergaat. Deze bevindingen geven richtlijnen bij het maken van weloverwogen keuzes bij het opzetten van een L-PBF thermisch model. Bovendien worden ook numerieke discretisatievereisten gegeven die bij de verschillende vereenvoudigingen horen. Vervolgens wordt een nader onderzoek gepresenteerd naar relevante vereenvoudigingen voor het detecteren van lokale oververhitting. Er worden nieuwe vereenvoudigingen gepresenteerd gebaseerd op de analytische uitwerking van de warmtevergelijking, die de rekentijd drastisch verminderd met behoud van het vermogen om de voor oververhitting vatbare vormen te identificeren. Het meest vereenvoudigde model in dit verband maakt gebruik van een gelocaliseerde steady-state analyse die een maximale versnelling van de berekening oplevert van ongeveer een factor 600 vergeleken met een nauwkeurige tijdsafhankelijke simulatie.

Het tweede deel van dit proefschrift presenteert de integratie van het genoemde steady-state L-PBF thermische model met de op dichtheid gebaseerde TO methode. Dit wordt bereikt door het formuleren van een nieuwe beperkende voorwaarde die de door het vereenvoudigde L-PBF model voorspelde piektemperatuur begrensd. Deze nieuwe op fysica gebaseerde TO methode wordt gevalideerd met behulp van in-situ optische tomografie (OT) metingen. Als OT oververhittingsgegevens worden vergeleken met zowel op geometrie als op fysica gebaseerde TO ontwerpen, wordt duidelijk dat de laatsten minder neigen naar oververhitting. Tenslotte wordt de bruikbaarheid van de nieuwe TO methode aangetoond op een industriële spuitgietmatrijs. Een andere toepassing van de nieuwe TO methode wordt gedemonstreerd door het ontwerpen van ondersteuningsstructuren voor een optimale warmteafvoer.

Gebaseerd op de bevindingen in dit proefschrift kan de conclusie worden getrokken dat een op fysica gebaseerde TO methode aanzienlijke voordelen biedt boven een benadering die enkel op geometrie is gebaseerd. In het bijzonder wordt aangetoond dat het voorkomen van oververhitting niet alleen kan worden gegarandeerd door het vermijden van kritische overhangende delen. Terwijl voor de opsporing van oververhitting zelfs een vereenvoudiging naar een steady-state analyse mogelijk blijkt, is de verwachting dat voor andere aspecten de volledige thermische geschiedenis moet worden geëvalueerd,

wat een uitdaging vormt voor toekomstig onderzoek. Behalve de ontwikkeling van de nieuwe TO benadering, is de tweede belangrijke bijdrage van dit proefschrift de ontwikkelde inzichten aangaande de vereenvoudiging van de modellen die helpen bij het drastisch verminderen van de rekentijd voor L-PBF modellering. Verwacht wordt dat de resultaten van dit proefschrift een positieve bijdrage zullen leveren aan de ontwikkeling van efficiënte modelleringstechnieken die ook inherent zullen bijdragen aan de verdere ontwikkeling van op fysica gebaseerde TO methoden.





# 1

## INTRODUCTION

*Adam Smith, widely considered father of Economics, discussed the economic significance of manufacturing in his famous 1776 book 'Wealth of Nations' [42]. Currently, manufacturing is an important contributor in the economic growth of any nation and it enables many technological advancements. The relatively recent and disruptive technology of Additive Manufacturing (AM) has altered the outlook of technology experts towards manufacturing. It is seen as an opportunity to realize new designs and design methods, cost-effective customization and democratization of manufacturing practices. In the past three decades, AM technology has made the transition from being a prototyping tool to become a mainstream industrial manufacturing method. Today, it finds widespread applications in industries ranging from aerospace, automotive, biomedical to fashion, food and entertainment. According to Wohlers Report, 2019, AM has grown into an industry with a sales revenue in excess of \$9 billion annually and a forecast suggests that the global AM industry is predicted to reach a size of \$70 billion in the year 2025. The primary competitive advantage that AM provides against other fabrication techniques is the immense design freedom it offers and traditional design practices are simply not suitable for efficiently leveraging it. However, the AM process still suffers from number of critical constraint which, if overlooked, could lead to serious defects. This factor also calls for efficient design methodologies which could address AM constraints during the design stage. Therefore, further research and development of AM techniques, especially for developing powerful design tools, will be instrumental in fulfilling the ever-increasing demands of the modern world.*

---

Parts of this chapter have been published in [Precision Metal Additive Manufacturing, Chapter 2: Topology Optimisation Techniques \(CRC Press, 2020\)](#).

## 1.1. ADDITIVE MANUFACTURING: BACKGROUND

### 1.1.1. HISTORICAL PERSPECTIVE

*"But this constructor is both efficient and flexible. I feed magnetronic plastics — the stuff they make houses and ships of nowadays — into this moving arm. It makes drawings in the air following drawings it scans with photo-cells. But plastic comes out of the end of the drawing arm and hardens as it comes. This thing will start at one end of a ship or a house and build it complete to the other end, following drawings only."*

This is an excerpt from a 1945 science fiction short story titled 'Things pass by' from the American author Murray [1]. The 'constructor' described in this 75 year old literary work has an uncanny resemblance with a modern day Additive Manufacturing (AM) machine, also referred to as a '3D printer'. The ideas associated with AM can be traced to even earlier periods in history. In the year 1861, François Willème, a French artist, filed a patent for developing a process called *sculpture photographique* (photographing sculpture) which used photographic and mechanical means for 3D modelling of the human body [46]. The subject/object was placed in a circular room and simultaneously photographed by 24 cameras placed at a regular angular intervals. Layers of wood were then cut in accordance with the silhouette of each photograph using a Pantograph. Finally, these layers were stacked together to create a 3D model of the subject/object. Another example associated with AM is from the field of topography. The patent by Blather in 1890 [6] described a method for creating 3D maps by cutting and stacking sheets of wax according to topographical elevations. Another interesting patent by Baker in 1925 [4] presented a method which used a moving weld head for creating 3D objects, shown in Figure 1.1a.

A number of concepts were patented during 1950–80 which can be seen as an immediate predecessor to the modern day AM techniques [15]. Among these, the patent by Ciraud is shown in Figure 1.1b [9]. It describes a part being fabricated in a layer-by-layer manner using an energy source and (re-cycled) metal powder, resembling the modern day direct energy deposition (DED) technique. Another patent by Housholder [18] described selective sintering of powdered metal. It is interesting to note that there were significant contributions conceptualizing many key concepts related with AM technologies, yet recognition of AM as a viable technology, even for prototyping, was waiting for another disruptive innovation: commercialization of desktop computers [17].

With increasing use of computers in manufacturing and emergence of direct numerical control, three patents were filed in the 1980s which are generally considered as the birth of industrial AM. These were associated with three separate classes of AM processes. The first patent was associated with Stereolithography which was invented for fast prototyping. UV light is used in Stereolithography for curing photosensitive polymers in a layer-by-layer manner. Chuck Hull, an American inventor, is generally credited with patenting the idea in 1986 and coining the term [19]. Curiously, a group of French inventors, led by Alain Le Méhauté, filed a patent three weeks earlier than Chuck Hull. Their patent was rejected on the ground of 'lack of business perspective'. Chuck Hull founded 3D Systems which developed SLA-1, the first ever commercial AM machine.

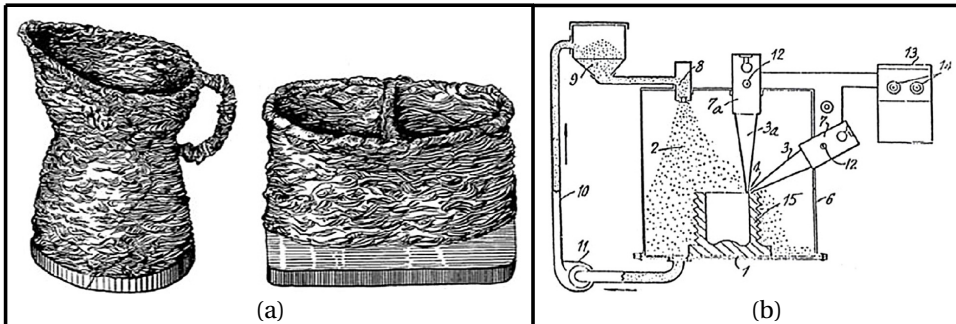


Figure 1.1: (a) Creation of 3D objects using weld overlay from a 1925 patent [4]. (b) A patent from 1972 shows a manufacturing process with metal powder (2) deposited used an energy source (7) for creating a 3D part (15) on a baseplate (1) [9].

The second patent was filed by Carl R. Deckard and Joe Beamen in 1986 [14] on a process where a laser is used for solidifying polymer powder particles. The technology was leased to DTM Inc. which was founded by Deckard and Beamen and the first commercial Selective Laser Sintering (SLS) machine was launched in 1991. Lastly, the third patent was filed by Scott Crump in 1989 [12] and considered creation of 3D objects by depositing multiple layers of a material in a fluid state onto a base. He later founded Stratysys Inc. which launched the first 'Fused deposition modelling' (FDM) machine. In the years following their inventions, these techniques were mainly used for prototyping, generally using polymers. However, advances in metal AM machines and processes in mid-1990s led to increased utilization of these techniques as mainstream manufacturing, impacting industries such as aerospace, defence, biomedical, and automotive [28].

In the context of metal AM, the SLS process invented by Deckard was thoroughly improved at the Fraunhofer Institute, Aachen, Germany and the term 'Selective Laser Melting' (SLM) was coined [27]. A significant amount of research in improving this process was also done at KU Leuven, Belgium [21], leading to formation of two spin-off companies: Materialise and LayerWise (now acquired by 3D Systems). Electro optical system (EOS) GmbH was founded in 1989 which commercialized the process under the name of Direct Metal Laser Sintering (DMLS) and remains to be global leader in industrial metal AM techniques. Based on the collaboration with Chalmers University of Technology, Gothenburg, the company Arcam was founded in 1997 which used an electron beam as the heat source, instead of a laser. These metal AM processes are now collectively referred to as powder bed fusion (PBF) with prefixes L-PBF and E-PBF indicating laser and electron beam, respectively. In this thesis, the focus remains on L-PBF as it is the most popular choice for creating precision metal AM parts.

### 1.1.2. WORKING PRINCIPLE

A schematic illustrating the working principle of L-PBF process is shown in Figure 1.2. The process involves spreading of a metal powder layer using a re-coater arm. Typically, the powder-layer thickness ranges between 20–80  $\mu\text{m}$  [33]. Next, a focused laser beam is utilized for selectively melting and fusing the newly laid powder layer. The laser beam, controlled by a scanning mirror, traverses a predefined scanning path which is based on the layer contour information obtained from the CAD model of the part being built. The powder bed is lowered after scanning each layer by an amount equal to the layer thickness and subsequently a new layer of powder is laid using the re-coater arm. In general, the laser energy is calibrated such that it melts the powder along with several previously deposited layers which ensures a seamless fusion across the layers [22]. The powder particles locally melt, fuse together and re-solidify to form a solid 3D shape, while the loose powder remains in the vicinity. For certain geometries, loose powder does not sufficiently support the layer above and therefore, sacrificial solid support structures are printed in order to provide the necessary mechanical support and conduct away the excess heat. Finally, the loose powder is cleaned off and the part is detached from the baseplate. Post-processing efforts such as support removal, finishing operations and heat treatment are often required.

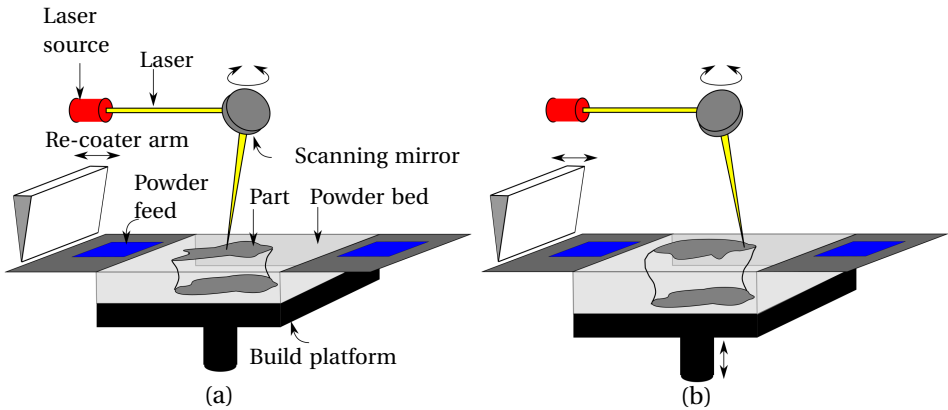


Figure 1.2: Schematic representation of Laser powder bed fusion (L-PBF) process. (a) The scanning mirror controls the position of laser beam on the powder bed which in turn selectively melts the powder which fuses with the existing part. (b) Once a layer has been deposited, the build platform moves downwards and the re-coater arm spreads a new layer of powder for scanning of the next layer.

### 1.1.3. ENHANCED DESIGN FREEDOM

For a conventional manufacturing method, such as milling, drilling and casting, cost is directly related to the geometric complexity of the part. In contrast, due to its inherent layer-by-layer fabrication method, L-PBF allows for fabricating metallic parts with immense geometric complexity without having a direct impact on manufacturing cost. The increased design freedom allows for achieving higher efficiency components which

were previously not possible to manufacture. The re-design of a General Electric (GE) fuel nozzle shown in Figure 1.3a is a representative case where L-PBF increased product efficiency while providing significant cost savings. The new design provided functional integration of 20 separate parts, thereby reducing the assembly efforts. The process resulted in 25% reduction of mass which, along with increased efficiency, led to a savings of three million dollar per aircraft, per year. Another example of an AM re-design is the ASML conditioning ring shown in Figure 1.3b. L-PBF allowed for more complex integrated cooling channels that improve the thermal performance by a factor of six. Both of these industrial examples demonstrate design freedom offered by L-PBF for improving the part performance [28].

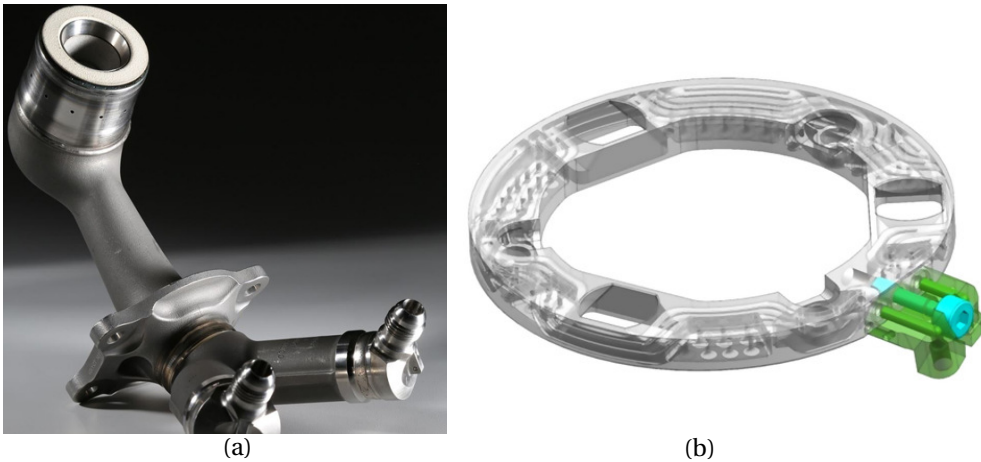


Figure 1.3: (a) The re-design of the GE fuel nozzle printed using the DMLS process. The nozzle provides functional integration of twenty separate parts while providing 25% reduction in mass. (b) Re-design of the ASML conditioning ring. AM facilitates design of more complex integrated cooling channels that improve the thermal performance by a factor of six. Reproduced from Leach and Carmignato [28] with permission.

## 1.2. MOTIVATION

### 1.2.1. OVERHEATING IN L-PBF

The L-PBF process is typically used for fabricating complex, high-performance metal AM parts. However, it is well known that the process is not free from limitations and, if overlooked, these limitations can cause various types of defects in the final parts. Defects lead to increased costs, as additional post-processing steps are required to address them. Moreover, in certain cases, defects lead to complete build failure [20] or a poor-quality part [32]. This issue is even more important for precision parts. One critical process limitation is that of local overheating or heat accumulation. The unmolten powder, which has significantly lower and non uniform thermal conductivity compared to the bulk material, does not allow for proper heat evacuation for a newly deposited layer [32]. This leads to an increase in the size of the melt pool, which could result in surface

defects such as dross and balling [41]. Examples of dross formation defects are shown in Figure 1.4a and c. Moreover, for high-quality AM parts, precise control of material microstructure is desired, and local overheating has an adverse effect on microstructural control [29]. The heating/cooling cycles experienced during the process cause thermal expansion and contraction, eventually leading to development of residual stresses which result in significant distortions in the final part, shown in Figure 1.4d. It is reported that zones prone to localised overheating are more susceptible to distortions which compromise precision [34]. In the study presented by [20], distortions due to local overheating lead to collision with the re-coater blade resulting in complete build failure. Therefore, it is clearly evident that local overheating is the root cause for several AM limitations.

Typically, the issue of overheating is associated with overhangs. This led to development of geometry based design rules which prescribe that downfacing surfaces below a critical value  $\theta^{\text{cr}}$  should be avoided. Here, overhang angles are defined as the angle between part surface and horizontal baseplate. So far, the issue is primarily dealt with a geometrical restriction and a number of experimental studies have determined the critical overhang angle, typically ranging between  $40^\circ$ – $50^\circ$  [11, 45]. However, recent experimental and numerical findings indicate that overhang control does not ensure overheating avoidance. For example, a specimen manufactured by Adam and Zimmer [2], shown in Figure 1.4b demonstrates overheating induced discoloration in the top region. The thin member in the lower part of the design acts as a thermal bottleneck for heat conduction when top layers are being deposited. This example shows features within a part with identical overhang angle can have different overheating behaviours. Next, the specimen fabricated by Patel et al. [35], shown in Figure 1.4a, demonstrates overheating induced dross leading to high surface roughness. Note that specimens in both these cases strictly follow the overhang design guideline, yet overheating is observed. Alternatively, when acute overhangs cannot be avoided, support structures are used for conducting away the excess heat [23]. However, an industrial vacuum seal manufactured by KMWE is shown in Figure 1.4c where overheating induced dross could not be avoided even after using support structures [28]. These experimental findings confirm that both overhang control and use of supports are not enough to avoid overheating.

### 1.2.2. NEED FOR COMPUTATIONAL DESIGN: TOPOLOGY OPTIMIZATION

The industrial examples presented in Section 1.1.3 showcase how AM can improve functional performance by taking advantage of the increased design freedom. However, the complications associated with the design process also increase significantly. Typically, multi-physics and multi-scale simulations are required to evaluate the functional performance of the industrial designs, especially in precision applications. This is far from trivial, making the design process complex and computationally involved. Furthermore, the dimensional tolerance requirements for such precision applications are typically tight. The second challenge associated with design process are the AM process limitations, as discussed in Section 1.2.1. Due account for the process limitations should be made during the design stage so that parts are easily manufacturable. Both these challenges collectively call for powerful computational design techniques.

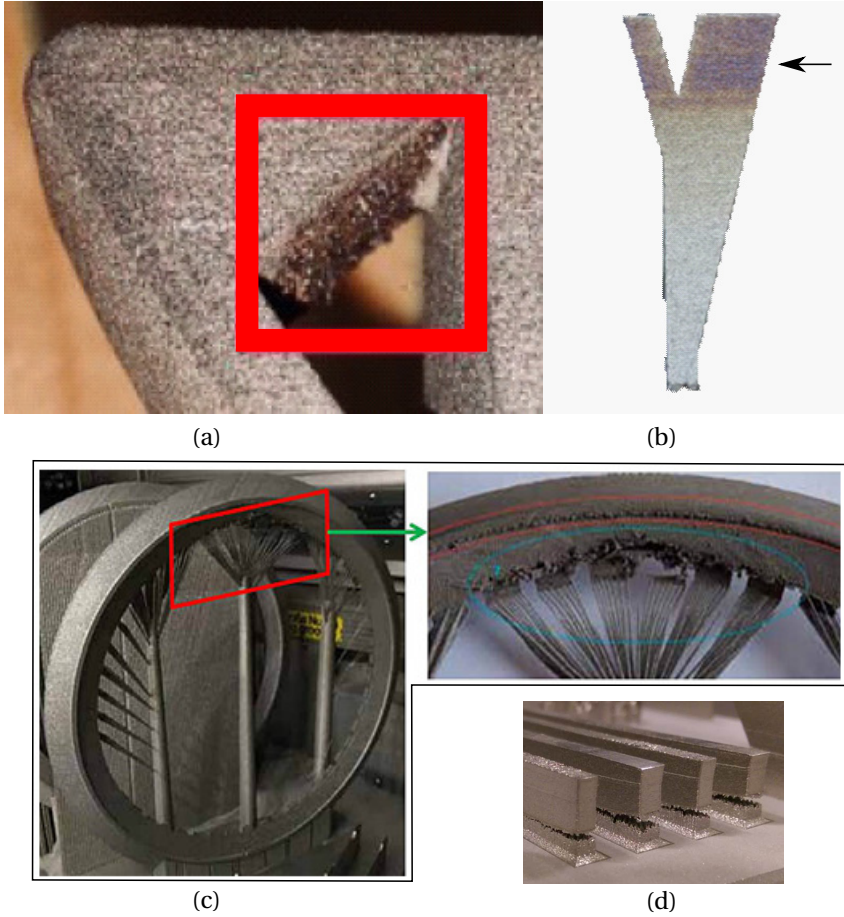


Figure 1.4: (a) Dross observed even after following the overhang design rule [35]. (b) SLM part showing local overheating effects because of insufficient heat dissipation. Here, heavy discoloration (marked by arrow) is an indicator of elevated temperatures. Reproduced from Adam and Zimmer [2] with permission. (c) A vacuum seal manufactured using L-PBF. The final printed part has heavy dross defects in the overhanging region. Thin supports were used to conduct away the excess heat, but were not effective enough [28]. (d) The build-up of residual stresses in the part during the AM process results in part distortion and, in extreme cases, part failure. [28]

In this context, topology optimization (TO) is highly beneficial for AM products as it allows for systematic mathematical exploration of the design space. It is a computational design method which aims to answer a fundamental engineering question: where to place material inside a design domain to get the best performance? The seminal paper by Bendsøe [5] on TO demonstrated the method by solving mechanical design problems, for example, finding the optimal material distribution having maximum stiffness for a predefined load. Over time, TO has evolved significantly and found other application fields, for example, fluid dynamics, heat transfer, optics, electromagnetics and their combinations. One of the advantages of TO is that it allows to address both functionality and manufacturability in a mathematically rigorous setting. Due to this, the potential of TO as the ideal tool for designing AM parts has been recognized widely [13].

In the context of addressing AM constraints within a TO framework, Clausen [10] proposed two categories: Non-directional and directional, based on their relationship with build orientation. Examples of non-directional constraints are feature size control and cavity avoidance. The minimum printable feature size for any given manufacturing process needs to be taken into account for ensuring manufacturability. Hence, multiple authors have addressed the issue of length scale within TO, see Lazarov, Wang, and Sigmund [26] for a review. A recent study by Pellens et al. [38] considered length scale particularly in context of TO for AM. The other example of a non-directional constraint is cavity avoidance as completely enclosed holes do not allow for powder evacuation. The ‘virtual temperature method’ presented by Liu et al. [31] accomplishes this by treating enclosed void regions as virtual heat source while constraining the maximum temperature. Unlike these, the directional constraints are in some way related with the build orientation and the most popular example of such a constraint is overhang avoidance.

Overhang control or avoidance in TO has been a major topic of research. Earlier works such as Brackett, Ashcroft, and Hague [7] and Leary et al. [29] dealt with the problem as a post-optimization step. The more advanced approaches include overhang control within the TO formulation along with sensitivity information. These can be classified into two groups: ‘local boundary angle control’ and ‘geometry based AM model’. The former category of approaches usually converge to -optimal local minima, creating saw-tooth like shapes which are not manufacturable [3, 39]. On the other hand, the latter category consists of methods that scan the topology in printing direction for imposing overhang control [24, 25, 43, 44, 16]. For a comprehensive review of these methods, readers are referred to Liu et al. [30]. All these TO formulations consider overhang control as a purely geometric problem and prohibit acute overhangs. However, as shown in Section 1.2.1, overheating is not necessarily linked with overhang control and designs created using these TO methods can still suffer from the overheating defects. This calls for a TO method which is directly related to the physics of the process and considers the thermal behavior during L-PBF.



### 1.2.3. CHALLENGES: COMPUTATIONAL TIMES AND MODELLING SIMPLIFICATIONS

In theory, a highly detailed process model, which captures the complex physical interactions during the L-PBF process, can be coupled with TO. However, the computational burden associated with such a model makes this an unrealistic approach for practical and industrial applications. For example, Patil et al. [36] reported a simulation time of 12.3 days for a high-fidelity simulation of an AM part (40 mm × 1.5 mm × 2 mm) using 1440 processors and parallel computing. L-PBF is essentially a multi-scale process as it typically involves high-energy laser beams with spot size diameter of the order of 80 μm (micro-scale) for fabricating parts that have dimensions up to 30 cm (macro-scale). Moreover, in the time domain, the phenomenon of melting and re-solidification is extremely fast, whereas the fabrication process can last up to days for large and complex parts. On top of this, it is a multi-physics process in which heat transfer, fluid dynamics, solid mechanics and phase transformations play critical roles [33]. Incorporating all these aspects while spanning a large range of spatio-temporal scales forms a tremendous computational challenge. In the context of TO, it becomes even more challenging as design evaluation, process simulation and the associated sensitivity computations have to be conducted for every design iteration, and typically repeated hundreds of times.

In order to reduce the computational times, it is a common practice to introduce simplifications while modelling the L-PBF process. For example, modelling an entire layer deposition in one simulation step [8] or simulation of thicker lumped layers [47] are examples of such commonly used simplifications. Another option is to use simplifications associated with the underlying physics. For example, some studies exclude convection and radiation as a mode of heat transfer while simulating the thermal process [37, 40]. Although beneficial in reducing computation times, the availability of many simplification concepts leads to high variability in modelling choices and it is extremely critical to understand the scope and limitations associated with each simplification before using it. This understanding would greatly help in selecting the appropriate set of simplifications for the given purpose of the L-PBF model.

## 1.3. RESEARCH OBJECTIVE

The primary aim of this thesis is to improve the designs and manufacturability of L-PBF parts by addressing the issue of local overheating using TO and physics-based modelling. TO allows for leveraging the enhanced design freedom while direct overheating control enhances manufacturability. Utilization of physics-based models for detecting overheating provides clear advantages over geometry-based overhang restrictions which are insufficient for ensuring manufacturability. However, first an 'adequate' L-PBF process model is required which can sufficiently capture the issue of local overheating in a computationally inexpensive manner. As discussed in Section 1.2.3, many simplifications are already available in literature. However, it is not yet clear that what are the implications of using any such simplification on the accuracy of the model, especially in

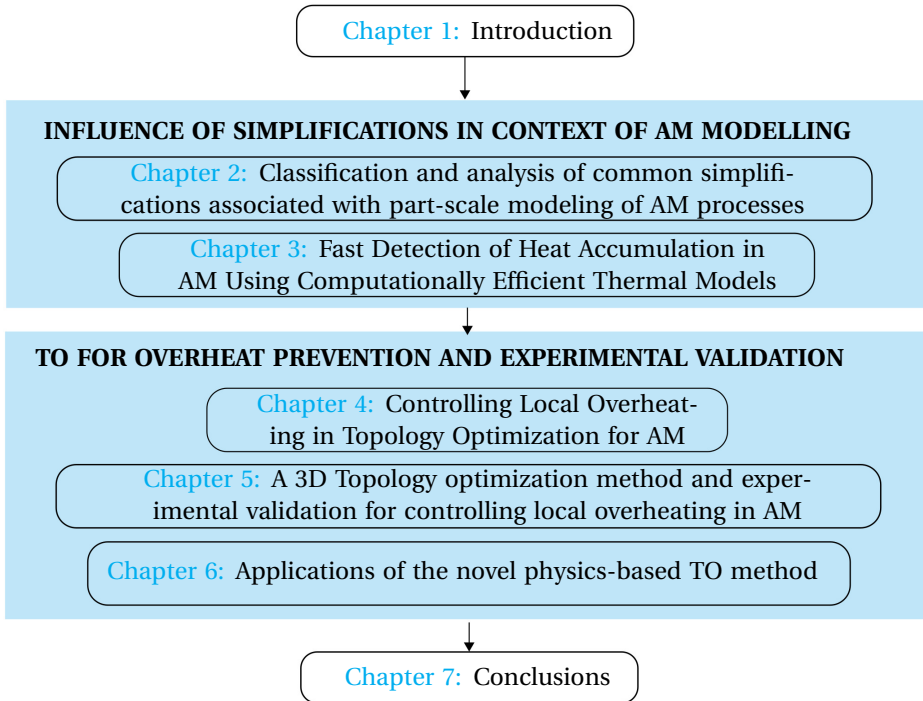


Figure 1.5: Visual outline of this thesis. The thesis is divided into seven chapters with two blocks addressing the two research questions.

the context of predicting overheating. Given the research objective as stated above, the following two research questions are deduced:

1. *What is the impact of commonly used simplifications in the context of thermal modelling of the AM process and which simplifications can be used to correctly predict the local overheating issue?*
2. *How can TO be used to obtain well-performing designs which are free from overheating-induced defects?*

#### 1.4. OUTLINE OF THIS THESIS

The structure of the thesis is shown in Figure 1.5. The first block is about systematically characterizing the influence of different modelling simplifications in the context of part-scale thermal modelling of the AM process. Within this block, Chapter 2 deals with developing a generalized understanding on simplifications and how they influence model accuracy. Chapter 3 focuses on the influence of simplifications specifically in the context of overheating prediction during part fabrication. Both these chapters collectively answer Research Question 1 and lead to development of an L-PBF process model

which can detect overheating in a computationally inexpensive manner. In the second block, this novel process model is integrated with TO and this new physics-based approach is referred to as hotspot-based TO. Chapter 4 presents the idea of hotspot-based TO and thoroughly analyzes its implementation in 2D setting while 3D extension is also presented. The experimental validation of the hotspot-based TO is carried out using in-situ monitoring based optical tomography technique and findings are presented in Chapter 5. In Chapter 6, two applications of the novel hotspot-based TO are presented where the problem is re-formulated from the context of optimizing support structures. Finally, Chapter 7 presents the conclusions and recommendations.

## REFERENCES

- [1] *'Things Pass by', Short story by Murray Leinster.* <https://archive.org/details/ThrillingWonderStoriesV27N021945Su/page/n9/mode/2up?view=theater>. Accessed: 6-10-2021.
- [2] Guido A.O. Adam and Detmar Zimmer. "Design for Additive Manufacturing—Element transitions and aggregated structures". In: *CIRP Journal of Manufacturing Science and Technology* 7.1 (2014), pp. 20–28. ISSN: 1755-5817.
- [3] G. Allaire, C. Dapogny, R. Estevez, A. Faure, and G. Michailidis. "Structural optimization under overhang constraints imposed by additive manufacturing technologies". In: *Journal of Computational Physics* 351 (2017), pp. 295–328. ISSN: 0021-9991.
- [4] Ralph Baker. *Method of making decorative articles*. U.S. Patent 473901, Apr. 1925.
- [5] Martin Bendsøe. "Optimal Shape Design as a Material Distribution Problem". In: *Structural Optimization* 1 (Jan. 1989), pp. 193–202.
- [6] Joseph E. Blanthier. *Manufacture of contour relief-maps*. U.S. Patent 473901, May. 1892.
- [7] D. Brackett, Ian Ashcroft, and Richard Hague. "Topology optimization for additive manufacturing". In: *22nd Annual International Solid Freeform Fabrication Symposium - An Additive Manufacturing Conference, SFF 2011* (Jan. 2011), pp. 348–362.
- [8] Michele Chiumenti, Eric Neiva, Emilio Salsi, Miguel Cervera, Santiago Badia, Joan Moya, Zhuoer Chen, Caroline Lee, and Christopher Davies. "Numerical modelling and experimental validation in Selective Laser Melting". In: *Additive Manufacturing* 18 (2017), pp. 171–185. ISSN: 2214-8604.
- [9] Pierre A Ciraud. "Process and Device for the Manufacture of any Objects Desired from any Meltable Material". In: *FRG Disclosure Publication 2263777* (1972).
- [10] Anders Clausen. "Topology Optimization for Additive Manufacturing". English. PhD thesis. 2016.
- [11] Michael Cloots, Livia Zumofen, Adriaan Spierings, Andreas Kirchheim, and Konrad Wegener. "Approaches to minimize overhang angles of SLM parts". In: *Rapid Prototyping Journal* 23 (Mar. 2017), pp. 362–369.
- [12] S. Scott Crump. *Apparatus and method for creating three-dimensional objects*. U.S. Patent 5121329, Oct. 1989.

- [13] Joshua Deaton and Ramana Grandhi. “A survey of structural and multidisciplinary continuum topology optimization: Post 2000”. In: *Structural and Multidisciplinary Optimization* 49 (Jan. 2014).
- [14] Carl R. Deckard. *Method and apparatus for producing parts by selective sintering*. U.S. Patent 4863538, Oct. 1986.
- [15] Fair JE Gale PL. *Method of Making Aluminum Piston with Reinforced Piston Ring Groove*. U.S. Patent 4125926, Nov. 1978.
- [16] Andrew T. Gaynor and James K. Guest. “Topology optimization considering overhang constraints: Eliminating sacrificial support material in additive manufacturing through design”. In: *Struct Multidiscip Optim* 54.5 (Nov. 2016), pp. 1157–1172. ISSN: 1615-1488.
- [17] Mikell P. Groover. *Fundamentals of Modern Manufacturing : Materials, Processes, and Systems*. Wiley Sons, Sept. 1996.
- [18] Tex A. Housholder R. *Molding Process*. U.S. Patent 4247508, Jan. 1981.
- [19] Charles W. Hull. *Apparatus for production of three-dimensional objects by stereolithography*. U.S. Patent 4575330, Mar. 1986.
- [20] Darya Kastsian and Daniel Reznik. “Reduction of local overheating in selective laser melting”. In: *In Proceedings of Simulation of Additive Manufacturing (SIM-AM), Munich, Germany*. Oct. 2017.
- [21] J.-P. Kruth, M.C. Leu, and T. Nakagawa. “Progress in Additive Manufacturing and Rapid Prototyping”. In: *CIRP Annals* 47.2 (1998), pp. 525–540. ISSN: 0007-8506.
- [22] Jean-Pierre Kruth, Peter Mercelis, J Van Vaerenbergh, Ludo Froyen, and Marleen Rombouts. “Binding mechanisms in selective laser sintering and selective laser melting”. In: *Rapid prototyping journal* 11.1 (2005), pp. 26–36.
- [23] Yu-Hsin Kuo, Chih-Chun Cheng, Yang-Shan Lin, and Cheng-Hung San. “Support structure design in additive manufacturing based on topology optimization”. In: *Struct Multidiscip Optim* 57.1 (2018), pp. 183–195.
- [24] Matthijs Langelaar. “An additive manufacturing filter for topology optimization of print-ready designs”. In: *Struct Multidiscip Optim* 55.3 (Mar. 2017), pp. 871–883. ISSN: 1615-1488.
- [25] Matthijs Langelaar. “Topology optimization of 3D self-supporting structures for additive manufacturing”. In: *Additive Manufacturing* 12 (2016), pp. 60–70. ISSN: 2214-8604.
- [26] Boyan Lazarov, Fengwen Wang, and Ole Sigmund. “Length scale and manufacturability in density-based topology optimization”. In: *Archive of Applied Mechanics* 86 (Jan. 2016), pp. 1–30.
- [27] R.K. Leach, D. Bourell, S. Carmignato, A. Donmez, N. Senin, and W. Dewulf. “Geometrical metrology for metal additive manufacturing”. In: *CIRP Annals* 68.2 (2019), pp. 677–700. ISSN: 0007-8506.
- [28] Richard Leach and Simone Carmignato. *Precision Metal Additive Manufacturing*. CRC Press, Sept. 2020. ISBN: 113834771X.

- [29] Martin Leary, Luigi Merli, Federico Torti, Maciej Mazur, and Milan Brandt. “Optimal topology for additive manufacture: A method for enabling additive manufacture of support-free optimal structures”. In: *Materials Design* 63 (2014), pp. 678–690. ISSN: 0261-3069.
- [30] Jikai Liu, Andrew T. Gaynor, Shikui Chen, Zhan Kang, Krishnan Suresh, Akihiro Takezawa, Lei Li, Junji Kato, Jinyuan Tang, Charlie C. L. Wang, Lin Cheng, Xuan Liang, and Albert. C. To. “Current and future trends in topology optimization for additive manufacturing”. In: *Struct Multidiscip Optim* 57.6 (June 2018), pp. 2457–2483. ISSN: 1615-1488.
- [31] Shutian Liu, Quhao Li, Wenjiong Chen, Liyong Tong, and G. Cheng. “An identification method for enclosed voids restriction in manufacturability design for additive manufacturing structures”. In: *Frontiers of Mechanical Engineering* 10 (June 2015), pp. 126–137.
- [32] Raya Mertens, Stijn Clijsters, Karolien Kempen, and Jean-Pierre Kruth. “Optimization of Scan Strategies in Selective Laser Melting of Aluminum Parts With Down-facing Areas”. In: *Journal of Manufacturing Science and Engineering* 136(6) (Dec. 2014).
- [33] Tuan D. Ngo, Alireza Kashani, Gabriele Imbalzano, Kate T.Q. Nguyen, and David Hui. “Additive manufacturing (3D printing): A review of materials, methods, applications and challenges”. In: *Composites Part B: Engineering* 143 (2018), pp. 172–196. ISSN: 1359-8368.
- [34] L. Parry, I.A. Ashcroft, and R.D. Wildman. “Understanding the effect of laser scan strategy on residual stress in selective laser melting through thermo-mechanical simulation”. In: *Additive Manufacturing* 12 (2016), pp. 1–15. ISSN: 2214-8604.
- [35] Shubham Patel, James Mekavibul, Jami Park, Anchit Kolla, Ryan French, Zachary Kersey, and Gregory Lewin. “Using Machine Learning to Analyze Image Data from Advanced Manufacturing Processes”. In: *2019 Systems and Information Engineering Design Symposium (SIEDS), Charlottesville, VA, USA* (Apr. 2019), pp. 1–5.
- [36] Nachiket Patil, Rishi Ganeriwala, Jerome M. Solberg, Neil E. Hodge, and Robert M. Ferencz. “Benchmark multi-layer simulations for residual stresses and deformation in small additively manufactured metal parts”. In: *Additive Manufacturing* (2021), p. 102015. ISSN: 2214-8604.
- [37] Ratnadeep Paul, Sam Anand, and Frank Gerner. “Effect of Thermal Deformation on Part Errors in Metal Powder Based Additive Manufacturing Processes”. In: *Journal of Manufacturing Science and Engineering* 136.3 (Mar. 2014), pp. 31009–31012. ISSN: 1087-1357.
- [38] Jeroen Pellens, Geert Lombaert, Boyan Lazarov, and Mattias Schevenels. “Combined length scale and overhang angle control in minimum compliance topology optimization for additive manufacturing”. In: *Structural and Multidisciplinary Optimization* 59 (June 2019).
- [39] Xiaoping Qian. “Undercut and overhang angle control in topology optimization: a density gradient based integral approach”. In: *International Journal for Numerical Methods in Engineering* 111.3 (2017), pp. 247–272.

- [40] Ibiye Aseibichin Roberts. “Investigation of residual stresses in the laser melting of metal powders in additive layer manufacturing”. In: (). PhD thesis, University of Wolverhampton, 2012.
- [41] W. J. Sames, F. A. List, S. Pannala, R. R. Dehoff, and S. S. Babu. “The metallurgy and processing science of metal additive manufacturing”. In: *Int Mater Rev* 61.5 (Mar. 2016), pp. 1–46.
- [42] Adam Smith. *The Wealth of Nations*. AuthorHouse, 2009. ISBN: 9781420932065.
- [43] Emiel Van de Ven, Matthijs Langelaar, Can Ayas, Robert Maas, and Fred Van Keulen. “A PDE-based approach to constrain the minimum overhang angle in topology optimization for additive manufacturing”. In: *12th World Congress on Struct Multidiscip Optim* (June 2017), pp. 1–11.
- [44] Emiel van de Ven, Robert Maas, Can Ayas, Matthijs Langelaar, and Fred van Keulen. “Overhang control based on front propagation in 3D topology optimization for additive manufacturing”. In: *Computer Methods in Applied Mechanics and Engineering* 369 (2020), p. 113169. ISSN: 0045-7825.
- [45] Di Wang, Yongqiang Yang, Ziheng Yi, and Xubin Su. “Research on the fabricating quality optimization of the overhanging surface in SLM process”. In: *Int J Adv Manuf Tech* 65.9 (Apr. 2013), pp. 1471–1484. ISSN: 1433-3015.
- [46] François Willème. *Photo-sculpture*. U.S. Patent 43822, Aug. 1864.
- [47] Wenyong Zhang, Mingming Tong, and Noel M. Harrison. “Resolution, energy and time dependency on layer scaling in finite element modelling of laser beam powder bed fusion additive manufacturing”. In: *Additive Manufacturing* 28 (2019), pp. 610–620. ISSN: 2214-8604.

# 2

## CLASSIFICATION AND ANALYSIS OF COMMON SIMPLIFICATIONS IN PART-SCALE THERMAL MODELLING OF METAL ADDITIVE MANUFACTURING PROCESSES

*Computational process modelling of metal additive manufacturing has recently gained significant attention. The cornerstone of many process models is the transient thermal response during the AM process. Since modelling the thermal response is computationally expensive, spatial and temporal simplifications, such as simulating deposition of an entire layer or multiple layers, and extending the laser exposure times, are commonly employed in the literature. Although beneficial in reducing computational costs, the influence of these simplifications on the accuracy of temperature history is reported on a case-by-case basis. In this paper, the simplifications from the existing literature are first classified in a normalised simplification space based on assumptions made in spatial and temporal domains. Subsequently, all types of simplifications are investigated with numerical examples and compared with a high-fidelity reference model. The required numerical discretisation for each simplification is established, leading to a fair comparison of computational times. The holistic approach to the suitability of different modelling simplifications for capturing thermal history provides guidelines for the suitability of simplifications while setting up a thermal AM model.*

---

Parts of this chapter have been submitted to Advanced Modeling and Simulation in Engineering Sciences journal

## 2.1. INTRODUCTION

Additive manufacturing (AM), also known as ‘3D printing’, refers to manufacturing techniques in which a three-dimensional part is built by depositing the material layer-by-layer [14]. The key advantage of AM over conventional manufacturing methods (*e.g.* milling, drilling, casting, etc.) is the form freedom, *i.e.* geometrically complex parts can be realised without additional process time, cost and assembly [14, 22]. Two sub-classes of AM techniques for building metal parts are powder bed fusion (PBF) and direct energy deposition (DED). Collectively, these techniques are referred to as metal additive manufacturing (MAM). Both use a focused, high-energy beam for locally melting powder particles. The molten particles fuse and solidify to form a 3D solid shape layer-by-layer. Although these techniques are very similar in process physics, they differ in printing resolution and speed. The layer thickness in the PBF process ranges between 20–100  $\mu\text{m}$  while that in the DED process varies between 250  $\mu\text{m}$  to a few millimeters [24, 49].

MAM can produce parts with mechanical properties comparable to those produced by conventional manufacturing methods. However, the process still suffers from manufacturing constraints which can cause defects leading to inferior part quality and even complete build failures [50]. For example, design features prone to local overheating adversely affect surface quality. Additionally, during the process, the part undergoes melting/solidification due to severe heating/cooling cycles. This leads to non-uniform thermal expansion and contraction, resulting in deformations and residual stresses [34]. Part geometry and process parameters (such as laser power, scanning pattern, layer thickness, etc.) play an important role in influencing in-process thermal gradients, which subsequently affect residual stress distribution and deformations [23]. Furthermore, the temperature history during the process controls the constituents and morphology of the resulting microstructure, which in turn influences the mechanical properties [46]. Therefore, to ensure consistent MAM part quality, it is crucial to understand the complex relationship between part geometry, process parameters and resulting thermal and mechanical fields. Numerical process modelling of MAM processes is instrumental in achieving this goal. Thermal histories predicted using a numerical model find multiple applications in characterising different aspects of the MAM process. For example, peak temperatures can indicate overheating [40, 15]. Consequently, a large number of studies on MAM models exist *e.g.* [19, 45, 54].

It is extremely challenging to model a MAM process, primarily due to two reasons. First, coupling phenomena from various domains of physics are required, *e.g.* , heat transfer, solid mechanics, phase transformation and fluid dynamics [52, 50, 20]. Second, there is a mismatch of characteristic spatial and temporal scales. For instance, in the laser based PBF process, the laser spot size is approximately 30  $\mu\text{m}$ , whereas the part size is in the order of centimetres. Moreover, in the time domain, melting and solidification are extremely rapid because of a fast-moving heat source, whereas the AM process can last up to days for large parts. This multi-scale nature of the process demands a high spatial and temporal resolution to adequately capture the MAM process physics. Consequently, a highly detailed MAM simulation becomes computationally intractable [45]. Therefore, simulations are performed on a very small domain or simplifi-



cations are introduced to consider a realistic part size. The former approach, *i.e.* models at powder or melt pool level [52, 44, 17, 29, 18, 12, 41, 26, 5, 7, 6] are local models. On the other hand, the latter approach provides a part-scale prediction of temperature, displacement and stress fields, and henceforth is usually called part-scale models [48, 53, 32, 36, 37, 1, 16, 39, 25, 51]. This study focusses on the part-scale transient thermal modelling of MAM processes since the thermal response forms the foundation of thermo-mechanical, microstructural and other process simulations. More specifically, we will investigate the implications of thermal modelling choices and simplifications on thermal response predictions.

The common simplifications in the part-scale MAM modelling literature can be mainly classified as simplifications in the spatial and temporal domains. For example, one common simplification in the spatial domain is the simultaneous deposition of an entire layer or a fraction of the layer instead of simulating the laser scanning pattern [55, 11, 31, 4]. These simplifications lead to so-called ‘layer-by-layer’ and ‘patch-by-patch’ models, respectively. Further extension of this idea includes simultaneous deposition of multiple layers, referred to as ‘layer lumping’, ‘superlayers’ or ‘meta-layers’ in the literature. In conjunction with spatial simplifications, assumptions in the temporal domain are also commonly utilised. For example, heating times of 1 ms and 20 ms are considered for each layer in a layer-by-layer simulation by Patil et al. [35] and Zaeh and Branner [53], respectively. Another strategy for defining the heating times of a layer is setting it equal to the total laser processing time of the layer [11, 31]. It is noteworthy that the choice for temporal simplification arises as a consequence of introducing the spatial simplifications.

These simplifications provide significant computational benefits at the cost of compromising some degree of accuracy. However, different experimental validation studies have shown that the predictions of such simplified models could be sufficiently accurate to capture specific process characteristics. For example, Chiumenti et al. [11] and Neiva et al. [31] showed that their simplified models could provide accurate predictions of far-field temperatures, *i.e.* the temperature sufficiently below the topmost layer that is being heated. Bayat et al. [4] showed predictions of a lumped patch-by-patch, thermo-mechanical model can predict deformations of the part with a 90% accuracy. These studies show that it is justified to use certain simplifications to capture specific attributes of the MAM process. However, the scope of the simplifications is discussed on a case-by-case basis in the literature. Generalisation of the validity of a particular simplification for a specific process attribute is absent. Consequently, a fundamental and comprehensive understanding of which simplification is adequate for which purpose is still lacking in the literature. Suitability assessment of different spatial/temporal simplifications for a desired attribute of the thermal history is essential. Therefore in this work, we aim to systematically investigate a range of simplifications and their implications on the accuracy and computational efficiency of thermal simulation predictions. The suitability of different simplifications is assessed and compared with the existing literature to make informed choices while setting up a MAM model.

The outline of the paper is as follows. In Section 2.2, a method for classifying common MAM spatial and temporal simplifications is presented. In Section 2.3, the governing physics and finite element implementation for MAM process models are described. Based on the novel numerical studies, implications of different simplifications are described in Section 2.4. An overview discussion of the insights developed in this study compared to the existing literature is given in Section 2.5. Recommendations about simplification choices are presented in Section 2.6. Finally, Section 2.7 states the conclusions and future directions.

## 2.2. CLASSIFICATION OF SIMPLIFICATIONS

In this section, a classification scheme is presented for commonly used simplifications in part-scale modelling of the MAM process. Note that this classification scheme is general, and next to thermal modelling, it is applicable to other (*e.g.* mechanical) MAM simulations. First, the spatial simplifications are further classified based on the material lumping directions. If a simultaneous deposition of material is assumed within the plane of a layer, it is referred to as *in-plane lumping*. A patch-by-patch or a layer-by-layer material deposition assumes various degrees of in-plane lumping. On the other hand, when the thickness of the material deposition is considered to be an integer multiple of the actual layer thickness, it is referred to as *out-of-plane lumping*. Note that these two types of lumping can also be combined. In the temporal domain, the simplification is characterised by the extension of the heating times  $t_h$ , *i.e.* how much is the duration of the heating step.

In order to compare the degree of spatial/temporal simplifications across different simplified models from the literature, a normalisation scheme is introduced. For the in-plane lumping, the area of the material  $A$  assumed to be deposited simultaneously, is normalised with the beam spot area  $A_o$ , whereas, for out-of-plane lumping, simulation layer thickness  $l$  is normalised with the actual layer thickness  $l_o$ . In the temporal domain, the normalisation constant is defined as the time laser beam traverses itself, *i.e.*  $t_f = D/v$ , where  $D$  and  $v$  are beam spot diameter and scanning speed, respectively. Consequently, the normalised in-plane lumping, out-of-plane lumping and heating times are given as

$$\hat{A} = \frac{A}{A_o}, \quad (2.1)$$

$$\hat{l} = \frac{l}{l_o} \quad \text{and} \quad (2.2)$$

$$\hat{t}_h = \frac{t_h}{t_f}, \quad (2.3)$$

respectively. Note that normalisation constants are process dependent and are different for DED and PBF. In PBF, the normalisation constants also differ for the type of high en-

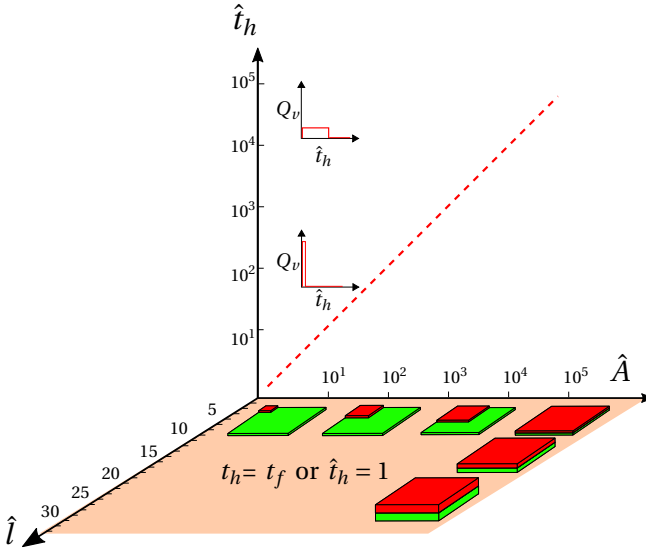


Figure 2.1: A 3D simplification space for quantifying the degree of spatial (in-plane and out-of-plane lumping) and temporal simplifications. The schematic illustrates the spatial simplifications, with the red region indicating the amount of volume assumed simultaneous deposition while the green region indicates previously deposited layer(s). The temporal simplification is represented by extending the heating time while  $Q_v$  denotes the input power. The dotted red line indicates the gradual heating concept introduced by Chiumenti et al. [11].

ergy beam<sup>1</sup> used to melt the powder. A list of normalisation constants used for each of these processes is given in Table 2.1.

A 3D simplification space is illustrated in Figure 2.1 with axes representing the normalised area deposited  $\hat{A}$ , normalised heating time  $\hat{t}_h$  and normalised layer thickness  $\hat{l}$ . The origin (1, 1, 1) corresponds to simulating the laser movement in real time with actual layer thickness with no simplification. All other points in this simplification space represent a simplified model. The plane of  $\hat{t}_h = 1$  is referred to as the plane of *flash heating models* using the terminology introduced by Bayat et al. [4]. These models have no temporal simplification, while the models above this plane assume extended heating times. Neiva et al. [31] and Chiumenti et al. [11] provides a basis for defining the heating time  $t_h$  for a patch/layer as the time it would take for the beam to process that patch/layer, *i.e.*

$$t_h = \frac{A}{hv}, \quad (2.4)$$

where  $A$  is the patch/layer area and  $h$  is the hatch thickness. This type of temporal simplification in this paper is called *gradual heating*. Gradual heating has been used in multiple studies, and it automatically ensures time consistent simulations, *i.e.* the simulated time is equal to the time elapsed during the AM process. In the literature, it is

<sup>1</sup>Electron beam based processes are referred to as E-PBF and laser based processes referred to as L-PBF

Table 2.1: List of the beam spot area  $A_o$ , interaction time  $t_f$  and layer thickness  $l_o$  for EB-PBF, L-PBF and DED processes.

Process	$A_o$ (mm <sup>2</sup> )	$t_f$ (ms)	$l_o$ (mm)
E-PBF [38]	0.007	0.5	0.1
L-PBF [30]	0.007	0.1	0.05
DED [21]	2.009	5.7	0.25

especially recommended to ensure time consistency for out-of-plane lumping as larger cooling times compensate for the higher heat capacity of thicker lumped layers [55, 27]. Any other definition of heating time for a spatially simplified model will require due adjustments in cooling time<sup>2</sup>  $t_c$  to be time consistent. The normalised heating time for gradual heating is denoted as  $\hat{t}_g = A/hv t_f$ . A dotted red line is drawn on the  $\hat{A}-\hat{t}_h$  plane in Figure 2.1 indicating gradual heating.

### 2.3. MODEL DESCRIPTION

L-PBF process is considered here for modelling. The temperatures during the L-PBF process are calculated by numerically solving the heat equation given as

$$\rho c_p \frac{\partial T}{\partial t} = \nabla \cdot (k \nabla T) - \rho \Delta H_{sl} \frac{\partial f_{liq}}{\partial t} + Q_v, \quad (2.5)$$

where  $\rho$ ,  $c_p$ ,  $k$ ,  $\Delta H_{sl}$ ,  $T$ , and  $t$  are density, specific heat capacity, thermal conductivity, latent heat of fusion, temperature and time, respectively. Thermal conductivity and specific heat capacity are volume-averaged during the solidification interval following

$$k = f_{sol} k_{sol} + f_{liq} k_{liq} \quad \text{and} \quad (2.6)$$

$$c_p = f_{sol} c_{p,sol} + f_{liq} c_{p,liq}, \quad (2.7)$$

respectively. Here  $f_{sol}$  and  $f_{liq}$  are the solid and liquid fractions, respectively, which sum up to unity and are determined as

$$f_{liq} = \begin{cases} 1 & T \geq T_{liq} \\ \frac{T - T_{sol}}{T_{liq} - T_{sol}} & T_{sol} < T < T_{liq} \\ 0 & T \leq T_{sol} \end{cases}, \quad (2.8)$$

where  $T_{liq}$  and  $T_{sol}$  are liquidus and solidus temperature of the alloy, respectively. The values for the thermo-physical properties are taken from Bayat et al. [4] and reported in Table 2.2.

<sup>2</sup>The time elapsed between two successive layer deposition is referred to as cooling time. The same is also referred to as inter-layer-dwell time or recoater time in the literature.

Table 2.2: Thermo-physical properties of Ti6Al4V alloy [4].

$k_{\text{sol}}$ and $k_{\text{liq}}$ ( $\text{Wm}^{-1}\text{K}^{-1}$ )	$c_{\text{p,sol}}$ and $c_{\text{p,liq}}$ ( $\text{J kg}^{-1}\text{K}^{-1}$ )	$\Delta H_{\text{sl}}$ ( $\text{J kg}^{-1}$ )	$T_{\text{sol}}$ (K)	$T_{\text{liq}}$ (K)	$\rho$ ( $\text{kgm}^{-3}$ )
13, 33	543, 750	286000	1893.2	1927.2	4400

The last term in Eq. (2.5) is the volumetric heat source  $Q_v$  due to the laser-material interaction. The following relationship

$$Q_v t_h = \phi = \frac{\gamma P}{h\nu l_o}, \quad (2.9)$$

ensures the energy equivalence between all simplified models. Here  $\phi$  is the volumetric energy density,  $\gamma$  is the absorption coefficient and  $P$  is laser power. Note that  $\phi$  remains constant for any spatial or temporal simplification, *i.e.* over the entire 3D simplification space presented in Figure 2.1. Therefore, Eq. (2.9) provides a basis for calculating the value of volumetric heat source  $Q_v$  for various simplifications while conserving energy. Based on the above given equations, simulations are performed using finite element analysis in ABAQUS [28] with eight-noded tri-linear C3D8T elements. A Python script is developed for sectioning the part based on the considered spatial simplifications. The element birth and death method is used for sequentially activating the growing domain during AM processes [41, 55].

## 2.4. NUMERICAL EXPERIMENTS

In order to study the impact of simplifications on the resulting thermal histories, L-PBF simulation of a simple cuboidal geometry shown in Figure 2.2 is considered. A low-volume ( $16 \text{ mm}^3$ ) and geometrically simple part comprising only 20 layers allows for a high-fidelity model located almost at the origin of the simplification space. The part is assumed to be deposited on a base plate, and the dimensions are indicated in Figure 2.2. Different levels of simplifications, *i.e.* different points in the 3D simplification space shown in Figure 2.3 are considered. The location of these simplified models in the 3D simplification space is carefully chosen so that the effect of each simplification can be systematically studied. The thermal histories obtained with different levels of simplifications are compared to understand the influence of a specific simplification. The center line normal to the plane of the layers is marked in Figure 2.2 passing through point P with coordinates (10 mm, 10 mm, 6 mm). Various points on this line, characterised by their  $x_3$  coordinate, are used for comparing the thermal histories across different simplified models marked on Figure 2.3.

The bottom face of the base plate is assumed to be maintained at a constant temperature, *i.e.*  $T = T_0$  on  $\partial\Omega_{\text{bot}}$ . The powder conductivity is reported to be approximately 1% of that of bulk material [43, 42]. Hence, the heat conduction through powder is neglected, and thus, the part-powder interface indicated by  $\partial\Omega_{\text{lat}}$  in Figure 2.2 is assumed to be thermally insulated. The volume of material assumed to be deposited simultaneously is represented as  $\Omega_{\text{heat}}$ . The volumetric heat source  $Q_v$  is defined over the volume

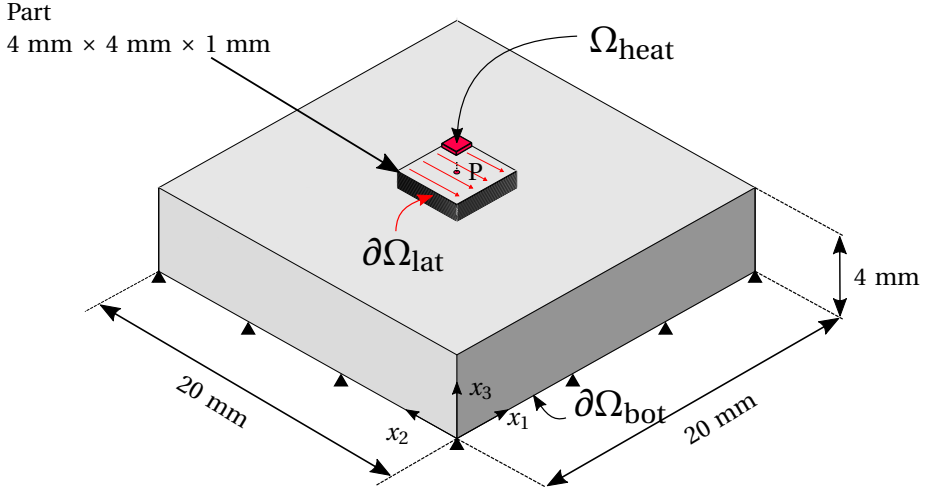


Figure 2.2: Part and baseplate geometry considered for the L-PBF simulation with dimensions. The lateral sides  $\partial\Omega_{\text{lat}}$  are assumed to be insulated while a Dirichlet boundary condition is assumed at the bottom of the baseplate  $\partial\Omega_{\text{bot}}$ .  $\Omega_{\text{heat}}$  represents the region assumed to be deposited simultaneously.

$\Omega_{\text{heat}}$ , which varies with the considered spatial simplification. For example,  $\Omega_{\text{heat}}$  denotes an entire layer for a layer-by-layer model whereas, for a patch-by-patch model, it represents only a sub-section of the entire layer as illustrated in Figure 2.2. Lastly, heat transfer through convection and radiation are considered for the entire topmost part surface with convection coefficient  $h_{\text{conv}}$ , emissivity  $\epsilon$  and ambient temperature  $T_a$ . Material dependent thermal properties for Ti6Al4V are taken from Bayat et al. [4] while relevant process parameters are listed in Table 3.1.

The simulations are performed for ten different simplified cases as indicated in Figure 2.3. The locations of the simplified models are selected such that the effect of each simplification can be isolated. Note that for the cuboid part, all 20 layers have the same area, which, after normalisation, is represented as  $\hat{A}_\Omega$ . The highest fidelity model divides the layer area  $\hat{A}_\Omega$  into 400 equal  $200 \mu\text{m} \times 200 \mu\text{m}$  patches with a thickness of  $50 \mu\text{m}$ . This is represented as  $(\hat{A}_\Omega/400 \approx 5, 1, 1)$  in the simplification space and hereon referred to as the reference model. In a similar manner, coordinates for the remaining nine models are labelled in Figure 2.3, which are used for referring to the respective model in the remainder.

### 2.4.1. MESH CONSIDERATIONS

In order to determine the numerical spatial and temporal discretisation requirements associated with a particular simplification, a simple numerical experiment is conducted considering 1D heat transfer. The motivation behind using a simplified 1D case is a

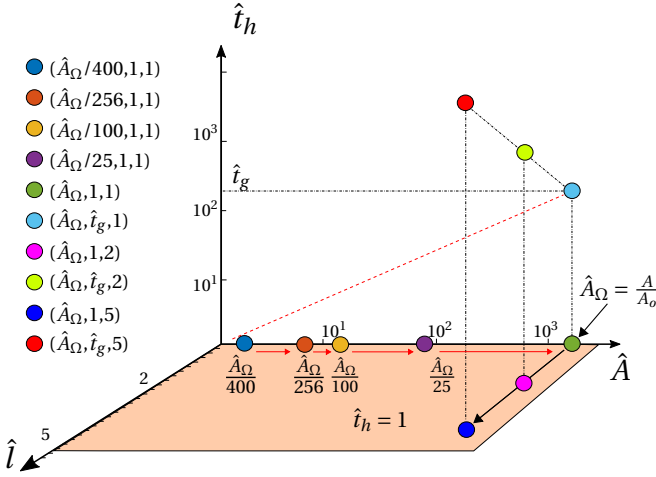


Figure 2.3: Simplified models plotted on the 3D simplification space for analysing the influence of simplifications on thermal history.

known analytical solution for a boundary value problem similar to L-PBF. Therefore the simple 1D model has been used to verify the accuracy of different spatial and temporal discretisation schemes. Details associated with the 1D case are presented in Appendix A, while the primary two findings are examined below.

First, it is found that the definition of heating time  $t_h$  has a direct implication on the required spatial and temporal resolution. This can be explained by appealing to the characteristic length scale  $\kappa = \sqrt{\alpha t_h}$ , [9] indicating the heat affected zone, where  $\alpha$  is thermal diffusivity. For short heating times, *i.e.*  $\hat{t}_h \approx 1$ , an extremely fine spatial and temporal resolution is required to capture the gradients within this small heat affected zone. As the heating time increases, *i.e.* temporal simplification approaches the condition of gradual heating  $t_h \approx t_g$ , coarser spatial and temporal discretisation can be used to capture the peak temperatures (see Appendix A). The required level of discretisation directly affects the computational burden associated with a simplified model. The gradual heating models allowing for a coarser mesh are computationally more advantageous than flash heating models. The computational times associated with different simplified models are reported in Section 2.5.

Next, far field temperatures away from the heat source during the cooling phase are investigated with the gradual heating scheme. For instance, a material point located a few layers below the topmost layer experiences the heat input with a delay. Consequently, the peak temperature for this point is attained later than that of the topmost layer. It is shown in the study presented in Appendix A that to capture this delayed peak during the cooling stage, it is important to have a fine temporal resolution, especially at the beginning of the cooling regime.

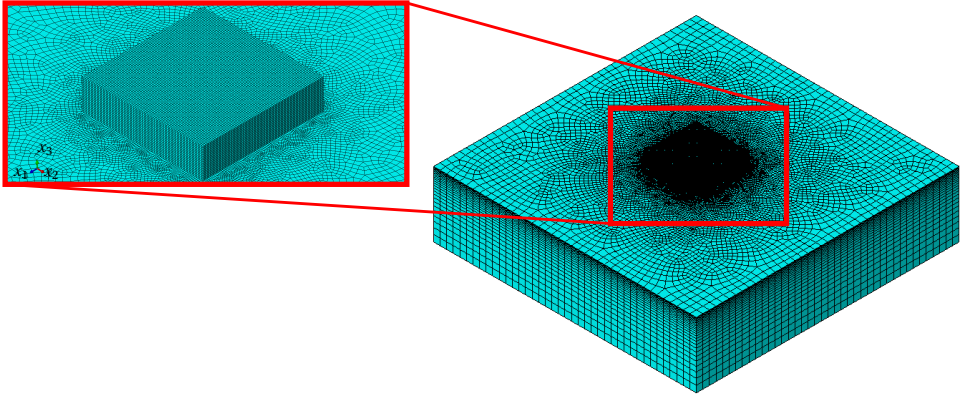


Figure 2.4: Meshing requirements for flash heating. The part is meshed using tetrahedral elements with  $r = 0.05$  mm in accordance with  $\kappa = \sqrt{\alpha t_h}$  considering melting point  $\alpha$  for Ti6Al4V and  $t_h = t_f$  or  $\hat{t}_h = 1$ . The baseplate is meshed with linearly increasing element size from  $r = 0.05$  to  $0.5$  mm, from top to bottom.

It remains to apply the findings of the 1D study to mesh the 3D geometry shown in Figure 2.2. The part is meshed with tetrahedral linear elements with a mesh size of  $r = 0.05$  mm while the element size for the base plate linearly increases from  $r = 0.05$  mm to  $0.5$  mm, away from the part baseplate interface. The meshed geometry is shown in Figure 2.4. This is in accordance with  $\kappa \approx 0.05$  mm for flash heating, assuming a constant  $\alpha$  value taken at the melting point<sup>3</sup>. This meshing scheme is referred to as mesh A and results in approximately 580,000 elements. To check mesh convergence, a more refined discretisation, mesh B is considered with  $r = 0.04$  mm in the part with baseplate elements varying from  $r = 0.04$  mm to  $0.3$  mm leading to approximately 1,060,000 elements. Deposition of a single patch shown in Figure 2.2 is simulated using the reference model characterised by the point  $(\hat{A}_\Omega/400, 1, 1)$  in Figure 2.3. The difference between peak and ambient temperatures for the centre point of this patch is compared across both meshing schemes, and it is found to be less than a 1%. This shows that mesh A is sufficient for mesh convergence. Note that  $(\hat{A}_\Omega/400, 1, 1)$  has the most stringent mesh requirements. Therefore the meshing scheme for mesh A ensures the mesh convergence for all the remaining flash heating simulations with a higher degree of spatial simplification. Hence, mesh A is used as the reference discretisation scheme, while coarser meshes are used for gradual heating models in accordance with the relaxed meshing criterion.

#### 2.4.2. INFLUENCE OF IN-PLANE LUMPING

First, deposition of the initial layer with different patch sizes is considered and obtained thermal histories are compared. These five cases are marked on the axis of in-plane lumping in Figure 2.3. The reference model is represented as  $(\hat{A}_\Omega/400, 1, 1)$  where patch-by-patch deposition is assumed in accordance with the scanning directions shown in

<sup>3</sup>Motivation behind using this value of  $\alpha$  comes from findings of Yang et al. [48] that using an  $\alpha$  value at the melting point of the material gives the best thermal predictions upon using temperature independent thermal properties.



Figure 2.2. The heating time for each patch is equal to the flash heating time  $\hat{t}_h = 1$ , and the heat source intensity is calculated using Eq. (2.9). The subsequent four models consider larger , with the largest patch size equal to the entire layer area.

The point at the top of the first layer along the centre line with  $x_3 = 5.05$  mm and labelled by M in Figure 2.5 is considered for comparing the thermal histories. This point is chosen since we are first interested in observing the effect of simplifications on the peak temperatures in the vicinity of the heat source. A typical thermal history obtained using a patch-by-patch deposition manifest multiple peaks. The first peak represents the deposition of the patch, which contains the point M and hence the highest temperature peak. The subsequent peaks occur when subsequent neighbouring patches are activated. The thermal history for the case  $(\hat{A}_\Omega, 1, 1)$  exhibits only one peak. The effect of scanning patterns is lost since the entire layer is simultaneously deposited. However, note that the peak temperatures predicted by these models are in close agreement with the highest difference of 3.6% between peak and ambient temperatures across all models. This suggests a layer-by-layer model can provide reasonably accurate predictions for peak temperatures. For example, Hodge, Ferencz, and Solberg [15] and Ranjan et al. [40] used peak temperatures calculated as explained above as an indicator of the overheating risk. Lastly, close observation reveals that the peak temperatures slightly increase with larger in-plane lumping. This is attributed to the less lateral flow of heat from a newly deposited patch to the already deposited neighbouring ones for larger in-plane lumping, and ultimately no lateral heat flow for the layer-by-layer deposition, resulting in slightly higher peak temperatures.

Next, we investigate the effects of in-plane lumping with flash heating on far-field temperatures, *i.e.* the variation of temperature at a point located notably below the heat source. As discussed in Section 2.1, the far-field temperature history is relevant for predicting microstructure evolution [2]. Moreover, it finds applications for calibrating thermal models against the experimental data obtained using thermocouples typically located a few layers below the topmost layer [11, 31, 21]. For that purpose, points D1 and D2 located on the centre line in Figure 2.2 at  $x_3 = 4.75$  mm and  $x_3 = 4.5$  mm, respectively, are considered. This means both D1 and D2 are located in the baseplate five and ten layers below, respectively. The temperature evolution for points D1 and D2 are plotted in Figure 2.6. It can be seen that the peak temperatures for the points located away from the heat source are attained after the deposition of the topmost layer is complete. This is demonstrated in the case of  $(\hat{A}_\Omega/400, 1, 1)$  where the end of the heating regime is marked with a dotted vertical line in Figure 2.6. Next, a significant influence of laser scanning is observed for patch-by-patch models with small patch sizes. For example, pronounced fluctuations in the thermal history are observed for  $(\hat{A}_\Omega/400, 1, 1)$  in Figure 2.6a for point D1 whereas at point D2 a relatively smooth temperature evolution is depicted in Figure 2.6b. This demonstrates the influence of scanning strategies is lost after a critical depth. Finally, similar to the behaviour of peak temperatures, it is found that the layer-by-layer model also overestimates the far-field temperatures, whereas other patch-by-patch models are reasonably close.

Table 2.3: List of parameters used for thermal modelling of the L-PBF process.

$P$ (W)	$\gamma$	$v$ ( $\text{ms}^{-1}$ )	$h$ (mm)	$l_o$ (mm)	$t_c$ (s)	$T_0$ ( $^{\circ}\text{C}$ )	$T_a$ ( $^{\circ}\text{C}$ )	$h_{\text{conv}}$ ( $\text{Wm}^{-2}\text{K}^{-1}$ )	$\epsilon$
120	0.3	0.8	0.08	0.05	4	180	25	10	0.35

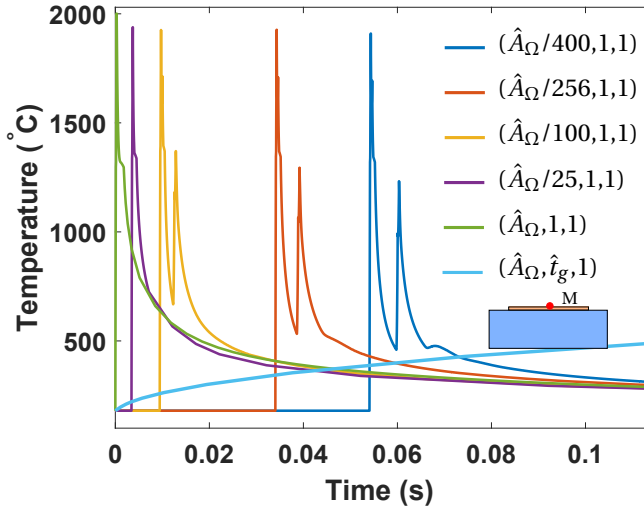


Figure 2.5: Temperature evolution for single layer deposition using simplified models shown in Figure 2.3. The temperatures at point M located at (10,5.05,10) in Figure 2.2 are plotted with respect to time. Multiple peaks in the thermal history signify the influence of laser scanning, which is not captured by a layer-by-layer simulation. Nevertheless, the variation in the peak temperatures across the range of cases considered is only 3.6%.

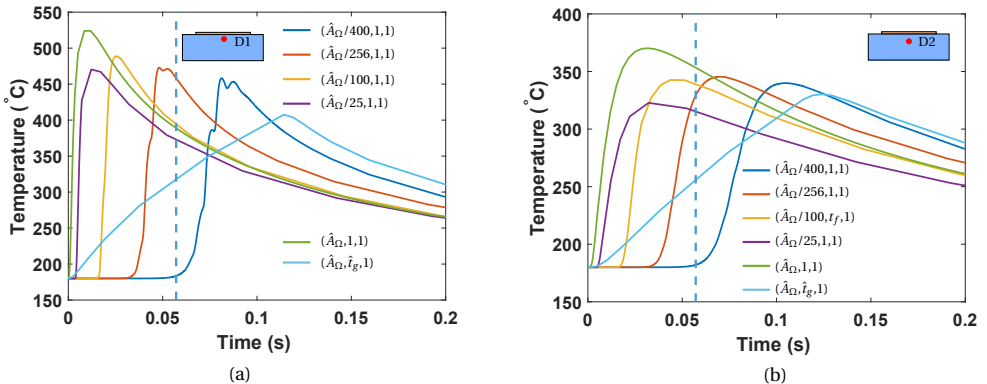


Figure 2.6: Comparison of temperature evolution for simulation of single layer deposition using different levels of fidelity. The variation is shown for points (a) D1 located at 5 layers below and (b) D2 located at 10 layers below in the baseplate.

### 2.4.3. INFLUENCE OF HEATING TIME

Next, we investigate the influence of extending heating times on thermal evolution. We first compare flash heating results presented in previous section with a layer-by-layer gradual heating model represented with  $(\hat{A}_\Omega, \hat{t}_g, 1)$  in Figure 2.3. The FE discretisation is carried out in accordance with characteristic length  $\kappa = \sqrt{\alpha t_h}$  with  $r = 0.8$  mm which leads to a model with only 19,256 elements. In order to check the mesh convergence, the calculation is repeated using mesh A with 580,000 elements, as discussed in Section 2.4 and a difference of less than 1% is observed considering the difference between the peak and ambient temperatures for point M.

The temperature evolution using the gradual heating model for points M, D1 and D2 are shown in Figure 2.5, Figure 2.6a and Figure 2.6b, respectively. Recall that point D1 is 5 layers below point M and point D2 is 5 layers below D1. It is observed that the gradual heating scheme significantly underestimates the peak temperature for point M located at the top of the deposited layer; see Figure 2.5. However, a better agreement between gradual heating and flash heating schemes is observed for far-field temperatures. For point D2 (see Figure 2.6b), the difference between peak and ambient temperatures is only 6% higher than the reference model. It is also seen that cooling rates of the gradual heating simulations approximate those of flash heating.

Until now, only single layer deposition has been investigated. It remains to analyse the temperature evolution for the deposition of all 20 layers. To ensure computational tractability, only layer-by-layer models are considered for the multi-layer simulations. Figure 2.7 shows the temperature variation for point M with  $x_3 = 5.05$  mm as obtained using layer-by-layer flash and gradual heating models. It can be seen from Figure 2.7 that the observation made in Section 2.4.2 about gradual heating underestimating peak temperatures remains valid only for the first few layers. However, as point M on the first layer becomes increasingly distant from the topmost layer for subsequent layers, the mismatch between the thermal histories significantly reduces. The percentage difference between flash and gradual peak temperatures is calculated for each layer, which is less than 20% after 8<sup>th</sup> layer. This is emphasised by the closeup view of the thermal history shown for 8–20 layers in Figure 2.7. This is simply another example of gradual heating capturing the far-field temperatures. Several examples in the literature show that gradual heating predictions are validated with thermocouples located at a certain distance from the topmost layer [31, 11, 10]. This is consistent with the findings illustrated in Figure 2.7.

Recall that flash and gradual heating schemes represent two extremes to define the heating times. Alternatively, any in between value can also be used. For example, Patil et al. [35] used  $t_h = 1$  ms for layer-by-layer simulation, arguing that the peak values reach the melting point, while higher  $t_h$  values lead to peak temperatures below the melting point. As seen in Section 2.4.1, the definition of heating time has a consequential effect on mesh requirements and computational cost. Therefore, the choice of heating time should be carefully made based on the model's purpose and the desired level of accuracy. While aiming to predict far-field temperatures, gradual heating allows for a coarser

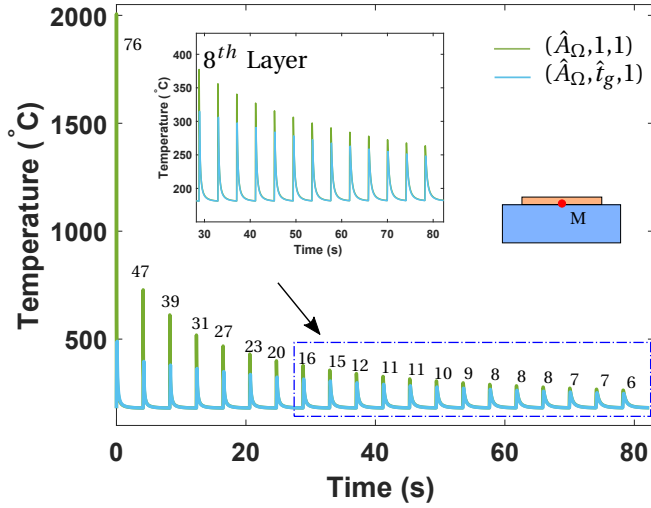


Figure 2.7: Temperature versus time at point M for deposition of all 20 layers in a layer-by-layer manner with flash heating,  $(\hat{A}_\Omega, 1, 1)$  and gradual heating,  $(\hat{A}_\Omega, \hat{t}_g, 1)$ . The percentage difference between temperature peaks using flash and gradual heating are indicated for every layer.

mesh, leading to a reduced computational cost. On the other hand, if peak temperatures in the vicinity of the layer being deposited are aimed to be captured, then flash heating is adequate. Another important aspect is the quantitative definition of far field distances *i.e.* at which distance the temperature values agree well with those found using extended heating times. For example, for the case shown in Figure 2.7, the error is less than 20% after the 8<sup>th</sup> layer. However, the exact determination of this distance depends on various factors such as part geometry, thermal properties and process parameters. Moreover, as evident from Figure 2.7, the pragmatic way to determine this length would be based on the desired level of accuracy. Consequently, extending heating times is promising for capturing far-field temperatures in a computationally inexpensive manner, and it has already been used in several studies in the literature. For example, Chiumenti et al. [11] and Neiva et al. [31] compared the thermal histories recorded using thermocouples located at 5.24 mm and 2.5 mm below, respectively, with gradual heating. An excellent agreement was found, which demonstrates the usefulness of this method.

The importance of having a fine temporal resolution to capture far-field temperatures during the cooling phase has already been emphasised in Section 2.4.1 motivated by the 1D analytical solution detailed in Appendix A. The effect of time step size on the predicted thermal history is given in Figure 2.8. Here, temperature variation for point M using the layer-by-layer flash heating model is calculated using two different time step values during the cooling stage. The green curve shows the temperature evolution with a time step  $t_c/100$  while the dotted black curve presents the same with a time step of  $t_c/10$ . Although the first temperature peaks are identical, far-field peak temperatures are

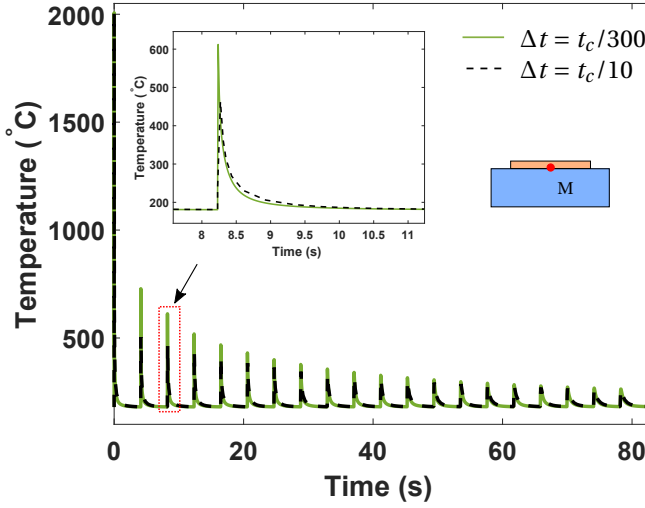


Figure 2.8: Thermal history for deposition of 20 layers using a layer-by-layer flash heating ( $\hat{A}_\Omega, 1, 1$ ) model with two selected time step values. The thermal history is reported for point M located at the top of the first layer.

underestimated when  $\Delta t = t_c/10$ . This error is especially pronounced at the beginning of the cooling stage when there is a sharp drop in temperature. This numerical error could lead to erroneous predictions of the thermal history information used to predict, for example, microstructure evolution. Therefore, it is essential to perform a temporal convergence study to obtain accurate temperatures.

#### 2.4.4. INFLUENCE OF OUT-OF-PLANE LUMPING

Recall that a volumetric heat source is used for prescribing the heat input in our simulations. Therefore, the energy input per layer should be increased for thicker (lumped) layers, making the lumped layer simulations energy consistent. Also, the cooling time for the out-of-plane lumped layers is adjusted so that the total simulation time remains the same. In this section, we consider point N located on the centre line shown in Figure 2.2 at  $x_3 = 5$  mm for comparing the thermal histories.

First, flash heating models with and without lumping are compared. Figure 2.9 depicts the thermal history for out-of-plane lumping with  $\hat{l} = 1$  (no out-of-plane lumping)  $\hat{l} = 2$  and  $\hat{l} = 5$ . The closeup view of the first peak is shown as an inset where it is observed that the peak temperatures increase with the number of layers lumped. This is because more energy is deposited during the flash heating time with increased lumping. However, this increment is not linear owing to highly non-linear boundary conditions where the radiation losses increase proportionally to  $T^4$ .

Next, gradual heating for  $\hat{l} = 5$  is considered and the resulting thermal history is

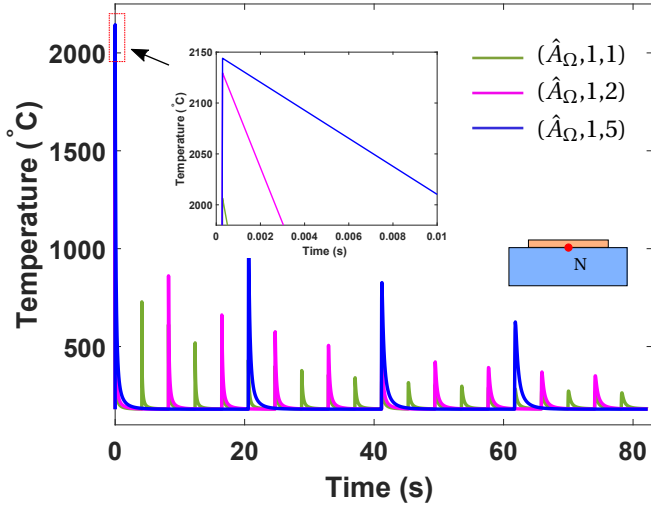


Figure 2.9: Temperature evolution for the entire part considering layer-by-layer flash heating with different degrees of out-of-plane lumping.

shown in Figure 2.10. Note that this implies that new layers are subjected to a heating time that is five times longer than that for the flash heating case  $(\hat{A}_\Omega, 1, 1)$  while the heat source value  $Q_v$  reduces following Eq. (2.9). As expected, significantly lower peak temperatures are exhibited compared to the case of flash heating. However, for the case of far-field temperature evolution, the lumped gradual model is more accurate than the lumped flash heating when compared to the high-fidelity (reference) model with  $(\hat{A}_\Omega, 1, 1)$ . Finally, the FE mesh used for lumped gradual heating models is even more coarse with 456 and 789 elements for lumping of  $\hat{l}=2$  and  $\hat{l}=5$ , respectively. Once again, convergence is ensured by checking against mesh A described in Section 2.4.1.

## 2.5. DISCUSSION

To gain a deeper perspective on the observations reported in Section 2.4, the findings of this paper are compared against the existing literature. For this purpose, a thorough review was conducted on part-scale MAM thermal or thermo-mechanical models. As thermal history acts as an input to mechanical analysis, thermal history directly impacts mechanical predictions. Hence, thermo-mechanical models were also considered in this review. The review includes both PBF and DED process models illustrated in the simplification space presented in Figure 2.11. Recall that different normalisation constants are used for different processes (see Table 2.1). Here, the points with the same colour signify multiple simplified cases considered in the same study. The simplified thermal models analysed in this paper are indicated in black. Circles are used for thermal models, while squares are used for thermo-mechanical models. A dotted red line on the  $\hat{A}-\hat{t}_h$  plane

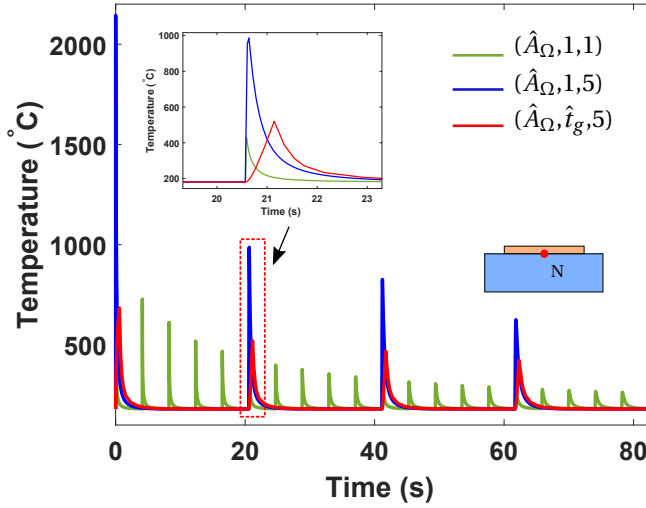


Figure 2.10: Temperature evolution for the entire part considering layer-by-layer flash and gradual heating.

indicates gradual heating. Recall that the concept of time consistency was introduced in Section 2.2, where cooling time is adjusted in accordance with spatial/temporal simplification. Time consistency is especially important for the case of out-of-plane lumping as larger cooling times compensate for the higher heat capacity of thicker lumped layers [55, 27]. The red boundary around the markers in Figure 2.11 indicates time consistency, and it is evident that most simplified models in the literature follow this idea. The time consistency condition could not be determined for the markers without a red boundary based on the information provided in the respective papers.

Table 2.4 summarises the qualitative trends observed in Section 2.4 in terms of the variation of peak temperatures and far-field temperatures with increasing in-plane lumping or patch size, heating time and out-of-plane lumping. Here, over and under estimation trends are represented by + and – symbols, respectively, while little or no effect of a particular simplification on the predictions is represented by  $\approx$ . Studies with similar findings are also tabulated next to the respective trend. It is apparent from Table 2.4 that these previous studies already provided insights into the influence of simplifications on the simulation outcomes. However, no single study investigated the entire simplification space. To emphasise this, models from existing literature are further classified based on the phenomena they aim to capture. Figure 2.12a and 2.12b show the simplification space with models discussing the effect of simplifications on peak and far-field temperatures, respectively. This classification highlights how the findings of this study complement existing knowledge. The models from this paper that investigate the influence of a particular simplification for the first time are enclosed in red boxes in Figure 2.12. The influence of out-of-plane lumping and heating times on peak temperatures and the influence of in-plane lumping on far-field temperatures is investigated

for the first time here. However, this does not make the other simplified models in this work redundant since a comprehensive investigation of the entire simplification space resulted in an improved understanding of trends that were observed previously. For example, Zhang, Tong, and Harrison [55] observed an increase in far-field temperatures with increasing out-of-plane lumping, and constant cooling time was conjectured to be the reason behind this increase. However, as found in this study, the primary reason for this increase is the simultaneous deposition of a larger amount of energy. Moreover, Neiva et al. [31] and Chiumenti et al. [11] showed that extended heating times can capture far-field temperatures. However, our analysis complemented this observation with the associated mesh requirements. Moreover, it is shown that the accuracy of far-field temperatures would depend on the distance between the point of interest and the top-most layer.

The wall-clock computational times associated with thermal models with different simplifications are listed in Table 2.5. All computations were performed using 16 cores on a HPC cluster. It is evident that computational time reduces as the level of simplifications increases. The computational times associated with thermal models are pictorially shown in Figure 2.13a where considered models, represented by circles, on the simplification space. The radii of the circles are in the same proportion as the associated computational time. It is important to note that four patch-by-patch models with varying in-plane lumping simulate only deposition of the first layer for computational tractability, while (lumped) layer-by-layer models simulate deposition of all 20 layers. It can be seen that even with only one layer deposition, the computational cost associated with  $(\hat{A}_\Omega/400, t_f, 1)$  is the highest. This shows that the computational burden increases significantly as a flash heating model approaches the origin of the simplification space. Examples of such high-fidelity but computationally burdensome models from the literature are Denlinger, Irwin, and Michaleris [13] and Patil et al. [35]. It is clear from Figure 2.13a that significant computational benefits are gained when considering (lumped) layer-by-layer flash heating models compared to models that consider patch-by-patch deposition. However, the maximum computational gains are achieved by gradual heating models with  $(\hat{A}_\Omega, t_g, 5)$  requiring only 0.23% of computational time as compared to  $(\hat{A}_\Omega/400, t_f, 1)$ . This is mainly because the gradual heating models have much lower spatio-temporal discretisation requirements for numerical convergence. This is evident by the fact that number of elements in model  $(\hat{A}_\Omega, t_g, 5)$  is only 1% of  $(\hat{A}_\Omega/400, t_f, 1)$ .

In the context of mechanical simulations, there are two effects through which the spatial and temporal simplifications influence the results. First, as discussed previously, the thermal history directly affects the thermal strain, which acts as an input to the mechanical simulation. Second, the spatial simplifications of in-plane and out-of-plane lumping control the mechanical boundary conditions influencing the mechanical field quantities. A brief discussion on both aspects is provided next.

Correct prediction of peak temperatures is crucial for further assessment of stresses and deformations. Based on this, it can be expected that models located on or close to the flash heating plane that correctly capture the peak temperature are appropriate for coupling with mechanical analysis. This is also observed from the existing literature



Table 2.4: Qualitative trends for each simplification considered for MAM. Similar observations from literature are denoted. The symbol of ‘↑’ signifies an increase in the degree of simplifications.

Simplification	Peak temp.	Far-field temp.
$\hat{A} \uparrow$	$\approx$ [4]	$\approx$
$\hat{t}_h \uparrow$	–	$\approx$ [11, 31]
$\hat{l} \uparrow$	+	+ [55, 21]

as most reviewed thermo-mechanical models are located on the flash heating plane; see Figure 2.11. The models located above the flash heating plane, *i.e.* in [35, 21, 53], a slightly higher heating times ensure the melting point has been reached. In fact, in [21, 35], attainment of melting point is used as a criterion to decide the value of heating time. Gradual heating models, which lead to under-estimation of peak temperatures are deemed not suitable as an input for the mechanical simulations.

The second effect through which in-plane and out-of-plane lumping simplifications influence the result of the mechanical analysis is through their implications on the mechanical boundary conditions. For example, Bayat et al. [4] showed that a layer-by-layer model leads to an unrealistic symmetrical stress pattern while a patch-by-patch model where patches emulate laser scanning leads to a more realistic stress development aligned with deposition direction. This is an example of the influence of in-plane lumping on stress directions. Similar observations have been made in the context of out-of-plane lumping as well. Williams, Davies, and Hooper [47] showed that accurate predictions can be made until a lumped layer thickness of 0.8 mm *i.e.*  $\hat{l} = 16$ . However, overestimation was observed for higher lumped layer thickness values. Another study by Zhang, Tong, and Harrison [55] investigated the effect of lumping on residual stresses and argued that out-of-plane lumping above  $\hat{l} = 4$  should be avoided. In both these studies, the common finding is that the concept of out-of-plane lumping works up to a certain degree while preserving reasonable accuracy. Note that for a given part, a simulation with a thicker layer implies an artificial reduction in the number of heating-cooling cycles, which also has a direct impact on residual stress development. Moreover, thicker layers have higher stiffness, which are less prone to deformations and lead to an underestimation of deformations. Lastly, other modelling choices such as inclusion of geometrical non-linearity and consideration of powder in the simulation domain can also influence the result of mechanical analysis, as analyzed by Burkhardt, Steinmann, and Mergheim [8].

## 2.6. RECOMMENDATIONS

The trends listed in Table 2.4 are pictorially shown over the simplification space in Figure 2.13. Here, the trends associated with the variation of peak and far-field tempera-

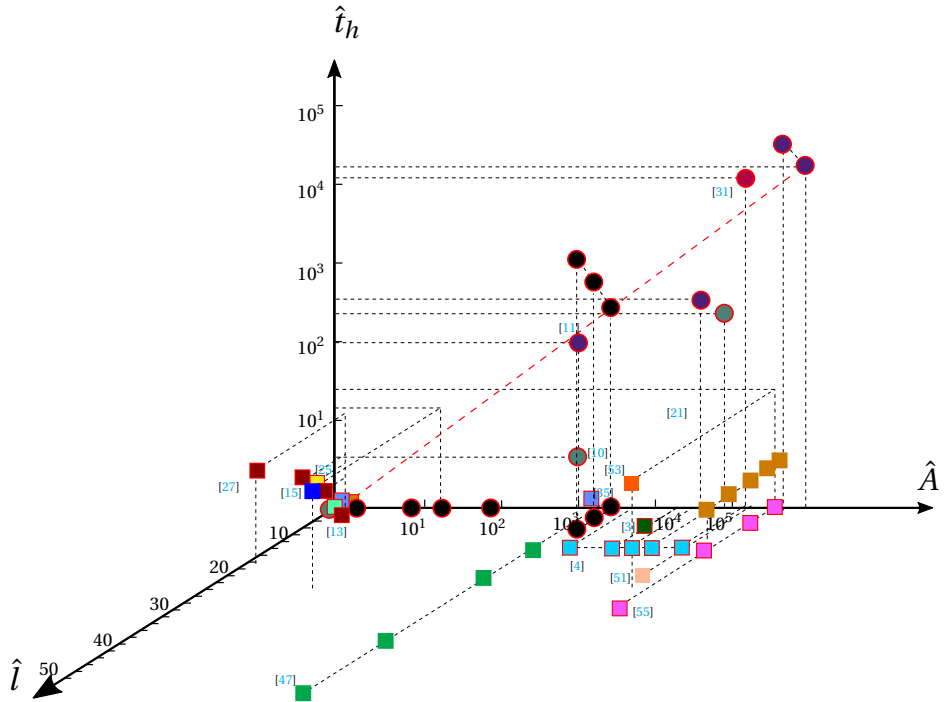


Figure 2.11: Classification of MAM thermal or thermo-mechanical models based on assumed spatial and temporal simplifications. The axes represent the normalised values of in-plane lumping ( $\hat{A}$ ), exposure time ( $\hat{t}_h$ ) and out-of-plane lumping ( $\hat{i}$ ). Note that scales are different for each axis, and the same colours denote different considerations in a single study. Thermal models are marked using circular markers, while thermo-mechanical models are shown with square markers. The models considered in this paper are indicated using black coloured markers. A red boundary around the marker signifies time consistency.

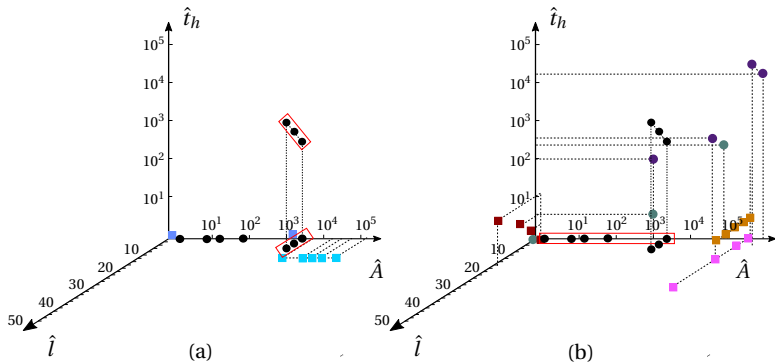


Figure 2.12: The simplification space showing the simplified models which focus on (a) peak and (b) far-field temperatures. Earlier papers that considered more than one point in the simplifications space are shown here. A red box is marked encapsulating the models which investigate the influence of any simplification for the first time.

Table 2.5: Computational (wall-clock) time in hours for thermal models presented in this paper. All computations are performed using 16 cores on a HPC cluster.

Simplification	Time (hrs)	Relative (%)	No. of layer(s)	No. of patch(es)
Thermal models				
$(\hat{A}_\Omega/400,1,1)$	302.1	100	1	400
$(\hat{A}_\Omega/256,1,1)$	193.5	64	1	256
$(\hat{A}_\Omega/100,1,1)$	79.1	26	1	100
$(\hat{A}_\Omega/25,1,1)$	18.2	6	1	25
$(\hat{A}_\Omega,1,1)$	50.6	16	20	1
$(\hat{A}_\Omega, \hat{t}_g, 1)$	1.1	0.4	20	1
$(\hat{A}_\Omega, 1, 2)$	30.1	10	20	1
$(\hat{A}_\Omega, \hat{t}_g, 2)$	1.0	0.3	20	1
$(\hat{A}_\Omega, 1, 5)$	12.5	4	20	1
$(\hat{A}_\Omega, \hat{t}_g, 5)$	0.7	0.2	20	1

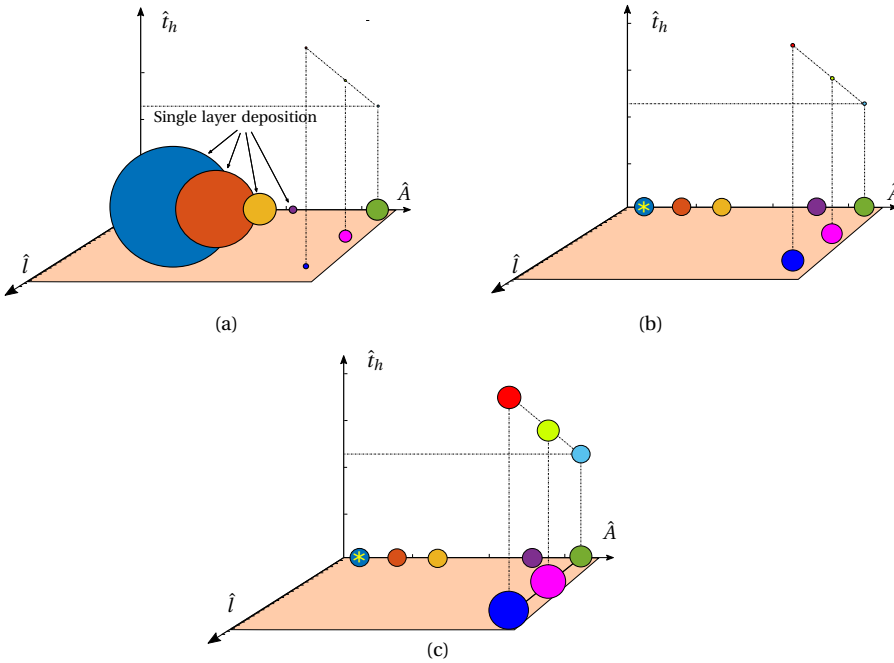


Figure 2.13: The 3D simplification space with the qualitative trend of variations for (a) computational time (b) peak temperatures and (c) far-field temperatures. The circle size shows the trends with radius indicating the relative values of respective parameters as observed in this paper. The reference value marked with '\*' sign is calculated using the reference model.

tures with respect to simplifications are shown in Figure 2.13b and c, respectively. The size of the circle associated with the reference model closest to the origin represents the reference value (marked with '\*'), while over or under prediction associated with a simplified model is represented by the relative size of the circle associated with that model.

2

These trends assist in making informed choices while setting up a part-scale MAM model. For example, if the aim is to capture the peak temperatures, then flash heating models should be used to provide accurate peak temperature predictions, as evident from Figure 2.13b. In literature, peak temperatures have been primarily used for three purposes: identification of problematic geometric features which accumulate heat [15, 40], calculation of cooling rate for microstructural analysis [3] and analysing the influence of scan strategy on residual stresses [33]. For the first two, layer-by-layer flash heating models are appropriately providing an adequate balance between accuracy and computational cost. However, if the purpose is to analyse the effect of the scanning strategy, a patch-by-patch model should be considered. On the other hand, gradual heating models should be avoided as they can lead to significant underestimation while capturing peak temperatures. However, values between flash and gradual heating can be used to find a balance between accuracy and computational cost. For example, as demonstrated by Patil et al. [35],  $t_h = 1$  ms, which is twice the flash heating time leads to peak temperatures around the melting point.

Next, if the aim of the model is to capture far-field temperatures, then gradual heating models should be preferred as they can provide accuracy with significantly less computational effort, as evident from Figure 2.13a and c. Finally, flash heating models are recommended if the thermal model is used as an input for mechanical analysis. As highlighted in Section 2.5, correct prediction of peak temperatures is important for mechanical analysis; hence, the earlier recommendations for capturing peak temperatures should be followed. The use of patch-by-patch models is suggested for capturing the directional nature of stresses, as shown in [4], while out-of-plane lumping is recommended for computational tractability. However, determining optimal patch size and out-of-plane lumping factor, which provide an adequate balance between accuracy and computational times, remains a non-trivial task and requires attention on a case-by-case basis. A numerical convergence study for finding these parameters is recommended. Finally, gradual heating models should not be used for this purpose as they significantly underestimate peak temperatures.

## 2.7. CONCLUSIONS

In this paper, the influence of commonly used spatio-temporal simplifications for part-scale modelling of MAM processes has been thoroughly investigated. The two spatial simplifications of in-plane and out-of-plane lumping and one temporal simplification of heating time have been studied. Using numerical models with varying levels of simplifications, it has been found that layer-by-layer models are sufficient for capturing peak temperatures. In contrast, patch-by-patch models are required for analysing the influence of scan vectors. Also, it has been concluded that if peak process temperatures are

to be captured, flash heating with no temporal simplification should be used. However, the strict numerical discretisation requirements associated with flash heating must be carefully ensured. On the other hand, the gradual heating schemes with temporal simplification have been shown to be suitable for capturing far-field temperatures in a computationally efficient manner since they also allow for much coarser spatial numerical discretisation.

No earlier work has holistically characterised the simplifications to the best of our knowledge, where the influence of each simplification has been studied on common MAM attributes. This study provides a broad perspective for choosing/avoiding any particular simplification while developing a MAM model. The work also led to the identification of certain open questions which require attention for further refining the understanding of simplifications. For example, guidelines for quantifying far-field distances could assist in a broader application of gradual heating models. Finding the appropriate lumping factor for in-plane and out-of-plane lumping, which provides an adequate balance between accuracy and computational time, is also an important avenue for future research. In this regard, first, an understanding of part sizes and shapes and their influence on lumping should be developed.

A direct extension of the approach presented in this paper can be the consideration of more simplifications and/or MAM attributes. Here, spatio-temporal simplifications were the primary focus. There are more physics-based simplifications *e.g.*, inclusion/exclusion of convection and/or radiation heat losses and consideration of temperature dependent properties. In this regard, the work by Ranjan et al. [40] analysed the influence of these physics-based simplifications, but only from the context of capturing peak temperatures. Hence, these simplifications can also be characterised using the holistic approach presented in this paper. Additionally, more MAM attributes can be included within the scope of characterising simplifications *e.g.* cooling rates. Lastly, the framework can also be extended to other AM processes where similar simplifications are commonly used *e.g.* wire arc additive manufacturing.

## REFERENCES

- [1] Toni A. Krol, Sebastian Westhäuser, M F Zäh, Johannes Schilp, and G Groth. “Development of a Simulation-Based Process Chain – Strategy for Different Levels of Detail for the Preprocessing Definitions”. In: *SNE Simulation Notes Europe* 21 (Dec. 2011), pp. 135–140.
- [2] D De Baere, M Bayat, S Mohanty, and J H Hattel. “Part-scale mechanical modelling of LPBF including microstructural evolution effects”. In: *IOP Conference Series: Materials Science and Engineering* 861 (June 2020), p. 012013.
- [3] D De Baere, M Bayat, S Mohanty, and J H Hattel. “Part-scale mechanical modelling of LPBF including microstructural evolution effects”. In: *IOP Conference Series: Materials Science and Engineering* 861 (June 2020), p. 012013.

- [4] Mohamad Bayat, Christopher G. Klingaa, Sankhya Mohanty, David De Baere, Jesper Thorborg, Niels S. Tiedje, and Jesper H. Hattel. “Part-scale thermo-mechanical modelling of distortions in Laser Powder Bed Fusion – Analysis of the sequential flash heating method with experimental validation”. In: *Additive Manufacturing* 36 (2020), p. 101508. ISSN: 2214-8604.
- [5] Mohamad Bayat, Sankhya Mohanty, and Jesper Henri Hattel. “Multiphysics modelling of lack-of-fusion voids formation and evolution in IN718 made by multi-track/multi-layer L-PBF”. In: *International Journal of Heat and Mass Transfer* 139 (2019), pp. 95–114. ISSN: 0017-9310.
- [6] Mohamad Bayat, Venkata K. Nadimpalli, Francesco G. Biondani, Sina Jafarzadeh, Jesper Thorborg, Niels S. Tiedje, Giuliano Bissacco, David B. Pedersen, and Jesper H. Hattel. “On the role of the powder stream on the heat and fluid flow conditions during Directed Energy Deposition of maraging steel—Multiphysics modeling and experimental validation”. In: *Additive Manufacturing* 43 (2021), p. 102021. ISSN: 2214-8604.
- [7] Mohamad Bayat, Aditi Thanki, Sankhya Mohanty, Ann Witvrouw, Shoufeng Yang, Jesper Thorborg, Niels Skat Tiedje, and Jesper Henri Hattel. “Keyhole-induced porosities in Laser-based Powder Bed Fusion (L-PBF) of Ti6Al4V: High-fidelity modelling and experimental validation”. In: *Additive Manufacturing* 30 (2019), p. 100835. ISSN: 2214-8604.
- [8] Christian Burkhardt, Paul Steinmann, and Julia Mergheim. “Thermo-mechanical simulations of powder bed fusion processes: accuracy and efficiency”. In: *Advanced Modeling and Simulation in Engineering Sciences* 9.1 (Sept. 2022), p. 18. ISSN: 2213-7467.
- [9] H S Carslaw and J C Jaeger. *Conduction of heat in solids*. English. Oxford: Clarendon Press, 1959.
- [10] Michele Chiumenti, Xin Lin, Miguel Cervera, Lei Wei, Yuxiang Zheng, and Weidong Huang. “Numerical simulation and experimental calibration of additive manufacturing by blown powder technology. Part I: Thermal analysis”. In: *Rapid Prototyping Journal* 23 (Mar. 2017), pp. 448–463.
- [11] Michele Chiumenti, Eric Neiva, Emilio Salsi, Miguel Cervera, Santiago Badia, Joan Moya, Zhuoer Chen, Caroline Lee, and Christopher Davies. “Numerical modelling and experimental validation in Selective Laser Melting”. In: *Additive Manufacturing* 18 (2017), pp. 171–185. ISSN: 2214-8604.
- [12] K Dai and L Shaw. “Thermal and mechanical finite element modeling of laser forming from metal and ceramic powders”. In: *Acta Materialia* 52.1 (2004), pp. 69–80. ISSN: 1359-6454.
- [13] Erik Denlinger, Jeff Irwin, and Pan Michaleris. “Thermomechanical Modeling of Additive Manufacturing Large Parts”. In: *Journal of Manufacturing Science and Engineering* 136 (Oct. 2014), p. 061007.
- [14] Ian Gibson, D. W. Rosen, and B. Stucker. *Additive Manufacturing Technologies*. Berlin: Springer, 2015.

- [15] N.E. Hodge, Robert Ferencz, and Jerome Solberg. "Implementation of a thermo-mechanical model for the simulation of selective laser melting". In: *Computational Mechanics* 54 (July 2014).
- [16] Nils Keller and Vasily Ploshikhin. "New Method for fast predictions of residual stress and distortion of AM parts". In: Aug. 2014.
- [17] Saad A. Khairallah, Andrew T. Anderson, Alexander Rubenchik, and Wayne E. King. "Laser powder-bed fusion additive manufacturing: Physics of complex melt flow and formation mechanisms of pores, spatter, and denudation zones". In: *Acta Materialia* 108 (2016), pp. 36–45. ISSN: 1359-6454.
- [18] Saad A. Khairallah and Andy Anderson. "Mesoscopic simulation model of selective laser melting of stainless steel powder". In: *Journal of Materials Processing Technology* 214.11 (2014), pp. 2627–2636. ISSN: 0924-0136.
- [19] W. King, A. T. Anderson, R. M. Ferencz, N. E. Hodge, C. Kamath, and S. A. Khairallah. "Overview of modelling and simulation of metal powder bed fusion process at Lawrence Livermore National Laboratory". In: *Materials Science and Technology* 31.8 (2015), pp. 957–968.
- [20] W. E. King, A. T. Anderson, R. M. Ferencz, N. E. Hodge, C. Kamath, S. A. Khairallah, and A. M. Rubenchik. "Laser powder bed fusion additive manufacturing of metals; physics, computational, and materials challenges". In: *Applied Physics Reviews* 2.4 (2015), p. 041304.
- [21] Abhilash Kiran, Josef Hodek, Jaroslav Vavřík, Miroslav Urbánek, and Jan Džugan. "Numerical Simulation Development and Computational Optimization for Directed Energy Deposition Additive Manufacturing Process". In: *Materials* 13.11 (2020), p. 2666.
- [22] Andreas Kirchheim, Hans-Jörg Dennig, and Livia Zumofen. "Why Education and Training in the Field of Additive Manufacturing is a Necessity". In: (Jan. 2018), pp. 329–336.
- [23] S. Kolossov, E. Boillat, R. Glardon, P. Fischer, and M. Locher. "3D FE simulation for temperature evolution in the selective laser sintering process". In: *International Journal of Machine Tools and Manufacture* 44.2 (2004), pp. 117–123. ISSN: 0890-6955.
- [24] Prashant Kulkarni, Anne Marsan, and Debasish Dutta. "Review of process planning techniques in layered manufacturing". In: *Rapid Prototyping Journal* 6 (Mar. 2000), pp. 18–35.
- [25] Xufei Lu, Xin Lin, Michele Chiumenti, Miguel Cervera, Yunlong Hu, Xianglin Ji, Liang Ma, Haiou Yang, and Weidong Huang. "Residual stress and distortion of rectangular and S-shaped Ti-6Al-4V parts by Directed Energy Deposition: Modelling and experimental calibration". In: *Additive Manufacturing* 26 (2019), pp. 166–179. ISSN: 2214-8604.

- [26] Sonny Ly, Alexander M Rubenchik, Saad A Khairallah, Gabe Guss, and Manyalibo J Matthews. “Metal vapor micro-jet controls material redistribution in laser powder bed fusion additive manufacturing”. In: *Scientific Reports* 7.1 (2017), p. 4085. ISSN: 2045-2322.
- [27] Andreas Malmelöv, Andreas Lundbäck, and Lars-Erik Lindgren. “History Reduction by Lumping for Time-Efficient Simulation of Additive Manufacturing”. In: *Metals* 10 (Dec. 2019), p. 58.
- [28] Abaqus User Manual. “Abaqus user manual”. In: *Abacus* (2020).
- [29] V Manvatkar, Amitava De, and Tarasankar Debroy. “Heat transfer and material flow during laser assisted multi-layer additive manufacturing”. In: *Journal of Applied Physics* 116 (Sept. 2014), pp. 124905–124905.
- [30] Raya Mertens, Stijn Clijsters, Karolien Kempen, and Jean-Pierre Kruth. “Optimization of Scan Strategies in Selective Laser Melting of Aluminum Parts With Down-facing Areas”. In: *Journal of Manufacturing Science and Engineering* 136(6) (Dec. 2014).
- [31] Eric Neiva, Michele Chiumenti, Miguel Cervera, Emilio Salsi, Gabriele Piscopo, Santiago Badia, Alberto F. Martín, Zhuoer Chen, Caroline Lee, and Christopher Davies. “Numerical modelling of heat transfer and experimental validation in powder-bed fusion with the virtual domain approximation”. In: *Finite Elements in Analysis and Design* 168 (2020), p. 103343. ISSN: 0168-874X.
- [32] L. Papadakis, A. Loizou, J. Risse, and J. Schrage. “Numerical Computation of Component Shape Distortion Manufactured by Selective Laser Melting”. In: *Procedia CIRP* 18 (2014). Proceedings of the International Conference on Manufacturing of Lightweight Components - ManuLight 2014, pp. 90–95. ISSN: 2212-8271.
- [33] L. Parry, I.A. Ashcroft, and R.D. Wildman. “Understanding the effect of laser scan strategy on residual stress in selective laser melting through thermo-mechanical simulation”. In: *Additive Manufacturing* 12 (2016), pp. 1–15. ISSN: 2214-8604.
- [34] L.A. Parry, I.A. Ashcroft, and R.D. Wildman. “Geometrical effects on residual stress in selective laser melting”. In: *Additive Manufacturing* 25 (2019), pp. 166–175. ISSN: 2214-8604.
- [35] Nachiket Patil, Rishi Ganeriwala, Jerome M. Solberg, Neil E. Hodge, and Robert M. Ferencz. “Benchmark multi-layer simulations for residual stresses and deformation in small additively manufactured metal parts”. In: *Additive Manufacturing* (2021), p. 102015. ISSN: 2214-8604.
- [36] Hao Peng, Morteza Ghasri-Khouzani, Shan Gong, Ross Attardo, Pierre Ostiguy, Bernice Aboud Gatrell, Joseph Budzinski, Charles Tomonto, Joel Neidig, M. Ravi Shankar, Richard Billo, David B. Go, and David Hoelzle. “Fast prediction of thermal distortion in metal powder bed fusion additive manufacturing: Part 1, a thermal circuit network model”. In: *Additive Manufacturing* 22 (2018), pp. 852–868. ISSN: 2214-8604.



- [37] Hao Peng, Morteza Ghasri-Khouzani, Shan Gong, Ross Attardo, Pierre Ostiguy, Ronald B. Rogge, Bernice Aboud Gatrell, Joseph Budzinski, Charles Tomonto, Joel Neidig, M. Ravi Shankar, Richard Billo, David B. Go, and David Hoelzle. “Fast prediction of thermal distortion in metal powder bed fusion additive manufacturing: Part 2, a quasi-static thermo-mechanical model”. In: *Additive Manufacturing* 22 (2018), pp. 869–882. ISSN: 2214-8604.
- [38] P. Prabhakar, W.J. Sames, R. Dehoff, and S.S. Babu. “Computational modeling of residual stress formation during the electron beam melting process for Inconel 718”. In: *Additive Manufacturing* 7 (2015), pp. 83–91. ISSN: 2214-8604.
- [39] Sebastian D. Proell, Wolfgang A. Wall, and Christoph Meier. “A simple yet consistent constitutive law and mortar-based layer coupling schemes for thermomechanical macroscale simulations of metal additive manufacturing processes”. In: *Advanced Modeling and Simulation in Engineering Sciences* 8.1 (Oct. 2021), p. 24. ISSN: 2213-7467.
- [40] Rajit Ranjan, Can Ayas, Matthijs Langelaar, and Fred van Keulen. “Fast Detection of Heat Accumulation in Powder Bed Fusion Using Computationally Efficient Thermal Models”. In: *Materials* 13.20 (2020). ISSN: 1996-1944.
- [41] Ibiye Aseibichin Roberts. “Investigation of residual stresses in the laser melting of metal powders in additive layer manufacturing”. In: (). PhD thesis, University of Wolverhampton, 2012.
- [42] John Romano, Leila Ladani, and Magda Sadowski. “Thermal Modeling of Laser Based Additive Manufacturing Processes within Common Materials”. In: *Procedia Manufacturing* 1 (2015). 43rd North American Manufacturing Research Conference, NAMRC 43, 8-12 June 2015, UNC Charlotte, North Carolina, United States, pp. 238–250. ISSN: 2351-9789.
- [43] Marleen Rombouts, L. Froyen, A. Gusarov, El Hassane Bentefour, and Christ Gloreux. “Photopyroelectric measurement of thermal conductivity of metallic powders”. In: *Journal of Applied Physics* 97 (Dec. 2004), p. 24905.
- [44] Alexander M. Rubenchik, Wayne E. King, and Sheldon S. Wu. “Scaling laws for the additive manufacturing”. In: *Journal of Materials Processing Technology* 257 (2018), pp. 234–243. ISSN: 0924-0136.
- [45] Babis Schoinochoritis, Dimitrios Chantzis, and Konstantinos Salonitis. “Simulation of metallic powder bed additive manufacturing processes with the finite element method: A critical review”. In: *Proceedings of the Institution of Mechanical Engineers, Part B: Journal of Engineering Manufacture* 231 (Jan. 2015).
- [46] Bo Song, Xiao Zhao, Shuai Li, Changjun Han, Qingsong Wei, Shifeng Wen, Jie Liu, and Yusheng Shi. “Differences in microstructure and properties between selective laser melting and traditional manufacturing for fabrication of metal parts: A review”. In: *Frontiers of Mechanical Engineering* 10.2 (June 2015), pp. 111–125. ISSN: 2095-0241.
- [47] Richard J. Williams, Catrin M. Davies, and Paul A. Hooper. “A pragmatic part scale model for residual stress and distortion prediction in powder bed fusion”. In: *Additive Manufacturing* 22 (2018), pp. 416–425. ISSN: 2214-8604.

- [48] Y. Yang, M.F. Knol, F. van Keulen, and C. Ayas. “A semi-analytical thermal modelling approach for selective laser melting”. In: *Additive Manufacturing* 21 (2018), pp. 284–297. ISSN: 2214-8604.
- [49] Yabin Yang, Xin Zhou, Quan Li, and Can Ayas. “A computationally efficient thermo-mechanical model for wire arc additive manufacturing”. In: *Additive Manufacturing* 46 (2021), p. 102090. ISSN: 2214-8604.
- [50] Chor Yen Yap, Chee Kai Chua, Zhi Li Dong, Zhong Hong Liu, Dan Qing Zhang, Loong Ee Loh, and Swee Leong Sing. “Review of selective laser melting: Materials and applications”. In: *Applied physics reviews* 2.4 (2015), p. 041101.
- [51] Tianyu Yu, Ming Li, Austin Breaux, Mukul Atri, Suleiman Obeidat, and Chao Ma. “Experimental and numerical study on residual stress and geometric distortion in powder bed fusion process”. In: *Journal of Manufacturing Processes* 46 (2019), pp. 214–224. ISSN: 1526-6125.
- [52] Pengpeng Yuan and Dongdong Gu. “Molten pool behaviour and its physical mechanism during selective laser melting of TiC/AlSi10Mg nanocomposites: simulation and experiments”. In: *Journal of Physics D: Applied Physics* 48.3 (Jan. 2015), p. 035303.
- [53] Michael F. Zaeh and Gregor Branner. “Investigations on residual stresses and deformations in selective laser melting”. In: *Production Engineering* 4.1 (Feb. 2010), pp. 35–45. ISSN: 1863-7353.
- [54] Kai Zeng, D Pal, and Brent Stucker. “A review of thermal analysis methods in laser sintering and selective laser melting”. In: *23rd Annual International Solid Freeform Fabrication Symposium - An Additive Manufacturing Conference, SFF 2012* (Jan. 2012), pp. 796–814.
- [55] Wenyou Zhang, Mingming Tong, and Noel M. Harrison. “Resolution, energy and time dependency on layer scaling in finite element modelling of laser beam powder bed fusion additive manufacturing”. In: *Additive Manufacturing* 28 (2019), pp. 610–620. ISSN: 2214-8604.

# 3

## FAST DETECTION OF HEAT ACCUMULATION IN AM USING COMPUTATIONALLY EFFICIENT THERMAL MODELS

*The powder bed fusion (PBF) process is a type of Additive Manufacturing (AM) technique which enables fabrication of highly complex geometries with unprecedented design freedom. However, PBF still suffers from manufacturing constraints which, if overlooked, can cause various types of defects in the final part. One such constraint is the local accumulation of heat which leads to surface defects such as melt ball and dross formation. Moreover, slow cooling rates due to local heat accumulation can adversely affect resulting microstructures. In this paper, first a layer-by-layer PBF thermal process model, well established in the literature, is used to predict zones of local heat accumulation in a given part geometry. However, due to the transient nature of the analysis and the continuously growing domain size, the associated computational cost is high which prohibits part-scale applications. Therefore, to reduce the overall computational burden, various simplifications and their associated effects on the accuracy of detecting overheating are analyzed. In this context, three novel physics-based simplifications are introduced motivated by the analytical solution of the one-dimensional heat equation. It is shown that these novel simplifications provide unprecedented computational benefits while still allowing correct prediction of the zones of heat accumulation. The most far-reaching simplification uses the steady-state thermal response of the part for predicting its heat accumulation behavior with a speedup of 600 times as compared to a conventional analysis. The proposed simplified thermal models are capable of fast detection of problematic part features. This allows*

---

Parts of this chapter have been published in [Fast detection of heat accumulation in powder bed fusion using computationally efficient thermal models](#), *Materials*, 2020

*for quick design evaluations and opens up the possibility of integrating simplified models with design optimization algorithms.*

### 3.1. INTRODUCTION

Additive manufacturing (AM) offers unprecedented design freedom as compared to conventional manufacturing techniques. The layer-by-layer material deposition allows for manufacturing functional parts with high geometric complexity. Due to this advantage, AM has already gained significant popularity among manufacturing industries such as automotive, aerospace and medical [37, 21]. However, the AM process is not free from manufacturing constraints and, if overlooked, these constraints can cause a wide range of defects in the final part which lead to an increased overall cost. Therefore, to fully capitalize on the benefits offered by AM, manufacturing limitations should be considered at the design stage.

Laser powder bed fusion (LPBF) process is one of the most common techniques for printing metal parts. It involves sequential deposition of metal powder layers which are selectively molten and fused together in predefined areas using a moving laser beam. This implies that heat primarily flows from each newly deposited topmost layer towards the thick baseplate at the bottom, which acts as a heat sink. It is observed that whenever the deposited heat is not properly evacuated towards the baseplate, it leads to local overheating or heat accumulation [24]. It typically refers to a situation where material locally experiences thermal process conditions that result in temperatures outside the desired temperature range needed to obtain the desired final product quality. Given the wide range of potential temperature-induced production failure mechanisms, overheating can manifest itself in many forms. In the in situ monitoring studies conducted by Hooper [15] and Craeghs et al. [11], overheating is characterized by the enlarged melt pool observed in the vicinity of lower conductivity regions which obstruct heat flow. In the numerical study conducted by Hodge, Ferencz, and Solberg [14], the overheating phenomenon is characterized by the overshoot of simulation temperatures above the melting point.

It has been widely recognized in the literature that local overheating or heat accumulation is detrimental for final part quality and can cause various defects. For example, Mertens et al. [24] investigated the defect of dross formation where an enlarged melt pool caused by local overheating leads to undesired sintering of loose powder in its vicinity. Charles et al. [7] also studied dross formation by investigating the correlation between process parameters, e.g., laser power, scan speed and the resulting surface roughness. High process temperatures along with the effect of surface tension lead to the defect of melt ball formation [35]. These cases are examples where overheating depends on the local distribution of conductivity in the vicinity of melt pool. Another more recently studied phenomenon is that of gradual accumulation of heat with increasing part height. As more layers are deposited, they act as a thermal barrier causing prolonged heated zones with slower cooling. This becomes increasingly significant in tall parts with high heat capacity. Therefore, the phenomenon was initially investigated for processes such as laser metal deposition (LMD) [36] and wire-arc-based AM process (WAAM) [39], where typical part sizes are larger than LPBF. More recently, it has been studied for the LPBF process as well. For example Mohr, Altenburg, and Hilgenberg [25] used in situ thermography for observing cooling conditions during the process. It is reported that

heat accumulation increases with increasing build height. Also, inter-layer time (ILT), i.e., the time elapsed between processing successive layers, is found to be an important parameter which inversely affects heat accumulation.

It is important to understand that both these phenomena, i.e., local overheating and gradual heat accumulation during the build, are intimately coupled. Elevated temperatures due to local overheating contribute to the gradual accumulation in the successive layers and accumulated heat will conversely intensify local overheating. Therefore, both these phenomena jointly determine the overall thermal history of the part, which subsequently has a direct effect on the final part quality. For example, Mohr, Altenburg, and Hilgenberg [25] performed metallographic analysis to study the influence of heat accumulation on observed microstructures. It is suggested in this paper that specific temperature ranges which are important from the context of phase transformations should be considered while analyzing the influence of heat accumulation. Another aspect investigated by Parry, Ashcroft, and Wildman [28] shows that regions susceptible to overheating generate significant residual stresses, which are likely to result in undesired deformations and potentially build failures. Kastsian and Reznik [18] analyzed a part geometry where local overheating led to excessive deformations causing recoater jamming. Heigel and Whitenton [13] presented layer-wise cooling rate maps which show that overheating zones tend to cool slower. Lastly, as suggested by Charles et al. [7], another aspect of overheating control is associated with selecting optimal process parameters. For example, Mertens et al. [24] varied laser power in accordance with the level of overhang for controlling dross formation. However, such approaches also rely on prior knowledge of overheating zones so that parameters can be tuned accordingly. Hence, early identification of geometric features which are prone to local overheating can assist designers and machine operators in judging manufacturability of the final design.

Typically, downfacing or overhanging features are prone to this phenomenon as loose powder, with significantly lower thermal conductivity than that of the bulk material, does not allow for rapid heat evacuation. The degree of overheating typically increases with decreasing the overhang angle defined as the angle between part surface and the base plate. Therefore, heuristic AM design guidelines are used, where features with overhang angles smaller than a critical value are avoided [10, 4]. Although overhangs are a salient example of features which cause overheating, the phenomenon is not uniquely linked to them. For example, LPBF specimens manufactured by Adam and Zimmer [1] and Patel et al. [29] demonstrate overheating induced discoloration and high surface roughness, respectively, even after strictly following the overhang design guideline. This indicates that not only the local overhang angle, but the thermal response should be considered for detecting and preventing overheating.

Numerical modeling of the transient heat transfer phenomena during the LPBF process can provide thermal history information which can be used for identification of features causing local overheating. However, excessive computational cost associated with detailed modeling of the LPBF process prohibits part-scale implementation, particularly in iterative design settings. Please note that the size of the laser spot is in the order of a

few microns whereas the part size is in the order of centimeters. Moreover, in time domain, the phenomenon of melting and re-solidification is extremely fast, whereas cooling between the layers is in order of tens of seconds. Hence, to capture the steep thermal gradients caused by a fast-moving laser, very fine spatial and temporal resolution is required which makes the modeling process computationally intractable. To address this issue, researchers reduce the computational complexity of models by introducing simplifications in various ways. For example, several studies motivate consideration of conduction as the only mode of heat transfer while neglecting convection and radiation [30, 32, 3]. Another commonly used simplification is to simulate an entire layer addition as a single simulation step, i.e., the entire layer area is simultaneously exposed to a heat flux. It has been demonstrated by King et al. [19] that during a new layer deposition, 4–8 previously deposited layers are also re-molten and fused. This re-melting is intentional as it allows for a seamless connection between the layers. Therefore, the concept of “superlayers” or layer lumping has been proposed where deposition of one superlayer refers to the simultaneous deposition of multiple real layers while modeling the process [31, 9, 22, 42].

These simplifications can provide significant computational gains as compared to high-fidelity models, with a reasonable compromise in accuracy. For example, Chiu-menti et al. [9] studied the impact of excluding powder conduction, simplifying laser scan strategies and lumping multiple layers during thermal simulation. The simulation data is analyzed for accuracy by comparing it with the experimental temperatures recorded using thermocouples embedded inside the printed parts. It is reported that powder exclusion results in 4 times faster simulation. Furthermore, the layer-by-layer approach is reported to be 6 times faster than the model which simulates scan strategies. Lastly, lumping of 4 layers provided another 3 fold decrease in the computational time. It is reported that with increased layer lumping, the model captures an average evolution of the temperature field during the manufacturing process. Another study by Zhang, Tong, and Harrison [42] investigated the effect of using lumped layers as thick as 4, 12 and 24 times the real layer thickness. The analysis was carried out for a 2D real-size part (height = 54.7 mm, width = 20.4 mm) and it was reported that lumping of 4 layers already results in a 20 times faster simulation compared to the one with no layer lumping. In both of these cases, although approximations provide significant computational gain, still the simulation times remain in the order of hours. For example, out of the two cases discussed above, the former reports that simulation with 4 layer lumping requires 1.33 h for parts with volume of  $107 \text{ cm}^3$  printed with 992 layers. For the latter 2D example, the model with lumping of 4 layers needed 4.6 h to complete.

In this paper, we aim to develop a model which could identify zones of local overheating and in order to assess manufacturability of designs and make quick design decisions, even faster computation times will be preferred. This is also motivated by the desire of integrating AM models within an optimization framework. Therefore, in this research, first a lumped layer-by-layer model is considered for simulating a real-size LPBF part and the temperature data is used to judge the heat accumulation tendencies of different design features. Details about this model are presented in Section 3.2. As highlighted in

the previous paragraph, even with the simplifications of powder exclusion and lumped layer-by-layer deposition technique, the simulation time remains prohibitive for large scale implementations. Therefore in Section 3.3, six additional simplifications are presented. The first three have been partially discussed in the literature but an analysis of their impact on specifically overheating detection was never done before, which is discussed in Section 3.3.1. Next, three further simplifications are proposed in Section 3.3.2 which are the primary novel contributions of this paper. An analysis based on the analytical solution of the one-dimensional heat equation provides the motivation for these novel simplifications. Subsequently, Section 3.4 presents results obtained using the different simplifications and it is shown that the proposed simplifications provide adequate prediction of overheating regions while providing significant computation gains. Lastly, conclusions and future directions are discussed in Section 3.5

## 3.2. REFERENCE THERMAL LPBF PROCESS MODEL

In this section, a layer-by-layer part-scale thermal model is presented, intended for judging manufacturability of designs from the context of local overheating. It is based on the thermal model previously presented by Chiumenti et al. [8] for simulating material deposition in the laser material deposition (LMD) process. The same concept was later used for LPBF modeling in several publications [9, 27, 26]. The experimental validation of the model has been presented in Chiumenti et al. [9] where simulation results were compared with temperatures empirically recorded using in situ thermocouples placed inside the part during the LPBF process. It was shown that this modeling method can correctly capture the thermal history as obtained using the thermocouples. More importantly, it was observed by Neiva et al. [26] that the model correctly predicts the high temperatures measured near an overhanging feature. Therefore, it is deemed suitable for the intended purpose of identifying geometric features which cause local heat accumulation during the LPBF process. The model presented in this section acts as a reference for the simplified models presented in the later sections.

### 3.2.1. MODEL DESCRIPTION

A typical LPBF process includes layer-by-layer deposition of material on a thick base-plate. Figure 3.1 shows a schematic where an arbitrary 3D object is considered with volume  $\Omega$  already deposited. The surfaces  $\partial\Omega$  of the partly manufactured object are classified as top, lateral and bottom represented as  $\partial\Omega_{\text{top}}$ ,  $\partial\Omega_{\text{lat}}$  and  $\partial\Omega_{\text{bot}}$ , respectively. The part remains submerged inside the powder bed while thermal energy provided through the newly deposited layer increases the part temperature in accordance with the heat equation given as

$$\rho(T)c_p(T)\frac{\partial T}{\partial t} = \nabla \cdot (k(T)\nabla T) + Q_v, \quad (3.1)$$

where  $T$  is temperature,  $t$  is time,  $Q_v$  is a volumetric heat source and  $\rho$ ,  $c_p$ ,  $k$  are temperature-dependent density, specific heat and thermal conductivity, respectively.



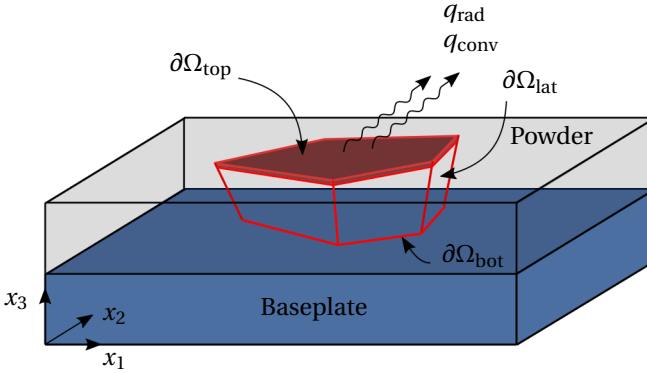


Figure 3.1: Schematic illustration of a body  $\Omega$  being fabricated during the LPBF process. The topmost crimson colored region signifies the newly deposited layer. The body is attached to the baseplate at the bottom surface  $\partial\Omega_{\text{bot}}$  while a laser scans the top surface  $\partial\Omega_{\text{top}}$ . The part-powder interface is denoted as the lateral surface  $\partial\Omega_{\text{lat}}$ . Thermal losses due to convection and radiation are shown as  $q_{\text{conv}}$  and  $q_{\text{rad}}$ , respectively.

Next, to formulate a boundary value problem (BVP), process-relevant boundary and initial conditions are specified. It is reported that the effective conductivity of powder layer is only 1% of bulk conductivity [34, 33]. Hence, it is justified to assume that the heat transfer through powder is negligible as compared to conduction within the part. Therefore, lateral sides of the part, i.e., the part-powder interface, is assumed to be thermally insulated

$$\frac{\partial T}{\partial x_i} n_i = 0 \quad \text{on} \quad \partial\Omega_{\text{lat}}, \quad (3.2)$$

where  $n_i$  are the components of the outward normal unit vector to  $\partial\Omega_{\text{lat}}$  and the repeated index indicates summation over  $i$ . The part remains bonded to the baseplate which is typically pre-heated and acts as a heat sink. This is taken into account by specifying a temperature boundary condition

$$T = T_0 \quad \text{on} \quad \partial\Omega_{\text{bot}}, \quad (3.3)$$

where  $T_0$  is the pre-heat temperature which is assumed to be constant. Next, heat losses through convection and radiation are considered at the top surface  $\partial\Omega_{\text{top}}$

$$q_{\text{conv}} = h_{\text{conv}}(T - T_a) \quad \text{on} \quad \partial\Omega_{\text{top}}, \quad (3.4)$$

where  $h_{\text{conv}}$  is the convective heat transfer coefficient and  $T_a$  is the ambient temperature, assumed to be constant within the machine chamber. The radiative heat transfer boundary condition is given as

$$q_{\text{rad}} = \sigma\epsilon(T^4 - T_a^4) \quad \text{on} \quad \partial\Omega_{\text{top}}, \quad (3.5)$$

where  $\sigma$  is Stefan-Boltzmann constant and  $\epsilon$  is emissivity of the radiating surface. Lastly, each newly added layer is assumed to be at an initial temperature of  $T_0$ .

It is important to note that during the process, melting and re-solidification of material also takes place. However, the influence of these phase transformations on resulting temperatures is not considered here. This is motivated by the fact that the energy absorbed during melting is released during re-solidification when the laser beam moves away from the melt zone. Hence, the net effect of phase transformations is negligible when considering part-scale temperatures [40]. As discussed in Section 3.1, lumped layer-by-layer material addition is considered here, which means that the uniform heat source  $Q_v$  is simultaneously applied over the entire volume of the newly deposited lumped layer. Both of these simplifications, i.e., lumping and layer-by-layer material addition, have been motivated and applied in number of previous LPBF simulation studies [31, 9, 42, 2, 22]. Apart from obvious computational benefits, these choices are motivated by the fact that it has been shown by Chiumenti et al. [9] that a model with these simplifications is adequate for correctly capturing the part-scale thermal response.

### 3.2.2. FINITE ELEMENT ANALYSIS AND SIMULATION PARAMETER SETTING

To solve the boundary value problem (BVP) given by Eqs. (3.1)–(3.5), finite element analysis is used. The element birth-and-death method is implemented which is a common technique used to simulate the growing domain during the AM processes [32, 42]. The implementation is done in CalculiX (a free and open source FE analysis code) [12] with a structured mesh where elements are aligned with the (lumped) layers. Eight-node linear cubic elements are used where mesh size is equal to the superlayer thickness which is assumed to be  $S = 500 \mu\text{m}$ . This choice is motivated by the study conducted by Zhang, Tong, and Harrison [42] where temperature histories for different degree of layer lumping are compared. It is shown that the temperature response remains reasonably accurate for a superlayer thickness of  $480 \mu\text{m}$  for Ti-6Al-4V parts with typical LPBF machine parameters. Typically, layer thickness for the LPBF process varies from  $20\text{--}80 \mu\text{m}$  and in this study we use a representative value of  $50 \mu\text{m}$  for real LPBF layer thickness i.e., the superlayer is 10 times thicker than the real layer thickness. The newly deposited superlayer is subjected to a uniform volumetric heat source  $Q_v$  [ $\text{W}/\text{m}^3$ ] for the heating time  $t_h$ . In accordance with Eq. (3.3), the finite element nodes associated with the bottom surface act as heat sink, i.e., their temperature remains fixed at  $T_0$ . The heating step is followed by a cooling step in which the newly deposited layer can cool for an inter-layer time (ILT)  $t_d$ . The cycle of sequential heating and cooling repeats while the thermal history of all previous heating/cooling steps influence the simulation of the next step.

As mentioned earlier, the modeling principles presented by Chiumenti et al. [9] and Neiva et al. [27] are used here which provides a basis for setting simulation parameters  $t_h$  and  $Q_v$ . The two key ideas presented by Chiumenti et al. [9] and Neiva et al. [27] are as follows:

- Heating time  $t_h$  for a layer with area  $A$  equals the time that the laser would take for

scanning that entire layer, i.e.,

$$t_h = \frac{A}{hv}, \quad (3.6)$$

where  $h$  is hatch spacing and  $v$  is laser scan velocity. Please note that by using this definition,  $t_h$  is calculated for each super layer and it depends on the local part geometry through layer scan areas.

- It is ensured that the total deposited energy matches that of the actual process. Deposited energy per unit time is given by  $E = \gamma P$ , where  $\gamma$  is the absorption coefficient and  $P$  is laser power. Using this principle, the volumetric heat source term can be calculated as

$$Q_v = \frac{\gamma P}{Al}, \quad (3.7)$$

where  $l$  is LPBF layer thickness.

Please note that the real LPBF layer thickness  $l$  which is different from the simulated superlayer thickness  $S$  is used for calculating  $Q_v$  in Eq. (3.7). This ensures that the input energy is automatically scaled when using thicker lumped layers. It is demonstrated by Chiumenti et al. [9] and Neiva et al. [27] that the described simulation scheme is capable of predicting the real physical temperatures recorded during the process as captured using the thermocouples located as close as 2.5 mm away from the topmost layer.

Next, the ILT parameter used for cooling down between layer depositions needs to be specified. As mentioned,  $S = 500 \mu\text{m}$  is used which is 10 times thicker than the real layer thickness. Hence, as suggested by Zhang, Tong, and Harrison [42], the ILT should also be scaled in order to compensate for the effect of large heat capacity of the superlayers. Peng et al. [31] used a method where ILT for a thick layer is adjusted such that thermal decay rates match with those of real-sized layers. However, the thermal decay rate varies at different locations within a part geometry which makes this estimation design dependent. Moreover, the ILT for the real size layers also depends on multiple factors such as layer area, scanning pattern, number of parts printed together inside the same chamber and recoater speed. Therefore, as per the linear scaling suggested by Zhang, Tong, and Harrison [42] and Malmelöv, Lundbäck, and Lindgren [22], we choose to use an estimated value of 100 s which is 10 times the typical recoater time of 10 s and later we discuss the implications of this choice. The temperature-dependent properties of Ti-6Al-4V are taken from Chiumenti et al. [9] covering the range from room to fusion temperatures and shown in Figure 3.2. Finally, Table 3.1 lists the modeling parameters which are common to all the shown results.

### 3.2.3. IDENTIFICATION OF OVERHEATING ZONES

Figure 3.3 illustrates the considered part geometry where dimensions and build direction are specified. The part dimensions are representative of a typical LPBF part. This particular design is chosen because of two key aspects. First, all overhanging features have

Table 3.1: List of process parameters used for simulation of LPBF process.

$P$ (W)	200
$\gamma$	0.45
$v$ ( $\text{ms}^{-1}$ )	1
$h$ (mm)	0.14
$l$ (mm)	0.05
$S$ (mm)	0.5
$T_0$ ( $^{\circ}\text{C}$ )	180
$T_a$ ( $^{\circ}\text{C}$ )	25
$h_{\text{conv}}$ ( $\text{Wm}^{-2}\text{K}^{-1}$ )	10
$\epsilon$	0.35

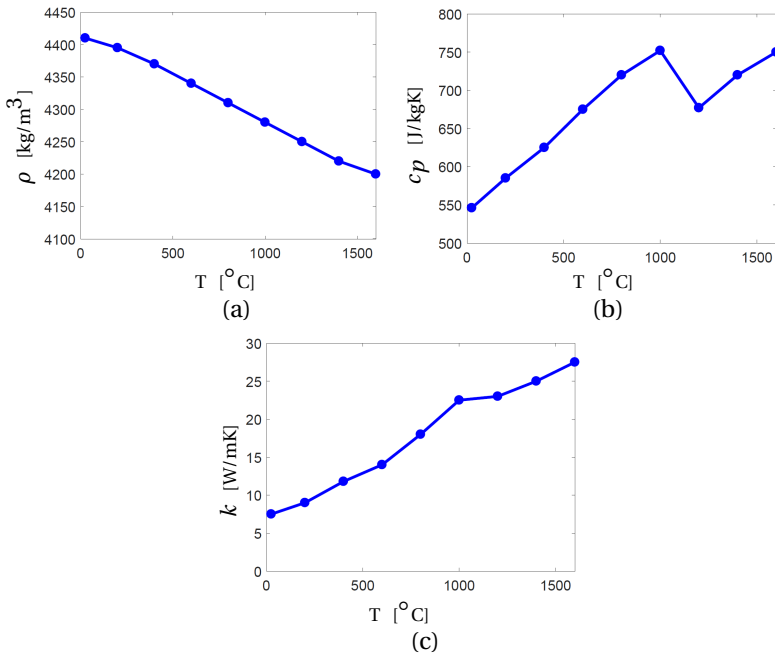


Figure 3.2: Variation of temperature-dependent bulk properties of Ti-6Al-4V. (a) Density (b) Specific heat and (c) Thermal conductivity [9].

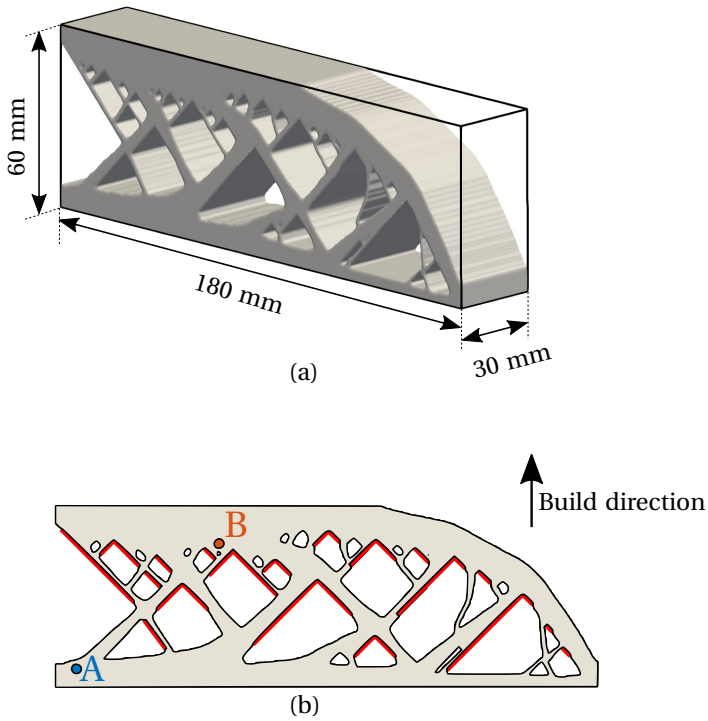


Figure 3.3: (a) The part geometry chosen for analysis with typical LPBF dimensions. (b) 2D cross section with overhangs marked with red lines.

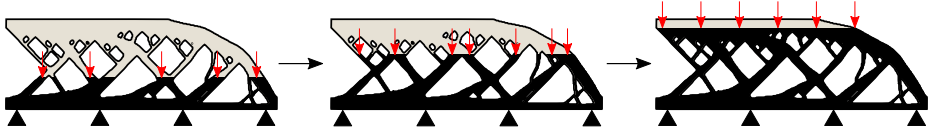


Figure 3.4: Three intermediate build instances with heat flux and sink boundary conditions represented by vertical arrows and triangles, respectively. The horizontal arrows indicate that thermal history of all previous heating/cooling steps are passed to the next simulation step.

3

the same overhang angle of  $45^\circ$ , marked with red lines in Figure 3.3b. In fact, the design is obtained by topology optimization method with overhang angle control as presented by Langelaar [20]. For our purpose, we choose this design to investigate whether the same overhang angle exhibits similar overheating behavior or not throughout the sample. Secondly, the design features do not change in the depth direction, i.e., the design is simply an extrusion of the 2D design shown in Figure 3.3b. This allows for convenient visualizations of temperatures fields as temperatures do not change in the direction of depth when considering layer-by-layer simulations.

Figure 3.4 presents three intermediate build instances of this part where each new layer addition is followed by a heating and cooling step, where the peak temperatures occur at the end of the heating step. As explained earlier, heating time  $t_h$  varies as per Eq. (3.6), while ILT  $t_d$  remains constant. Please note that in this model the thermal history of all previous heating/cooling steps is stored and influences the next step. Figure 3.5 shows typical variation of the temperature with respect to time for nodes located at two different locations marked as A and B in Figure 3.3b. First, note that the temperature first rises and reaches to a maximum when a layer is activated and then it rapidly drops during the inter-layer time. Next, the temperature rises again when the next layer is added. This phenomenon repeats until the final layer is deposited. Secondly, note that peak temperature attained at Point B is significantly higher than that at Point A. This is due to the geometric features in the vicinity of Point B, which do not allow for efficient heat evacuation, hence resulting in a higher peak temperature. Also, Point A is located closer to the baseplate facilitating quicker heat evacuation. This suggests that peak temperature value can be used as an indicator of overheating risk associated with a geometrical feature.

Figure 3.6 shows the peak temperatures attained for the entire domain during the build process. Please note that peak temperatures for different spatial locations may occur at different time instances during the simulation. It is evident that higher peak temperatures are exhibited near the overhangs, indicating local heat accumulation. Moreover, the funnel-shaped geometries in the region labelled as D in Figure 3.6 exhibit higher maximum temperatures than region labelled as C. This is in line with the experimental observations reported in Adam and Zimmer [1] and Patel et al. [29] where LBPF specimens exhibit local overheating in the vicinity of similar funnel-shaped features which act as a thermal bottleneck. This map of peak temperatures is used for judging design features for their heat accumulation behavior and referred to as the *hotspot map*. More-

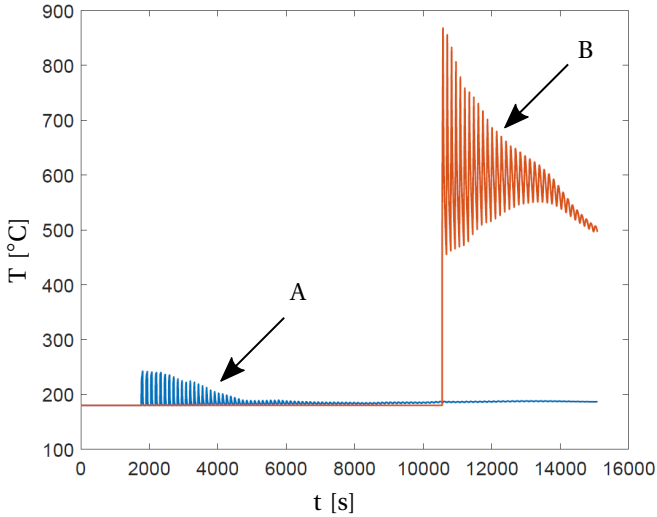


Figure 3.5: Variation of temperatures with respect to time for the node located at Points A and B in Figure 3.3b. Temperatures are calculated using the described transient thermal model of the LPBF process.

over, although all features of the part have the same overhang angle of  $45^\circ$ , the thermal behavior in their vicinity is not similar. This implies that use of a purely geometric design rule can be insufficient for avoiding local overheating.

It is important to note that in the actual AM process, the temperatures rise till the melting point and then stabilize due to phase change with excess heat resulting in a larger melt-pool. Therefore, some LPBF simulation studies put an upper limit on the temperature to address this phenomenon, e.g., Badrossamay and Childs [3]. However, for the reference model we choose not to use this concept and instead use the overshoot of temperature as an indicator of heat accumulation tendency of the neighboring geometry. It is still important to mention that the temperatures found using this model are representative values and are not exact in-process temperatures, due to the simplifications already introduced in the presented reference model. However, the relevance of the presented model for judging design manufacturability is demonstrated by the presented example where it is shown that peak temperatures detect overheating tendencies associated with geometric features.

Finally, the computational cost associated with the presented reference model remains significantly high due to the ever-growing analysis domain and the time integration to account for the transient nature of the problem. The model presented here is discretized using 2.16 million elements leading to 2.22 million nodal degrees of freedom (DOF) and the corresponding simulation time is 21 h 28 min 32 s. All computations reported in this paper are done on a HPC cluster node with 20 cores. The computational burden is still prohibitive for high-volume parts, interactive design iterations or integra-

tion with design optimization techniques. Therefore, to further reduce computational cost, additional physics-based simplifications are proposed in the next section.

### 3.3. THERMAL MODELING SIMPLIFICATIONS AND COMPARISON METRICS

In total, six physics-based simplifications are presented in this section which are applied in addition to the simplifications already existing in the reference model detailed in Section 3.2. Section 3.3.1 discusses the influence of neglecting convective and radiative heat losses. Also, the effect of neglecting temperature-dependent properties is investigated. Although these simplifications have been applied in the literature, their impact in the context of detecting overheating was never studied. In Section 3.3.2, an analytical solution for one-dimensional heat equation is presented which serves as a basis for introducing three novel simplifications. With each simplification, a slightly different hotspot temperature field  $T_{\text{sim}}$  is obtained. Hence, to compare these with the reference hotspot temperature field  $T_{\text{ref}}$ , three comparison metrics are defined in Section 3.3.3.

#### 3.3.1. INFLUENCE OF NEGLECTING CONVECTIVE AND RADIATIVE HEAT LOSSES

As discussed in Section 3.2.1 and described by Eqs. (3.4) and (3.5), heat is lost through convection and radiation from the topmost layer. However, the relative importance of heat losses through convection and radiation as compared to the conduction within the part is still debated in the literature. Some studies present arguments in favor of neglecting these losses [30, 32, 31], while others advocate for their inclusion in the thermal modeling of the AM processes [9, 23]. A basic estimate can be made to quantify the thermal losses due to each mode of heat transfer. The convective loss near the melt zone can be estimated as

$$q_{\text{conv}} = h_{\text{conv}}(T_m - T_a) \approx 2 \times 10^4 \text{ W/m}^2, \quad (3.8)$$

where  $T_m$  is the melting point of Ti-6Al-4V taken as 1604 °C and other parameters are given in Table 3.1. Similarly, radiative loss can be estimated as

$$q_{\text{rad}} = \sigma \epsilon (T_m^4 - T_a^4) \approx 1.3 \times 10^5 \text{ W/m}^2. \quad (3.9)$$

Next, in order to compare, the rate of energy transfer within the part due to conduction,  $q_{\text{cond}}$  can be estimated using a simplified version of Fourier's law for one-dimensional heat flow:

$$q_{\text{cond}} \approx -k \frac{\Delta T}{\Delta x}, \quad (3.10)$$

where  $\Delta T$  is the temperature difference measured over a distance  $\Delta x$ . The melt zone is considered for making this estimation as the highest thermal gradients occur there. Consequently, conductivity at the melting point is considered in Eq. (3.10). Due to extremely high thermal gradients and optical inaccessibility, it is extremely challenging to accurately record actual temperatures near the melt zone. Nevertheless, available data from the literature can be used to make an estimate. For example, empirical observations from Neiva et al. [27] reported a temperature difference  $\Delta T = 1200$  °C between the



topmost point of the melt zone and a point located 2.5 mm below it, i.e.,  $\Delta x = 2.5$  mm. Putting these values in Eq. (3.10) gives  $|q_{\text{cond}}| = 1.4 \times 10^7$  W/m<sup>2</sup>. Please note that these are only rough estimates as heat fluxes continuously change with time-varying temperature fields. Moreover, this estimation of  $q_{\text{cond}}$  is an underestimation as even higher temperature gradients are observed in the vicinity of melt zone by melt-pool simulation studies [5]. Nevertheless, it can be observed from these estimates that indeed heat losses through convection and radiation are orders of magnitude lower near the melt zone than those by conduction, as argued by Paul, Anand, and Gerner [30]. Also, radiation accounts for more heat loss than convection. The effect of neglecting one or both of these loss terms will be studied. In the remainder of this paper, simplification by exclusion of radiation is referred to as **S1** and that for excluding convection is termed as **S2**.

Another aspect that makes the PDE given by Eq. (3.1) nonlinear, and consequently computationally expensive, is the temperature dependence of the thermal properties. Hence, another simplification (**S3**) is considered where along with exclusion of convection and radiation, constant thermal properties are considered. Yang et al. [40] and Yang, van Keulen, and Ayas [41] performed a calibration study and showed that use of constant melting point properties are suitable when probing local temperatures near the heat deposition zone. Hence, in simplification **S3**, constant values of  $\rho = 4200$  kg/m<sup>3</sup>,  $c_p = 750$  J/kg K and  $k = 27.5$  W/m K are used. Results for detecting hotspots and computational gains achieved using these simplifications are reported in Section 3.4.

### 3.3.2. NOVEL SIMPLIFICATIONS MOTIVATED BY ONE-DIMENSIONAL HEAT TRANSFER ANALYSIS

To gain fundamental insights in the nature of transient heat transfer phenomena relevant to the LPBF process, a simplified case of one-dimensional heat transfer is considered and the analytical solution is presented for the boundary conditions analogous to the reference model. The detailed derivation is presented in Appendix B while the final solution and its implications are discussed here. A one-dimensional domain with length  $L$  is shown in Figure 3.7a. The heat equation given by Eq. (3.1) can be simplified for one-dimensional heat transfer as

$$\frac{1}{\alpha} \frac{\partial T}{\partial t} = \frac{\partial^2 T}{\partial x^2}, \quad (3.11)$$

where  $x$  is position and  $\alpha$  is the thermal diffusivity given by  $\alpha = k/\rho c_p$ . Please note that the temperature dependence of thermal properties has been neglected for simplicity and constant values as given in Section 3.3.1 are used. First, a heating step is considered in which the topmost point  $x = L$  is subjected to a heat flux  $Q$  analogous to the volumetric heat source used in the reference model. Next, a heat sink condition is assumed at the bottom, i.e.,  $x = 0$ . To derive a more general solution, the sink temperature is specified as  $T_s$  unlike the reference model where it was assumed same as the initial temperature  $T_0$ . These boundary conditions are given as

$$-k \frac{\partial T}{\partial x} \Big|_{x=L} = Q, \quad \text{and} \quad (3.12)$$

$$T(0, t) = T_s \quad \text{for } t \geq 0. \quad (3.13)$$

The initial condition is

$$T(x, 0) = T_0 \quad \text{for } x > 0. \quad (3.14)$$

The rod is heated for a time  $t_h$  followed by a cooling step in which  $Q = 0$ . Using the method of separation of variables, the analytical solution is derived in Appendix B reads

$$T_h(x, t) = T_s + T_h(L, \infty) \frac{x}{L} + 2 \sum_{n=1}^{\infty} \left( \frac{T_0 - T_s}{\lambda_n} - \frac{T_h(L, \infty)(-1)^{(n+1)}}{\lambda_n^2} \right) \sin\left(\lambda_n \frac{x}{L}\right) e^{-\frac{\lambda_n^2 \alpha t}{L^2}}, \quad (3.15)$$

where  $T_h$  represents the temperature distribution during heating step and  $T_h(L, \infty) = QL/k$  represents the steady-state temperature value at  $x = L$  while  $\lambda_n = (2n-1)\pi/2$ . Next, the rod is allowed to cool, i.e., the boundary condition given by Eq. (3.12) becomes

$$-k \frac{\partial T}{\partial x} \Big|_{x=L} = 0, \quad (3.16)$$

while the other boundary condition remains the same as given by Eq. (3.13). For this case, the temperature distribution at the end of the heating step becomes the initial condition, i.e.,

$$T(x, 0) = T_h(x, t_h) \quad \text{for } x > 0. \quad (3.17)$$

Again, the PDE given by Eq. (3.11) is solved and the solution for the cooling regime is given as

$$T_c(x, t) = T_s + 2 \sum_{n=1}^{\infty} \left( \frac{T_h(L, \infty)(-1)^{(n+1)}}{\lambda_n^2} (1 - e^{-\frac{\lambda_n^2 \alpha t_h}{L^2}}) + \frac{T_0 - T_s}{\lambda_n} e^{-\frac{\lambda_n^2 \alpha t_h}{L^2}} \right) \sin\left(\lambda_n \frac{x}{L}\right) e^{-\frac{\lambda_n^2 \alpha t}{L^2}}, \quad (3.18)$$

where  $T_c$  represents the temperature distribution during the cooling step. A visual depiction of the derived equations is given in Figure 3.7 b where temperature variation for the topmost point ( $x = L$ ) with respect to time is shown. Below, the derived solutions will be used to motivate three novel simplifications, aimed at further reduction of the computational burden associated with the reference model.

#### OBSERVATION 1: TEMPORAL DECOUPLING

First, we focus our attention on the magnitude of the temperature drop that occurs in the cooling phase between layer depositions, using the one-dimensional model. When this drop is sufficiently large, a decoupling in time of deposition steps can be considered in the process model. Recall from Section 3.2 that the peak temperatures at the end of the heating step are used to construct the hotspot map. Hence, the temperature difference between  $x = L$  and  $x = 0$  is considered. This difference during the cooling regime is normalized with the maximum temperature difference attained at the end of the heating step. The normalized temperature difference  $\hat{T}_c(L, t)$  for the topmost point then reads

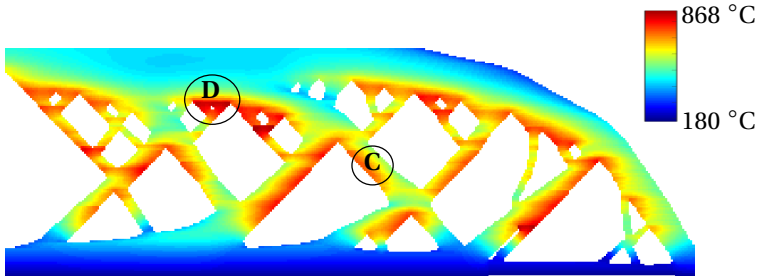


Figure 3.6: Contour plot for maximum temperature attained at each point of the part geometry during the entire build simulation using the layer-by-layer reference model. The region labelled as D shows higher maximum temperatures than that near the region C, while both regions are in the vicinity of a 45° overhang. The temperature scale spans from initial temperature  $T_0 = 180\text{ °C}$  to the maximum value predicted by the simulation.

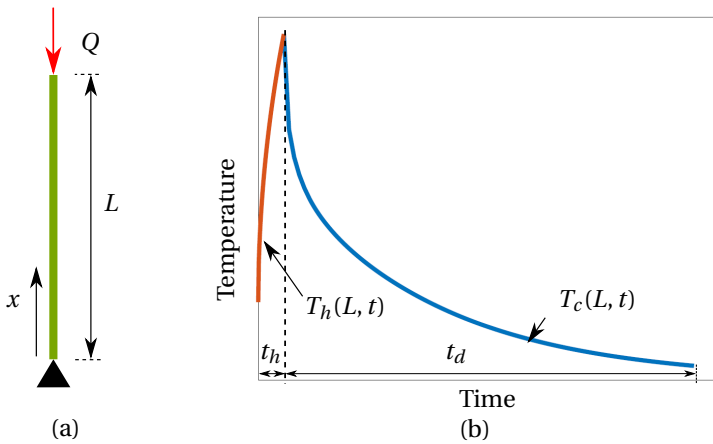


Figure 3.7: (a) one-dimensional domain with length  $L$  subjected to boundary conditions reminiscent to the reference model, i.e., heat flux  $Q$  acts at  $x=L$  while bottom temperature is fixed at  $T = T_s$ . (b) Thermal history of the topmost point ( $x=L$ ) of the rod during a heating and cooling cycle.

$$\hat{T}_c(L, t) = \frac{T_c(L, t) - T_s}{T_h(L, t_h) - T_s} = \frac{2 \sum_{n=1}^{\infty} \frac{1}{\lambda_n^2} \left( e^{-\frac{\lambda_n^2 \alpha t}{L^2}} - e^{-\frac{\lambda_n^2 \alpha (t+t_h)}{L^2}} \right)}{1 - 2 \sum_{n=1}^{\infty} \frac{1}{\lambda_n^2} e^{-\frac{\lambda_n^2 \alpha t}{L^2}}}. \quad (3.19)$$

Please note that the sink temperature is assumed to be the same as the initial temperature in accordance to the boundary conditions used for defining the reference model, i.e.,  $T_s = T_0$ . It can be deduced from Eq. (3.19) that the cooling behavior depends on the duration of the heating stage  $t_h$  and the characteristic time of the heat equation  $\tau = L^2/\alpha$ .

Figure 3.8a,b show the variation of  $\hat{T}_c$  for a range of  $t_h$  and  $\tau$  values, respectively. These ranges are selected in the context of the LPBF process. For example,  $t_h$  is typically very short in LPBF considering a typical scanning velocity  $v = 1$  m/s with a laser spot diameter of 100  $\mu\text{m}$ . Therefore,  $t_h = 10^{-3}, 10^{-2}, 10^{-1}$  s are selected to demonstrate the effect of heating time. Similarly, parts as high as 300 mm can be built in LPBF machines giving  $\tau_{\text{max}} \approx 10^4$  s, assuming  $\alpha$  for Ti-6Al-4V. Hence, this value is used along with lower values to study the variation. Also, constant  $\tau = 10^4$  s and  $t_h = 0.01$  s are used for plotting graphs for varying  $t_h$  and  $\tau$ , i.e., Figure 3.8a,b, respectively. The infinite series in Eq. (3.19) is converging and  $n = 10^4$  is found to be sufficient. Both graphs show that a slower cooling is observed as  $t_h$  or  $\tau$  increases. The graphs are shown for the first 10 s of cooling which is close to typical ILT values used in LPBF [25, 42, 31]. The crucial observation here is that in both graphs the topmost point cools down to approximately 10–20% of its highest temperature value in this time frame. This suggests that topmost point cools down to an estimated value of 150–300 °C assuming  $T_m$  as the highest temperature.

It is noteworthy that this finding is based on the simple one-dimensional model which assumes a constant conductivity throughout the domain. However, in the real three-dimensional setting, there could be local zones of lower conductivity near the topmost layer which would add to the heat accumulation and decrease the local cooling rate. As described in Section 3.1, examples of such features are acute overhangs and thin connections. Nevertheless, it is found that the findings based on this one-dimensional model are in agreement with the experimental observations reported by Neiva et al. [27] where thermocouples embedded inside an overhanging part recorded temperatures during the build. It is shown that the part temperatures remain in the range of 100–400 °C at different locations below the topmost layer when the pre-heated baseplate temperature is at 100 °C. This suggests that the one-dimensional insights can be extended to real parts. Another interesting observation made on the same data is that the recorded temperatures increase with the height at which thermocouples are placed. The effect of build height is also investigated by Mohr, Altenburg, and Hilgenberg [25] and slower cooling is reported for increasing part height. As a qualitative comparison, this is in accordance with cooling curves shown in Figure 3.8b, since  $\tau \propto L^2$ . It suggests that the effect of build height and thermal properties can be combined as characteristic time  $\tau$  in order to study the cooling behavior. A more detailed quantitative comparison between  $\tau$  and cooling data will better establish this correlation. However, it is deemed out of the scope of this paper.

The observations from the one-dimensional analytical model and experimental data from literature indicates that the ILT in the LPBF process allows for ample cooling between the layers. Moreover, it is also recommended as good manufacturing practice to design process such that appropriate cooling happens between two successive layers [25]. This suggests that the previously deposited layers do not significantly affect the peak temperatures recorded for the next layer. This enables decoupling the thermal history of different layers from each other for peak temperature prediction, which essentially means that each layer addition can be assumed to have an initial temperature equal to the baseplate temperature  $T_0$ . Peak temperatures attained this way would still capture the local overheating associated with the geometrical features of the part. A schematic representation of this idea is given in Figure 3.9a, where previous thermal history is not transferred to the next layer addition. There are two major computational benefits associated with this simplification. First, only simulation of the heating step suffices for capturing the first peak temperatures for each layer. Second, heating steps associated with every layer of the structure can be computed in parallel. The model which makes use of this simplification is referred to as the 'temporally decoupled model' and represented as **S4**. It is important to note that this model cannot capture the gradual heat accumulation that may occur over layer depositions, as information about the thermal history is lost. Nevertheless, it is found that features prone to local overheating can still be quickly and adequately identified when making use of this simplification. Recall that these features also contribute significantly to the gradual heat build-up that happens over the layers.

#### OBSERVATION 2: SPATIAL DECOUPLING

Another useful observation is made by focusing on the relationship between the peak temperature at the end of the heating step  $T^h(L, t_h)$  and domain size  $L$ . This implies substituting  $t = t_h$ ,  $x = L$  and  $T_s = T_0$  in Eq. (3.15) which gives

$$T_h(L, t_h) = T_s + T_h(L, \infty) \left( 1 - 2 \sum_{n=1}^{\infty} \frac{1}{\lambda_n^2} e^{-\frac{\lambda_n^2 \alpha t_h}{L^2}} \right). \quad (3.20)$$

This relationship is pictorially presented in Figure 3.10 for three different heating times. It is evident that there exists a saturation domain length  $L_s$  and increasing the domain size beyond this value has no effect on the peak temperatures. This phenomenon is characterized by the exponent term in Eq. (3.20) which constitutes the Fourier number given as  $Fo = \alpha t_h / L^2$ . Please note that  $Fo$  is reducing along the horizontal axis in Figure 3.10 as  $L$  increases. It can be deduced from the graph that the saturation regime starts at  $Fo = 0.3$  which is marked by the vertical lines. Physically, it implies that for a given domain size  $L$ , thermal diffusivity  $\alpha$  and heating time  $t_h$ , if  $Fo \leq 0.3$  then considering larger spatial domains will not influence the peak temperatures. It follows that the corresponding saturation length is  $L_s = 1.82 \sqrt{\alpha t_h}$ .

In the context of LPBF modeling, this observation implies that during the heating step, if the domain beyond  $L_s$  is discarded from the analysis, peak temperatures will not

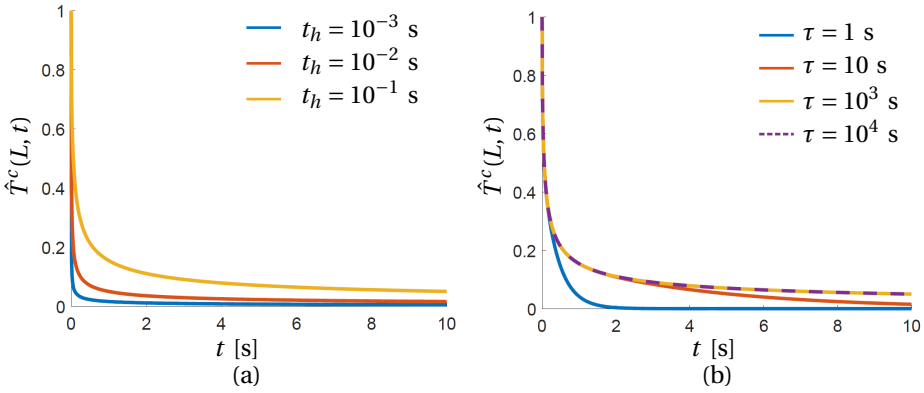


Figure 3.8: Variation of normalized cooling temperatures  $\hat{T}^c$  with respect to time as given by Eq. (3.19) for the considered one-dimensional rod illustrated in Figure 3.7a. (a) Plots for different values of heating time  $t_h$  for  $\tau = 10^4$  s. (b) Plots for different values of characteristic time  $\tau$  for  $t_h = 0.1$  s.

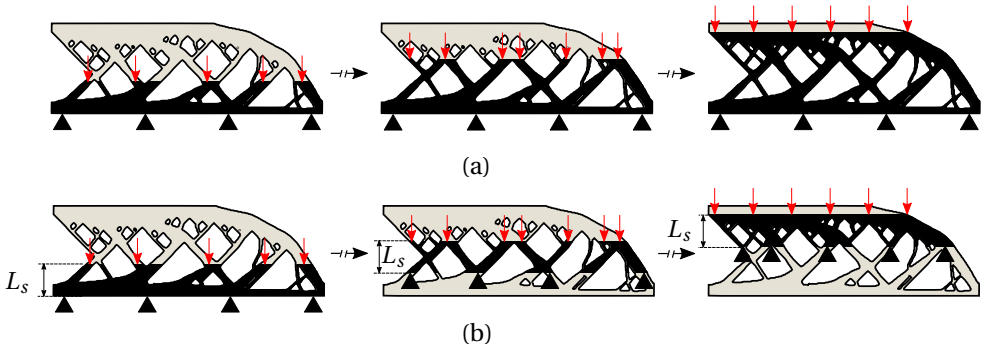


Figure 3.9: (a) Temporal decoupling: each new layer is assumed to be added at initial temperature  $T_0$  and peak temperatures at the end of the heating step are used for preparing the hotspot map. This enables parallel simulation of all the layer additions providing computational gains. In this model, no data is shared between the simulations which is indicated by the horizontal broken arrows. (b) Spatial decoupling: only a relevant sub-geometry is considered for transient thermal analysis. This simplification is applied in addition to the temporal decoupling simplification introduced in (a).

be affected. Although derived using the one-dimensional model, the idea can be easily extended to higher dimensions where low conductivity regions influence the peak temperatures, only if they are present in the vicinity of topmost layer. Recall that temperature dependence is neglected, and the value of thermal properties estimated at the melting point are used for analytical derivation. However, since the highest value of  $\alpha$  is achieved at the melting point, this choice gives an upper limit for the saturation length. Figure 3.9b shows an implementation of this idea, where the Dirichlet boundary condition given by Eq. (3.3) is now applied at a distance  $L_s$  below the heat source instead of at the baseplate. This simplification will be applied together with the previously introduced simplification of decoupling the layers in time. Hence, it is referred to as ‘spatially and temporally decoupled model’ and represented as **S5**. The reduced domain size enables further reduction of the computational cost.

### OBSERVATION 3: STEADY-STATE RESPONSE FOR DETECTING OVERHEATING

It is well-known from the theory of heat conduction that lower conductivity regions inside a domain would influence the steady-state response of a thermal analysis [6]. Consequently, a steady-state response can also be used for detecting regions of lower conductivity within a given domain. The computation of steady-state responses is much faster than a transient analysis which makes it an attractive option for quickly detecting regions prone to overheating. In the context of the one-dimensional rod, substituting  $t = \infty$  in Eq. (3.15), the steady-state temperature distribution along the length of the rod is found as

$$T_h(x, \infty) = T_s + \frac{Qx}{k}. \quad (3.21)$$

This linear thermal profile is depicted in Figure 3.11a where  $x$  varies from 0 to  $L$  along the vertical axis while temperatures are plotted along the horizontal axis. Another case shown in Figure 3.11b considers that a subsection of the one-dimensional rod has lower thermal conductivity than the rest of the domain. This is shown by the orange patch at Location A. The steady-state temperature distribution for this case is computed and plotted, where a higher thermal gradient is observed in the patch of lower conductivity. Please note that also a higher steady-state temperature at  $x = L$  is found compared to the case without the patch, indicated by the dotted line. This signifies that the steady-state temperatures can also be used for identifying regions with lower conductivity which are prone to overheating. In three-dimensional setting, examples of such features are acute overhangs and thin connections which would create a local zone of lower conductivity.

However, the steady-state response should be cautiously used as it does not take into account the proximity of low conductivity regions to the topmost point where the heat flux is applied. This is illustrated in Figure 3.11c where the same low conductivity patch is now situated at Location B and still causes the same increase in the steady-state temperature at  $x = L$ . This implies that a low conductivity region situated far away from the heat deposition zone has the same effect on the top temperature when situated close to the topmost point, when analyzed using steady-state response. In context of the three-dimensional parts, this is unrealistic as heat transfer phenomenon is transient and only

nearby regions of low conductivity (e.g., acute overhangs, thin connections) would influence the thermal behavior near the melt zone. Therefore, in order to rectify this inherent limitation of steady-state analysis, only the domain close to the topmost layer must be considered. Hence, this simplification is applied together with previously explained simplifications of temporal and spatial decoupling. In other words, instead of performing a transient analysis in the spatially and temporally decoupled model shown in Figure 3.9b, a computationally fast steady-state analysis is performed and the simplified model which involves this approximation is referred to as ‘steady-state model’ represented as **S6**.

### 3.3.3. COMPARISON METRICS

To assess the ability of each proposed model to detect hotspots in a part, three different comparison metrics are defined in order to capture different aspects associated with overheating detection. Recall that reference and simplified temperature fields are referred to as  $\mathbf{T}_{\text{ref}}$  and  $\mathbf{T}_{\text{sim}}$ , respectively. The first metric is defined as the percentage error between the maximum temperatures recorded for both fields,

$$\delta = \frac{\max(\mathbf{T}_{\text{sim}}) - \max(\mathbf{T}_{\text{ref}})}{\max(\mathbf{T}_{\text{ref}})} \times 100 \%. \quad (3.22)$$

This quantity compares the intensity of worst overheating as predicted by the reference and the simplified models. It indicates how much the corresponding simplification under/over-predicts as compared to the reference case. A positive  $\delta$  signifies over-prediction and vice versa. Please note that this quantity compares the absolute maxima between two temperature fields without requiring that these maxima occur at the same spatial point. Therefore, to assess the spatial similarity between two temperature fields, the Jaccard index is used. This is a measure commonly used in the field of image recognition for quantifying similarity between two images and is defined as the ratio of intersection and union between the two images [16]. For our case, first  $\mathbf{T}$  is normalized using  $\max(\mathbf{T})$ , i.e.,  $\hat{\mathbf{T}} = \mathbf{T}/\max(\mathbf{T})$ , where  $\hat{\mathbf{T}}$  indicates the normalized temperature field. Next, the Jaccard index is defined as

$$J = \frac{\sum_{i=1}^n \min(\hat{T}_{\text{ref}}^{(i)}, \hat{T}_{\text{sim}}^{(i)})}{\sum_{i=1}^n \max(\hat{T}_{\text{ref}}^{(i)}, \hat{T}_{\text{sim}}^{(i)})} \times 100 \%, \quad (3.23)$$

where  $\hat{T}_{\text{ref}}^{(i)}$ ,  $\hat{T}_{\text{sim}}^{(i)}$  represent normalized temperature values for node  $i$  for the reference and the simplified fields, respectively and  $n$  is the total number of nodes in the finite element analysis. A high Jaccard index implies that the overall temperature distributions over the part are highly similar.

The third metric is defined for a qualitative comparison of two hotspot fields. A critical zone identification (CZI) map is defined which highlights the worst overheated zones while suppressing the cooler, less critical, regions in a given geometry. This allows for judging simplifications based on their capability of detecting the correct worst overheating locations while the actual temperature predictions might be significantly off. It is



defined as the contour map of the normalized temperature field with four contour levels, here chosen at 50%, 70%, 80% and 90% of the maximum temperature in the field. Using this, different design features can be identified from least to most critical in terms of overheating.

Finally, in order to quantify the degree of computational gain achieved by a simplification, a gain factor is defined as

$$\eta = \frac{t_{\text{ref}}^c}{t_{\text{sim}}^c}, \quad (3.24)$$

where  $t_{\text{ref}}^c$  and  $t_{\text{sim}}^c$  are the wall-clock times for completing the reference and simplified analysis, respectively.

### 3.4. NUMERICAL RESULTS AND DISCUSSION

To illustrate the validity of the proposed simplifications and discuss the associated implications, hotspot maps for the part shown in Figure 3.3 are generated using simplified models. For ease of visual comparison, all hotspot fields are presented in Figure 3.12 along with corresponding CZI maps. Simulation times and calculated comparison metrics are listed in Table 3.2 while the default simulation parameters are used from Table 3.1. All computations are performed using 20 cores on a HPC cluster. Discussion about each simplification is presented in the same order in which simplifications were introduced in Section 3.3.

#### 3.4.1. HOTSPOT MAP WITHOUT CONSIDERING CONVECTIVE/RADIATIVE HEAT LOSSES

To compare the relative importance of convection and radiation heat losses, two hotspot maps are prepared. One by excluding radiation, shown in Figure 3.12c and other by excluding convection, shown in Figure 3.12e. All other simulation parameters remain the same as in the case of the reference model, depicted in Figure 3.12a. The first observation is that neglecting convection or radiation leads to a conservative estimation of overheating zones. This is due to the fact that both convection and radiation contribute to the thermal losses and hence lead to higher simulation temperatures, when excluded. Also, as estimated, exclusion of radiation has a greater impact than exclusion of convection. It is manifested by the fact that the maximum temperature attained by excluding radiation is 22.4% higher than that obtained with the reference model, i.e.,  $\delta(\mathbf{S1}) = 22.4\%$ . On the other hand,  $\delta(\mathbf{S2}) = 4.2\%$  when convection is excluded from the analysis. Moreover, when looking at the overall temperature distribution over the entire domain, the hotspot map obtained considering radiation while neglecting convection is very similar to that obtained using reference model. This is supported by the Jaccard index  $J(\mathbf{S2}) = 96.4\%$ . Please note that even with exclusion of convection or radiation, the hotspot map still correctly predicts the funnel-shaped geometries as the worst overheating features. This is also clear from the CZI maps shown in Figure 3.12b,d,f where the same features are identified as critical. Lastly, excluding radiation and convection provides marginal computa-

tional gains of  $\eta(\mathbf{S1}) = 1.06$  and  $\eta(\mathbf{S1}) = 1.03$ , respectively. The radiation boundary condition is nonlinear and hence its exclusion provides a slightly higher computational gain.

### 3.4.2. HOTSPOT MAP WITHOUT CONSIDERING TEMPERATURE-DEPENDENT PROPERTIES

The influence of neglecting temperature dependence of thermal properties is studied next. The hotspot map presented in Figure 3.12g considers this simplification in addition to the simplifications of excluding convection and radiation. The thermal properties as listed in Section 3.3.1 are used for preparing this map. An interesting observation here is that a significant heat accumulation is observed between the layers. This is indicated by the temperature gradient that is seen in the build direction where the topmost layers exhibit significantly higher peak temperatures than the reference model. Due to this, the overall distribution of the peak temperatures over the domain is considerably different from those found using the reference model. This difference is quantified by  $J(\mathbf{S3}) = 75.4\%$ . Moreover, the maximum temperature is overestimated by  $\delta(\mathbf{S3}) = 19\%$ . Nevertheless, the funnel-shaped geometries are still detected as the worst overheating zones, as shown in the CZI map presented in Figure 3.12h. The computational gain factor is found to be  $\eta(\mathbf{S3}) = 2.1$ .

The observations made using these simplifications can be used for making appropriate modeling choices when investigating different aspects of the LPBF process. It is shown here that the exclusion of convection, radiation and temperature dependence halves the simulation time while correctly detecting design features responsible for severe local overheating. However, if the aim of the simulation is to study the effect of gradual heat accumulation during the build, for example as conducted by Jamshidinia and Kovacevic [17], then using these simplifications might lead to overly conservative fields and, thus, leading to false positives. This will become more critical in the case of tall parts with high heat capacity and/or processes with short ILT. Therefore, suitable modeling choices should be made.

### 3.4.3. HOTSPOT MAP WITH TEMPORAL DECOUPLING

Inspired by the observations from the analytical model, the simplification of decoupling layer addition is studied. The hotspot map in Figure 3.12i shows the peak temperatures obtained at the end of the heating step. The computations associated with each intermediate layer addition are carried out in parallel and the hotspot map is prepared as a post-simulation step. As discussed in Section 3.3, this simplification assumes constant initial temperature  $T_0$  for each new layer addition. In other words, it assumes that the part cools down to  $T_0$  between successive layer additions. Consequently, this simplification cannot capture the effect of gradual heat accumulation which builds up over the layers. In fact, this effect is opposite to the preceding case ( $\mathbf{S3}$ ) where gradual heat build-up was overestimated. This is also evident by the fact that peak temperatures are underestimated here, as quantified by  $\delta(\mathbf{S4}) = -5.8\%$ . Nevertheless, the hotspot map prepared using this simplification yields result very similar to the reference case. This is evident by comparing the CZI maps shown in Figure 3.12b,j which highlight same set of design features. This is also quantified by high similarity between the two temperature fields

with  $J(\mathbf{S4}) = 89.9\%$ . Lastly, a computational gain factor  $\eta(\mathbf{S4}) = 85.2$  is achieved where thermal analysis takes only 15 m 7 s while the difference between peak temperature values  $\delta(\mathbf{S4})$  remains less than 6%. Recall that reduction in wall-clock time is attributed to the parallel simulation of each new layer addition and omission of the cooling step simulation between the layers. As mentioned, this model cannot capture the gradual heat accumulated during the build which is inversely proportional to the ILT [25], and similar precautions apply as mentioned for  $\mathbf{S3}$ .

#### 3.4.4. HOTSPOT MAP WITH SPATIAL DECOUPLING

As per the observation discussed in Section 3.3.2, the simplification of considering only the thermally relevant domain during the heat addition step is applied and the resulting hotspot map is presented in Figure 3.12k. Recall that this simplification is applied in addition to the simplification of decoupling in time, as shown in Figure 3.9b. The domain size for each new layer addition is calculated using the concept of saturation length presented in Section 3.3.2. The resulting hotspot map is found to be very similar to the one found using the concept of temporal decoupling ( $\mathbf{S4}$ ). This signifies that very small additional errors are introduced when considering local domains instead of the full geometry. Reduction of the size of simulation domain provides a further improvement in computational gain factor, which reaches 144.2.

#### 3.4.5. HOTSPOT MAP WITH STEADY-STATE ANALYSIS

Next, use of computationally fast steady-state analysis instead of the transient response is studied. The hotspot map shown in Figure 3.12m shows the obtained hotspot map with steady-state peak temperatures. As expected, the temperature values are significantly higher than those found using the transient analysis. Moreover, the overall temperature distribution is also considerably different. These are quantified by  $\delta(\mathbf{S6}) = 65.3\%$  and  $J(\mathbf{S6}) = 74.8\%$ . Nevertheless, the hotspot map found using steady-state analysis also identifies the correct critical zones of overheating, as observed in the CZI map presented in Figure 3.12n. The analysis is completed in only 2 min 9 s with a computational gain factor of 600.

#### 3.4.6. COMPARATIVE ANALYSIS

A pictorial representation of maximum percentage error  $\delta$  and Jaccard index  $J$  obtained using different simplifications is given in Figure 3.13a and computational gain factors are plotted in Figure 3.13b. Please note that  $\delta$  is a measure of difference between two fields while  $J$  is a measure of similarity. Therefore, the simplifications which yield low  $\delta$  and high  $J$  signify higher conformance with the reference hotspot map. Upon comparison, it becomes clear from Figure 3.13a that the analysis which includes radiation ( $\mathbf{S2}$ ) is more accurate than the one which excludes it ( $\mathbf{S1}$ ). Also, the analysis with decoupled layers ( $\mathbf{S4}$ ) and local domain ( $\mathbf{S5}$ ) are almost the same in terms of accuracy. Figure 3.13b highlights the considerable computational gains provided by the novel simplifications proposed in this paper. Please note that these gains are achieved in part due to the parallel processing, which becomes possible due to the proposed simplifications. The total processing CPU times are also reported in Table 3.2 which presents the total computation time used by all the processors. This also implies that the wall-clock time will directly

Table 3.2: Comparison of maximum percentage error  $\delta$ , Jaccard index  $J$ , simulation times and computational gains for all simplified models. All computations are performed using 20 cores on a HPC cluster.

Model Description	Wall-Clock Time	CPU Time	$\delta$	$J$	$\eta$
<b>R:</b> Reference case	21 h 28 min	20 h 52 min	0	100	1
<b>S1:</b> R-radiation	20 h 11 min	19 h 35 min	22.4	90.6	1.06
<b>S2:</b> R-convection	20 h 39 min	20 h 3 min	4.2	96.4	1.03
<b>S3:</b> R-(rad, conv, temp depend)	15 h 3 min	14 h 48 min	18.8	75.4	1.7
<b>S4:</b> S3+Temporally decoupled	15 min	13 h 20 min	-5.8	89.9	85.2
<b>S5:</b> S4+Spatially decoupled	8 min	7 h 18 min	-7.2	89.9	144.2
<b>S6:</b> S5+Steady-state model	2 min	1 h 25 min	65.3	74.8	599.3

depend on the number of processors used. Please note that even without using parallel processing, the novel simplifications provide significant gains where the steady-state model is still 15 times faster than the reference model when CPU times are compared. To conclude, a summary of disadvantages or risk associated with each simplification is presented in Table 3.3.

### 3.5. CONCLUSIONS AND FUTURE WORK

In this paper, first an established thermal model is used to predict the overheating behavior in an LPBF part. A representative part with a 162 cm<sup>3</sup> deposition volume is considered which is simulated using 2.22 million DOFs. It is revealed that using purely geometric design guidelines might not be sufficient for avoiding overheating. It is shown that even with the simplifications of layer lumping and simultaneous simulation of entire layer deposition, the computational time is still prohibitive for quick manufacturability assessment needed for efficient design modifications, process-parameter tuning and optimizations. Hence, a total of six further simplifications are investigated, ranging from omission of radiation and convection and use of constant material properties, to novel simplifications involving temporal and spatial decoupling and ultimately the use of localized steady-state responses. It is shown that in particular the three novel simplifications provide very high computational gains. The results from the simplifications of temporal and spatial decoupling show that even after omitting the simulation of the cooling step and reducing the computational domain size, these simplifications can still provide crucial information about design features and their thermal behavior during the LPBF process. Using these simplifications, the correct locations prone to overheating can be identified and error in maximum temperature prediction is less than 10% when compared with the reference case. Moreover, the localized steady-state response is shown to provide accurate qualitative information about the location of problematic features while it is 600 times faster than the reference model. Note that this computational gain directly depends on the number of processors used.

The high computational gains achieved using simplified models makes them espe-

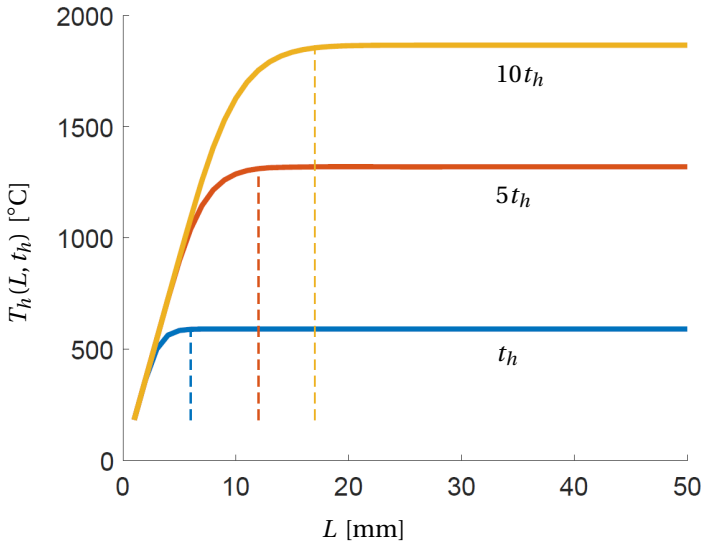


Figure 3.10: Variation of peak temperatures attained at the end of the heating step with respect to domain size  $L$  as described by Eq. (3.20). Three graphs are shown for varying heating time  $t_h$  and vertical lines are shown for respective  $Fo = 0.3$ . First 10,000 terms of the infinite series given by Eq. (3.20) are considered for plotting.

Table 3.3: A summary of disadvantages associated with each simplification.

Model Description	Disadvantage
<b>S1:</b> R-radiation	Conservative prediction, risk of false positives
<b>S2:</b> R-convection	Conservative prediction, risk of false positives
<b>S3:</b> R-(radiation, convection, temp. dependent)	Conservative prediction, risk of false positives
<b>S4:</b> S3+Temporally decoupled	Thermal history lost, cannot capture gradual heat build-up
<b>S5:</b> S4+Spatially decoupled	Thermal history lost, cannot capture gradual heat build-up
<b>S6:</b> S5+Steady-state model	Qualitative indication only

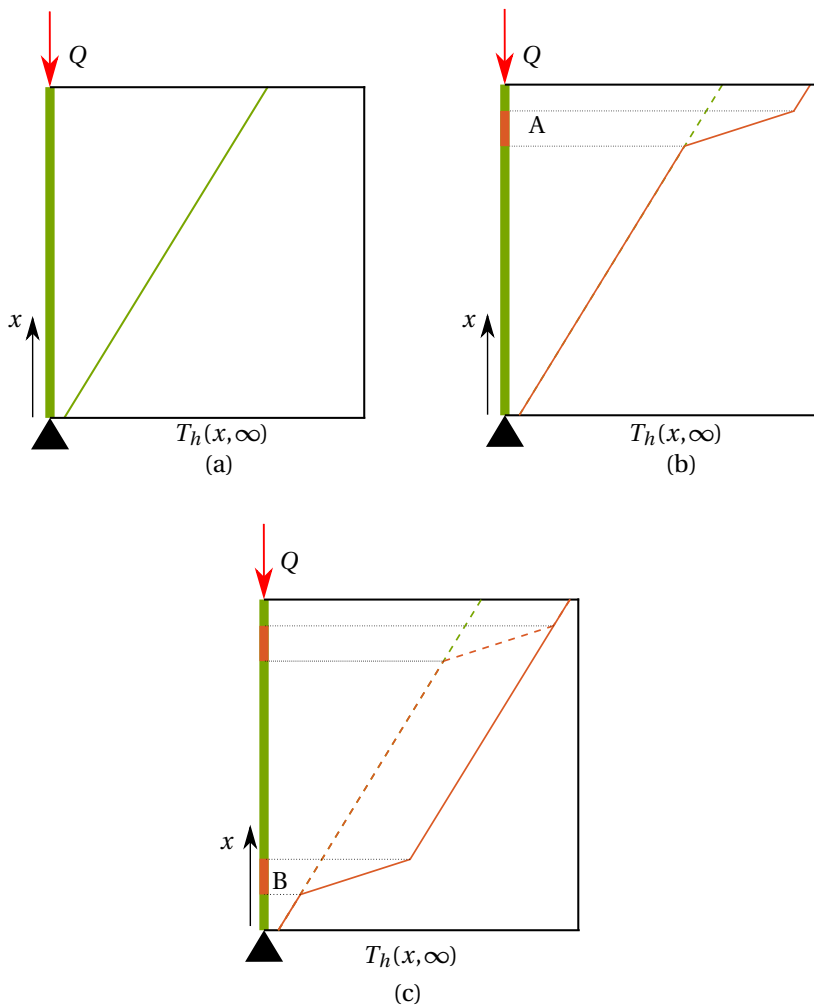


Figure 3.11: (a) Variation of steady-state temperature along the length of the domain as per Eq. (3.21). (b) steady-state temperature with a patch of low conductivity located at A (c) steady-state temperature with a patch of low conductivity located at B.

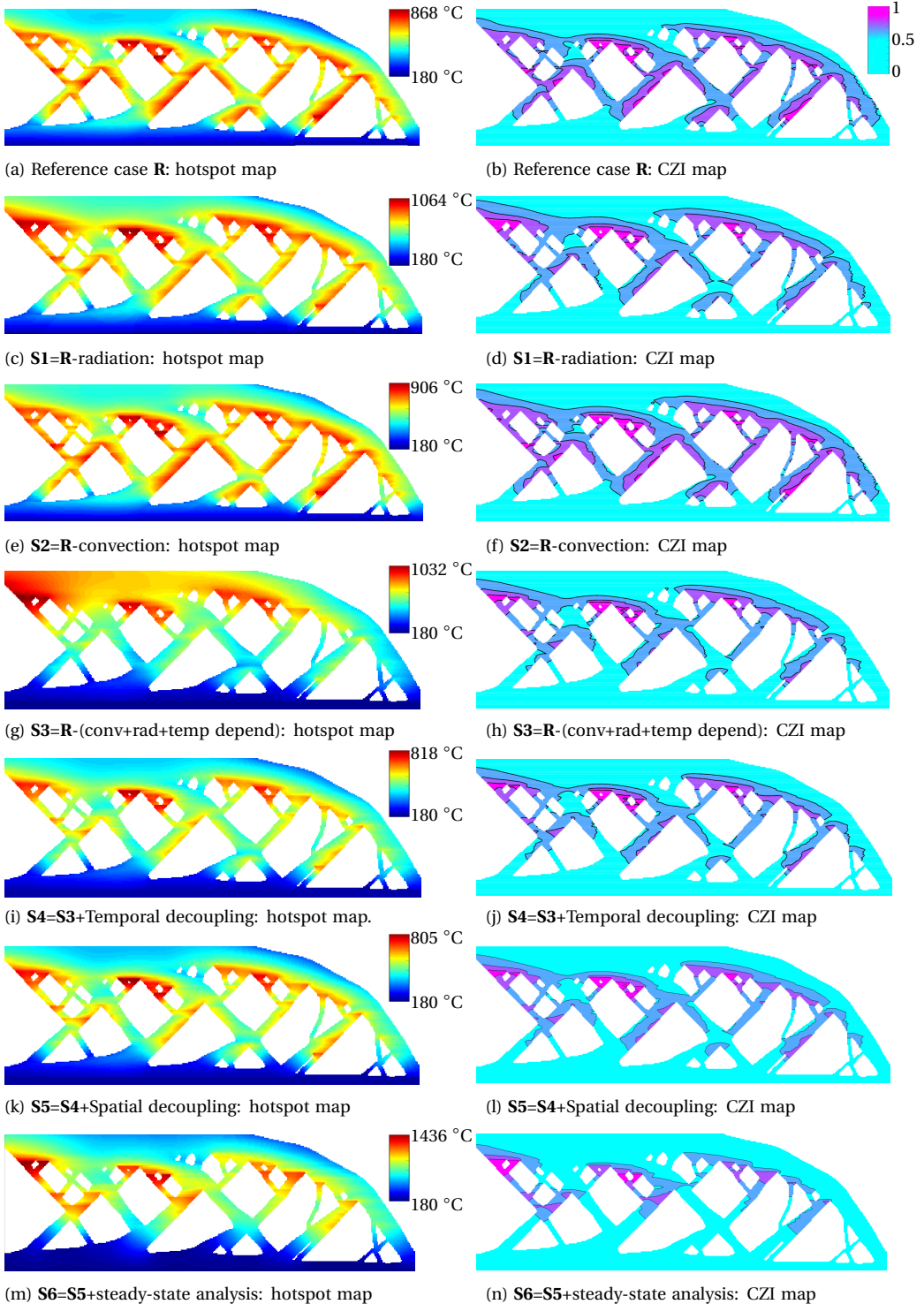


Figure 3.12: Peak temperature plots, i.e., the hotspot maps for different simplifications are presented in (a), (c), (e), (g), (i), (k) and (m) while the CZI maps for different simplifications are presented in (b), (d), (f), (h), (j), (l) and (n). Sub-captions are provided to specify the respective simplifications.

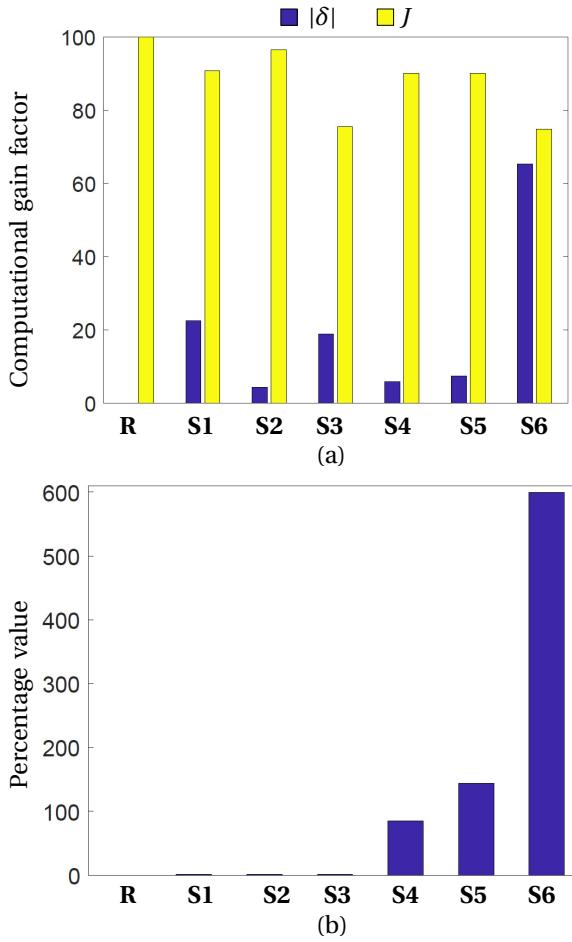


Figure 3.13: (a) Comparison metrics  $\delta$  and  $J$  for judging the accuracy of the simplifications from the context of detecting heat accumulation. Low  $\delta$  and high  $J$  implies higher conformance with the reference case. (b) Computational gain factors  $\eta$  for the simplifications.



cially suitable for design optimization problems where several hundred design evaluations might be needed for finding the optimized design. For example, integration of simplified models with topology optimization techniques holds the promise to deliver highly efficient designs which are also robust from the context of overheating. Typically, design optimization methods make use of gradient information and it has been shown by Van Keulen, Haftka, and Kim [38] that gradient computation for a transient analysis is computationally much more expensive as compared to a steady-state analysis. Consequently, the steady-state model which correctly identifies overheating zones is a perfect candidate for integration with topology optimization, which is seen as the immediate next step.

The layer-by-layer model used in this research cannot capture the influence of laser scanning vectors on local overheating. Therefore, development of higher fidelity models which simulate laser movement and analysis of the generated thermal history for identification of local overheating is seen as a future step. It is expected that the introduced simplifications of temporal and spatial decoupling would remain valid for such higher fidelity models. However, thorough investigation of their validity would still be needed and seen as a possible research step. The thermal history also dictates the development of residual stresses which cause deformations and even part failures. Therefore, the possibility of extending simplified thermal models for capturing mechanical aspects is a promising research direction. Another avenue of future research is to experimentally validate the simplified models. For this purpose, a study is underway where the beam design investigated in this paper is manufactured and a metallographic study is being performed. The specimen will be cut and examined near the funnel shapes which are identified as critical zones by the simplified models.

## REFERENCES

- [1] Guido A.O. Adam and Detmar Zimmer. “Design for Additive Manufacturing—Element transitions and aggregated structures”. In: *CIRP Journal of Manufacturing Science and Technology* 7.1 (2014), pp. 20–28. ISSN: 1755-5817.
- [2] Shukri Afazov, Willem A.D. Denmark, Borja Lazaro Toralles, Adam Holloway, and Anas Yaghi. “Distortion prediction and compensation in selective laser melting”. In: *Additive Manufacturing* 17 (2017), pp. 15–22. ISSN: 2214-8604.
- [3] M. Badrossamay and T.H.C. Childs. “Further studies in selective laser melting of stainless and tool steel powders”. In: *International Journal of Machine Tools and Manufacture* 47.5 (2007), pp. 779–784. ISSN: 0890-6955.
- [4] Joran Booth, Jeffrey Alperovich, Pratik Chawla, Jiayan Ma, Tahira Reid, and Karthik Ramani. “The Design for Additive Manufacturing Worksheet”. In: *Journal of Mechanical Design* 139 (July 2017).
- [5] Nicholas P Calta, Jenny Wang, Andrew M Kiss, Aiden A Martin, Philip J Depond, Gabriel M Guss, Vivek Thampy, Anthony Y Fong, Johanna Nelson Weker, Kevin H Stone, et al. “An instrument for in situ time-resolved X-ray imaging and diffrac-

- tion of laser powder bed fusion additive manufacturing processes”. In: *Review of Scientific Instruments* 89.5 (2018), p. 055101.
- [6] H S Carslaw and J C Jaeger. *Conduction of heat in solids*. English. Oxford: Clarendon Press, 1959.
- [7] Amal Prashanth Charles, Ahmed Elkaseer, Lore Thijs, V. Hagenmeyer, and Stefan Scholz. “Effect of Process Parameters on the Generated Surface Roughness of Down-Facing Surfaces in Selective Laser Melting”. In: *Applied Sciences* 9 (Mar. 2019).
- [8] Michele Chiumenti, Xin Lin, Miguel Cervera, Lei Wei, Yuxiang Zheng, and Weidong Huang. “Numerical simulation and experimental calibration of additive manufacturing by blown powder technology. Part I: Thermal analysis”. In: *Rapid Prototyping Journal* 23 (Mar. 2017), pp. 448–463.
- [9] Michele Chiumenti, Eric Neiva, Emilio Salsi, Miguel Cervera, Santiago Badia, Joan Moya, Zhuoer Chen, Caroline Lee, and Christopher Davies. “Numerical modelling and experimental validation in Selective Laser Melting”. In: *Additive Manufacturing* 18 (2017), pp. 171–185. ISSN: 2214-8604.
- [10] Michael Cloots, Livia Zumofen, Adriaan Spierings, Andreas Kirchheim, and Konrad Wegener. “Approaches to minimize overhang angles of SLM parts”. In: *Rapid Prototyping Journal* 23 (Mar. 2017), pp. 362–369.
- [11] Tom Craeghs, Florian Bechmann, Sebastian Berumen, and Jean-Pierre Kruth. “Feedback control of Layerwise Laser Melting using optical sensors”. In: *Physics Procedia* 5 (2010). Laser Assisted Net Shape Engineering 6, Proceedings of the LANE 2010, Part 2, pp. 505–514. ISSN: 1875-3892.
- [12] Guido Dhondt. *CalculiX CrunchiX user’s manual version 2.16*. <http://www.dhondt.de/> (accessed on 10 September 2022).
- [13] Jarred C. Heigel and Eric Whitenton. “Measurement of Thermal Processing Variability in Powder Bed Fusion”. In: *In Proceedings of ASPE and euspen Summer Topical Meeting - Advancing Precision in Additive Manufacturing, Berkeley, CA, USA*. 2018.
- [14] N.E. Hodge, Robert Ferencz, and Jerome Solberg. “Implementation of a thermo-mechanical model for the simulation of selective laser melting”. In: *Computational Mechanics* 54 (July 2014).
- [15] Paul A. Hooper. “Melt pool temperature and cooling rates in laser powder bed fusion”. In: *Additive Manufacturing* 22 (2018), pp. 548–559. ISSN: 2214-8604.
- [16] Paul Jaccard. “The Distribution of the Flora of the Alpine Zone”. In: *New Phytologist* 11.2 (0), pp. 37–50.
- [17] Mahdi Jamshidinia and Radovan Kovacevic. “The influence of heat accumulation on the surface roughness in powder-bed additive manufacturing”. In: *Surface Topography: Metrology and Properties* 3 (Mar. 2015), p. 014003.
- [18] Darya Kastsian and Daniel Reznik. “Reduction of local overheating in selective laser melting”. In: *In Proceedings of Simulation of Additive Manufacturing (SIM-AM), Munich, Germany*. Oct. 2017.

- [19] Wayne E. King, Holly D. Barth, Victor M. Castillo, Gilbert F. Gallegos, John W. Gibbs, Douglas E. Hahn, Chandrika Kamath, and Alexander M. Rubenchik. “Observation of keyhole-mode laser melting in laser powder-bed fusion additive manufacturing”. In: *Journal of Materials Processing Technology* 214.12 (2014), pp. 2915–2925. ISSN: 0924-0136.
- [20] Matthijs Langelaar. “An additive manufacturing filter for topology optimization of print-ready designs”. In: *Structural and Multidisciplinary Optimization* (July 2016).
- [21] Richard Leach and Simone Carmignato. *Precision Metal Additive Manufacturing*. CRC Press, Sept. 2020. ISBN: 113834771X.
- [22] Andreas Malmelöv, Andreas Lundbäck, and Lars-Erik Lindgren. “History Reduction by Lumping for Time-Efficient Simulation of Additive Manufacturing”. In: *Metals* 10 (Dec. 2019), p. 58.
- [23] Mustafa Megahed, Hans-Wilfried Mindt, Narcisse N’Dri, Hongzhi Duan, and Olivier Desmaison. “Metal additive-manufacturing process and residual stress modeling”. In: *Integrating Materials and Manufacturing Innovation* 5 (Feb. 2016).
- [24] Raya Mertens, Stijn Clijsters, Karolien Kempen, and Jean-Pierre Kruth. “Optimization of Scan Strategies in Selective Laser Melting of Aluminum Parts With Down-facing Areas”. In: *Journal of Manufacturing Science and Engineering* 136(6) (Dec. 2014).
- [25] Gunther Mohr, Simon J. Altenburg, and Kai Hilgenberg. “Effects of inter layer time and build height on resulting properties of 316L stainless steel processed by laser powder bed fusion”. In: *Additive Manufacturing* 32 (2020), p. 101080. ISSN: 2214-8604.
- [26] Eric Neiva, Santiago Badia, Alberto F. Martín, and Michele Chiumenti. “A scalable parallel finite element framework for growing geometries. Application to metal additive manufacturing”. In: *International Journal for Numerical Methods in Engineering* 119.11 (2019), pp. 1098–1125.
- [27] Eric Neiva, Michele Chiumenti, Miguel Cervera, Emilio Salsi, Gabriele Piscopo, Santiago Badia, Alberto F. Martín, Zhuoer Chen, Caroline Lee, and Christopher Davies. “Numerical modelling of heat transfer and experimental validation in powder-bed fusion with the virtual domain approximation”. In: *Finite Elements in Analysis and Design* 168 (2020), p. 103343. ISSN: 0168-874X.
- [28] L.A. Parry, I.A. Ashcroft, and R.D. Wildman. “Geometrical effects on residual stress in selective laser melting”. In: *Additive Manufacturing* 25 (2019), pp. 166–175. ISSN: 2214-8604.
- [29] Shubham Patel, James Mekavibul, Jami Park, Anchit Kolla, Ryan French, Zachary Kersey, and Gregory Lewin. “Using Machine Learning to Analyze Image Data from Advanced Manufacturing Processes”. In: *2019 Systems and Information Engineering Design Symposium (SIEDS), Charlottesville, VA, USA* (Apr. 2019), pp. 1–5.

- [30] Ratnadeep Paul, Sam Anand, and Frank Gerner. “Effect of Thermal Deformation on Part Errors in Metal Powder Based Additive Manufacturing Processes”. In: *Journal of Manufacturing Science and Engineering* 136.3 (Mar. 2014), pp. 31009–31012. ISSN: 1087-1357.
- [31] Hao Peng, Morteza Ghasri-Khouzani, Shan Gong, Ross Attardo, Pierre Ostiguy, Bernice Aboud Gatrell, Joseph Budzinski, Charles Tomonto, Joel Neidig, M. Ravi Shankar, Richard Billo, David B. Go, and David Hoelzle. “Fast prediction of thermal distortion in metal powder bed fusion additive manufacturing: Part 1, a thermal circuit network model”. In: *Additive Manufacturing* 22 (2018), pp. 852–868. ISSN: 2214-8604.
- [32] Ibiye Aseibichin Roberts. “Investigation of residual stresses in the laser melting of metal powders in additive layer manufacturing”. In: (). PhD thesis, University of Wolverhampton, 2012.
- [33] John Romano, Leila Ladani, and Magda Sadowski. “Thermal Modeling of Laser Based Additive Manufacturing Processes within Common Materials”. In: *Procedia Manufacturing* 1 (2015). 43rd North American Manufacturing Research Conference, NAMRC 43, 8-12 June 2015, UNC Charlotte, North Carolina, United States, pp. 238–250. ISSN: 2351-9789.
- [34] Marleen Rombouts, L. Froyen, A. Gusarov, El Hassane Bentefour, and Christ Glorieux. “Photopyroelectric measurement of thermal conductivity of metallic powders”. In: *Journal of Applied Physics* 97 (Dec. 2004), p. 24905.
- [35] W. J. Sames, F. A. List, S. Pannala, R. R. Dehoff, and S. S. Babu. “The metallurgy and processing science of metal additive manufacturing”. In: *Int Mater Rev* 61.5 (Mar. 2016), pp. 1–46.
- [36] Felix Spranger, Benjamin Graf, Michael Schuch, Kai Hilgenberg, and Michael Rethmeier. “Build-up strategies for additive manufacturing of three dimensional Ti-6Al-4V-parts produced by laser metal deposition”. In: *Journal of Laser Applications* 30.2 (2018).
- [37] L.E.J. Thomas-Seale, J.C. Kirkman-Brown, M.M. Attallah, D.M. Espino, and D.E.T. Shepherd. “The barriers to the progression of additive manufacture: Perspectives from UK industry”. In: *International Journal of Production Economics* 198 (2018), pp. 104–118. ISSN: 0925-5273.
- [38] F Van Keulen, RT Haftka, and NH Kim. “Review of options for structural design sensitivity analysis. Part 1: Linear systems”. In: *Computer methods in applied mechanics and engineering* 194.30-33 (2005), pp. 3213–3243.
- [39] Dongqing Yang, Gang Wang, and Guangjun Zhang. “Thermal analysis for single-pass multi-layer GMAW based additive manufacturing using infrared thermography”. In: *Journal of Materials Processing Technology* 244 (2017), pp. 215–224. ISSN: 0924-0136.
- [40] Y. Yang, M.F. Knol, F. van Keulen, and C. Ayas. “A semi-analytical thermal modelling approach for selective laser melting”. In: *Additive Manufacturing* 21 (2018), pp. 284–297. ISSN: 2214-8604.

- [41] Y. Yang, F. van Keulen, and C. Ayas. “A computationally efficient thermal model for selective laser melting”. In: *Additive Manufacturing* 31 (2020), p. 100955. ISSN: 2214-8604.
- [42] Wenyong Zhang, Mingming Tong, and Noel M. Harrison. “Resolution, energy and time dependency on layer scaling in finite element modelling of laser beam powder bed fusion additive manufacturing”. In: *Additive Manufacturing* 28 (2019), pp. 610–620. ISSN: 2214-8604.



# 4

## CONTROLLING LOCAL OVERHEATING IN TOPOLOGY OPTIMIZATION FOR ADDITIVE MANUFACTURING

*A novel constraint to prevent local overheating is presented for use in topology optimization (TO). The very basis for the constraint is the Additive Manufacturing (AM) process physics. AM enables fabrication of highly complex topologically optimized designs. However, local overheating is a major concern especially in metal AM processes leading to part failure, poor surface finish, lack of dimensional precision and inferior mechanical properties. It should therefore be taken into account at the design optimization stage. However, including a detailed process simulation in the optimization would make the optimization intractable. Hence, a computationally inexpensive thermal process model, recently presented in the literature, is used to detect zones prone to local overheating in a given part geometry. The process model is integrated into density-based TO in combination with a robust formulation, and applied in various numerical test examples. It is found that existing AM oriented TO methods which rely purely on overhang control do not ensure overheating avoidance. Instead, the proposed physics-based constraint is able to suppress geometric features causing local overheating and delivers optimized results in a computationally efficient manner.*

---

Parts of this chapter have been published in [Controlling local overheating in topology optimization for additive manufacturing](#), *Structural and Multidisciplinary Optimization*, 2022

## 4.1. INTRODUCTION

The unprecedented design freedom offered by additive manufacturing (AM) techniques makes them a promising option for fabricating highly complex and performant components. However, AM processes suffer from specific limitations and, if overlooked during the design stage, these limitations can cause various defects. Both these factors, *i.e.* increased design freedom and the need to address AM limitations during the design stage, make the design process for AM highly challenging. Topology optimization (TO) allows for computational exploration of the design space while considering pre-defined constraints [5]. Hence, it has been universally recognized as the ideal tool for designing AM parts [25]. There has been a significant research effort to integrate AM limitations within TO schemes, with a strong emphasis on controlling overhanging features [27]. However, an important AM limitation, which is not yet explicitly addressed in the context of TO, is that of local overheating or heat accumulation during the manufacturing process. Recent experimental observations and better understanding of AM process physics reveal that overheating is not uniquely associated to overhangs and dedicated analysis of the local thermal history is needed to characterize overheating [1, 35]. The effect is observed in both polymer and metal manufacturing. However, it is especially relevant for the metal precision parts as operating temperatures are higher and overheating adversely impacts the part quality. For this reason, we focus on Laser Powder Bed Fusion (LPBF) which is the most prevalent metal AM technique and discuss local overheating in more detail below.

The LPBF process involves selective melting of powder layers using laser beams as a heat source. This means that heat flows from the newly deposited topmost layer towards the baseplate. It is observed that whenever incident thermal energy is not transmitted quickly enough to the baseplate, local overheating or heat accumulation occurs [37, 29]. In the in-situ monitoring study conducted by Craeghs et al. [11], local overheating is characterized by an enlarged melt-pool observed near regions which obstruct heat flow. Overheating leads to defects such as balling and dross formation, which compromise the surface quality of manufactured parts [12]. Moreover, local overheating can adversely affect the micro-structural evolution, which has a significant impact on resulting physical properties [26]. Kastsian and Reznik [16] highlight that local overheating can lead to undesired deformations, which cause re-coater jamming and, consequently, in build failure. Lastly, Parry, Ashcroft, and Wildman [31] reported that local overheating contributes significantly to residual stresses resulting into part distortions upon removal from the substrate. The issue becomes even more relevant for precision components with tight geometric tolerances [25]. Hence, considerations should be made for avoiding local overheating at the design and process planning stage.

The factors causing local overheating can be characterized into three broad groups. The first group is associated with the AM process parameters, *e.g.*, scanning strategy, scan velocity, laser power etc. As the input energy density depends on the process parameters, they have a significant impact on the local thermal history of the part [42]. The second group is related to the thermal properties of the material used. For example, material with high thermal diffusivity will facilitate faster heat evacuation as compared to a



material with lower diffusivity. Finally, the third group is associated with the part design. Geometric features which do not allow sufficiently fast evacuation of heat, cause local overheating [12].

In this research, the main focus is on the aspects directly controlled by the part design, *i.e.* the relationship between part layout and its thermal behavior during the printing process. In other words, we study the design-related factors that influence local overheating while assuming a constant set of process parameters and material properties.

The most common example of design features which cause local overheating are down-facing or overhanging surfaces. In the LPBF process, a down-facing surface is scanned with loose powder beneath it, instead of solid material. Due to lower (and non-uniform) conductivity of loose powder as compared to the bulk material, the applied laser energy is less effectively conducted towards the baseplate than in non-overhanging regions, causing local overheating near the melt zone [12, 29]. Therefore, design guidelines related to overhang angles have been recommended, *i.e.* the angle as measured between part surface and the baseplate should not be less than a critical value  $\theta^{\text{cr}}$  which typically amounts to  $40^\circ$ – $50^\circ$  [9, 45]. However, a number of studies suggest that thermal behaviour of an overhanging feature is not uniquely determined by the overhang angle. As a consequence, geometric overhang control does not necessarily guarantee overheating control. For example, [1] fabricated a Y-shaped specimen, for which discoloration, which is an indicator of overheating, was observed near the top region of an overhanging design feature. Although, the feature had a constant overhang angle, the lower part of the overhang was free from overheating. A similar observation was presented by [32], showing dross formation even when acute overhangs were avoided. Finally, Ranjan et al. [35] presented LPBF thermal models and showed that the same degree of overhang can result in different thermal behaviour, depending on the heat evacuation capacity of other features in the vicinity. Hence, the geometrical approach of using a unique critical overhang angle throughout the domain could be insufficient for preventing overheating in some regions. On the other hand, using a single critical overhang angle might be over-restrictive. In such cases, nearby features can facilitate the heat conduction towards the baseplate and henceforth, a lower critical overhang angle can be allowed. For example, it is well-known that for overhangs of limited length, more acute overhang angles can be tolerated [29].

In the context of TO, multiple researchers have successfully integrated a geometrical overhang constraint within TO procedures, for example, Gaynor and Guest [14], Langelaar [21, 20], and Van de Ven et al. [44]. These TO formulations tackle the issue as a purely geometric problem and prevent overhanging features with an angle less than a prescribed critical value. However, a TO method which could address the issue of overheating by directly taking into account the thermal evolution during the AM process, would provide important advantages over existing geometric approaches.

Integration of a detailed AM simulation with TO is challenging as the computational cost associated with detailed AM models is extremely high (see, for example, Denlinger,

Irwin, and Michaleris [13] and Keller and Ploshikhin [17]). Therefore, there has been a research interest in developing simplified AM models which capture essential AM-related aspects and make it possible to address them in a TO framework. For example, Wildman and Gaynor [47] coupled a simplified thermo-mechanical AM model with density based TO for reducing deformations. For approximating the thermal history, a constant temperature drop was assumed for each time step and therefore, the relationship between part layout and its thermal behaviour was not captured. Next, Allaire and Jakabcin [3] also integrated a thermo-mechanical AM model with the level set TO method in order to minimize thermal stresses and deformations. However, it was reported that the associated computational cost was very high. More recently, Boissier, Allaire, and Tournier [6] coupled a simplified thermal model with a 2D level-set TO where scanning path optimization is performed. However, it is expected that the computational cost of such a model remains high.

4

Alternatively, there is another category of AM-oriented TO methods where part design is considered fixed and supports are optimized considering structural and/or thermal aspects [2, 52, 19]. Among these methods, [52] is most relevant for our purpose as it integrates a transient thermal AM simulation with density based TO. As a simplification, a slow laser velocity of 1 mm/s and thick layers of 1 mm were assumed. Still, the computational cost remained significantly high (5 minutes per iteration for  $10^4$  finite elements in Matlab). Therefore, to the best of our knowledge, a TO method which focuses on local overheating of AM parts and delivers optimized part designs within a practical time frame is still lacking.

In order to address overheating within the context of TO, first an adequate AM process model is required which can quickly identify design features that lead to overheating. In our previous study Ranjan et al. [35], a series of simplifications in thermal modelling of the LPBF process was investigated along with their implications in the context of detecting overheating. The most simplified model employs a steady-state thermal response in a local domain close to the heat source. It was demonstrated that this model can accurately capture overheating tendencies while providing very high computational gains. Therefore, in this paper, the computationally inexpensive steady-state process model presented by Ranjan et al. [35] is coupled with density-based TO. The robust TO method presented by Wang, Lazarov, and Sigmund [46] is used and compliance minimization is considered. Throughout this paper, identified zones of local overheating are referred to as ‘hotspots’ and hence, the simplified thermal model is referred to as ‘hotspot detection’ method. By including the hotspot information as a constraint, optimized designs can be found with reduced overheating risks.

The remainder of the article is organized as follows. For self-containment, the concept of hotspot detection following Ranjan et al. [35] is summarized in Section 4.2. Formulation of the novel hotspot constraint and a finite element (FE) based numerical implementation is presented in Section 4.3. A quantitative relationship between overhang angles and hotspot temperatures is established in Section 4.4, which is used to calibrate the overheating constraint. Problem definition, integration of overheating constraint

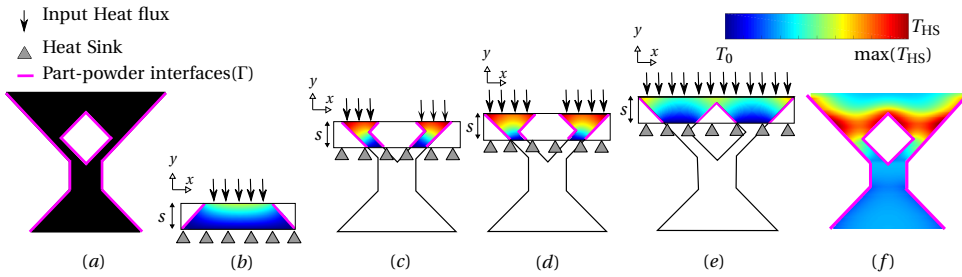


Figure 4.1: Detecting heat accumulation using slab-based analysis. (a) The geometry under consideration, (b)–(e) Subsections of the geometry with the contour levels of temperature attained with a steady-state thermal analysis. For each slab a heat flux is applied at its top, while its bottom act as a heat sink. Part-powder interfaces  $\Gamma$  are insulated and denoted by magenta. The maximum temperature for each material point is recorded and shown in (f), which is referred to as ‘hotspot map’  $T_{HS}$ .

with topology optimization and preliminary results are presented in Section 4.5. Further results obtained by investigating the effect of several key parameters are presented in Section 4.6. A comparative study is presented in Section 4.7 where the novel TO method is compared with an existing geometry based TO approach. The primary aim of this paper is to introduce the novel TO method while thoroughly investigating the behaviour of the optimization problem. For this purpose, we choose to discuss the idea in a 2D setting for clarity and perform experiments for characterizing the influence of different parameters. However, the formulation can be directly extended to the 3D setting which is shown by a 3D numerical example presented in Section 4.8. Finally, conclusions and future directions are given in Section 4.9.

## 4.2. SIMPLIFIED AM MODEL AND MODIFICATIONS FOR TO INTEGRATION

### 4.2.1. HOTSPOT DETECTION

The 2D geometry shown in Figure 4.1a is used to explain the hotspot detection method. It is purposefully designed to include overhanging features along with relatively thin sections, since these features are the most commonly known sources of overheating [26, 45, 12]. Note that all overhanging regions have identical overhang angle ( $\theta = 45^\circ$ ) so that variation in their thermal response due to local conductivity of nearby features can be observed, if any. Figure 4.1b–e represents different stages of the AM process when the part is manufactured with a vertical build direction. It was shown in [35] that a computationally fast *slab-based* steady-state thermal analysis can capture hotspots under two considerations: it leads to qualitative temperature field representing overheating risks, and local domains (slabs) should be considered for analysis. A brief description of these considerations is given below. For an in-depth discussion along with validation using higher fidelity AM process models the reader is referred to [35].

The first consideration associated with the use of steady-state thermal analysis for

hotspot detection is that the resulting temperature field no longer represents a quantitative prediction of the actual temperature transients. Instead, it provides a representation of the overheating risks associated with design features [35]. For integration with TO, an overheating constraint needs to be formulated. Later, in Section 4.2.2, a normalization scheme is introduced which facilitates the formulation of the overheating constraint.

The second consideration for using steady-state analysis is that a relevant local computational domain must be considered, instead of the entire part. Steady-state analysis provides information about the overall conductance of the entire domain that is considered. However, heat flow during the AM process is a transient phenomenon where only features in the vicinity of the top layers are relevant for overheating. In order to address this, we consider only a subset of the geometry near the topmost layer in the intermediate build, as shown in Figure 4.1b–e. We refer to this subset geometry as *slab* with *slab thickness*  $s$ . These slabs are defined such that subsequent slabs largely overlap, see Figure 4.1c–e. The physical significance of slabs and motivation behind slab overlap is provided later in Section 4.2.2.

A steady-state thermal analysis is performed on every slab with a heat flux applied at the topmost surface, while the bottom surface acts as a heat sink. These boundary conditions (BC) are inspired by the AM process, where the thermal energy is applied at the topmost layer while the previously deposited layers and the thick baseplate acts as a heat sink. Note that the temperature BC for the slab's bottom surface is a choice made in this study, while other options, *e.g.* flux-based BC, can also be investigated. Apart from the most significant simplification of using a localized steady-state analysis, several additional simplifications are used. Instead of simulating the actual laser scanning, we assume the entire top layer is simultaneously exposed to the incident heat flux. The interfaces between the solid and the powder, represented by  $\Gamma$  in Figure 4.1, are assumed to be thermally insulated as conduction through powder is neglected. Also, convection and radiation heat losses from the top surface are neglected. Furthermore, we do not consider phase transformation and material properties are assumed to be temperature independent. These additional simplifications are commonly used in part-scale modeling of AM processes in order to reduce the computational burden [50, 51, 33, 49]. A detailed discussion about implications associated with these simplifications can be found in [35].

Under these assumptions, the 2D steady-state heat equation for each slab is given as

$$\frac{\partial^2 T}{\partial x^2} + \frac{\partial^2 T}{\partial y^2} = 0, \quad (4.1)$$

while the heat flux, insulated and sink boundary conditions are given as

$$-k_0 \frac{\partial T}{\partial y} \Big|_{y=s} = q_0, \quad (4.2)$$

$$\frac{\partial T}{\partial x} \nu_x + \frac{\partial T}{\partial y} \nu_y = 0 \quad \text{on } \Gamma, \quad (4.3)$$

$$T(x, 0) = T_0, \quad (4.4)$$

respectively. Here  $T(x, y)$  is the temperature field,  $T_0$  is the sink temperature,  $x$  and  $y$  represent spatial coordinates within the slabs with origin located at left bottom,  $v_x$  and  $v_y$  are the  $x$  and  $y$  components of the outward unit normal vectors on  $\Gamma$ , and  $k_0$  and  $q_0$  are thermal conductivity and input heat flux, respectively. The boundary value problem given by Eqs. (4.1–4.4) is solved numerically using finite element analysis (FEA) and temperature field  $T(x, y)$  is obtained for each slab, as shown in Figure 4.1b–e. Details on the FEA implementation are given in the next section.

Subsequent slabs may overlap to a large extent. Consequently, every material point is associated with multiple slabs. As a final step, the maximum temperature is obtained for each material point from all slabs it is associated with. This temperature field is referred to as ‘hotspot map’ denoted by  $T_{\text{HS}}$ , and is plotted in Figure 4.1f. It can be seen that relatively higher temperatures are found near the thin sections, at the overhanging boundaries. This shows that the simplified model for overheating prediction is in agreement with experimental observations [1, 43, 32]. It is noteworthy that although the considered geometry has a single overhang angle of  $45^\circ$ , the thermal response varies based on the local conductivity of the features in the vicinity of the topmost layer of an intermediate build. This demonstrates that a computationally inexpensive thermal model can be used for detecting overheating.

#### 4.2.2. ADAPTATION FOR TO INTEGRATION: NORMALIZATION

The hotspot detection method is based on the physics of the AM process, unlike the widely used purely geometrical overhang constraints. However, as discussed in Section 4.2.1, the predicted temperatures are only a qualitative representation of the overheating risks associated with design features. Therefore, we propose a normalization step which facilitates formulation of an overheating thermal constraint. For this purpose, the steady-state thermal response from each slab’s geometry is compared with that of a fully solid rectangular slab of same material and height, subjected to the same boundary conditions. An example of such a slab is shown in Figure 4.2a. The solid slab is subjected to a heat flux  $q_0$  at the top while the bottom acts as a heat sink. The rectangular geometry and the boundary conditions allow for an 1D analysis. Using Fourier’s law of heat conduction, the temperature difference between top and bottom of this fully-solid slab at steady-state is  $N_c = (q_0 s) / k_0$ . The normalization is done as  $\hat{T} = T / N_c$ , where  $\hat{T}$  and  $N_c$  are normalized temperatures and normalization constant, respectively. Note that a rectangular slab with no void represents the best case scenario of unobstructed heat flow. This essentially means that, for any given geometry,  $\hat{T}$  values close to 1 indicate thermal behaviour similar to a bulk solid with no void, while higher values indicate overheating with increasing severity. Figure 4.2b gives the normalized hotspot map  $\hat{T}_{\text{HS}}$  for the geometry considered in Figure 4.1.

Apart from facilitating TO integration, there is another benefit associated with the proposed normalization step. The normalized hotspot map becomes invariant of  $q_0$ ,

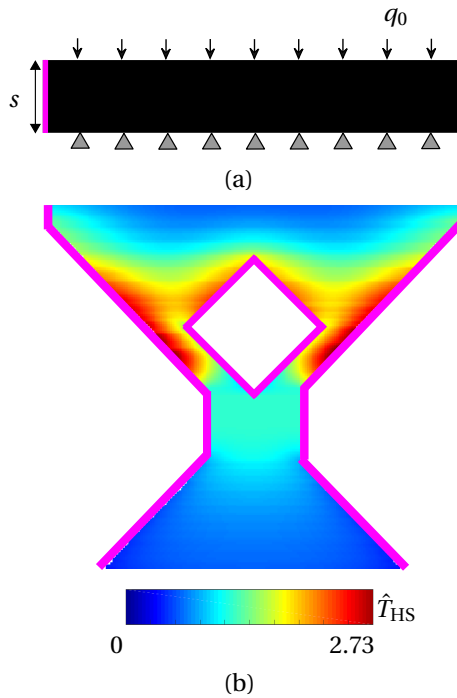


Figure 4.2: (a) A fully-solid rectangular slab with the same thermal conductivity and boundary conditions as the slabs during the hotspot detection. (b) The normalized hotspot map for the geometry shown in Figure 4.1. Magenta boundaries indicate fully insulated part-powder interface.

$k_0$  and  $T_0$ . However, the value of the slab thickness  $s$  influences the hotspot temperatures. The selected slab thickness dictates which subset of the geometry will be included within the slab and this has a direct influence on the normalized temperatures. It basically signifies the *thermal interaction length*  $\kappa$  up to which features significantly influence the heat flow at the newly deposited layer. In case of LPBF, this distance  $\kappa$  is significantly larger than thickness of a layer and hence, subsequent slabs are defined with large overlaps. In [35], the appropriate slab thickness is taken to be the characteristic length<sup>1</sup> which is given as  $\sqrt{\alpha t_h}$ , where  $\alpha$  is the thermal diffusivity and  $t_h$  is the heating time for the layer. The heating time further depends on process conditions, *e.g.* layer area, number of lasers, number of parts and their relative position in the build chamber etc. In the context of TO, the design is not known beforehand and hence, it is difficult to pre-determine the heating time. Thus, in this paper, we consider slab thickness as a constant parameter for simplicity and will discuss in detail about the implications of this choice in Section 4.6.1.

### 4.3. NUMERICAL IMPLEMENTATION

In this section, a 2D finite element (FE) implementation of the hotspot detection method is presented which is subsequently used for formulating the hotspot constraint. The presented finite element implementation can be applied to any geometry. Here we choose the geometry already considered in Figure 4.1 to explain the numerical implementation. As a first step, an embedding domain is discretized with a structured mesh of bi-linear four-node square elements, as shown in Figure 4.3. Next, an extra slab is added beneath the part for emulating the thermal influence of the baseplate (shown in red color in Figure 4.3). We choose to keep the baseplate only as thick as a slab for simplicity. The number of elements used to discretize the part in  $x$ -direction and  $y$ -direction are represented by  $n_x$  and  $n_y$ , respectively. The number of elements required to discretize a slab in the  $y$ -direction is  $n_s$ . In Figure 4.3,  $n_s$  is arbitrarily chosen as 2 as an example. A slab numbering scheme is introduced in Figure 4.3, that starts from the baseplate slab. The second slab is defined by shifting the first slab by one element in build direction (indicated by  $y$  axis). The process continues until the topmost, *i.e.* the  $m^{\text{th}}$  slab, where  $m = n_y + 1$ . It is evident from the choice of boundary conditions that for the steady-state thermal analysis, maximum temperatures are attained always at the top most nodes of any given slab. Consequently, this procedure of defining subsequent slabs ensures the detection of any hotspots for the given mesh resolution, since every node in the part geometry is at the top of a slab.

We aim to integrate the hotspot detection method with a density-based TO approach [5]. A density variable  $\bar{\rho}$  ranging between 0 and 1 is defined for each element in order to describe the layout of a design. As per the AM process, heat should only be applied to the top surface where material is present. Therefore, following the classical approach, we use a SIMP-inspired relationship [5] for scaling the elemental conductivity and heat

<sup>1</sup>For derivation of thermal characteristic length, readers are referred to *e.g.* Incropera and DeWitt [15].

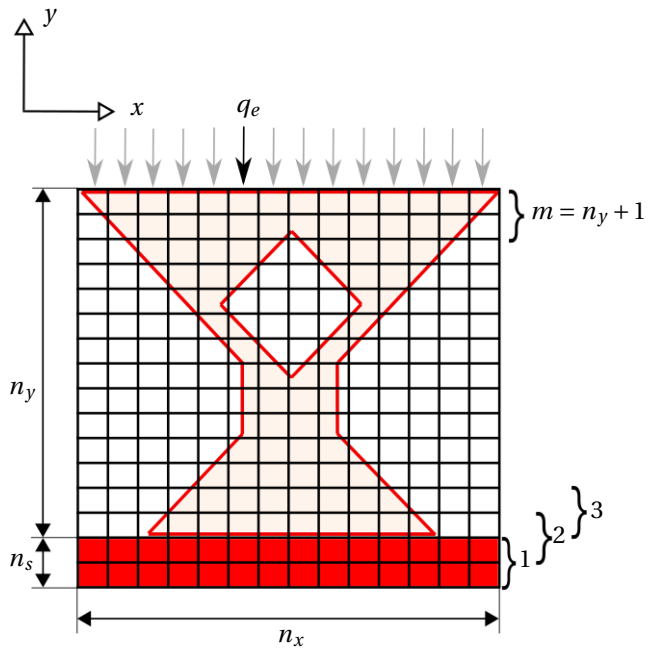


Figure 4.3: Discretization of an example geometry along with the baseplate into finite elements. A set of overlapping slabs is defined such that slab numbering starts from the bottom baseplate. Each slab is subjected to a thermal loading, for example, loading for the topmost slab is indicated by vertical arrows.



flux with the density as

$$k_e = k_{\min} + (k_0 - k_{\min})\bar{\rho}_e^r, \quad (4.5)$$

and

$$q_e = q_0\bar{\rho}_e^r, \quad (4.6)$$

respectively. Here,  $k_e$  and  $q_e$  are thermal conductivity and heat flux for Element  $e$ , respectively. The exponent  $r$  represents penalization for an intermediate density and  $k_{\min}$  is introduced to avoid singularity<sup>2</sup>. Using elemental values for conductivity and surface flux, the global conductivity matrix  $\mathbf{G}$  and thermal load vector  $\mathbf{Q}$  are assembled for each slab, following standard FE procedures [10]. Next, a set of discretized steady-state heat equations given by

$$\mathbf{G}^{(J)}\mathbf{T}^{(J)} = \mathbf{Q}^{(J)} \quad \forall J \in [1, m] \quad (4.7)$$

is numerically solved and nodal temperatures  $\mathbf{T}^{(J)}$  are obtained for Slab  $J$ . Next, slab temperatures are normalized with  $N_c$  *i.e.*

$$\hat{\mathbf{T}}^{(J)} = \frac{\mathbf{T}^{(J)}}{N_c}. \quad (4.8)$$

It is noteworthy that Eq. (4.7) can be solved independently for each slab  $J = 1 \dots m$  and hence, temperature fields associated with all the slabs can be computed in parallel.

Recall that due to the considered boundary conditions and steady-state analysis, maximum temperatures are attained only at the top most nodes of any given slab. Therefore, as the next step, normalized temperatures for these nodes are collected in an array  $\hat{\mathbf{T}}^\Omega$ , where  $\Omega$  represents the design domain. Note that the array  $\hat{\mathbf{T}}^\Omega$  basically represents the hotspot map information. Finally, if the maximum temperature in the hotspot map is less than a critical value *i.e.*  $\max(\hat{\mathbf{T}}^\Omega) \leq T^{\text{cr}}$ , the part layout is not prone to overheating during AM. Determination of  $T^{\text{cr}}$  is discussed in the next section.

The max operator is non-differentiable whereas a smooth operation is required for calculating the sensitivities needed in TO. Therefore, a P-mean aggregation scheme is used over  $\hat{\mathbf{T}}^\Omega$  for specifying the constraint as

$$f = \frac{1}{T^{\text{cr}}} \left[ \frac{1}{n} \sum_{i=1}^n (\hat{T}_i^\Omega)^P \right]^{\frac{1}{P}} - 1 \leq 0. \quad (4.9)$$

Here,  $\hat{T}_i^\Omega$  is the  $i^{\text{th}}$  member of array  $\hat{\mathbf{T}}^\Omega$ ,  $P$  is the exponent used for defining P-mean and  $n$  is the total number of nodes.<sup>3</sup>

<sup>2</sup>It can be worked out that different penalization exponents for conductivity and flux can lead to  $\hat{T} > 1$  even for a fully solid slab with uniform density, which is misleading. Hence equal penalization is preferred.

<sup>3</sup>Note that in Eq. (4.9), the P-mean is applied on the array  $\hat{\mathbf{T}}^\Omega$  which contains nodal temperature information from all the slabs. Alternatively, using the property of partitioning for generalized means [8], it is equivalent to do a two step aggregation where first the maximum for each slab is found, followed by finding global maximum across all the slabs.

#### 4.4. DEFINING CRITICAL TEMPERATURE USING A GEOMETRY-TEMPERATURE RELATIONSHIP

It remains to determine a critical temperature  $T^{\text{cr}}$  for the hotspot constraint. For this purpose, we propose a calibration procedure where features known to be causing unacceptable overheating issues are first analyzed using the hotspot detection method. Next, the associated hotspot temperatures are used for setting up  $T^{\text{cr}}$ . Here, we choose to use overhanging geometries as they are the most commonly identified cause of overheating [29]. It should be noted that this is not the only option and with advancing capabilities of capturing in-situ experimental data, an empirical calibration can also be done. Finally, it is important to note that by using overhangs for calibration purposes, our aim is not to propose an overhang avoidance scheme. Instead, the method evaluates thermal behaviour of designs and avoids local overheating not necessarily linked with an overhang. This distinction is further elaborated in Section 4.6 and 4.7.

Typically, a limiting overhang value  $\theta^{\text{cr}}$  for an AM system is experimentally determined using benchmark geometries, see for example, Cloots et al. [9]. Here, AM system refers to a combination of material and process parameters. This implicitly means that the thermal conditions while fabricating overhangs with  $\theta < \theta^{\text{cr}}$  can lead to overheating. We use a similar idea for calibrating the hotspot constraint. For this purpose, geometries with overhang angles  $\theta$  ranging between  $30^\circ$ – $60^\circ$  with an interval of  $5^\circ$  are constructed and subjected to thermal loading, using the slab-based analysis discussed in Section 4.3. Figure 4.4 shows one of such geometry with a height that is equal to the slab height  $s$  and thickness  $b$ . This mimics the situation when an overhanging geometric feature is encountered within one of the slabs. The aspect ratio associated with this geometry is defined as  $a = b/s$ . The temperature field normalized using  $N_c$  is shown in Figure 4.4 and referred to as  $\hat{T}_C$ , where subscript  $C$  denotes its calibration functionality. Note that  $\hat{T}_C$  is different from a hotspot map  $\hat{T}_{\text{HS}}$ , as the latter is found by combining  $\hat{T}_C$  from multiple slabs. The maximum normalized temperature  $\hat{T}_C^{\text{max}}$  occurs at the top left vertex of the wedge, as shown in Figure 4.4. The minimum feature size, typically controlled in TO using filtering techniques, gives a lower bound for the thickness  $b$  while a constant value of slab thickness  $s$  is selected before starting the optimization<sup>4</sup>. In practice, the minimum feature size is determined based on the resolution of the manufacturing process that is used to realize the TO design.

In Figure 4.5,  $\hat{T}_C^{\text{max}}$  is plotted as a function of  $\theta$  for selected aspect ratios  $a$ . A first observation is that  $\hat{T}_C^{\text{max}}$  decreases with increasing overhang angle  $\theta$ , for a constant  $a$  value. This signifies higher overheating for more acute overhangs. Next, for a constant  $\theta$ ,  $\hat{T}_C^{\text{max}}$  increases with increasing aspect ratios, ranging from  $a = 0.1$  until it saturates near  $a = 4$ . Note that the slab thickness  $s$  remains constant during the optimization while thickness  $b$  varies for different features during design iterations. This implies that the range of  $a$  from 0.1 to 4 corresponds to increasing  $b$ . Also note that the width of the top surface, which is subjected to the heat flux, increases with a higher  $b$  value. Hence, the increase in  $\hat{T}_C^{\text{max}}$  with  $a$  is an artefact caused by the fact that an entire layer is assumed

<sup>4</sup>More details about selection of slab thickness in Section 4.6.1.

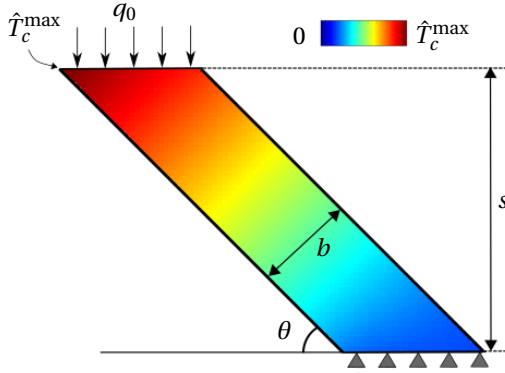


Figure 4.4: Normalized temperature field  $\hat{T}_C$  obtained by subjecting an overhanging geometry to heat flux on the top surface with the bottom as heat sink.

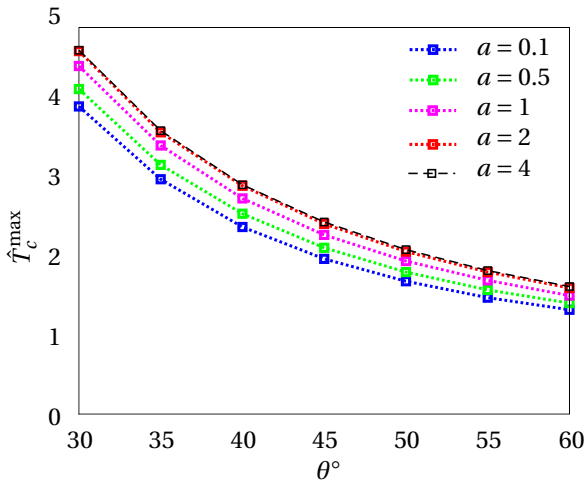


Figure 4.5: The variation of maximum normalized temperatures  $\hat{T}_C^{\max}$  with respect to overhang angles for selected values of aspect ratios  $a = b/s$ .

to be exposed to heat simultaneously while a concentrated heat load is used in the real process. The true heat load will depend on the scanning strategy, and the chosen model constitutes a worst-case situation, hence guarantees overheating prevention. Therefore,  $T^{\text{cr}}$  is set as  $\hat{T}_c^{\text{max}}$  obtained for  $\theta^{\text{cr}}$  and minimum aspect ratio  $a = b/s$ , defined using the selected minimum feature size and slab thickness.

## 4.5. INTEGRATION WITH TO

The 88-line topology optimization Matlab code by Andreassen et al. [4] has been extended to incorporate hot spot detection. The method of moving asymptotes (MMA) [41] has been used for optimization. Here, we used default MMA parameters for all the results. An investigation into the influence of MMA parameters is considered outside the scope of this study. The problem definition along with default TO parameters are given in Section 4.5.1. In the remainder, the baseplate is located underneath the domain, defining the print direction with exception of Section 4.6.2 where various other printing directions are studied.

### 4.5.1. PROBLEM DEFINITION

The primary focus of this section is to show the usability of the novel TO method with hotspot constraint. Consequently, we restrict our discussion to linear elastic compliance minimization with a volume constraint, using the SIMP interpolation scheme [5]. An additional thermal constraint described by Eq. (4.9) is included to suppress design features associated with overheating during the AM process. The complete problem is stated as:

$$\min_{\boldsymbol{\rho}} : C(\boldsymbol{\rho}) = \mathbf{u}^T \mathbf{K} \mathbf{u}, \quad (4.10a)$$

$$\text{subject to} \quad (4.10b)$$

$$\frac{V(\boldsymbol{\rho})}{V_o} - f_o \leq 0, \quad (4.10c)$$

$$\frac{1}{T^{\text{cr}}} \left[ \frac{1}{n} \sum_{i=1}^n (\hat{T}_i^{\Omega})^p \right]^{\frac{1}{p}} - 1 \leq 0, \quad (4.10d)$$

$$\mathbf{G}^{(J)} \mathbf{T}^{(J)} = \mathbf{Q}^{(J)} \quad \forall J \in [1, m], \quad (4.10e)$$

$$\mathbf{K} \mathbf{u} = \mathbf{f}, \quad (4.10f)$$

$$\mathbf{0} \leq \boldsymbol{\rho} \leq \mathbf{1}. \quad (4.10g)$$

Here,  $C$  is the compliance,  $\mathbf{u}$  and  $\mathbf{f}$  are the arrays containing the global displacements and nodal forces, respectively,  $\mathbf{K}$  is the global stiffness matrix,  $\boldsymbol{\rho}$  is the array of design variables,  $V(\boldsymbol{\rho})$  and  $V_o$  are the total material volume and design domain volume, respectively, and  $f_o$  is the prescribed volume fraction. The meshing scheme as described in Section 4.3 is used. The density filtering scheme described by Bruns and Tortorelli [7] has been used to impose a length-scale and avoid checkerboarding. It gives the relation between design variables and element densities as

Table 4.1: Default parameters

Poisson's ratio	0.3
SIMP penalization	3
Volume fraction $f_o$	0.5
P-mean exponent $P$	15
Slab thickness $s$ (mm)	12
Thermal penalization $r$	3
No. of iterations	400

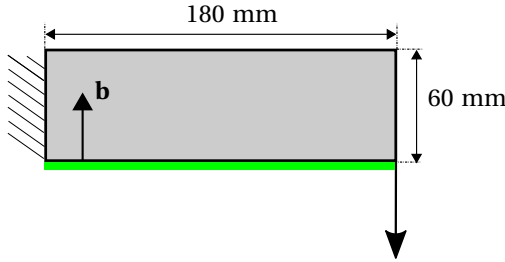


Figure 4.6: The cantilever test case with a concentrated load on the lower right vertex and fixed left edge. Build orientation is considered in the direction of  $\mathbf{b}$  which is normal to the baseplate, indicated by the green rectangle underneath the domain.

$$\tilde{\rho}_e = \frac{\sum w_{e,i} \rho_i}{\sum w_{e,i}}, \quad (4.11)$$

where,  $\tilde{\rho}_e$  is the density of an element  $e$  centered at position  $\mathbf{r}_e$  and  $w_{e,i}$  is a weight factor at position  $\mathbf{r}_i$ . The weight factor is defined using a linearly decaying distance function:  $w_{e,i} = \max(0, R - \|\mathbf{r}_i - \mathbf{r}_e\|)$  with filter radius  $R$ . The sensitivity derivation for the novel thermal constraint, see Eq. (4.9) or Eq. (4.10d), is given in Appendix C.

A cantilever design case is considered here for demonstrating the performance of the proposed hotspot-based TO method. The design domain measuring 180 mm  $\times$  60 mm is shown in Figure 4.6 along with a concentrated load acting on the lower right vertex while the left edge is considered fixed. The structural problem assumes plane stress condition for solving the 2D problem. For the thermal analysis, out-of-plane thickness has no influence on the hotspot map. This is due to the fact that input heat flux is defined per unit area and a layer-by-layer heat deposition is assumed. However, an out-of-plane thickness of 50 mm is assumed for the theoretical calculation of slab thickness value, as discussed later in Section 4.6.1. The optimization problem given by Eq. (4.10) is initiated with uniform density of  $\rho = f_o$  and filter radius  $R = 2$  mm is used. Finite elements of 1 mm  $\times$  1 mm are used. Build orientation is indicated with  $\mathbf{b}$  in Figure 4.6 and default values of parameters are listed in Table 4.1.

As explained in Section 4.3, a P-mean is used for estimating the maximum temperature. A P-mean typically underestimates the true maximum and the error decreases with increasing  $P$  value. However, in our case a correct estimate of the maximum temperature is important since an overshoot beyond  $T^{\text{cr}}$  indicates the risk of overheating which defeats the purpose. Hence, an adaptive scheme suggested by Le et al. [24] is applied for correcting the maximum found by the P-mean by scaling it with the true maximum. This means that a scaling factor  $\Psi$  is incorporated in the hotspot constraint given by Eq. (4.9) as

$$f = \frac{\Psi}{T^{\text{cr}}} \left[ \frac{1}{n} \sum_{i=1}^n (\hat{T}_i^{\Omega})^P \right]^{\frac{1}{P}} - 1 \leq 0. \quad (4.12)$$

where  $\Psi$  is defined as the ratio of the true and P-mean maximum from the previous iteration, *i.e.*

$$\Psi^{(I)} = \left[ \frac{\max(\hat{\mathbf{T}}^{\Omega})}{\left( \frac{1}{n} \sum_{i=1}^n (\hat{T}_i^{\Omega})^P \right)^{\frac{1}{P}}} \right]^{I-1}, \quad (4.13)$$

where  $I$  represent iteration number. Due account for the scaling factor  $\psi$  are made for the sensitivity calculation. As discussed in Le et al. [24], this scheme can cause convergence difficulties as  $\Psi$  changes in a discontinuous manner. Hence, the scaling factor  $\Psi$  is adjusted only once every 25 iterations in a total of 400 iterations permitted for the optimization. With this continuation scheme, numerical investigation reveals that  $P = 15$  is suitable for calculating the P-mean while still achieving desirable accuracy in predicting the maximum values for the temperature constraint. Note that due to the utilization of the scaling scheme which compensates for the error in prediction, P-norm can also be used instead of P-mean which overpredicts the true maximum temperature.

#### 4.5.2. TOPOLOGY OPTIMIZATION

The minimum compliance design without the hotspot constraint is shown in Figure 4.7a which is referred to as the reference design with compliance as  $C_{\text{ref1}}$ . The design obtained with the hotspot constraint is shown in Figure 4.7b. It is observed that due to the hotspot constraint, there is a tendency for avoiding the long overhangs present in the reference design, which are expected to cause overheating. However, there is a high utilization of intermediate densities for artificially meeting the hotspot constraint, which is satisfied for the shown design. The measure of non-discreteness  $M_{\text{nd}}$ , as introduced by Sigmund [38], is used to quantify this effect. A fairly high value of  $M_{\text{nd}} = 27.4\%$  is reported for the design shown in Figure 4.7b compared to the  $M_{\text{nd}} = 14.1\%$  for the reference design shown in Figure 4.7a. The results presented here are for  $T^{\text{cr}}$  calculated using  $\theta^{\text{cr}} = 45^\circ$ . It was also observed that the tendency of using intermediate densities becomes more pronounced for cases with lower  $T^{\text{cr}}$  or high  $\theta^{\text{cr}}$ . This is due to the fact that the constraint becomes more strict and presumably forces the optimizer towards intermediate densities. Lastly, note that the compliance of the hotspot-constrained design is 1.13 times the compliance for the design without the hotspot constraint. This is

seen as a compromise in compliance performance by activating the hotspot constraint and thereby reducing the design freedom.



(a)  $C = C_{\text{ref1}}$ ,  $M_{\text{nd}} = 14.1\%$



(b)  $\theta^{\text{cr}} = 45^\circ$ ,  $C/C_{\text{ref1}} = 113\%$ ,  $M_{\text{nd}} = 27.4\%$ ,  $r = 3$



(c)  $\theta^{\text{cr}} = 45^\circ$ ,  $C/C_{\text{ref1}} = 118\%$ ,  $M_{\text{nd}} = 25.1\%$ ,  $r = 9$

Figure 4.7: (a) TO without the hotspot constraint (b) TO with the hotspot constraint (c) TO with the hotspot constraint using higher thermal penalization exponent  $r = 9$ . The green rectangle at the bottom signifies the baseplate. Default parameters listed in Table 4.1 are used while any variations are reported.

The default value of  $r = 3$  is used for generating the design shown in Figure 4.7b. Increasing it to  $r = 9$  only marginally improves the discreteness of the result shown in Figure 4.7c with  $M_{\text{nd}} = 25.1\%$ . This is due to the fact that steady-state temperatures are proportional to the ratio of heat flux and conductivity. Recall that conductivity  $k_e$  and flux  $q_e$  were equally penalized for intermediate densities in Eq. (4.5) and Eq. (4.6), respectively. This implies that intermediate densities are not explicitly penalized in the current formulation as they do not significantly influence the resulting temperatures.

The high utilization of intermediate densities is a serious problem for fabrication. Typically, a thresholding operation is performed to convert a density based TO result into an STL file for printing. When converted to 0/1 using a threshold, a design with high

non-discreteness might result in an STL file which does not meet the hotspot constraint and exhibits overheating, defeating the purpose of the proposed TO method. Adding Heaviside filter proved ineffective to lower non-discreteness. Hence, in order to solve this issue, we use the robust TO formulation which is discussed in the next section.

### 4.5.3. ROBUST TOPOLOGY OPTIMIZATION

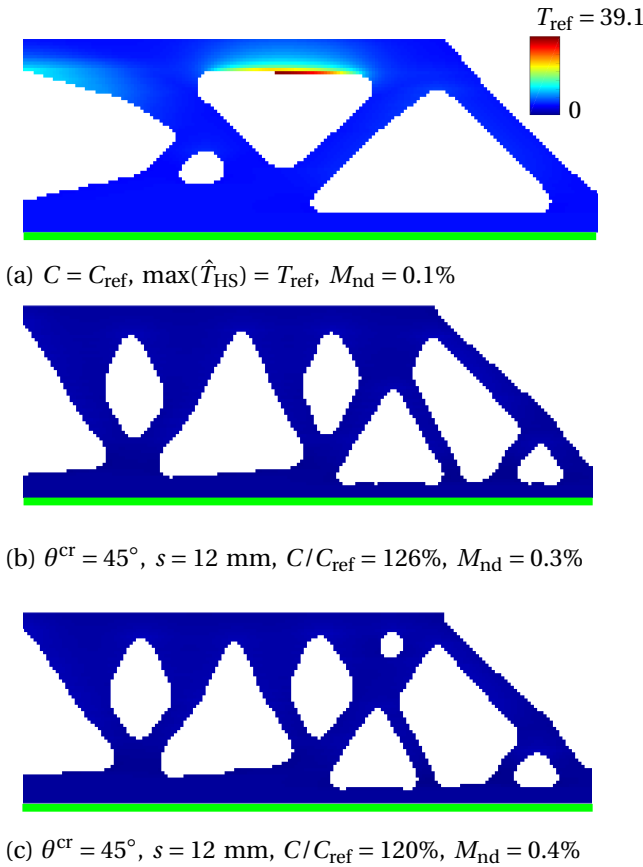


Figure 4.8: (a) Robust TO without the hotspot constraint. (b) Robust TO with the hotspot constraint on eroded, intermediate and dilated designs (c) Robust TO with the hotspot constraint only on intermediate design.

In order to prevent the aforementioned problem of intermediate densities, the robust formulation [46] is employed. It uses dilated, intermediate and eroded designs using three projection thresholds  $\eta = 0.25$ ,  $\eta = 0.5$  and  $\eta = 0.75$ , respectively. The Heaviside thresholding operation is given as

$$\tilde{\rho} = \frac{\tanh(\beta\eta) + \tanh(\beta(\tilde{\rho} - \eta))}{\tanh(\beta\eta) + \tanh(\beta(1 - \eta))}, \quad (4.14)$$



where  $\tilde{\rho}$  is the projected density and  $\hat{\rho}$  is the filtered density obtained using Eq. (4.11). For all the results using robust TO,  $\tilde{\rho}$  represents physical density and  $R = 6$  mm is used.  $\beta$  is a parameter which controls the intensity of the Heaviside projection. In this study,  $\beta$  is initialized as  $\beta = 1$  and then doubled every 50 iterations till  $\beta_{\max} = 64$ . For details about this method, readers are referred to Wang, Lazarov, and Sigmund [46] and Sigmund [39].

Typically, the robust optimization problem is formulated as a min-max optimization problem where the objective is calculated for all three projection designs. However, for the case of compliance minimization, Lazarov, Wang, and Sigmund [23] showed that it is sufficient to consider the eroded design only which results in reduced computational cost for evaluating the objective. Hence, we use the eroded design for calculating the compliance while the hotspot constraint, given by Eq. (4.10d), is initially implemented on all three projected designs. The intermediate design found using the robust TO without the hotspot constraint is shown in Figure 4.8a while that with the hotspot constraint is presented in Figure 4.8b. The compliance for the reference design is referred to as  $C_{\text{ref}}$ . Once again, we present results for the commonly used  $\theta^{\text{cr}} = 45^\circ$  for the TO with hotspot constraint. Hotspot maps superimposed on the optimized designs are normalized to a common scale ranging from 0 to the maximum temperature obtained for the reference design shown in Figure 4.8a. The long overhang in the top region of the design shown in Figure 4.8a is identified as a source of severe overheating. It is observed that by using the hotspot constraint material is redistributed such that this long overhang is avoided. Also, the robust TO design is almost black and white with  $M_{\text{nd}} = 0.35\%$ . Again, compliance of the hotspot-constrained intermediate design is 1.26 times that of the design without the hotspot constraint. Note that the design shown in Figure 4.8a becomes significantly different from that shown in Figure 4.7a due to the length scale considerations associated with Robust formulation.

The robust method is generally used for providing robustness against the uncertainties of the manufacturing process where the part boundaries might shift during fabrication. However, the targeted LPBF process offers high precision and STL files can generally be printed with high accuracy. Hence, in the remainder we choose to apply the hotspot constraint only on the intermediate design which is seen as the final result, while eroded and dilated designs are used for evaluating compliance and applying the volume constraint, respectively. This offers another computational gain as hotspot constraint has to be evaluated only once instead of three times. The result of this lean robust formulation is shown in Figure 4.8c where the topology is very similar to that shown in Figure 4.8b. Imposing the hotspot constraint only on intermediate design allows for relatively higher design freedom and hence it reduces the compromise in performance caused by the hotspot constraint. This is evident by the reduced compliance value ( $= 1.2C_{\text{ref}}$ ) for the case where hotspot constraint is imposed only on the intermediate design. This formulation is found to be able to generate crisp designs with desired overheating control. Hence, it is used for creating all the results presented in subsequent sections.

#### 4.5.4. EVALUATION USING HIGH FIDELITY TRANSIENT SIMULATION

In order to further investigate the susceptibility of optimized designs to overheating, they are subjected to a high fidelity transient LPBF simulation. The high fidelity simulation performs an FE analysis on the heat equation within a time integration and is detailed in Ranjan et al. [35]. Consequently, time evolution of design's thermal response is determined for layer-by-layer material deposition with temperature-dependent thermal properties while convective and radiative thermal losses are also accounted for. The maximum temperature for each FE node is recorded across the entire history of the simulation and used for creating the corresponding hotspot map. The hotspot maps constructed from high fidelity simulations for the designs obtained with (Figure 4.8a) and without (Figure 4.8c) the hotspot constraint are shown in Figure 4.9a and Figure 4.9b, respectively. For a better comparison, a common temperature scale ranging from the sink temperature of 180 °C to the maximum temperature found within both of the designs is used. Note that no normalization is performed and the actual maximum temperatures are reported. It is evident that the long overhang in Figure 4.9a causes severe overheating leading to a peak temperature of 6708 °C. On the other hand, the maximum temperature for the design shown in Figure 4.9b remains at a much lower value of 1678 °C. This high fidelity transient simulation which better mimics the LPBF process physics shows that indeed the design found using hotspot TO is not susceptible to overheating, as compared to that found using TO without any hotspot constraint. It is noteworthy that the evaluation performed here simply compares the thermal behaviour of both designs using a high fidelity model and should not be seen as a validation of the actual temperatures found by the steady-state model. For latter, readers are referred to Ranjan et al. [35] where a quantitative comparison of the simplified model with high fidelity simulations is presented.

### 4.6. PARAMETER STUDY

#### 4.6.1. INFLUENCE OF HOTSPOT ANALYSIS PARAMETERS

In this section, we analyze the effect of various parameters associated with the hotspot analysis on optimization results. There are a total of six parameters that are introduced in this formulation, *i.e.* critical temperature  $T^{\text{cr}}$ , slab thickness  $s$ , thermal penalization exponent  $r$ , input heat flux  $q_0$  and the thermal conductivity of solid and void regions,  $k_0$  and  $k_{\text{min}}$ , respectively. Recall that the temperatures are normalized using  $N_c = q_0 s / k_0$ , hence the material property  $k_0$  and input flux  $q_0$  have no effect on the optimization process. Also recall that due to this normalization scheme, temperatures are reported relative to those obtained for a solid slab. Next, it was found that the relative value of  $k_{\text{min}}$  with respect to  $k_0$  affects the optimization process. Extremely low void conductivity, such as  $k_{\text{min}} \approx k_0 \times 10^{-10}$ , leads to very high hotspot temperatures in an intermediate slab where material is disconnected from the bottom heat sink. This causes multiple thermal constraint violations leading to slow convergence. For this reason,  $k_{\text{min}} = k_0 \times 10^{-4}$  is used for all the examples. This is also reminiscent of the fact that surrounding powder has lower but finite thermal conductivity [36]. For the robust TO, it is found that the thermal penalization exponent  $r$  has a negligible effect on the optimized

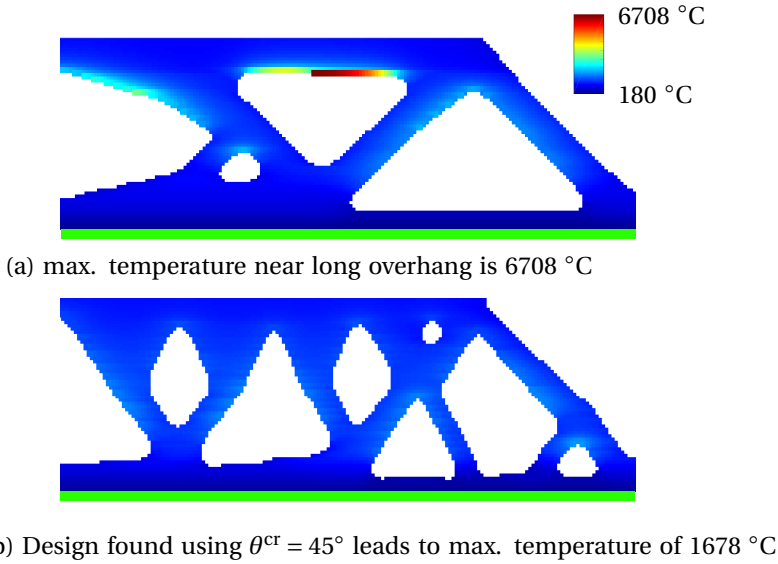


Figure 4.9: Hotspot map obtained from high-fidelity LPBF transient simulation for designs found using (a) Robust TO without the hotspot constraint (b) Robust TO with the hotspot constraint. The high-fidelity transient simulation considers temperature dependent thermal properties, convection and radiation and all simulation parameters are taken from Ranjan et al. [35].

designs. This is because the physical density  $\tilde{\rho}$  is driven towards 0/1 as optimization progresses. The influence of the remaining two parameters is discussed in detail as they significantly effect the resulting optimized design.

#### INFLUENCE OF CRITICAL TEMPERATURE

Recall that in Section 4.4 a numerical calibration step is used for determining  $T^{\text{cr}}$  based on a critical overhang value  $\theta^{\text{cr}}$  and aspect ratio  $a$ , *i.e.*  $T^{\text{cr}} = \hat{T}_C(\theta^{\text{cr}}, a)$ . Here  $a$  is the ratio of minimum feature size  $b$  and slab thickness  $s$ . A relationship between  $b$ ,  $\eta$  and  $R$  is presented graphically in Qian and Sigmund [34] which, for our implementation with  $\eta = 0.25$  and  $R = 6$  mm, leads to  $b = 6$  mm. This further gives  $a = b/s = 0.5$  for the default value of  $s = 12$  mm. This implies that the green curve in Figure 4.5 is used for deciding critical hotspot temperatures. The results for  $\theta^{\text{cr}} = 30^\circ, 40^\circ$  and  $50^\circ$  are presented in Figure 4.10a, b and c, respectively. The critical temperatures found using the described calibration process are  $T^{\text{cr}}(30^\circ) = 4.1$ ,  $T^{\text{cr}}(40^\circ) = 2.5$  and  $T^{\text{cr}}(50^\circ) = 1.8$  for the designs shown in Figure 4.10a, b and c, respectively. The temperature constraints are met in all hotspot TO implementations as the maximum hotspot temperatures remain lower than the respective  $T^{\text{cr}}$ . It can be seen that the hotspot occurring due to the long horizontal overhang in the reference case, shown in Figure 4.8a, is avoided. Consequently, the maximum hotspot temperatures for the cases shown in Figure 4.10 remain much lower than that obtained in the reference case  $T_{\text{ref}} = 39.1$ . Also, as  $\theta^{\text{cr}}$  increases or  $T^{\text{cr}}$  decreases, different designs are found such that the maximum hotspot temperature is further reduced

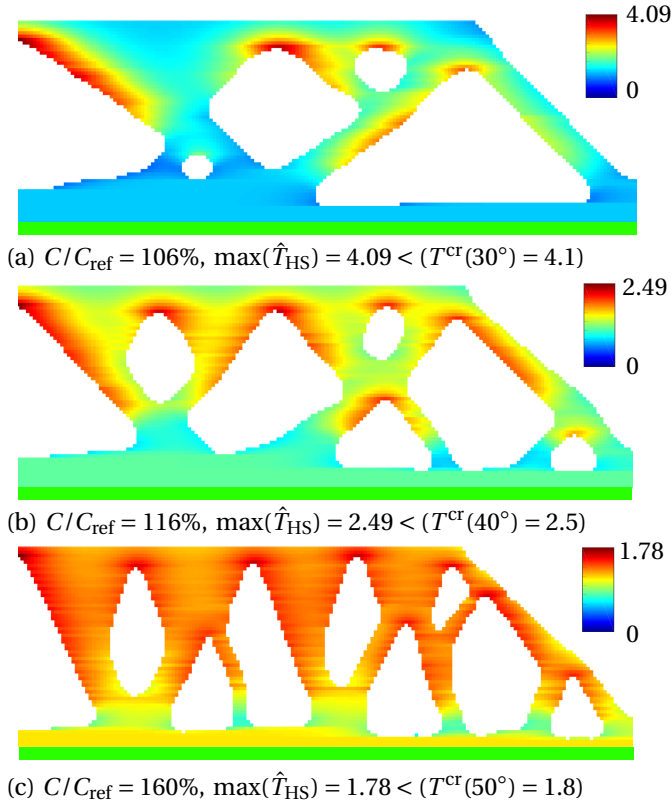


Figure 4.10: Designs and hotspot fields  $\hat{T}_{\text{HS}}$  obtained for the cantilever beam problem with critical temperatures  $T^{\text{cr}}$  calculated using (a)  $\theta^{\text{cr}} = 30^\circ$ , (b)  $\theta^{\text{cr}} = 40^\circ$  and (c)  $\theta^{\text{cr}} = 50^\circ$ . All designs are obtained after 400 MMA iterations and  $\max(\hat{T}_{\text{HS}})$  denotes the maximum hotspot temperature of the corresponding sub-figure. The thermal constraints were met for all hotspot implementations. The relative compliances of the hotspot designs and reference case shown in Figure 4.8a are given by  $C/C_{\text{ref}}$ .

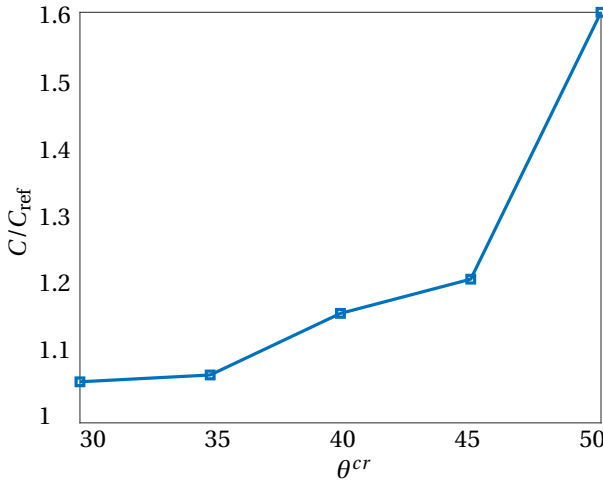


Figure 4.11: The variation of compliance with respect to the overhang angles used for defining the critical hotspot temperatures. The compliances are normalized against that for the reference design shown in Figure 4.8a.

in accordance with the constraint. A green colored baseplate is added at the bottom of the designs to indicate the build direction.

The variation of compliances for different critical overhang values is shown in Figure 4.11. It is observed that as  $\theta^{cr}$  increases or  $T^{cr}$  reduces, the constraint becomes more strict and design freedom reduces. Consequently, the compliance of the corresponding designs increases, as more material is dedicated to manage the temperature and less freedom remains to improve structural performance. This is also highlighted by the hotspot fields presented in Figure 4.10. For example, in the most strict case of  $\theta^{cr} = 50^\circ$ , hotspot temperature remains close to the critical value for most of the features. This shows that the optimizer has to give a lot of priority in meeting the hotspot constraint over improving compliance.

The optimization with hotspot constraint converges relatively smoothly for a problem involving constraint aggregation, as shown in Figure 4.12. However, convergence requires more iterations when the constraint becomes more strict. Snapshots of density fields are shown in Figure 4.12 for iteration number 50, 100, 150 and 300. Also, there is an observable jump at iterations where  $\beta$  is doubled which disrupts the convergence.

Lastly, in order to examine the influence of the critical temperature on overhanging features, the density fields of the optimized designs are presented in Figure 4.13 and the actual overhang angles<sup>5</sup> are superimposed on the designs. It can be observed that as  $\theta^{cr}$  increases, fewer features with acute overhang angle tend to appear. Also, note that

<sup>5</sup>In order to determine the overhang angles, the contour of the density field is created using a threshold of 0.5. The contour points are joined and angles of connecting lines are calculated.

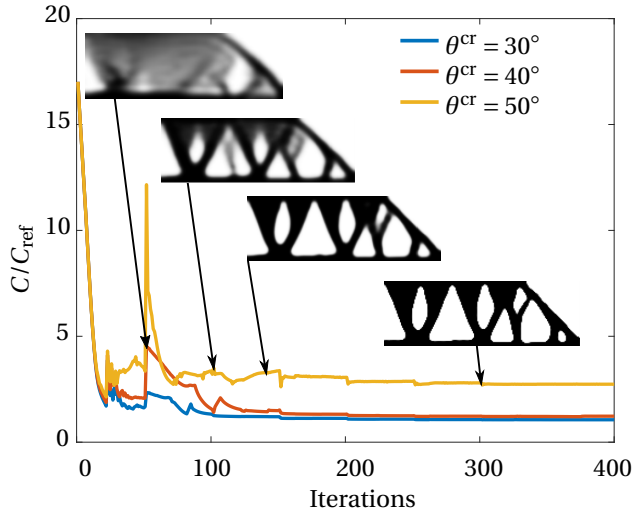


Figure 4.12: Convergence behaviour for the cantilever case with hotspot TO implementations for  $\theta^{cr} = 30^\circ$ ,  $40^\circ$  and  $50^\circ$ . The snapshots of intermediate designs are given at iterations 50, 150, 250 and 400 for  $\theta^{cr} = 50^\circ$ .

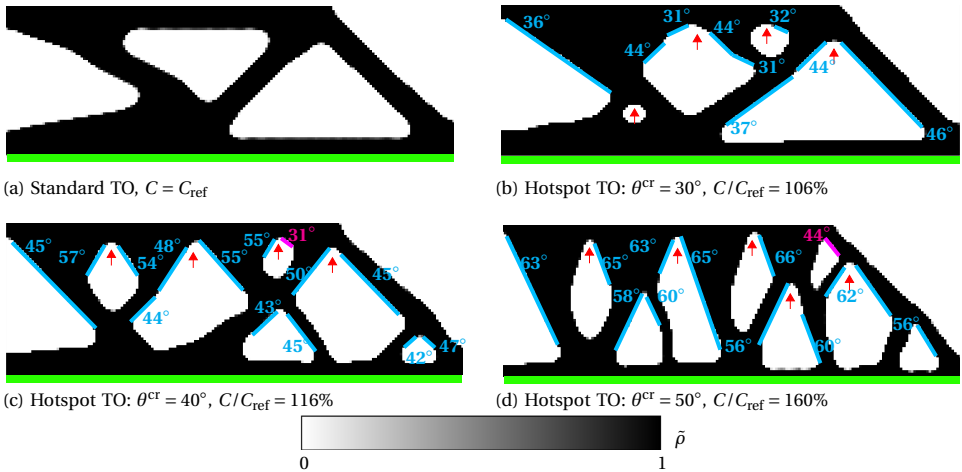


Figure 4.13: Density fields of designs optimized for the cantilever beam problem using (a) Robust TO without hotspot constraint (b)–(d) hotspot TO formulation with critical temperatures set using different  $\theta^{cr}$ . All designs are obtained after 400 MMA iterations. Overhang angles are geometrically determined and printed near the respective overhanging feature.

most overhangs are higher than  $\theta^{cr}$  which suggests that hotspot-constrained TO leads toward conservative designs. This is due to the consideration of worst case scenario of simultaneous layer heating which leads to higher temperatures for thicker geometries, as demonstrated in Section 4.4. As a consequence, the optimizer prefers  $\theta > \theta^{cr}$  in order to meet the hotspot constraint for features which are thicker than minimum feature size  $b$ . As a downside, this could lead to over-restrictive designs compromising the performance while ensuring overheating avoidance. It is expected that a more detailed AM model can address this issue.

Next, it is also observed that few overhangs with an overhang angle less than  $\theta^{cr}$ , are permitted in the final designs. These are marked in magenta (Figure 4.13) and referred to as ‘benign’ overhangs. Recall that all presented designs meet the thermal constraint which implies that for all benign overhangs, hotspot temperatures do not exceed the respective  $T^{cr}$ . Presence of geometric features which facilitate effective heat flow in the proximity of the benign overhangs is identified as the cause for maintaining acceptable temperatures. This allows for the benign overhangs to exist without violating the thermal constraint. Another observation reveals that even short horizontal overhangs are allowed, as indicated by red arrows in Figure 4.13b, c and d. It is known that difficulties associated with manufacturing of flat overhangs increases with increasing length [29] and hence, small flat overhangs can be thermally benign. The hotspot-based approach naturally recovers this phenomenon without any explicit geometrical rule, which is one of the advantages of a physics-based manufacturing constraint.

#### INFLUENCE OF SLAB THICKNESS

Until now, we used  $s = 12$  mm for all the presented results. Next, in order to understand the influence of  $s$ , we present results for  $s = 6$  mm and 20 mm in Figure 4.14a and c, respectively, along with slabs marked as magenta color boxes. For comparison, the design for  $s = 12$  mm is also shown in Figure 4.14b. They all are crisp and satisfy the respective hotspot constraint. A close comparison of these designs reveals that slab thickness governs how the hotspot constraint influences the design freedom during the optimization, which is explained in the subsequent paragraphs.

First, recall that  $T^{cr}$  reduces with the aspect ratio  $a = b/s$ , as shown in Figure 4.5. This implies that  $T^{cr}$  slightly decreases with increasing slab thickness  $s$  making the hotspot constraint more strict and hence, reducing the design freedom. However, there is another more dominant effect of neighboring features influencing the local overheating, which defines the influence of slab thickness on hotspot constraint. As a general understanding, a larger slab thickness would more likely include nearby geometric features which could influence heat flow at the top of the slab. On the other hand, for small slab thickness values, the thermal analysis domain remains small and the effect of neighboring features on each other’s thermal behavior diminishes. It is found that hotspot constraint can both increase or decrease design freedom with increasing slab thickness, depending on the heat evacuation/obstruction capacity of nearby design features. Examples for both are discussed below.

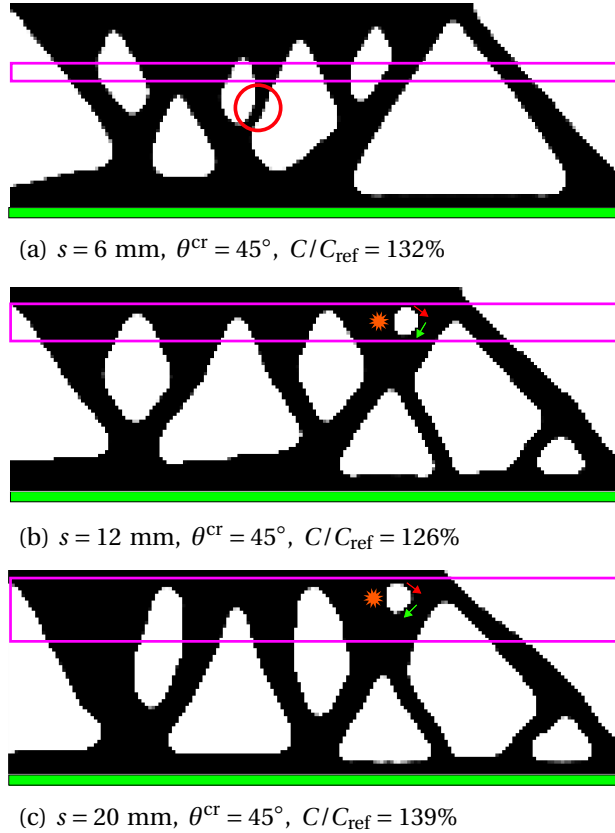


Figure 4.14: Hotspot TO designs obtained using (a)  $s = 6 \text{ mm}$  (b)  $s = 12 \text{ mm}$  and (c)  $s = 20 \text{ mm}$ . The magenta box represents the slab used for finding the design. The thermal influence of different neighboring features increases with increasing slab thickness which could both reduce or increase the design freedom. The former is explained by analyzing the thin funnel shaped feature marked with a red circle in (a) while latter is explained by analyzing the presence of a hole, marked by the orange star in (b) and (c). The red arrow next to the hole represent a converging feature leading to overheating while the green arrow denotes a diverging feature.



First, consider a nearby geometric feature that helps in heat evacuation. A larger slab would more likely encapsulate it, reducing the hotspot temperatures at the top of the slab. This would result in a less strict hotspot constraint, thereby increasing the design freedom. Contrary to this, a smaller slab excludes such a feature and thus faces a more strict hotspot constraint. An example of this phenomenon are the small holes marked by orange star signs in Figure 4.14b and Figure 4.14c. As the entire hole is included in a single slab, the diverging feature near the lower half of the hole (marked by green arrows) helps in dissipating the heat which would accumulate in the converging feature near the upper half (marked by red arrows). In order to verify this, we subject the design optimized with  $s = 20$  mm (shown in Figure 4.14c) to a post-optimization hotspot analysis with  $s = 6$  mm. The hotspot map for  $s = 6$  mm is shown in Figure 4.15a and it can be seen that the small hole indeed violates the hotspot constraint, signifying that a similar hole is less likely to appear for the case of  $s = 6$  mm.

Next, consider a nearby geometric feature that acts as a thermal bottleneck. For example, the funnel like shape in Figure 4.14a (marked by red circle) is a thermal bottleneck but it does not violate the hotspot constraint with  $s = 6$  mm. On the other hand, when this design is subjected to hotspot analysis using  $s = 20$  mm as a post-optimization step, the funnel like feature violates the hotspot constraint, as shown in Figure 4.15b. Hence, in this case, increasing the slab thickness would force the optimizer to avoid such a thin funnel like feature, even though it might be beneficial for reducing compliance. Consequently, designs with larger slab thicknesses show a tendency for having thicker members since thin members can cause hotspots. An upper bound on member sizes can be imposed if thicker members are not desired [22]. This second example shows that design freedom can also reduce with increasing slab thickness. This varying influence on design freedom is also responsible for the non-monotonic behaviour of design performances, as observed in Figure 4.14.

These findings suggest that overheating avoidance cannot be guaranteed if the slab thickness is much higher or lower than the thermal interaction length  $\kappa$  applicable for the given set of process and material parameters. Therefore, an accurate estimate of  $\kappa$  is crucial for obtaining feasible designs. For example, while considering Aluminium parts, a larger  $\kappa$  would be more suitable than that for Ti-6Al-4V parts as thermal diffusivity of Aluminium is higher. Similarly, a slow laser speed would allow for longer time spans for thermal interactions, thus encouraging a higher value of  $\kappa$ . This implies that  $\kappa$  needs to be determined on a case-by-case basis. In this context, the recent studies by Moran, Warner, and Phan [30] and Yan et al. [48] present a methodology for estimating  $\kappa$  by using high fidelity transient thermal models. Ranjan et al. [35] used the analytical solution for the 1D heat equation and showed that  $\kappa$  is characterized by  $\sqrt{\alpha t_h}$  where  $\alpha$  is the thermal diffusivity and  $t_h$  is the layer heating time. The parameter for heating time is further estimated as  $t_h = A/hv$ , where  $A$ ,  $h$  and  $v$  are layer area, laser hatch thickness and scanning velocity, respectively. Using this, slab thickness  $s = 12$  mm is estimated assuming relevant process parameters and Ti-6Al-4V parts. This is used as a default value in the remainder.

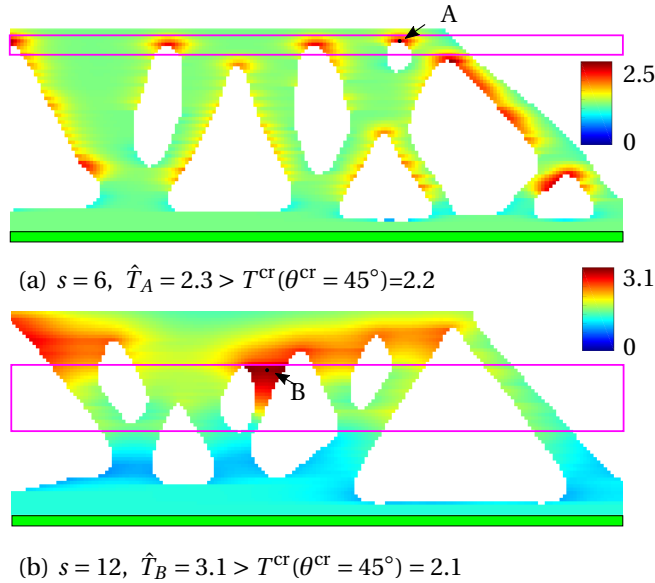


Figure 4.15: (a) Hotspot map for the design optimized using  $s = 20$  mm but analyzed using  $s = 6$  mm as a post optimization step. Hotspot temperature at point A above the circular hole violates the hotspot constraint. (b) Hotspot map for the design optimized using  $s = 6$  mm but analyzed using  $s = 20$  mm as a post optimization step. Hotspot temperature at point B inside the funnel shape violates the hotspot constraint.

#### 4.6.2. INFLUENCE OF PART ORIENTATION

In order to demonstrate the versatility of the method in different configurations, four different build orientations are considered. Based on the relative position of the baseplate with respect to the part, these orientations are referred to as South/North/East/West. The results shown in Figure 4.16 where build directions are also marked. In our implementation, the structural boundary conditions remain the same whereas the thermal loading direction and boundary conditions changes according to the build orientation. The problem definition along with all other optimization parameters remain the same as in Section 4.5.3. Therefore, the result of robust TO shown in Figure 4.8a is used to compare the compliance values. Results are shown for 400 MMA iterations and the thermal constraint is met for all presented results.

The results for Figure 4.16c and d are only marginally different from the standard TO result. This is also reflected in the fact that  $C/C_{ref}$  values for these designs are close to 100%. On the other hand, designs shown in Figure 4.16a and b differ significantly from the reference design. In particular, in the North orientation, a lot of material has to be used near the bottom for avoiding the long overhang. This makes the optimization problem rather strict and a high value for  $C/C_{ref}$  is found.

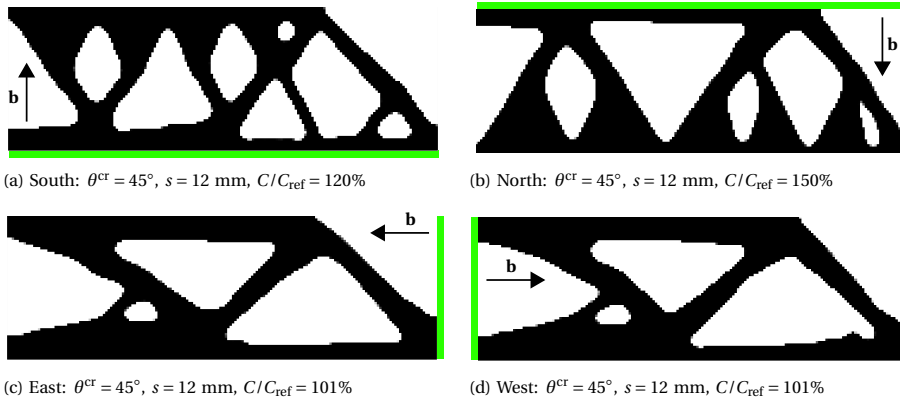


Figure 4.16: Results for four different build orientations where vector  $\mathbf{b}$  denotes build direction. These cases are named as South/North/East/West based on the relative position of the baseplate (shown in green) with respect to the part. Compliances relative to that of the standard TO design (shown in Figure 4.8a) are reported.

## 4.7. COMPARISON WITH GEOMETRY BASED TO METHOD

Another interesting observation is made by comparing hotspot TO design with that obtained using a geometry-based AM-TO method. For this purpose, the cantilever problem is optimized using the overhang control method proposed by Langelaar [20] with the same set of applicable parameters as used in Section 4.5.1. This method efficiently prohibits overhanging features with  $\theta < 45^\circ$  in the optimized design. The obtained self-supporting design is subjected to hotspot analysis with  $s = 12$  mm as a post-optimization step and the design along with its hotspot field is shown in Figure 4.17a. The same optimization problem is solved using hotspot TO with  $\theta^{cr} = 45^\circ$ ,  $s = 12$  mm and the obtained design with its hotspot field is shown in Figure 4.17b. Both fields are normalized to a common scale for comparison. For this purpose, the  $\max(\hat{T}_{HS})$  of the hotspot field shown in Figure 4.17a is used as a normalization factor. It is observed that the design shown in Figure 4.17a has several funnel-shaped features which are identified as severe hotspots with  $\max(\hat{T}_{HS}) = 4.5$  which is significantly greater than  $T^{cr}(\theta^{cr} = 45^\circ) = 2.1$ . Note that all features satisfy the geometrical overhang design rule, resembling the situation reported in the literature where overheating is observed even after following the overhang criterion [1, 32]. In contrast, the hotspot-based TO redistributes material in such a way that these hotspots are avoided. Lastly, the compliance for the hotspot TO design is found to be slightly higher than that for the geometry based TO.

It is demonstrated in Figure 4.17 that a geometry-based TO is insufficient for preventing local overheating as overhang avoidance does not necessarily ensure overheating avoidance. Moreover, it is demonstrated in Figure 4.13 and discussed in Section 4.6.1 that by virtue of neighboring features which facilitate heat evacuation, the hotspot-constrained TO method allows for short acute overhangs without violating the hotspot constraint. This is also in line with the experiences from LPBF practice [29]. These advantages establish the superiority of the proposed hotspot avoidance scheme over TO methods which

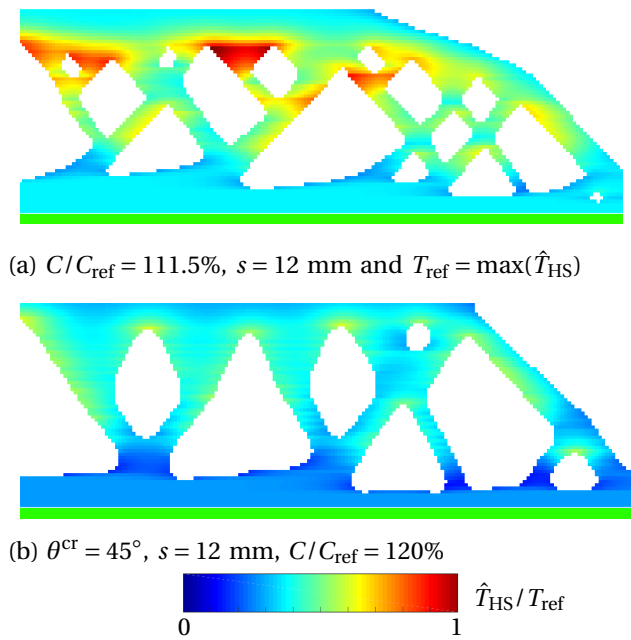


Figure 4.17: Comparison of hotspot fields for designs found by optimizing the cantilever problem using (a) AM filter based TO [20] (b) hotspot-based robust TO. Discretization and other TO parameters are as mentioned in Section 4.5.1.

prohibit overhangs on a purely geometric basis.

A recent advancement in LPBF machines allows for in-situ control of input laser energy based on part geometry with the aim of reducing the possibility of overheating. However, the control algorithms are presumably based on geometry based information which might not be enough to guarantee overheating avoidance. Moreover such in-situ control practices are currently in development stage and not a default feature of every LPBF machine. Hence, designs which are less prone to overheating are still highly desirable.

## 4.8. EXTENSION TO 3D

Although the main focus of this paper is to thoroughly investigate the hotspot-based TO in 2D setting, the extension to 3D also deserves attention and is, in fact, straightforward. The formulation of the simplified LPBF model remains the same while the FE implementation is slightly altered to tackle a 3D case. For this purpose, the 3D TO implementation from Liu and Tovar [28] is used as a basis and robust formulation [46], simplified LPBF thermal model and hotspot constraint are integrated into the code.

In general, the critical overhang angle for a given LPBF system is experimentally determined with printing wedge shaped geometries. These parts are simply an extrusion of 2D shapes and provide information about degree of overheating due to the overhanging angle of choice, see for example Cloots et al. [9] and Kranz, Herzog, and Emmelmann [18]. Using the same logic, the procedure described in Section 4.4 is directly applied for 3D cases, where a critical temperature  $T^{\text{cr}}$  corresponding to a  $\theta^{\text{cr}}$  is determined.

For demonstration purposes, a 3D cantilever beam problem is considered, as shown in Figure 4.18a and Figure 4.18b, where the surface shaded in green is assumed to be fixed while a uniformly distributed load is applied on the right bottom edge. The problem is solved using both standard and hotspot TO. The domain is discretized using isoparametric cubic (side = 1 mm) 8-noded finite elements with tri-linear shape functions. The design domain then requires 100, 50 and 50 elements in the  $x$ ,  $y$  and  $z$  directions, respectively.

The optimized design found using standard TO and hotspot TO are presented in Figure 4.18a and Figure 4.18b, respectively. Both designs are obtained after 150 MMA iterations using a volume constraint of  $f_o = 0.3$  while the latter accounts for  $T^{\text{cr}}(45^\circ) = 2.1$  with a slab thickness  $s = 8$  mm. We note in passing that the slab thickness is again calculated in accordance with the characteristic length  $\sqrt{\alpha t_h}$  where heating time  $t_h$  is now computed using the layer area of the design domain. Similar to the observations in Section 4.7, a sacrifice in compliance performance is made for ensuring manufacturability. For comparing the thermal performances, hotspot fields associated with both designs are presented in Figure 4.18c and Figure 4.18d which show that the long almost horizontal overhang in standard TO design leads to severe overheating with  $\max(\hat{T}_{\text{HS}}) = 16.8$ . A section view shown in Figure 4.18e reveals the location of the maximum temperature.

On the other hand, the design obtained from hotspot based TO maintains much lower temperatures everywhere in accordance with the hotspot constraint. Figure 4.18f once again depicts this hotspot field using its full range of temperature values to clearly show the  $\hat{T}_{HS}$  distribution.

Regarding computational times, the scalability of the simplified LPBF model has already been shown in our previous work [35]. It was reported that the wall-clock time for a real-size 3D part with 2.2 million nodes was in order of only few minutes. For the new 3D TO example presented in this paper with approximately 0.8 million degrees of freedom, each TO iteration takes approximately 3.5 minutes on a HPC cluster. The implementation has been done in Matlab R2020b and has not been heavily optimized/parallelized. Nevertheless, this shows that the inexpensive steady-state analysis still keeps the 3D TO problem computationally tractable.

4

## 4.9. CONCLUSIONS

This paper presents a novel TO scheme which addresses the issue of local overheating in AM parts. A computationally inexpensive AM thermal model that utilizes localized steady-state analysis for detecting hotspots is taken from the literature. It is demonstrated that this simplified modeling approach captures the influence of local geometry on heat evacuation during the AM process. This model is then integrated with density-based TO. A thermal constraint is formulated using temperatures relative to a solid slab with no void. It is shown through several numerical examples that the proposed method, combined with robust TO formulation, can deliver designs that outperform standard TO designs, when analyzed for local overheating behaviour during the fabrication process. The use of steady-state analysis offers significant computational gain which makes it possible to find optimal topologies within practical time-frames.

It is observed that geometry-based design rules do not ensure overheating avoidance. Moreover, the proposed method allows for localized benign horizontal and acute overhangs in optimized designs, enhancing the design freedom. As physics-based approaches capture relevant local conditions in a more realistic manner, their integration with TO offers promising advantages. However, the model employed here invoke several simplifications and still remains an approximate representation of the real process. Efficient integration of TO with more detailed models *e.g.* a transient thermal simulation remains a challenge for future research. In this regard, a more detailed transient model which *e.g.* accounts for laser movement, can also be considered. The main challenge of integrating a higher fidelity AM model with TO is that of addressing the associated high computational cost. Another important aspect is to develop a framework for estimating slab thickness for a given set of material and process parameters, instead of relying on (empirical) calibration.

A major AM issue is that of residual stresses and deformations which develop during the part fabrication. There exists a strong relationship between the process thermal history and resulting mechanical behavior. Hence, it is foreseen that the hotspot

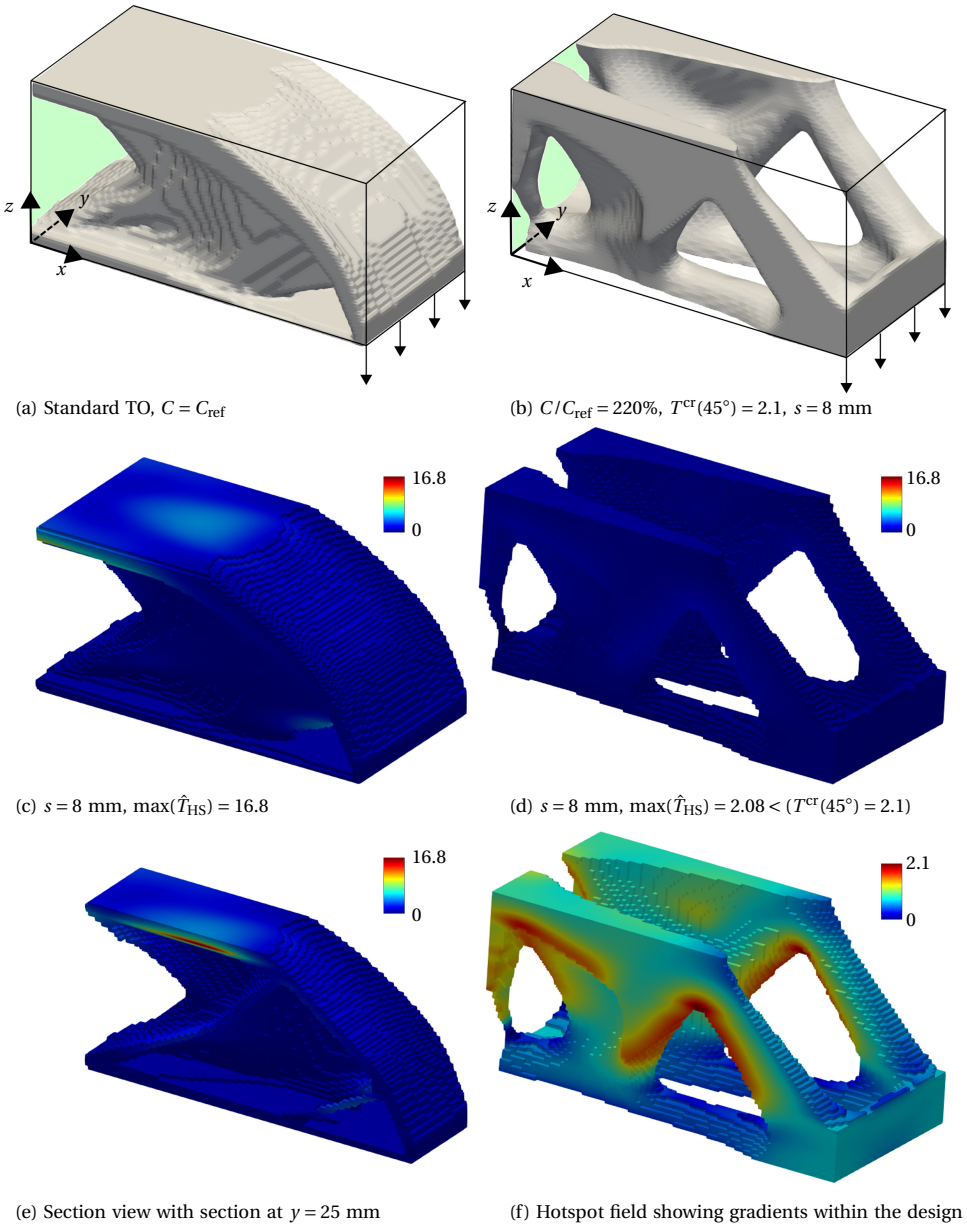


Figure 4.18: Result of a cantilever problem obtained using (a) standard TO (b) hotspot based TO implemented in 3D. Both problems are solved for a volume constraint of  $f_o = 0.3$  and results are reported after 150 MMA iterations. The hotspot based TO is carried out using  $T^{ct}(45^\circ) = 2.1$  and a slab thickness of  $s = 8$  mm. The hotspot fields are presented for (c) standard TO design (d) Hotspot TO design. A section view at  $y = 25$  mm is presented in (e) reveals the location of the maximum temperature. As (c), (d) and (e) use a common temperature scale, the temperature distribution associated with hotspot TO design are not clearly visible in (d). For this purpose, the hotspot field depicted in (d) is again presented in (f) with scale ranging between 0 and  $\max(\hat{T}_{HS})$ .

maps can also be used to identify problematic features from the context of deformations. However, the idea needs thorough investigation which is seen as an avenue of future research. Lastly, it was shown here that extension of the hotspot constraint to a 3D setting is straightforward. This is also exemplified by Sinico et al. [40] where the method was applied for TO of an industrial injection mold design. Experimental validation of 3D designs using optical tomography based in-situ monitoring technique is currently under investigation.

## REFERENCES

- [1] Guido A.O. Adam and Detmar Zimmer. “Design for Additive Manufacturing—Element transitions and aggregated structures”. In: *CIRP J Manuf Sci Tec* 7.1 (2014), pp. 20–28. ISSN: 1755-5817.
- [2] Grégoire Allaire and Benjamin Bogosel. “Optimizing supports for additive manufacturing”. In: *Struct Multidiscip Optim* 58.6 (2018), pp. 2493–2515.
- [3] Grégoire Allaire and Lukas Jakabcin. “Taking into Account Thermal Residual Stresses in Topology Optimization of Structures Built by Additive Manufacturing”. In: *Math Models Methods Appl Sci* 28.12 (July 2018), pp. 2313–2366.
- [4] Erik Andreassen, Anders Clausen, Mattias Schevenels, Boyan S. Lazarov, and Ole Sigmund. “Efficient topology optimization in MATLAB using 88 lines of code”. In: *Struct Multidiscip Optim* 43.1 (Jan. 2011), pp. 1–16. ISSN: 1615-1488.
- [5] Martin P Bendsøe and Ole Sigmund. *Topology optimization: theory, methods and applications*. Springer-Verlag Berlin Heidelberg, 2003.
- [6] M. Boissier, G. Allaire, and C. Tournier. “Additive manufacturing scanning paths optimization using shape optimization tools”. In: *Structural and Multidisciplinary Optimization* 61.6 (June 2020), pp. 2437–2466. ISSN: 1615-1488.
- [7] Tyler E. Bruns and Daniel A. Tortorelli. “Topology optimization of non-linear elastic structures and compliant mechanisms”. In: *Comput Method Appl M* 190.26 (2001), pp. 3443–3459. ISSN: 0045-7825.
- [8] Peter Bullen. *Handbook Of Means And Their Inequalities*. Springer, Dordrecht, Jan. 2014.
- [9] Michael Cloots, Livia Zumofen, Adriaan Spierings, Andreas Kirchheim, and Konrad Wegener. “Approaches to minimize overhang angles of SLM parts”. In: *Rapid Prototyping Journal* 23 (Mar. 2017), pp. 362–369.
- [10] Robert D. Cook, David S. Malkus, Michael E. Plesha, and Robert J. Witt. *Concepts and Applications of Finite Element Analysis*. 4th ed. Wiley, Oct. 2001. ISBN: 0471356050.
- [11] Tom Craeghs, Florian Bechmann, Sebastian Berumen, and Jean-Pierre Kruth. “Feedback control of Layerwise Laser Melting using optical sensors”. In: *Physics Procedia* 5 (2010). Laser Assisted Net Shape Engineering 6, Proceedings of the LANE 2010, Part 2, pp. 505–514. ISSN: 1875-3892.



- [12] Tom Craeghs, Florian Bechmann, Sebastian Berumen, and Jean-Pierre Kruth. “Feedback control of Layerwise Laser Melting using optical sensors”. In: *Physics Procedia* 5 (2010). Laser Assisted Net Shape Engineering (LANE) 6, pp. 505–514. ISSN: 1875-3892.
- [13] Erik Denlinger, Jeff Irwin, and Pan Michaleris. “Thermomechanical Modeling of Additive Manufacturing Large Parts”. In: *Journal of Manufacturing Science and Engineering* 136 (Oct. 2014), p. 061007.
- [14] Andrew T. Gaynor and James K. Guest. “Topology optimization considering overhang constraints: Eliminating sacrificial support material in additive manufacturing through design”. In: *Struct Multidiscip Optim* 54.5 (Nov. 2016), pp. 1157–1172. ISSN: 1615-1488.
- [15] Frank P. Incropera and David P. DeWitt. *Fundamentals of Heat and Mass Transfer*. 4th Edition. New York City, New York: John Wiley Sons, Inc., 1996.
- [16] Darya Kastsian and Daniel Reznik. “Reduction of local overheating in selective laser melting”. In: *In Proceedings of Simulation of Additive Manufacturing (SIM-AM), Munich, Germany*. Oct. 2017.
- [17] Nils Keller and Vasily Ploshikhin. “New method for fast predictions of residual stress and distortion of AM parts”. In: *Solid Freeform Fabrication Symposium, Austin, Texas*. 2014, pp. 1229–1237.
- [18] J. Kranz, D. Herzog, and C. Emmelmann. “Design guidelines for laser additive manufacturing of lightweight structures in TiAl6V4”. In: *J Laser Appl* 27.S1 (2015), p. 4001.
- [19] Yu-Hsin Kuo, Chih-Chun Cheng, Yang-Shan Lin, and Cheng-Hung San. “Support structure design in additive manufacturing based on topology optimization”. In: *Struct Multidiscip Optim* 57.1 (2018), pp. 183–195.
- [20] Matthijs Langelaar. “An additive manufacturing filter for topology optimization of print-ready designs”. In: *Struct Multidiscip Optim* 55.3 (Mar. 2017), pp. 871–883. ISSN: 1615-1488.
- [21] Matthijs Langelaar. “Topology optimization of 3D self-supporting structures for additive manufacturing”. In: *Additive Manufacturing* 12 (2016), pp. 60–70. ISSN: 2214-8604.
- [22] Boyan Lazarov and Fengwen Wang. “Maximum length scale in density based topology optimization”. In: *Computer Methods in Applied Mechanics and Engineering* 318 (Feb. 2017).
- [23] Boyan Stefanov Lazarov, Fengwen Wang, and Ole Sigmund. “Length scale and manufacturability in density-based topology optimization”. English. In: *Archive of Applied Mechanics* 86.1-2 (2016), pp. 189–218. ISSN: 0939-1533.
- [24] Chau Le, Julian Norato, Tyler Bruns, Christopher Ha, and Daniel Tortorelli. “Stress-based topology optimization for continua”. In: *Struct Multidiscip Optim* 41.4 (Apr. 2010), pp. 605–620. ISSN: 1615-1488.
- [25] Richard Leach and Simone Carmignato. *Precision Metal Additive Manufacturing*. CRC Press, Sept. 2020. ISBN: 113834771X.

- [26] M. Leary, Matthew McMillan, D.P. Shidid, Hans VanToor, Maciej Mazur, and Milan Brandt. “Numerical methods to predict overheating in SLM lattice structures”. In: Jan. 2014, pp. 895–902.
- [27] Jikai Liu, Andrew T. Gaynor, Shikui Chen, Zhan Kang, Krishnan Suresh, Akihiro Takezawa, Lei Li, Junji Kato, Jinyuan Tang, Charlie C. L. Wang, Lin Cheng, Xuan Liang, and Albert. C. To. “Current and future trends in topology optimization for additive manufacturing”. In: *Struct Multidiscip Optim* 57.6 (June 2018), pp. 2457–2483. ISSN: 1615-1488.
- [28] Kai Liu and Andrés Tovar. “An efficient 3D topology optimization code written in Matlab”. In: *Structural and Multidisciplinary Optimization* 50.6 (Dec. 2014), pp. 1175–1196. ISSN: 1615-1488.
- [29] Raya Mertens, Stijn Clijsters, Karolien Kempen, and Jean-Pierre Kruth. “Optimization of Scan Strategies in Selective Laser Melting of Aluminum Parts With Down-facing Areas”. In: *J Manuf Sci E-T ASME* 136.6 (Oct. 2014), pp. 61012–61017. ISSN: 1087-1357.
- [30] T.P. Moran, D.H. Warner, and N. Phan. “Scan-by-scan part-scale thermal modelling for defect prediction in metal additive manufacturing”. In: *Additive Manufacturing* 37 (2021), p. 101667. ISSN: 2214-8604.
- [31] L.A. Parry, I.A. Ashcroft, and R.D. Wildman. “Geometrical effects on residual stress in selective laser melting”. In: *Additive Manufacturing* 25 (2019), pp. 166–175. ISSN: 2214-8604.
- [32] Shubham Patel, James Mekavibul, Jami Park, Anchit Kolla, Ryan French, Zachary Kersey, and Gregory Lewin. “Using Machine Learning to Analyze Image Data from Advanced Manufacturing Processes”. In: *2019 Systems and Information Engineering Design Symposium (SIEDS), Charlottesville, VA, USA* (Apr. 2019), pp. 1–5.
- [33] Hao Peng, Morteza Ghasri-Khouzani, Shan Gong, Ross Attardo, Pierre Ostiguy, Bernice Aboud Gatrell, Joseph Budzinski, Charles Tomonto, Joel Neidig, M. Ravi Shankar, Richard Billo, David B. Go, and David Hoelzle. “Fast prediction of thermal distortion in metal powder bed fusion additive manufacturing: Part 1, a thermal circuit network model”. In: *Additive Manufacturing* 22 (2018), pp. 852–868. ISSN: 2214-8604.
- [34] Xiaoping Qian and Ole Sigmund. “Topological design of electromechanical actuators with robustness toward over- and under-etching”. In: *Computer Methods in Applied Mechanics and Engineering* 253 (2013), pp. 237–251. ISSN: 0045-7825.
- [35] Rajit Ranjan, Can Ayas, Matthijs Langelaar, and Fred van Keulen. “Fast Detection of Heat Accumulation in Powder Bed Fusion Using Computationally Efficient Thermal Models”. In: *Materials* 13.20 (2020), p. 4576.
- [36] Marleen Rombouts, L. Froyen, A. Gusarov, El Hassane Bentefour, and Christ Glorieux. “Photopyroelectric measurement of thermal conductivity of metallic powders”. In: *Journal of Applied Physics* 97 (Dec. 2004), p. 24905.

- [37] W. J. Sames, F. A. List, S. Pannala, R. R. Dehoff, and S. S. Babu. “The metallurgy and processing science of metal additive manufacturing”. In: *Int Mater Rev* 61.5 (Mar. 2016), pp. 1–46.
- [38] Ole Sigmund. “Morphology-based black and white filters for topology optimization”. In: *Struct Multidiscip Optim* 33.4 (Apr. 2007), pp. 401–424. ISSN: 1615-1488.
- [39] Ole Sigmund. “Morphology-based black and white filters for topology optimization”. English. In: *Structural and Multidisciplinary Optimization* 33.4-5 (2007), pp. 401–424. ISSN: 1615-147X.
- [40] Mirko Sinico, Rajit Ranjan, Mandanà Moshiri, Can Ayas, Matthijs Langelaar, Ann Witvrouw, F Keulen, and Wim Dewulf. “A mold insert case study on topology optimized design for additive manufacturing”. In: *30th Annual International Solid Freeform Fabrication Symposium, SFF* (2019).
- [41] Krister Svanberg. “The method of moving asymptotes - A new method for structural optimization”. In: *International Journal for Numerical Methods in Engineering* 24 (Feb. 1987), pp. 359–373.
- [42] Lore Thijs, Frederik Verhaeghe, Tom Craeghs, Jan Van Humbeeck, and Jean-Pierre Kruth. “A study of the microstructural evolution during selective laser melting of Ti-6Al-4V”. In: *Acta Mater* 58.9 (2010), pp. 3303–3312. ISSN: 1359-6454.
- [43] J. A. Van Toor. “A Knowledge Based System to Support Design for Selective Laser Melting. MSc thesis, TU Delft”. In: (2014).
- [44] Emiel Van de Ven, Robert Maas, Can Ayas, Matthijs Langelaar, and Fred Van Keulen. “Continuous front propagation-based overhang control for topology optimization with additive manufacturing”. In: *Struct Multidiscip Optim* 57.5 (May 2018), pp. 2075–2091. ISSN: 1615-1488.
- [45] Di Wang, Yongqiang Yang, Ziheng Yi, and Xubin Su. “Research on the fabricating quality optimization of the overhanging surface in SLM process”. In: *Int J Adv Manuf Tech* 65.9 (Apr. 2013), pp. 1471–1484. ISSN: 1433-3015.
- [46] Fengwen Wang, Boyan Lazarov, and Ole Sigmund. “On projection methods, convergence and robust formulations in topology optimization”. In: *Structural and Multidisciplinary Optimization* 43 (June 2011), pp. 767–784.
- [47] Raymond A Wildman and Andrew T Gaynor. *Topology Optimization for Reducing Additive Manufacturing Processing Distortions*. Tech. rep. Weapons and Materials Research Directorate, US Army Research Laboratory., 2017.
- [48] Wentao Yan, Yan Lu, Kevontrez Jones, Zhuo Yang, Jason Fox, Paul Witherell, Gregory Wagner, and Wing Kam Liu. “Data-driven characterization of thermal models for powder-bed-fusion additive manufacturing”. In: *Additive Manufacturing* 36 (2020), p. 101503. ISSN: 2214-8604.
- [49] Y. Yang, M.F. Knol, F. van Keulen, and C. Ayas. “A semi-analytical thermal modelling approach for selective laser melting”. In: *Additive Manufacturing* 21 (2018), pp. 284–297. ISSN: 2214-8604.

- [50] Michael F Zaeh and Gregor Branner. “Investigations on residual stresses and deformations in selective laser melting”. In: *Production Engineering* 4.1 (Feb. 2010), pp. 35–45.
- [51] K. Zeng, D. Pal, H. J. Gong, N. Patil, and B. Stucker. “Comparison of 3DSIM thermal modelling of selective laser melting using new dynamic meshing method to ANSYS”. In: *Materials Science and Technology* 31.8 (2015), pp. 945–956.
- [52] Mingdong Zhou, Yichang Liu, and Zhongqin Lin. “Topology optimization of thermal conductive support structures for laser additive manufacturing”. In: *Computer Methods in Applied Mechanics and Engineering* 353 (2019), pp. 24–43. ISSN: 0045-7825.

# 5

## A 3D TOPOLOGY OPTIMIZATION METHOD AND EXPERIMENTAL VALIDATION FOR CONTROLLING LOCAL OVERHEATING IN AM

*Overheating is a major issue especially in metal Additive Manufacturing (AM) processes, leading to poor surface quality, lack of dimensional precision, inferior performance and/or build failures. A 3D density-based topology optimization (TO) method is presented which addresses the issue of local overheating during metal AM. This is achieved by integrating a simplified AM thermal model and a thermal constraint within the optimization loop. The simplified model, recently presented in literature, offers significant computational gains while preserving the ability of overheating detection. The novel thermal constraint ensures that the overheating risk of optimized designs is reduced. This is fundamentally different from commonly used geometry-based TO methods which impose a geometric constraint on overhangs. Instead, the proposed approach takes the process physics into account. The proposed method is validated via an experimental comparative study. Optical tomography (OT) is used for in-situ monitoring of process conditions during fabrication and obtained data is used for evaluation of overheating tendencies. The novel TO method is compared with two other methods: standard TO and TO with geometric overhang control. The experimental data reveals that the novel physics-based TO design experienced less overheating during the build as compared to the two classical designs. A study further investigated the correlation between overheating observed by high OT values and the defect of porosity. It shows that overheated regions indeed show higher defect of porosity. This suggests that geometry-based guidelines, although enhance printability, may not be*

---

Parts of this chapter have been published in [Overheating control in additive manufacturing using a 3D topology optimization method and experimental validation](#), *Additive Manufacturing*, 2023

*sufficient for eliminating overheating issues and related defects. Instead, the proposed physics-based method is able to deliver efficient designs with reduced risk of overheating.*

## 5.1. INTRODUCTION

The unprecedented design freedom offered by additive manufacturing (AM) is ideal for fabricating performance optimized metal parts that are typically highly complex in geometry. Therefore AM has found extensive application in various industrial domains such as automotive, aerospace, sports and biomedical [20]. Although beneficial, the increased design freedom also makes the design process challenging and requires reconsideration of traditional design practices. Moreover, AM parts are typically utilized in hi-tech industry where the design process is inherently complex. This aspect along with the desire to capitalize on the increased design freedom, makes it advantageous to use advanced computational design tools. Topology Optimization (TO) is one such computational design method which aims to find the optimal material layout for a given design objective [5]. It is especially efficient for designing AM parts as it can address both functionality and manufacturability in a mathematically rigorous setting. Due to this, the potential of combining TO and AM has been recognized by both academia and industry [21].

Although AM processes offer several key advantages over conventional methods, there are certain manufacturing constraints which, if not addressed during the design stage, could lead to inferior part quality or build failure [20]. One such constraint which has been extensively studied within TO frameworks is that of overhang avoidance. Design rules associated with overhang angles, defined as the angle between part surface and horizontal base plate, have been empirically developed [24]. It is recommended that the overhang angle should be higher than a certain critical value  $\theta^{cr}$ , typically ranging between  $40^\circ$ – $50^\circ$  [11, 40]. Features with acute overhangs are difficult to fabricate for both polymer and metal based AM processes, although the fundamental causes behind the difficulty of their fabrication vary. For extrusion based polymer AM, such as fused deposition modelling (FDM), the overhanging regions lack sufficient supports against gravity. On the other hand, in powder based metal AM processes, such as Laser Powder Bed Fusion (L-PBF), loose powder beneath an overhanging feature provides structural support but the low and non-uniform thermal conductivity of powder does not allow for proper heat evacuation [24]. This leads to severe local overheating which manifests itself in form of defects, *e.g.* dross [8], inferior mechanical properties [25], increased surface roughness [8] and/or build failure [16]. In this paper, we aim to investigate the issue of local overheating and hence, in the remainder, we focus on the L-PBF process where this is a critical issue. Note that in certain cases, for example [25], the heat accumulation over the layers may have a positive effect such as in-situ heat treatment improving the properties. However, generally local overheating is associated with increased risk of defects and therefore our focus is to reduce the amount of overheating. In this context, recent advancements in L-PBF machines allows for in-situ control of laser power reducing the risk of overheating. However, this feature is currently under development and not a default option. Hence, part geometries with low overheating risks are still highly desirable.

In the context of TO, a significant number of studies have been presented in literature which aim to integrate overhang avoidance within TO algorithms, see, for example, Gaynor and Guest [14], Qian [29], Langelaar [19, 18], and van de Ven et al. [37]. These

methods prohibit or penalize overhanging features less than the critical overhang angle  $\theta^{CT}$  during the optimization process, improving the manufacturability of the optimized designs. For a detailed review of these and related methods, see Liu et al. [21]. These formulations, referred to as geometry-based TO, use overhang detection for avoiding acute overhangs under the assumption that geometric overhang control ensures printability. However, recent experimental and numerical findings indicate that overheating can occur even after avoiding acute overhangs. For example, Adam and Zimmer [1] fabricated a funnel shaped specimen in which overheating was observed in the form of discoloration. Another specimen by Patel et al. [28] showed overheating induced dross. It is noteworthy that specimens in both cases were free from acute overhangs. A recent numerical study by Ranjan et al. [31] demonstrated that overheating behaviour associated with the same overhang angle can vary significantly, depending on local thermal conditions. These findings suggest that the relationship between overhang and overheating is not straightforward. Hence, a TO method which focuses directly on the issue of overheating will offer significant advantages over geometry-based TO methods.

A detailed thermal L-PBF process model is required to capture the overheating issues in a part during the additive fabrication process. It is well known that L-PBF process models are computationally expensive (see, for example, Denlinger, Irwin, and Michaleris [12] and Keller and Ploshikhin [17]). Moreover, integration of such elaborate models within TO is especially cumbersome, as the simulation should be repeated for each design iteration, and design sensitivities must be calculated in addition. Therefore, developing simplified AM models which can capture essential aspects of the thermal evolution is of paramount importance, making it possible to integrate such models with TO. This leads to the so called physics-based TO methods which incorporate to some extent the physics of the AM process. Research presented by Amir and Mass [4] and Allaire et al. [3] are examples of such approaches, where self-weight of the manufactured part is considered in a layer-by-layer manner, mimicking the real process. In the context of overheating control, Zhou, Liu, and Lin [47] integrated simplified thermal AM simulation with density-based TO for finding optimal supports, while keeping the part design fixed. However, even with several simplifications, the computational cost remained significantly high, even for a 2D implementation. More recently, Boissier, Allaire, and Tournier [6] coupled a simplified thermal model with 2D level-set TO where scanning path optimization is performed. Although it provides insights about influence of scanning paths on temperatures, it is expected that computational cost remains high. In this regard, the simplified model presented by Ranjan et al. [31] which used a localized *slab based* steady-state thermal analysis is suitable for detecting overheating zones (hotspots) at relatively low computational cost. Therefore, it has been integrated with density based TO and the concept has been investigated in Ranjan et al. [30], where it is referred to as hotspot TO. The aim of the present paper is to experimentally compare the overheating tendencies associated with the hotspot TO design against those observed for the designs obtained using other TO strategies. In this context, the ‘AM-filter’ method presented by Langelaar [19, 18], which is an example of geometry-based TO, and standard TO without any AM constraint are considered for experimental comparison. For the experimental investigation, optical tomography is used to monitor manufacturing conditions during



fabrication.

Optical tomography (OT) is an in-situ technique to monitor the L-PBF process and detect overheating resulting from the heat accumulation. It is a camera-based measurement technique for the observation of the thermal radiation over the process plane while the laser beam scans the powder bed surface [44]. Deviations in the measured signals can be derived from the OT images as implications of process anomalies where internal defects can be formed in the manufactured products [26, 42]. The detection of hotspots is of particular interest in this work for the comparison of different TO strategies for avoiding overheating. Additionally, to the best of our knowledge, this is the first research study where a physics-based TO method is experimentally validated using the OT technique.

The remainder of the article is organized as follows. The physics-based hotspot detection method and formulation of overheating constraint are presented in Section 5.2. The simplified AM model which was previously presented in Ranjan et al. [31] and Ranjan et al. [30] is briefly summarized for completeness. Different TO strategies and the test problem considered for comparing optimized designs are presented in Section 5.3. The details associated with the experimental procedure are given in Section 5.4, while the comparative results are presented in Section 5.5. Finally, discussion and conclusions are presented in Section 5.6 and 5.7, respectively.

## 5.2. HOTSPOT DETECTION

Here, we first summarize our simplified L-PBF process model for detecting heat accumulation. The model is taken from our previous study [31] where several simplifications associated with thermal modelling of the L-PBF process were investigated in context of detecting overheating. It was established that hotspot detection is possible by computationally inexpensive steady-state local thermal analyses near the heat source [31]. Although the thermal fields in an actual L-PBF process are more accurately predicted with a transient thermal model, their integration with design optimization methods is highly cumbersome as shown by [38], making it computationally intractable for real-size 3D parts. Consequently, the steady-state model which correctly identifies overheating zones is a perfect candidate for integration with topology optimization.

The part shown in Figure 5.1a is used to demonstrate the simplified L-PBF thermal model. This design results from an AM-filter geometry-based TO method [18]. We purposefully choose this design for explaining the simplified model as it has several features with overhang angles close to the threshold value of  $\theta^{\text{cr}} = 45^\circ$ . Therefore, it enables a close examination whether the same overhang angle leads to similar overheating behaviour. Figure 5.1c–f show subsequent stages of L-PBF fabrication where the part is divided into a set of so-called *slabs* represented by yellow colored bounding boxes with *slab thickness*  $s$ . These slabs are defined such that subsequent slabs largely overlap, compare for example, Figure 5.1c and d. The section of the part inside a slab is subjected to a steady-state thermal analysis where the top surface is subjected to a heat flux  $\mathbf{q}_0$  (in-

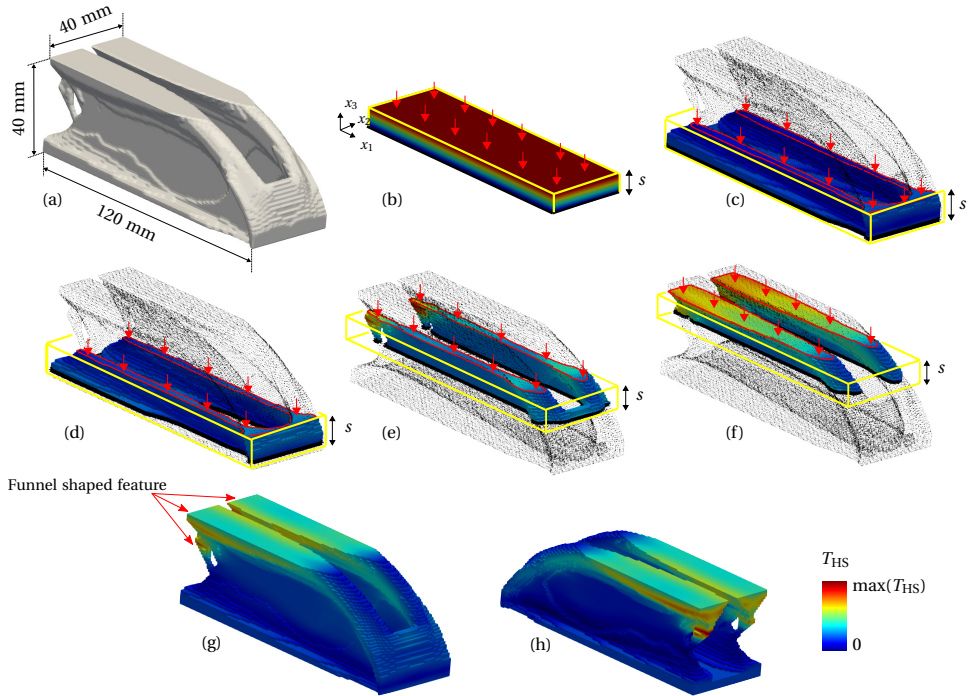


Figure 5.1: Simplified AM model for detecting heat accumulation using slabs [31]. (a) Part considered for explaining the method. (b) A solid slab used for obtaining normalized temperatures is shown with corresponding temperature gradients. (c)–(f) Subsections of the geometry with contour levels of temperature attained with a steady-state thermal analysis. For each slab heat flux is applied at its top (indicated by arrows) while its bottom acts as a heat sink (indicated by black boundaries). Part-powder interfaces are assumed to be insulated. The maximum temperature for each material point is recorded and the resulting maximum temperature field is referred to as hotspot field  $T_{HS}$  which is shown from front (g) and back (h). The funnel shaped features which lead to high normalized temperatures are indicated with red arrows in (g).

icated by red arrows) and the bottom of the slab acts as a heat sink (indicated by black boundary). These boundary conditions are inspired by the L-PBF process where heat is deposited from the top layer using a laser, while previously deposited layers and base-plate act as a heat sink. A list of simplifications which are assumed in addition to the use of localized steady-state analysis is given below:

- Laser scanning path is not considered for computational efficiency, following layer-by-layer L-PBF modeling approaches [45, 31].
- Thermal properties are assumed to be constant and hence independent of temperatures.
- Part-powder interface is assumed to be insulated as effective conductivity for powder layer is reported to be around only 1% of bulk conductivity [33, 32].
- Phase transformations are not considered.
- Convective and radiative heat transfer from the top surface are not considered.

In order to verify the usefulness of the simplified L-PBF model, a brief comparison is presented between thermal predictions of the simplified model and a higher-fidelity transient L-PBF simulation later in Section 5.3.2. It shows that a model with these simplifications can still correctly predict which design features are at the risk of overheating. Additionally, a deeper and quantitative study of various modelling simplifications is presented in [31] where detailed rationalizations are provided about each of the above listed simplification in the context of overheating detection.

Under these simplifications, the temperatures are calculated using the 3D steady-state heat equation [15]. The partial differential equation (PDE) is solved numerically using finite element analysis (FEA) and resulting temperature fields are shown in Figure 5.1c–f. The details on the finite element mesh for solving the thermal problems are given in the next section. Due to the overlapping definition of slabs, every material point is analyzed multiple times within different slabs, leading to multiple temperature values for each point. These temperatures depend on the local effective conductivity of the neighbourhood and the maximum value attained for each point is attributed to the overheating risk associated with that point. Due to the considered boundary conditions, the maximum temperature for the steady-state thermal field always occurs at the topmost layer of each slab. Therefore, temperatures found at the topmost layer from each slab are assembled into a *hotspot field* for the given geometry. The hotspot field for the considered geometry is shown in Figure 5.1g and h as seen from the front and back, respectively. Note that all thermal fields are shown with a common scale ranging from sink temperature  $T_0$  to the maximum value observed across all slabs.

It is noteworthy that the funnel like features, marked with arrows in Figure 5.1g, lead to high temperatures even though they comply with the overhang design rule, yet their thermal response is not uniform. A more quantitative analysis of the found hotspot field is given later in Section 5.3.2, where hotspot fields for all topology optimized designs are

compared.

As the above summarized L-PBF model is a simplified steady-state representation of the thermal interactions during the process, the resulting predictions do not quantitatively describe the actual temperature field during the process. Instead, they simply give a qualitative indication about the overheating risk associated with different design features [31]. In order to formulate an overheating constraint in TO, a threshold value needs to be specified. Therefore, a normalization step is introduced where temperatures from each slab are normalized against those found using a solid slab containing no void with the same thermal properties and subjected to the same thermal boundary conditions. An example of such temperature field is shown in Figure 5.1b. A solid slab with no void represents the ideal situation of unobstructed heat flow. Thus, the hotspot temperatures normalized against such a solid slab quantify the heat accumulation tendencies. This implies that the normalized temperature is dimensionless and values greater than 1 indicate overheating with increasing severity. Moreover, the normalized temperature values are independent of the input heat flux  $\mathbf{q}_0$ , the sink temperature and the thermal conductivity as the solid slab used for normalization has identical thermal properties and is subjected to the same thermal boundary conditions.

5

The slab thickness parameter represents the *thermal interaction length*  $\kappa$  i.e., the distance up to which features influence the heat flow at the newly deposited layer. For L-PBF, thermal interaction length is significantly higher than the layer thickness [27]. From this observation follows that subsequent slabs overlap each other considerably. The slab thickness value depends on material and process parameters. For example, a material with lower thermal diffusivity is better modelled with thin slabs as compared to one with higher thermal diffusivity. Alternatively, a slow moving laser would allow for more thermal interaction time and hence, larger interaction distances. In [31], using an analytical solution to the heat equation, it was shown that thermal interaction length can be estimated as  $\kappa = \sqrt{\alpha t_h}$ , where  $\alpha$  is the thermal diffusivity and  $t_h$  is the heating time for a given layer. The heating time for a layer further depends on a number of factors, e.g., layer area, laser speed, number of lasers etc. More recently in [30], this concept was used for determining slab thickness in context of TO and a detailed analysis was provided on the influence of this parameter on TO results. In this paper, we used the same concept to determine slab thickness and the methodology is summarized below for the sake of completeness.

First, based on the building direction, maximum layer area  $A$  is determined for the design domain which is then used for calculating heating time as  $t_h = A/hv$ , where  $h$  is hatch spacing and  $v$  is scan velocity. The parameters used in this study are reported later in Section 5.4. Next, based on the concept of thermal characteristic length, slab thickness is calculated as  $\kappa = \sqrt{\alpha t_h}$ . The thermal diffusivity  $\alpha$  is calculated using thermal properties reported at melting point temperatures [2]. This is motivated by the findings of [43] which showed that using an  $\alpha$  value close to the melting point gives the best thermal predictions when using temperature independent thermal properties.

### 5.3. TOPOLOGY OPTIMIZATION

In this section, first the test problem considered for comparing different TO strategies is introduced in Section 5.3.1. The mathematical formulation for TO is also presented here and different TO algorithms considered in this paper are described. The physics-based TO is explained in more detail than the other two more established approaches. Next, the TO results for the test problem are presented in Section 5.3.2.

#### 5.3.1. TEST PROBLEM AND TO APPROACHES

In this paper, we consider topology optimized designs using three different TO approaches, *i.e.*, standard TO, hotspot TO (physics-based TO) and AM-filter TO (geometry-based TO). As the main focus here is to analyze the overheating tendencies of different designs during L-PBF fabrication, the discussion is restricted to the commonly used linear elastic compliance minimization problem with a volume constraint which is a structural optimization problem.

The standard density based TO approach using SIMP interpolation [5] scheme is applied as:

$$\min_{\boldsymbol{\rho}} : C(\boldsymbol{\rho}) = \mathbf{u}^T \mathbf{K} \mathbf{u}, \quad (5.1a)$$

$$\text{subject to} \quad (5.1b)$$

$$\frac{V(\boldsymbol{\rho})}{V_0} - f_o \leq 0, \quad (5.1c)$$

$$\mathbf{K} \mathbf{u} = \mathbf{f}, \quad (5.1d)$$

$$\mathbf{0} \leq \boldsymbol{\rho} \leq \mathbf{1}. \quad (5.1e)$$

Here,  $C$  is the compliance,  $\mathbf{u}$  and  $\mathbf{f}$  are the arrays containing the nodal displacements and forces, respectively,  $\mathbf{K}$  is the global stiffness matrix,  $\boldsymbol{\rho}$  is the array of design variables assigned to FE elements,  $V(\boldsymbol{\rho})$  and  $V_0$  are the total material volume and design domain volume, respectively, and  $f_o$  is the maximum volume fraction allowed in the design domain. The optimization problem is initiated with uniform density of  $\boldsymbol{\rho} = f_o$ . The density filtering scheme presented by [7] is used with filter radius  $R = 2$  mm in order to control minimum feature size and avoid checkerboarding. The Matlab 3D TO implementation presented by [22] is used for solving this optimization problem while the method of moving asymptotes (MMA) is used as the optimizer [36].

A cantilever loading case is considered with a design domain with dimensions  $120 \times 40 \times 40$  mm as shown in Figure 5.2. Here, a 40 N load is uniformly distributed over the lower front edge while the back face ( $x = 0$ ) remains fixed. The domain is discretized using isoparametric cubic 8-node finite elements with tri-linear shape functions with 120, 40 and 40 elements in  $x$ ,  $y$  and  $z$  directions, respectively. All common TO parameters are listed in Table 5.1. Note that Figure 5.2 only presents the design domain and the resulting optimized cantilever beams are presented later in Section 5.3.2.

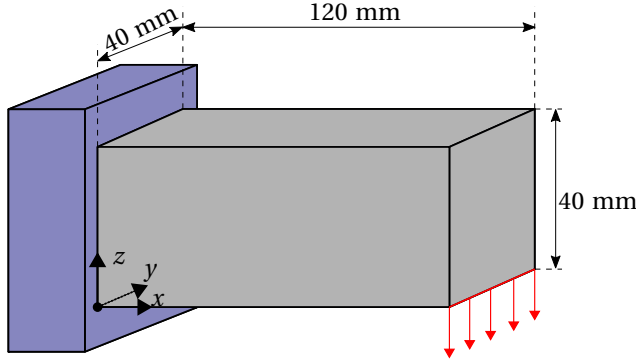


Figure 5.2: The test problem used for creating optimized designs using different TO approaches.

5

In case of the physics-based TO, an additional constraint is formulated which is referred to as the hotspot constraint. It is added in the standard optimization problem given in Eqs. (5.1) and its formulation is explained below. During physics-based TO, each intermediate design is subjected to the hotspot analysis described in Section 5.2. The structured mesh used for solving the structural problem is also used for the thermal analysis. All normalized temperatures from the hotspot analysis are stored in an array denoted as  $\hat{\mathbf{T}}$ . In order to avoid local overheating, it is required that the normalized temperatures should not exceed a critical value  $\hat{T}^{cr}$ , *i.e.*  $\max(\hat{\mathbf{T}}) \leq \hat{T}^{cr}$ . Note that the max operator is non-differentiable whereas a smooth operator is required for calculating the sensitivities needed in gradient based TO. Therefore, a P-mean aggregation is performed over the array  $\hat{\mathbf{T}}$  to define the hotspot constraint:

$$g = \left[ \frac{1}{n \hat{T}^{cr}} \sum_{i=1}^n \hat{T}_i^P \right]^{\frac{1}{P}} - 1 \leq 0. \quad (5.2)$$

Here,  $\hat{T}_i$  is the  $i^{\text{th}}$  member of array  $\hat{\mathbf{T}}$ ,  $P$  is the exponent used for defining the P-mean and  $n$  is the total number of nodes considered. Recall that the maximum temperature always occurs at the topmost layer of each slab, hence, only top nodes from each slab are considered in the aggregation. The sensitivity derivation for the hotspot constraint is presented in Appendix C.

For determining the critical normalized temperatures  $\hat{T}^{cr}$ , a calibration step was proposed in [30] which is used here. Typically, a critical overhang angle for a given L-PBF system is determined by experimental studies [11, 40]. Here, an L-PBF system refers to a combination of material and process parameters and such empirical studies basically signify that the thermal conditions while manufacturing overhangs with an overhang angle  $\theta < \theta^{cr}$  can lead to fabrication difficulties. In order to determine the critical overhang angle for a system, it is a common practice to use a 2.5D wedge shape where a 2D wedge with a certain overhang angle is simply extruded in the out-of-plane direction [11, 40].

Table 5.1: Topology optimization parameters

Poisson's ratio	0.3
SIMP penalization	3.0
Volume fraction $f_o$	0.3
P-mean exponent $P$	15
Slab thickness $s$ (mm)	12
No. of iterations	200

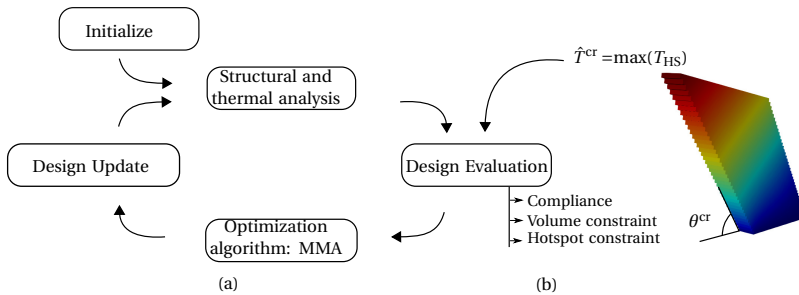


Figure 5.3: Schematic illustrating the hotspot TO framework and critical temperature calibration. (a) The steps associated with the TO algorithm with additional hotspot analysis and constraint. (b) 2.5D wedge geometries are used to determine associated  $\hat{T}^{cr}$  with a particular  $\theta^{cr}$ .

Following a similar approach for numerically determining  $\hat{T}^{cr}$ , the calibration step presented for 2D wedges in [30] can be directly applied to 3D. Wedge-shaped geometries, see Figure 5.3a, with varying wedge inclinations were subjected to hotspot analysis and corresponding normalized hotspot temperatures were used as  $\hat{T}^{cr}$ . It is worth emphasizing that this does not correspond to geometrically prohibiting overhanging features less than a specific overhang angle, as it is done in the geometry-based approaches [19]. Instead, the *thermal behavior* associated with an overhanging feature is used to set the hotspot temperature threshold. A schematic is shown in Figure 5.3 where the calibration process is pictorially presented in (a) while (b) shows how the hotspot constraint is integrated with the TO process. Using this calibration step,  $\hat{T}^{cr}$  for three different values of  $\theta^{cr}$ , *i.e.*,  $40^\circ$ ,  $45^\circ$  and  $50^\circ$ , are found to be 2.5, 2.1 and 1.8, respectively. These values are later used in Section 5.3.2.

Next, it was highlighted in [30] that when a hotspot constraint is implemented in combination with standard TO, this may result in designs with significant amount of intermediate densities. A design with high fractions of intermediate densities becomes problematic for fabrication [5]. In order to solve this issue, the robust formulation presented by [41, 35] was used with  $R = 5$  mm. Slab thickness  $s = 12$  mm is used for all the cases, calculated in accordance with the concept of thermal characteristic length using the constant thermal properties of Inconel 718 at melting point.

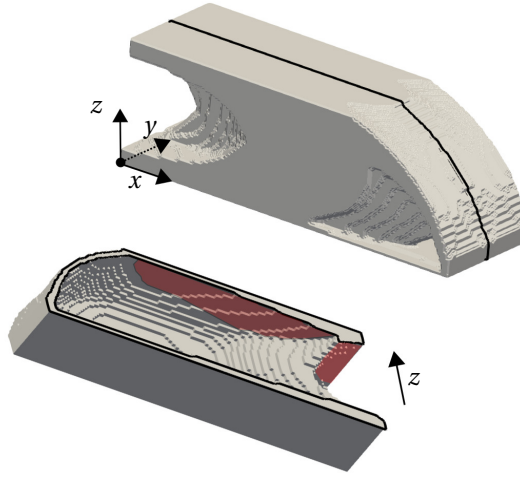


Figure 5.4: The optimized beam using standard TO outlined by Eqs. (5.1) with  $C = C_{\text{ref}}$ . The highlighted red region shows significantly long overhangs that are present in this design.

Lastly, the AM-filter TO presented by [19] is considered as an example of geometry-based overhang control TO method. The method basically imposes a progressive layer-wise filtering scheme during TO iterations which results in fully self-supported optimized designs. In this regard, the basic TO problem remains the same as outlined by Eqs. (5.1) while one additional filtering step is added. For the details of the mathematical formulation of AM-filter, readers are referred to [18, 19].

### 5.3.2. OPTIMIZED TO DESIGNS AND HOTSPOT FIELDS

In this subsection, all the topology optimized designs which are subsequently fabricated and monitored using OT are presented. The density fields obtained from TO are post-processed for visualization by extracting iso-surfaces with a threshold value of 0.5. As the standard TO result is used as a benchmark for comparing compliances of the optimized designs, it is presented first with compliance referred to as  $C_{\text{ref}}$ . A comparison of hotspot fields for all TO designs is presented in Section 5.3.2.

#### STANDARD TO

Figure 5.4 shows the optimized beam while a section view with a sectioning plane at  $y = 20$  mm is also given for clear visualization of inner features. The build direction ( $z$ ) is marked and it is evident that there is a long overhanging feature near the top region of the design (marked in red). It is expected that fabrication of such a long overhang, without any supports, will be extremely problematic due to excessive heat accumulation.



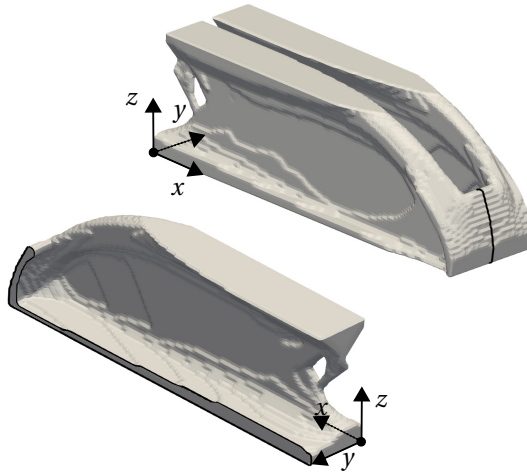


Figure 5.5: The optimized design found using AM-filter [19] with  $C = 0.92C_{\text{ref}}$ . It is evident the the method ensures manufacturability by avoiding long overhangs, present in the standard TO design.

#### GEOMETRY-BASED TO FOR OVERHANG AVOIDANCE

The test problem given in Section 5.3.1 was optimized in the original paper by [19] and the resulting design is presented in Figure 5.5. In order to clearly visualize the optimized design, a section view at  $y = 20$  mm is also presented. The method uses a structured mesh with cubic elements leading to  $\theta^{\text{cr}} = 45^\circ$ . It is evident that the AM-filter design is free from the extensive overhangs present in the standard TO design and it is expected that it can be realized without the need of any additional supports. Typically, inclusion of additional process constraints into the TO process leads to reduced performance, *i.e.* higher compliance (for this case). This is seen as a compromise between manufacturability and design freedom. Between the standard and AM-filter TO designs, remarkably the latter slightly outperforms the former. This has also been observed previously [19] and is caused by potentially finding a better local optimum in combination with a reduction of intermediate density elements at the structural boundaries, due to the applied filter. Lastly, as highlighted in Section 5.2, this design contains several funnel shaped features, where the overhang angle is close to the limiting value, *i.e.*  $\theta^{\text{cr}} = 45^\circ$ .

#### HOTSPOT TO

For the TO with hotspot constraint, three different values of  $\hat{T}^{\text{cr}}$  are used based on three values of  $\theta^{\text{cr}}$ , *i.e.* ,  $40^\circ$ ,  $45^\circ$  and  $50^\circ$ . As presented in Section 5.3.1,  $\hat{T}^{\text{cr}}$  for  $40^\circ$ ,  $45^\circ$  and  $50^\circ$  are found to be 2.5, 2.1 and 1.8, respectively. This leads to three optimized designs shown in Figure 5.6 with  $\hat{T}^{\text{cr}}$  used for  $40^\circ$ ,  $45^\circ$  and  $50^\circ$ . In the remainder, these designs are referred to as HS XX, where XX denotes the overhang angle used for setting up  $\hat{T}^{\text{cr}}$ . HS 40, HS 45 and HS 50 are shown in Figure 5.6a–c while their section views are shown in Figure 5.6d–f, respectively. The HS 45 design is later compared with the AM-filter design as both are based on  $\theta^{\text{cr}} = 45^\circ$  as threshold. The final compliances for HS 40, HS 45 and HS

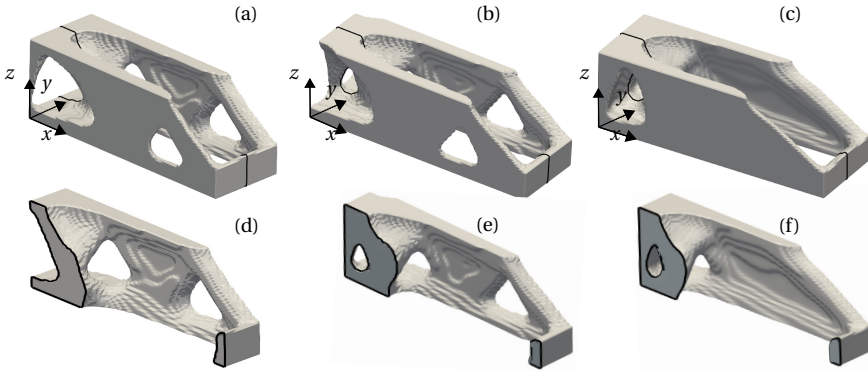


Figure 5.6: The optimized beam using hotspot TO presented in Section 5.2. These designs use three different critical normalized temperatures and hence, are referred to as HS XX, where XX stands for the overhang angle used to set critical temperature. Using this nomenclature, designs shown in (a) HS 40 is found using  $\hat{T}^{cr} = f(\theta^{cr} = 40^\circ)$  resulting in  $C = 2.3C_{ref}$  (b) HS 45 is found using  $\hat{T}^{cr} = f(\theta^{cr} = 45^\circ)$  resulting in  $C = 2.6C_{ref}$  (c) HS 50 is found using  $\hat{T}^{cr} = f(\theta^{cr} = 50^\circ)$  resulting in  $C = 3.2C_{ref}$ . Section view with section at  $y = 20$  mm are given in (d) (e) and (f) for HS 40, HS 45 and HS 50, respectively.

5

50 are found to be  $C = 2.3C_{ref}$ ,  $C = 2.6C_{ref}$  and  $C = 3.2C_{ref}$ , respectively. The compliances show an increasing trend with higher  $\theta^{cr}$  or lower  $\hat{T}^{cr}$  implying that a stricter constraint leads to reduced design freedom and hence, a performance penalty. This was also previously discussed in [30]. Next to the restriction imposed by the hotspot constraint itself, unlike the standard and AM-filter design, the hotspot TO process requires a robust formulation. This results in additional restrictions on minimum length scale and solution space [41]. The difference in mechanical performance is therefore expected. However the primary focus on this paper is on the differences in thermal behavior during printing between designs produced by the three TO methods, as analyzed below.

#### COMPARISON OF HOTSPOT FIELDS

This section is divided into three sets of comparisons between hotspot fields of the presented TO designs. The first set compares standard TO, AM-filter and HS 45 designs, with their corresponding hotspot fields shown in Figure 5.7a–c. For sake of comparison, all normalized temperatures are scaled between 0 and the maximum value obtained across these designs which is found to be  $\hat{T} = 11.6$  for standard TO. It is clearly seen that the long overhang towards the back of the standard TO design leads to extremely high normalized temperatures. Contrary to this, the other two designs remain significantly cooler, signifying that both geometry and physics-based TO methods enhance printability. However, since both AM-filter and HS 45 designs are at significantly lower normalized temperatures compared to the standard TO, it is difficult to compare between Figure 5.7b and c. Therefore, in Figure 5.7d–f, these two designs are shown again but with normalized temperatures scaled between 0 and 4.2, which is the maximum value obtained for AM-filter design. For the AM-filter design, the funnel like features which remain close to the threshold overhang angle value of  $45^\circ$  lead to high normalized temperature values

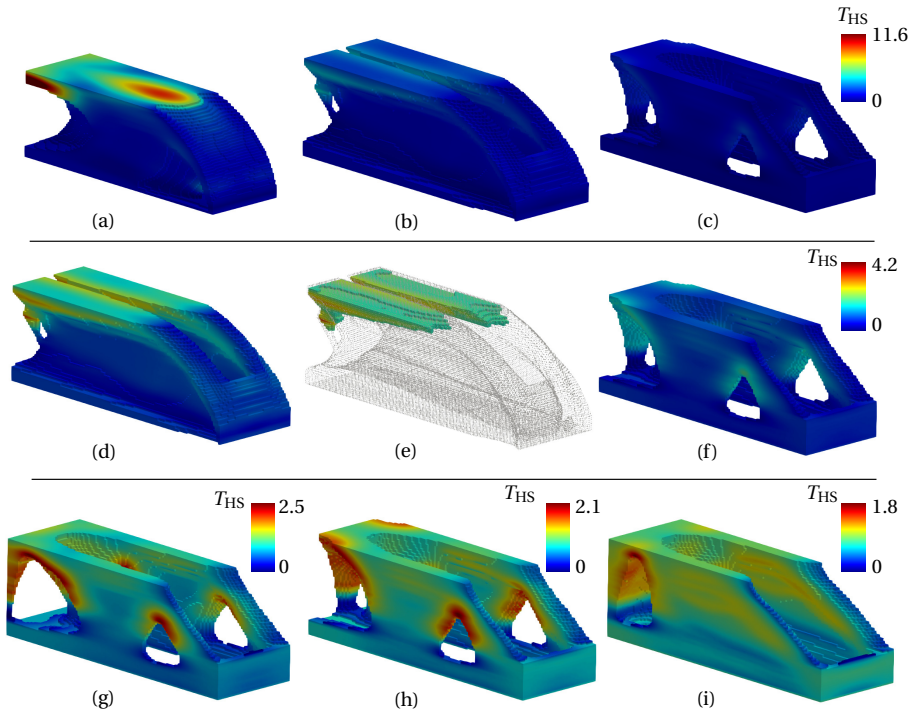


Figure 5.7: Hotspot fields obtained for (a) standard TO design (b) AM-filter design (c) HS 45 design. For the sake of comparison, all three fields are shown with a common normalized temperature scale with values ranging between 0 and maximum value obtained for these designs. For a closer comparison between AM-filter and HS 45 designs, same hotspot fields are presented again in (d) and (f), respectively, with normalized temperature scale ranging between 0 and maximum value obtained between these two designs. The regions of AM-filter design which violate the hotspot constraint with  $\hat{T} > \hat{T}^{\text{cr}} (\theta^{\text{cr}} = 45^\circ)$  are highlighted in (e). Lastly, individual hotspot fields for HS 40, HS 45 and HS 50 designs are shown in (g), (h) and (i), respectively.

in Figure 5.7d. Note that the critical temperature found for  $\theta^{\text{cr}} = 45^\circ$  using the calibration step is  $\hat{T}^{\text{cr}} = 2.1$ , which is used for defining hotspot constraint given by Eq. (5.2). However, normalized temperatures for the AM-filter design exceed this value, signifying that this design violates the hotspot constraint. The AM-filter design with regions which overshoot beyond the  $\hat{T}^{\text{cr}} = 2.1$  are highlighted in Figure 5.7e. Compared to this, the HS 45 design, shown in Figure 5.7f, remains below the highest value prescribed by the hotspot constraint. Lastly, for presenting the thermal gradients within the hotspot TO designs and highlighting the influence of  $\hat{T}^{\text{cr}}$ , HS 40, HS 45 and HS 50 designs are shown in Figure 5.7g, h and i, respectively. Here, normalized temperatures are scaled between 0 and the maximum value attained for each design. It is evident that short near-horizontal overhangs which do not violate the hotspot constraint are allowed to exist in these designs.

### EVALUATION USING HIGHER FIDELITY TRANSIENT L-PBF MODEL

In order to evaluate the thermal performance of different optimized designs and to verify the performance of the simplified L-PBF model, the three designs are subjected to a higher fidelity transient L-PBF simulation based on a layer-by-layer deposition strategy. Unlike the simplified approach, this model considers losses due to convection and radiation. Moreover, variation of thermal properties with respect to temperature is also considered. Details about the process parameters used for higher fidelity simulation can be found in [31]. The material properties for Inconel 718 are taken from [2].

Following the same logic presented while discussing the simplified steady-state L-PBF model, the maximum temperature is picked for each spatial point across all time steps for preparing the hotspot field for each design. Figure 5.8 shows the found hotspot fields for the standard TO, AM-filter and HS 45 designs. In order to compare, 5.8(a), (b) and (c) present the results with common temperature scale ranging between baseplate temperature and maximum attained for standard TO part. Regarding hotspot location and relative intensity, the higher fidelity simulation results are in agreement with those shown in Section 5.3.2 where the simplified model detected the worst hotspot in the standard TO design. Next, in order to highlight the gradient within the part, 5.8(e) and (f) show the temperature fields ranging between baseplate value and maximum obtained for AM-filter and HS 45, respectively. Again, it can be observed that funnel shapes for the AM-filter design are identified as hotspots with maximum temperature occurring at same locations as predicted by the simplified steady-state model (see Figure 5.1g). However, a deeper comparison between 5.8(e) and Figure 5.1g shows that overall spatial distribution of hotspot temperatures is different when found using simulation with different fidelity. The primary reason for this discrepancy is the gradual accumulation of heat that occurs as layers are deposited. A simplified steady-state model misses this aspect and hence only highlights the features which are responsible for local overheating. Nevertheless, in context of TO, the simplified model is able to capture crucial worst-case scenario information in an inexpensive manner, hence making it suitable for TO integration. Finally, using the higher fidelity simulation, it can be observed that HS 45 design shows lowest peak temperature of the three designs.

## 5.4. EXPERIMENTAL PROCEDURES

The L-PBF experiment was conducted using an EOS M290 machine equipped with a continuous fibre laser of maximum 400 W powder output. The feedstock powder used was Inconel 718 powder supplied by Höganäs Germany GmbH, with particle size ranging from 15  $\mu\text{m}$  to 45  $\mu\text{m}$ . The platform pre-heating temperature was set at 80 °C. The process chamber was flooded with argon gas and the oxygen level was kept under 1000 ppm throughout the build process. The parts were built with 310 W laser power, 800 mm/s laser scan speed, 0.11 mm hatch distance and 80  $\mu\text{m}$  layer thickness. This set of parameters was previously optimized for nearly full density and high production speed. A stripe scan strategy was employed with a stripe width of 10 mm and 0.12 mm overlap between stripes. In each layer of the process, the laser scanning of the stripes is specified to traverse against the gas flow direction. The motivation behind this is to minimize the chances of process by-products being directed by the gas flow towards the laser scan

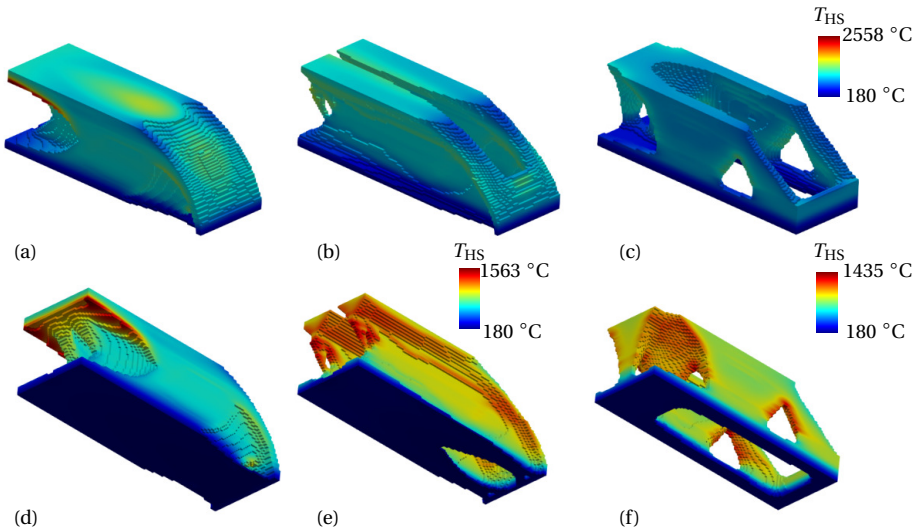


Figure 5.8: The hotspot fields obtained using higher fidelity transient LPBF simulation. (a) Standard TO (b) AM-filter and (c) HS 45 designs are shown with fields ranging between a common scale for comparison. The same designs are shown again from the back side with (e) AM-filter and (f) HS 45 designs hotspot fields ranging between baseplate temperature and maximum value obtained within respective designs.

pathway. This is achieved using the option available in EOSPRINT 2.8 software named as ‘flow optimization’. Another machine feature named as ‘downskin parameter settings’ allows to automatically regulate laser power near overhanging features for better control of overheating. However, it was disabled for our experiments in order to clearly see and compare the overheating tendencies in different design features.

Three separate build jobs were run with build chamber configurations shown in Figure 5.9. The first one is shown in Figure 5.9a and referred to as Build 1. It comprised of five parts including the standard TO part, the three parts designed by the hotspot TO method, and the AM-filter TO part. As seen in Figure 5.9a, the parts were placed close to one another and occupy a large portion of the build area. It was found that the processing conditions deviated for the parts that extended to the edges and corners of the build plate. Similar observations have been reported in literature for other L-PBF systems [9, 13, 34, 46]. For the EOS M290 machine used in the present study, the lower bottom corner (close to powder overflow and gas outlet) and the top right corner (close to the gas inlet and powder dispenser chamber) of the build area where the AM-filter part and the HS-TO 40 reside (see Figure 5.9a) show re-occurrences of random hotspots throughout the build height. This could lead to local overheating issues not strictly related to the geometric layout of the part. Considering this, two more build jobs were run with two selected parts, namely the AM-filter part and the HS 45 part, placed at the centre of the build plate. These two are the most interesting samples in terms of overheating monitoring as they provide a direct comparison between a geometry-based method and a physics-based method. Note that, both relate to  $\theta^{\text{CT}} = 45^\circ$  with the former explicitly pro-

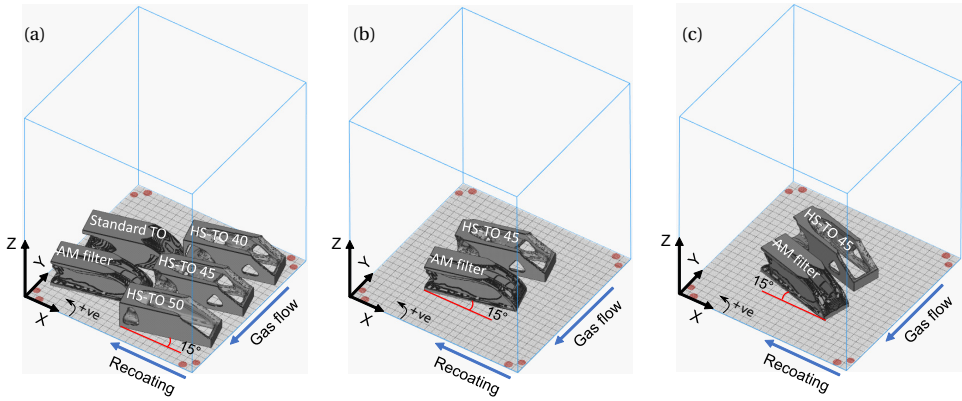


Figure 5.9: Build layout for the three experiments with X, Y and Z representing the global co-ordinate axes for the build chamber. (a) Build 1 comprising five parts: Standard TO, AM-filter, HS 40, HS 45 and HS 50. (b) Build 2 with two parts: AM-filter and HS 45 such that long edges for the parts are oriented at +15° with respect to X axis. (c) Build 3 with two parts: AM-filter and HS 45 such that long edges for the parts are oriented at -15° with respect to X axis.

5

hibiting overhangs lower than  $\theta^{cr}$  while the latter uses the thermal conditions associated with 45° overhang as a threshold for overheating. The second and third build, referred to as Build 2 and 3, respectively, have different orientations between the part edges and the re-coating direction, see Figure 5.9b and Figure 5.9c. This is motivated by the desire of examining the influence of re-coater direction on the OT data.

The experiments were monitored by an EOSTATE Exposure OT (optical tomography) system. The OT camera records near infrared radiations from the process area with an sCMOS camera having a band-pass filter at  $900 \text{ nm} \pm 12.5 \text{ nm}$ . The sCMOS camera takes a long exposure image of the entire build area for each layer of the process with each pixel of the image corresponding to an area of  $125 \mu\text{m} \times 125 \mu\text{m}$ . Considering the build area is  $250 \text{ mm} \times 250 \text{ mm}$ , there are  $2000 \times 2000$  pixels in each OT image. All images are stored in 16 bit format, hence the data ranges between 0 and 65535. Due to this, this highest value of 65535 is used as a normalization parameter so that all OT values are scaled between 0 and 1. The OT values from these images basically correspond to the integrated radiation over the period of time for each layer deposition. Hence, it is directly related to the total radiated energy over time and is thus an indication for overheating during the L-PBF process.

## 5.5. RESULTS

Figure 5.10 shows all the built parts in the Build 1 configuration where the long overhang of the standard TO part is marked with an arrow. There are a total 500 layers in each part, calculated as part height (= 40 mm) divided by layer thickness (= 0.08 mm). Each layer is recorded as one OT image which, when piled on top of each other, leads to a 3D data set with resolution of  $2000 \times 2000 \times 500$  voxels for the entire build chamber. Using the

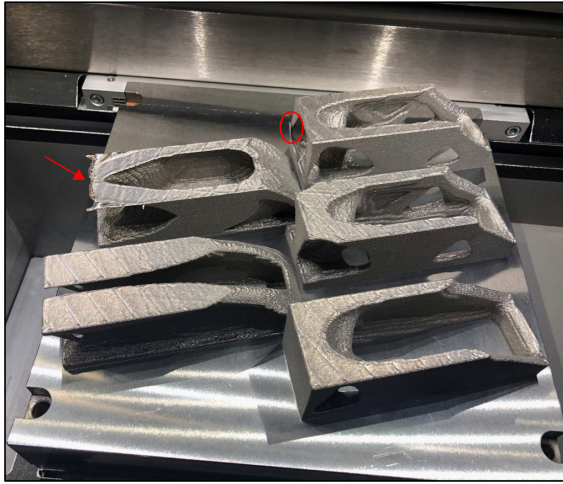


Figure 5.10: Image of built parts in Build 1 configuration. The red arrow indicates the long overhang in standard TO part which caused recoater jamming. The thin wall in HS 40 design, marked with a red circle, fractured due to recoater collision.

known location of samples, data corresponding to every sample is first extracted. Recall that each sample measured  $120 \text{ mm} \times 40 \text{ mm} \times 40 \text{ mm}$  and voxel size in  $x$  and  $y$ -axes is  $125 \mu\text{m}$  while that in  $z$ -axis is  $80 \mu\text{m}$ . It can be worked out that this leads to a resolution of  $960 \times 320 \times 500$  voxels in  $x$ ,  $y$  and  $z$  directions, respectively, for each sample. This gives total 150 million voxels for each part. In order to conveniently visualize the 3D dataset, a convolution operation is performed over each layer where 3 and 2 voxels are averaged together in  $x$  and  $y$ -directions, respectively. This operation leads to a 3D dataset with 26 million voxels and makes it possible to easily visualize the obtained data. Note that this convolution operation is done only for the 3D visualization purpose while all other data analysis operations are performed on the non-convoluted data set.

The visualizations of 3D OT data is presented in Section 5.5.1. From the visualizations, it is found that the scanning strategy directly influences the OT values. This effect is discussed in detail in Section 5.5.2. Lastly, the data is used for comparing the overheating tendencies of different designs and a quantitative discussion is given in Section 5.5.3.

### 5.5.1. DATA VISUALIZATION AND FIRST IMPRESSIONS

Figure 5.11 presents the 3D OT data fields obtained using the aforementioned convolution operation. The data is only shown for values ranging between 0.5 and 1 as lower values are less significant and obstruct the visualization of critical hotspots. As the standard TO makes no consideration for the manufacturability of the L-PBF design, it is as expected that some process issue would occur. In the experiment, the standard TO part experienced severe overheating, which led to significant thermal distortion and collision with the recoater. The build process was interrupted when a significant thermal distur-

tion happened at the left edge of the TO part as the recoater was jammed at the raised edge, as indicated in Figure 5.10. The building of the standard TO optimization was then cancelled manually at a build height of 34.7 mm (layer no 433) and the building of the remaining four parts continued. The 3D OT data field for standard TO design obtained from Build 1 is shown in Figure 5.11a (front) and d (back). High OT values close to 1 can be seen near the long overhang. This is in accordance with the hotspot field presented in Figure 5.7a where this long overhang caused high normalized temperatures. Lastly, the thin wall at the back of the HS 40 part fractured due to recoater collision, encircled in Figure 5.10.

Further, as discussed in Section 5.4, the OT data for the AM-filter part obtained from Build 1 contained random noise due to improper gas flow. Also, it was found by comparing the data from Build 2 and 3 that part orientation with respect to re-coater has negligible effect on OT data. Hence, data from Build 2 and 3 were averaged for creating visualizations shown for AM-filter and HS 45 parts in Figure 5.11b,e and c,f, respectively. It can be seen in the AM-filter design that funnel shaped 45° overhangs indeed lead to high OT values, *i.e.* they remain at higher temperature for longer duration. This is in direct accordance with the hotspot fields shown in Figure 5.7e where these funnels were identified as zones of heat accumulation using simplified L-PBF model. Lastly, as a first observation, the HS 45 degree design shows reduced intensity of high OT values. A more quantitative comparison is given in Section 5.5.3.

A close observation of the 3D hotspot fields for AM-filter and HS 45 parts reveals that one side of overhanging features shows a higher tendency for overheating than the other side, even though, the parts are symmetrical. For example, note that in Figure 5.11e, one side of the funnels manifest high OT intensity (indicated by red arrow) while the other symmetric side shows a lower intensity. A similar observation can be made for HS 45 in Figure 5.11c and f. This directional distribution of overheating is found to be caused by scanning strategy and the effect is discussed in detail in the next section.

### 5.5.2. INFLUENCE OF SHORT HATCHES

As the local heat transfer conditions varies with part geometry, the OT values are found to be higher at overhangs which is in accordance with the simplified L-PBF thermal model. However, the overhangs are not the only source of hotspots in the OT images and it is found that high OT values or local overheating can also be caused by short scanning vectors. Figure 5.12a shows a schematic presenting the scanning strategy used in this experiment. Here, the stripe scan strategy divides the exposure area into a number of stripes with a fixed width of 10 mm as specified by the operator. The scan vectors are placed perpendicular to the strip boundaries and the laser moves in a serpentine pattern shown in Figure 5.12a starting from point S and terminating at point E. Inevitably there are shorter converging scan vectors at the corners and edges of the parts where a scan terminates, one such point marked by E in Figure 5.12a. In a short-hatched corner, the laser scans back and forth in a confined zone for a shorter period of time, allowing less time for heat extraction from the melted zone. The laser heat therefore accumulates



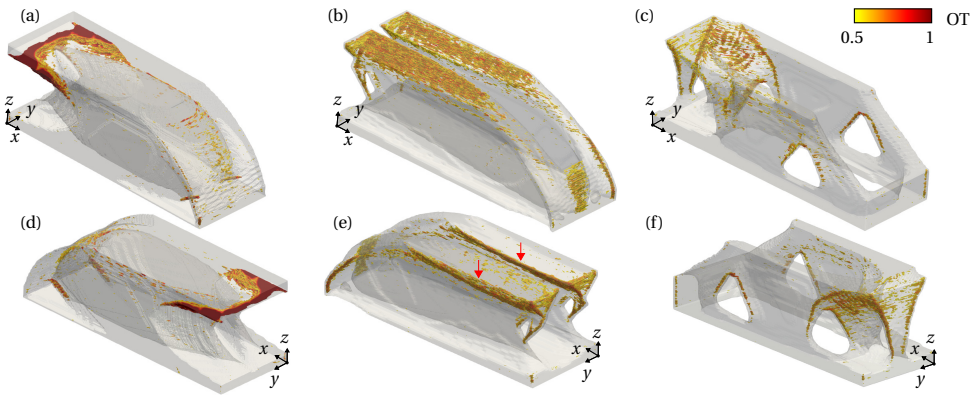


Figure 5.11: Visualization of convoluted OT data for (a) and (d) Standard TO design obtained through Build 1 (b) and (e) AM-filter design obtained by averaging over Build 2 and 3 (c) and (f) HS 45 design obtained by averaging over Build 2 and 3. Here, only data above 0.5 is shown as it represents the possibility of overheating.

locally and creates a hotspot. The starting spot for the laser, marked as point S, also remains in vicinity of short hatches. However, in this case, the scan vectors are increasingly larger, allowing more time for heat dissipation. This leads to asymmetrical heat accumulation towards the end of the laser path.

An OT image of layer number 456 for the AM-filter part is shown in Figure 5.12b. Here, this asymmetrical effect is clearly seen with high OT values only on one side of the overhangs. It is noteworthy here that high OT values in Figure 5.12b are a combined effect of an overhang feature as well as short hatches. Another OT image for layer number 16 is shown in Figure 5.12d. Here also short hatches are present similar to layer number 456. However, they alone do not lead to high OT values, signifying the role of overhangs. Although, in case of thin features, hatches are inevitably short and they alone can cause high OT values. For example, the thin wall marked in Figure 5.12c shows high OT values mainly due to short hatches. The stripe orientation is rotated by  $67^\circ$  between neighbouring layers. Therefore, the location of short hatches keeps changing for consecutive layers. It is inevitable to avoid short hatches and it is desirable that a design should not manifest overheating even with presence of short hatches.

### 5.5.3. COMPARISON FOR EVALUATING OVERHEATING BEHAVIOR

In this subsection, data analysis is done on the OT values found for the AM-filter and HS 45 designs. As discussed earlier, data from Build 2 and 3 is averaged for both the samples while data from Build 1 is not considered due to noise. In order to analyze the spatial distribution of OT data inside the samples, the normalized data is divided into packets of equal size and the volume it occupies in different designs is compared. This gives an idea about which design has a larger density of high OT values signifying that a larger portion of it remained at an elevated temperature for a longer duration during the build. Figure 5.13a presents this comparison where the percentage range of the OT data

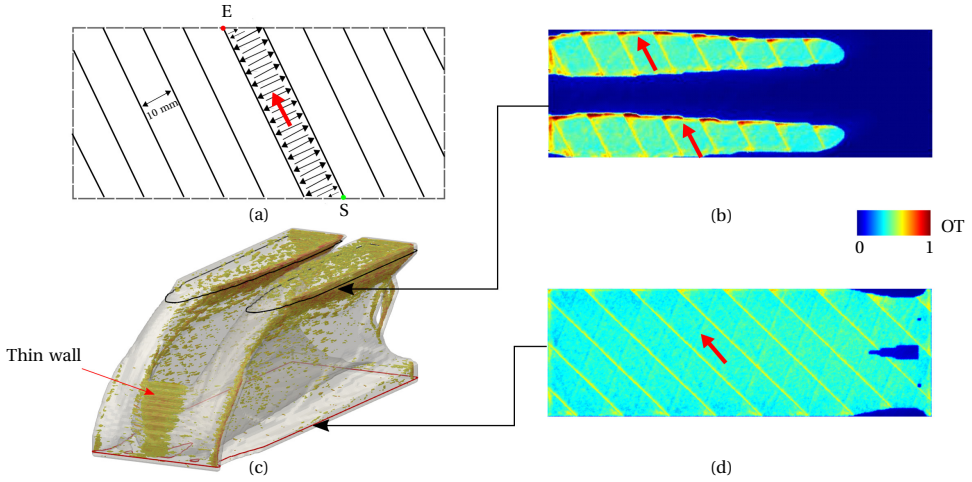


Figure 5.12: Influence of short hatches on OT data. (a) A schematic representation of the scanning strategy used in this experiment where entire layer is first divided into number of stripes which are then scanned using a serpentine path. Short and converging hatches lead to local heat accumulation in vicinity of point E. (b) OT image for layer number 456 demonstrating high OT values near overhanging feature due to short hatch effect. (c) The 3D OT data field for AM-filter part showing the directional increase in high OT values due to short hatch effect. The front thin wall also shows high OT values due to short scanning vectors. (d) OT image for layer number 16 demonstrating that short hatches alone do not cause high OT values.

5

is marked on the horizontal axis and the corresponding percentage volume it occupies is shown in form of a bar chart. Once again, data above 0.5 or 50% is used as it is more critical and signifies possible overheating. Moreover, Figure 5.13b shows a closeup view for the same bar chart for data above 70% as this is most critical for overheating. The error bars signify the range of variation in corresponding percentage volumes across Build 2 and 3. It is evident that for any given range of OT data, the HS 45 design occupies less volume than that of the AM-filter design. Also, it can be calculated by adding up percentage volumes that 20% of the AM-filter volume is above 50% of the OT data while only 12% volume is above 50% for HS 45 design.

Due to the gas flow issues with Build 1, the HS 40 design which was placed in the top right corner suffered from noisy OT data, making it difficult to draw any conclusions. The HS 50 design data from Build 1 was analysed and it showed a lower density of high OT values as compared to HS 45, with 9% volume occupying OT data with 50% value. This is as expected since increasing  $\hat{T}^{cr}$  makes the design less prone to overheating.

#### 5.5.4. CORRELATION WITH DEFECTS

In order to analyze the correlation between overheating and part quality, an investigation is carried out focused on identification of defects within the printed parts. It is reported in the literature that the excess energy deposited due to overheating can lead to keyhole porosity [23, 10]. Hence a quantitative analysis of porosity is performed to iden-

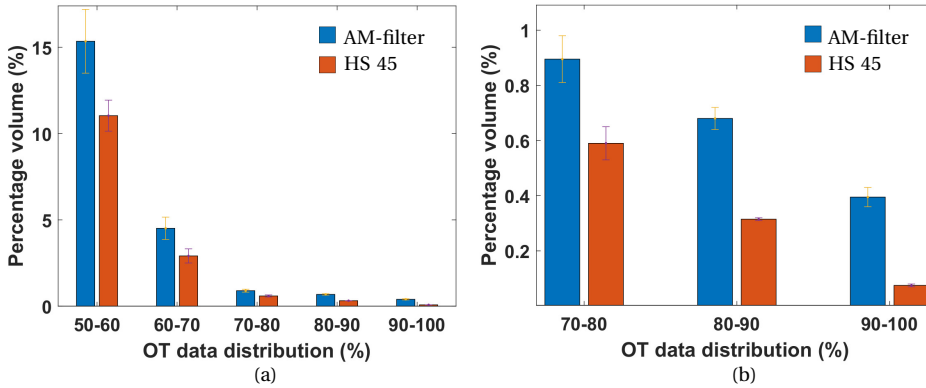


Figure 5.13: Comparison of OT data distribution by part volume it occupies for the AM-filter and the HS 45 designs. The results are averaged over the data obtained from Build 2 and 3. The error bars indicate the variation in the values of percentage volumes over both the builds. (a) shows data above 50% while (b) highlights the distribution for data above 70% as it is more critical from the context of overheating.

tify the relationship between defects and overheating indicated by high OT values. For this purpose, the fabricated pieces were cut using Electron Discharge Machining (EDM) to obtain multiple cross-sections for analysis of defects. The samples were mounted in polymer resin, ground and polished to obtain mirror-finish following standard metallographic sample preparation steps. Optical images were taken using a ZEISS-AxioScope7 optical microscope across the entire cross sections of samples by taking consecutive images with 10 % overlap between each. The images were then combined to form a single image file for analysis.

Figure 5.14 shows the AM-filter part with cuts marked at  $x = 1.5$  mm, 3.0 mm, 5.2 mm, 24.6 mm and  $x = 44.6$  mm and these sections are subsequently labelled as  $A^{AM}$ ,  $B^{AM}$ ,  $C^{AM}$ ,  $D^{AM}$  and  $E^{AM}$ , respectively. The cross-section locations are decided based on the OT observations such that defects can be analyzed across a wide range of OT values. As suggested by thermal simulations in Section 5.3.2 and observed by OT experiments in Section 5.5.1, the funnel like shapes in the AM filter designs are identified as thermal bottlenecks. Hence, they are selected for analysis in the obtained cross-sectional images. In Figure 5.14, the OT data maps corresponding to the cross-sections are presented. In order to adequately quantify the OT values associated with a particular cross-section, first a thresholding operation is performed. Since focus here remains on keyhole defects which are typically associated with excess energy deposition, it was deemed suitable to use a high threshold value of 0.8. Recall that OT values ranges between 0–1 while the population density of high OT values on a cross-section signifies the level of overheating. Therefore, to quantify a cross-section's OT value, the area of the cross-section where the OT values are above the threshold value 0.8 is multiplied with the mean OT value of this area and indicated by  $\overline{OT}$ . The corresponding  $\overline{OT}$  values are given in Figure 5.14 for each cross-section and it can be seen that cross-section  $A^{AM}$  shows highest  $\overline{OT}$  value.

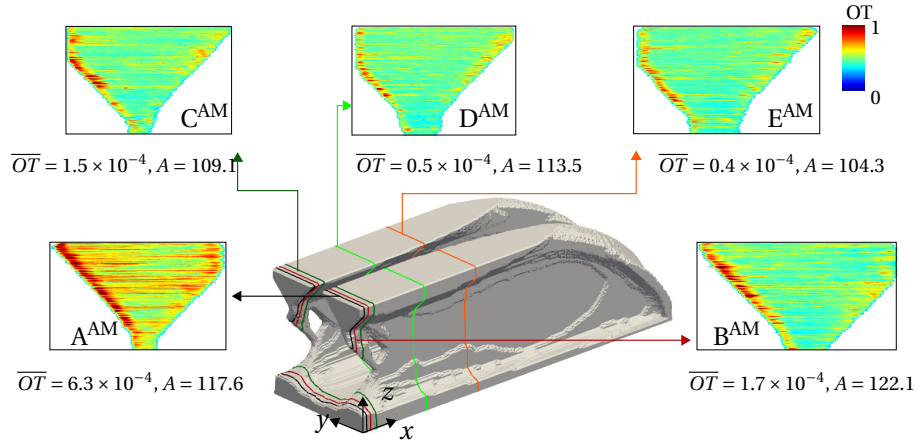


Figure 5.14: The AM-filter part is cut at 5 sections locations at  $x = 1.5$  mm, 3.0 mm, 5.2 mm, 24.6 mm and 44.6 mm on the  $y$ - $z$  plane. The OT maps for the funnel like shapes are shown and labelled in sequence of increasing  $x$  coordinates. The critical OT area  $\overline{OT}$  and total area of the funnel shapes  $A$  are also provided in  $\text{mm}^2$  for each cross-section.

5

Similarly, the HS45 sample was cut at 4 locations located at  $x = 1.5$  mm, 46.5 mm, 57 mm and  $y = 20$  mm as shown in Figure 5.15. These are labelled as  $A^{\text{HS}}$ ,  $B^{\text{HS}}$ ,  $C^{\text{HS}}$  and  $D^{\text{HS}}$  and note that cross-section  $C^{\text{HS}}$  and  $D^{\text{HS}}$  provide two disjointed sub-sections that are treated individually for the analysis, hence in total six cross-sections are analyzed. The OT maps, critical OT area and  $\overline{OT}$  values are also marked in Figure 5.15. Lastly, the total areas  $\Omega$  associated with the cross-sections are also reported and used for defect calculation explained below.

The images for  $A^{\text{AM}}$  and  $B^{\text{AM}}$  are shown in Figure 5.16a and b, respectively, while that for  $A^{\text{HS}}$  is presented in Figure 5.16d. Here, only images corresponding to the three highest critical OT area values  $\overline{OT}$  are presented for the sake of brevity while all remaining images are provided as supplementary material. In order to quantify the amount of porosity, the cross-section images are subjected to a Matlab based boundary tracing algorithm and pore boundaries found are indicated in red color in Figure 5.16. The image resolution is such that each pixel measures  $0.88 \mu\text{m} \times 0.88 \mu\text{m}$ . In order to develop a quantitative measure of porosity associated with each cross-section image, first a shape analysis step is carried out which uses the concept of Feret diameter  $d_f$  for classifying pores as defects [39]. The Feret diameters associated with pore shapes are calculated using the boundary information and then pores with  $d_f$  larger than  $10 \mu\text{m}$  are considered while others are discarded. Figure 5.16c highlights two such pores from the image obtained from  $C^{\text{AM}}$  where large pores near the overhang surface can be observed. Such pores can induce stress concentration and adversely influence mechanical properties [23]. A parameter called pore area fraction is calculated for every cross-section. It is given by  $\frac{\sum_{i=1}^n a_i}{\Omega}$  where  $a_i$  represents area of the  $i^{\text{th}}$  pore associated with a particular cross-section while  $\Omega$  represents total area of the cross-section. The areas for every

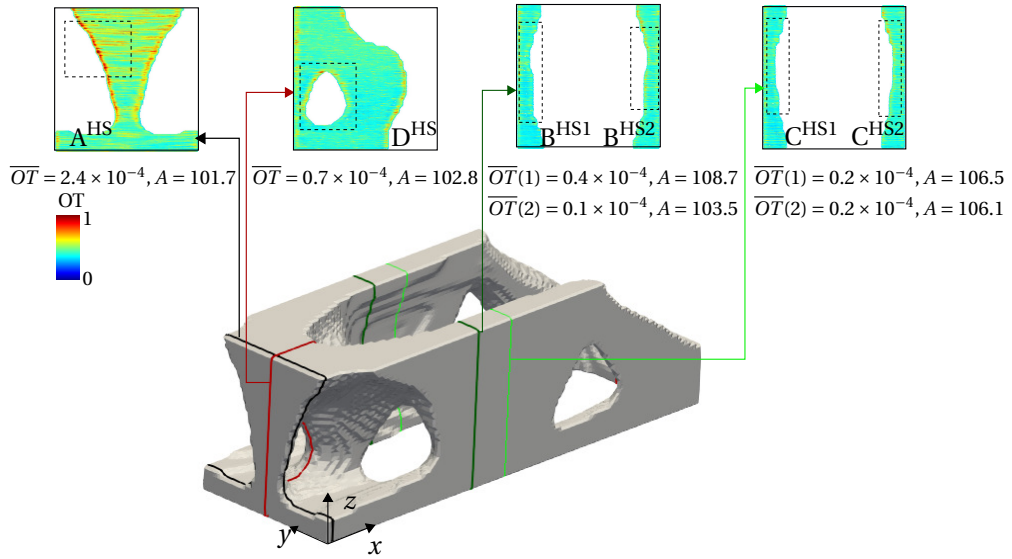


Figure 5.15: The HS 45 part is cut at 4 locations at  $x = 1.5$  mm, 46.5 mm, 57.0 mm and  $y = 20.0$  mm. The OT maps for the sections are shown and these sections are labelled as A<sup>HS</sup> to C<sup>HS</sup> with increasing  $x$  coordinates while the section along  $x$ - $z$  plane is numbered as D<sup>HS</sup>. Note that cross-section B and C provide two disjointed sub-sections each and they are treated as an individual section, referred to as '1' and '2' in the analysis. Here, cross-section A<sup>HS</sup> shows relatively highest OT values while all other cross-sections have considerably low OT values. This is also exemplified by the  $\overline{OT}$  values provided for each cross section. Lastly, the surface area  $\Omega$  of the region enclosed within the dotted rectangles are also reported. Both  $\overline{OT}$  and  $\Omega$  are in mm<sup>2</sup>.

cross-section are reported in Figure 5.14 and Figure 5.15. Given the stochastic nature of pore formation, it is deemed more appropriate to consider sections with similar area values across samples. Therefore, sub-sections are considered from the larger sections of HS 45 design so that the considered areas are similar to that of AM-filter design. These sub-sections are marked on the OT maps in Figure 5.15 using dotted rectangles and areas of the regions enclosed within these rectangles are also reported. It is ensured that these sub-sections also encapsulate high OT regions.

Finally, Figure 5.17 shows the variation of pore fraction area with respect to critical OT area for all 11 sections from both designs. The data points in red are from the AM-filter design and data points in green belong to the HS 45 design. It can be observed that propensity of pore formation increases with increasing regions of high OT values. For example, AM-filter cross-section 1 has largest  $\overline{OT}$  value and is reported to have the highest pore area fraction as well. On the other extreme, it can be seen that sections with lower  $\overline{OT}$  values tend to have a lower pore area fraction, signified by the data points located in the lower left corner of Figure 5.17. However, the data points located in between these two extremes show a less consistent pattern. The results presented here show a broad trend which is consistent with the common understanding that higher energy density or high OT values will increase the likelihood of pore formation. Nevertheless, it is well-known that local melt-pool physics significantly influence the mechanism of keyhole formation and there could be factors other than geometry-induced local overheating which could influence pore formation, for example, anomalous behaviour of gas flow [23]. These effects require further investigation which is beyond the scope of this paper.

## 5.6. DISCUSSION

The reported experimental investigation demonstrates that the proposed physics-based hotspot TO method can efficiently generate designs which are less prone to overheating and are less likely to manifest the defects associated with overheating, such as porosity. On the other hand, widely popular geometry-based TO schemes do not ensure overheating avoidance as the thermal behavior is not uniquely linked with overhang angles. In order to emphasize this point, Figure 5.18a and b show the AM-filter and HS 45 designs, respectively, with STL facets which have overhang angles less than  $\theta^{cr} = 45^\circ$  marked in red color. It is evident that AM-filter design is largely free from such overhang violations and the combined area of such facets for AM-filter design is found to be 248 mm<sup>2</sup>. Note that all such facets are near the baseplate and it is suspected that these are results of iso-surface extraction as the AM-filter strictly prohibits such facets. Contrary to this, the combined area of facets with overhang angles less than  $\theta^{cr} = 45^\circ$  for the HS 45 design is 438 mm<sup>2</sup> and these facets are located in multiple zones. In spite of this, as shown in Section 5.5.3 and 5.5.4, the trend for overheating is opposite where the HS 45 design has a lower density of high OT values. This is due to the funnel shapes (marked with arrows in Figure 5.18a) in the AM-filter design which, although satisfy the overhang criteria, act as a thermal bottleneck causing heat accumulation which leads to high OT values. This demonstrates that local thermal behaviour does not uniquely depend on overhang angle. Instead it is governed by the combined heat evacuation capacity of neighboring features.

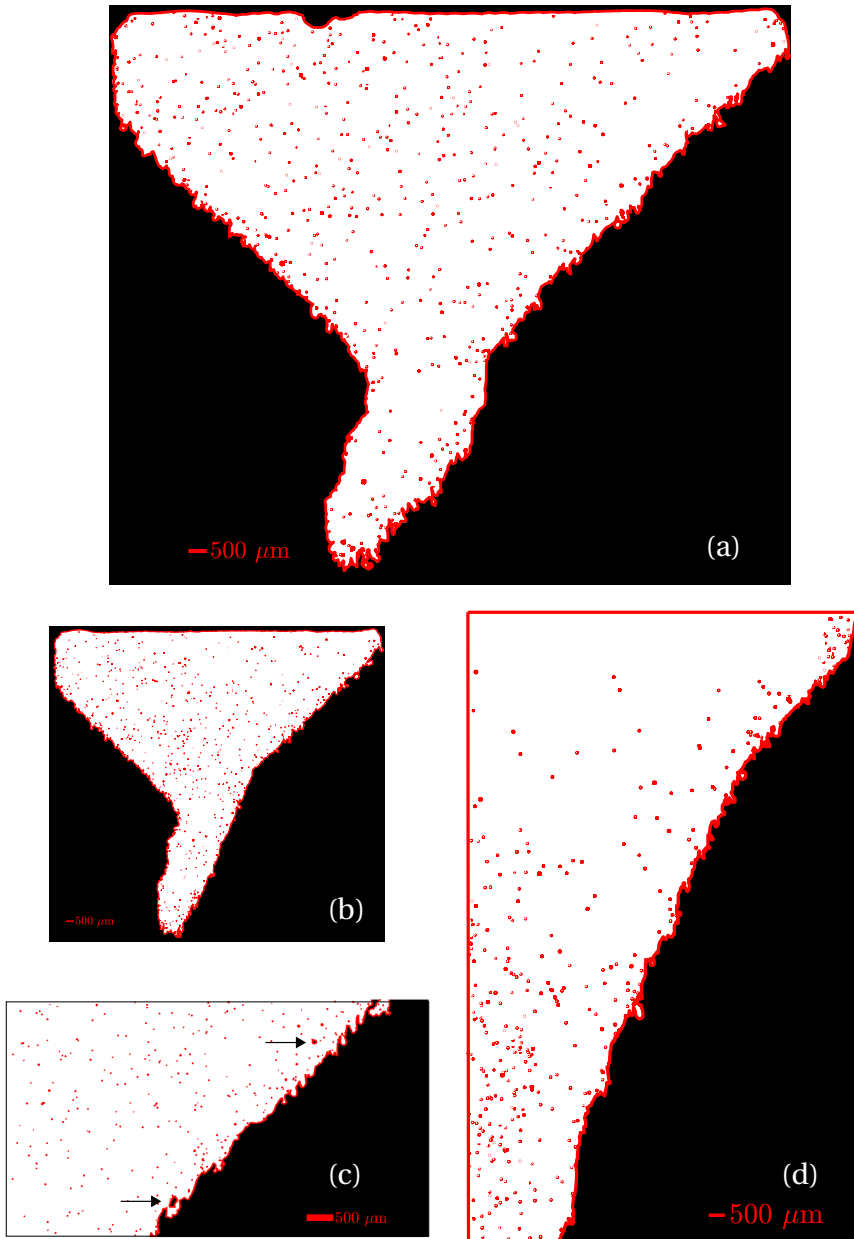


Figure 5.16: Cross-sectional images obtained for (a)  $A^{\text{AM}}$  (b)  $B^{\text{AM}}$  (c)  $C^{\text{AM}}$  (magnified to highlight defects) and (d)  $A^{\text{HS}}$ . A Matlab based boundary tracing algorithm is used to identify pores indicated in red color.

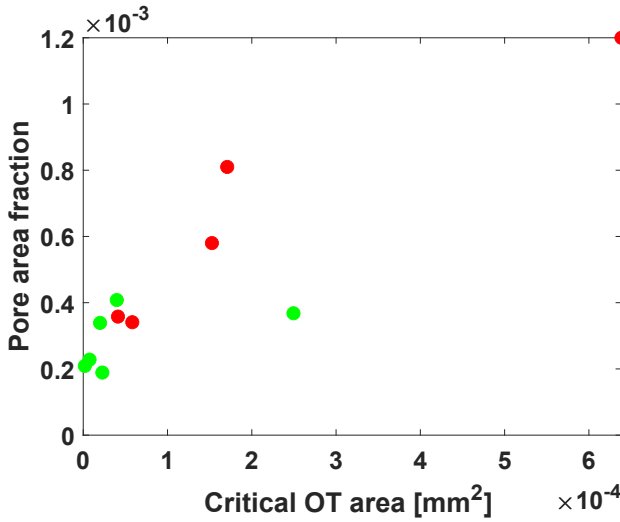


Figure 5.17: The variation of pore area fraction with respect to respective critical OT area  $\overline{OT}$ . It is evident that  $\overline{OT}$  values for HS 45 cross-sections remain on the lower side resulting in lower pore formation as compared to the AM-filter design.

5

The hotspot TO focuses on geometry induced overheating and the influence of scanning pattern is not included within the simplified L-PBF model. However, it is found from the OT data that short and converging scans can aggravate overheating tendencies associated with geometric features. Note that the choice of a scanning pattern is mainly based on relieving the residual stresses in successive layers and often predetermined. It is noteworthy that both the AM-filter and HS 45 designs encountered short hatches during fabrication as both were subjected to similar scanning patterns where laser movement was directed against the gas flow. The AM-filter design has several funnel shaped features close to 45° which, in combination with short hatches, lead to high OT values. The HS 45 design, even with similar short hatches, leads to lower OT values since it is designed for efficient heat evacuation. Nevertheless, the findings here suggest that it will be beneficial to consider the influence of scanning strategy during designing the part. Alternatively, a scan pattern optimization can potentially be done based on a given part design.

Here, a quantitative investigation was done co-relating overheating with defects. For this purpose, a total of 9 cuts were made which revealed useful insights. However, an even deeper analysis can be carried out by performing volumetric analysis and analyzing more regions of the parts. For example, computer tomography (CT) can be used to capture defects and associate them with high OT values. Another possible option is to perform a microstructural evaluation of the critical zones. These studies can potentially identify the limiting OT value which can be treated as threshold for a quantitative definition of overheating.



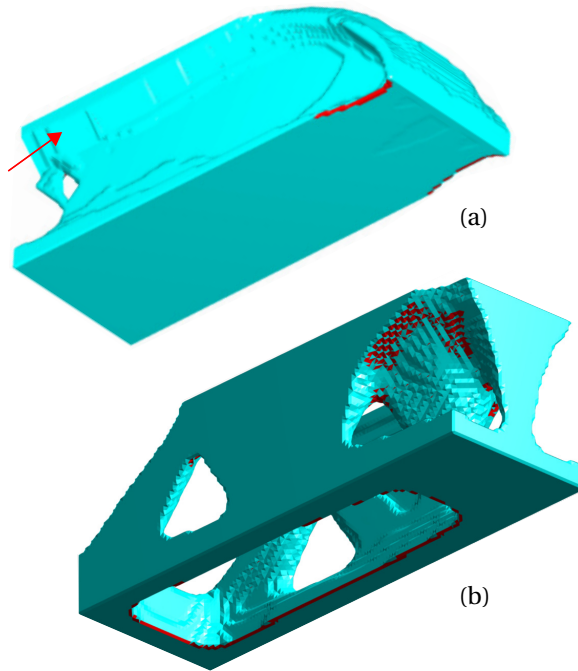


Figure 5.18: STL facets which have overhang angles less than  $\theta^{\text{ct}} = 45^\circ$  are marked red for (a) AM-filter and (b) HS 45 designs.

While the numerical examples and experimental investigations shown in this paper demonstrate that the novel physics-based hotspot TO can be applied successfully, its limitations should also be reported. First, the simplified L-PBF model which is integrated with TO here captures the overheating tendencies associated with design features in a qualitative manner. However, it is an approximation of the thermal interactions which occur during the process and only focuses on capturing overheating. A higher fidelity model, *e.g.* including transient heat transfer and/or mechanical analysis, will be able to address other important process characteristics, such as cooling rates, residual stresses and deformations. A model which could include the influence of hatch scanning will also be beneficial in developing a design which remains robust against process uncertainties. In this context, the challenge of high computational cost associated with the higher fidelity L-PBF models needs to be addressed. Another limitation is that a single build orientation is considered, which cannot change during the optimization. While there are multiple factors which dictate the choice of build direction (part height, surface finish, support accessibility, etc.), it would be beneficial to develop a generalized formulation where build orientation is simultaneously optimized.

## 5.7. CONCLUSIONS

This paper presents a TO method which utilizes a simplified thermal model of the L-PBF process for generating designs less prone to overheating defects. The simplified model makes it possible to integrate L-PBF process physics within the optimization while remaining computationally tractable. The capability of the novel TO method is compared experimentally with two other TO approaches, standard TO and geometry-based overhang control (AM-filter) TO. Designs obtained using all three TO methods are fabricated using L-PBF and the process is monitored using optical tomography (OT). It was found by comparing OT data, which is an indicator of overheating, that standard TO which does not address manufacturability, leads to severe overheating and build failure. Further, comparing TO methods which include AM constraints, the design obtained by the novel TO method presented in this paper shows a significant reduction in overheating compared to the AM-filter design. Finally, a correlation between overheating and defects was shown. These observations reveal that overheating is not uniquely linked to an overhang angle, and commonly used guidelines of avoiding acute overhangs are insufficient for avoiding overheating.

The hotspot TO uses a simplified L-PBF model and realizes 3D designs which show reduced risk of overheating. The proposed method with experimental validation presents a promising opportunity for addressing AM physics within the optimization loop with carefully selected simplifications [31]. Nevertheless, there are certain improvements that can be considered. As discussed in Section 5.3, a constant slab thickness of  $s = 12$  mm is used in this paper which is calculated based on the concept of thermal characteristic length. A more detailed numerical study can be done to for estimating the slab thickness value. For example, [27] presented a framework for determining thermal interaction length using higher fidelity AM simulations. Next, the influence of machine parameters, such as downskin settings, baseplate pre-heat temperature, laser power and velocity etc. was not investigated here for simplicity but can be considered in future. Further, it was found that short and converging hatches also significantly influence the overheating behavior. Since the hotspot TO method is based on a layer-by-layer simulation, such detailed effects related to specific scan patterns are not captured and inclusion of more detailed models is necessary to address this. In this regard, developing similar computationally inexpensive models which can accurately capture more complicated physics-based parameters, *e.g.* scanning effects, residual stresses, deformation, is seen as an important avenue for future research.

## REFERENCES

- [1] Guido A.O. Adam and Detmar Zimmer. “Design for Additive Manufacturing—Element transitions and aggregated structures”. In: *CIRP Journal of Manufacturing Science and Technology* 7.1 (2014), pp. 20–28. ISSN: 1755-5817.
- [2] A Sh Agazhanov, D A Samoshkin, and Yu M Kozlovskii. “Thermophysical properties of Inconel 718 alloy”. In: *Journal of Physics: Conference Series* 1382.1 (Nov. 2019), p. 012175.

- [3] Grégoire Allaire, Charles Dapogny, Alexis Faure, and Georgios Michailidis. “Shape optimization of a layer by layer mechanical constraint for additive manufacturing”. In: *CR Math* 355.6 (2017), pp. 699–717. ISSN: 1631-073X.
- [4] Oded Amir and Yoram Mass. “Topology optimization for staged construction”. In: *Struct Multidiscip Optim* 57.4 (Apr. 2018), pp. 1679–1694. ISSN: 1615-1488.
- [5] Martin P Bendsøe and Ole Sigmund. *Topology optimization: theory, methods and applications*. Springer-Verlag Berlin Heidelberg, 2003.
- [6] M. Boissier, G. Allaire, and C. Tournier. “Additive manufacturing scanning paths optimization using shape optimization tools”. In: *Structural and Multidisciplinary Optimization* 61.6 (June 2020), pp. 2437–2466. ISSN: 1615-1488.
- [7] Tyler E. Bruns and Daniel A. Tortorelli. “Topology optimization of non-linear elastic structures and compliant mechanisms”. In: *Comput Method Appl M* 190.26 (2001), pp. 3443–3459. ISSN: 0045-7825.
- [8] Amal Prashanth Charles, Ahmed Elkaseer, Lore Thijs, V. Hagenmeyer, and Stefan Scholz. “Effect of Process Parameters on the Generated Surface Roughness of Down-Facing Surfaces in Selective Laser Melting”. In: *Applied Sciences* 9 (Mar. 2019).
- [9] Yu Ren Chen, Guglielmo Vastola, and Yan Zhang. “Optimization of inert gas flow inside laser powder bed fusion chamber with computational fluid dynamics”. In: 2018.
- [10] Bo Cheng, Lukas Loeber, Hannes Willeck, Udo Hartel, and Charles Tuffile. “Computational investigation of melt pool process dynamics and pore formation in laser powder bed fusion”. In: *Journal of Materials Engineering and Performance* 28.11 (2019), pp. 6565–6578.
- [11] Michael Cloots, Livia Zumofen, Adriaan Spierings, Andreas Kirchheim, and Konrad Wegener. “Approaches to minimize overhang angles of SLM parts”. In: *Rapid Prototyping Journal* 23 (Mar. 2017), pp. 362–369.
- [12] Erik Denlinger, Jeff Irwin, and Pan Michaleris. “Thermomechanical Modeling of Additive Manufacturing Large Parts”. In: *Journal of Manufacturing Science and Engineering* 136 (Oct. 2014), p. 061007.
- [13] B. Ferrar, L. Mullen, E. Jones, R. Stamp, and C.J. Sutcliffe. “Gas flow effects on selective laser melting (SLM) manufacturing performance”. English. In: *Journal of Materials Processing Tech.* 212.2 (2012), pp. 355–364.
- [14] Andrew T. Gaynor and James K. Guest. “Topology optimization considering overhang constraints: Eliminating sacrificial support material in additive manufacturing through design”. In: *Struct Multidiscip Optim* 54.5 (Nov. 2016), pp. 1157–1172. ISSN: 1615-1488.
- [15] Frank P. Incropera and David P. DeWitt. *Fundamentals of Heat and Mass Transfer*. 4th Edition. New York City, New York: John Wiley Sons, Inc., 1996.
- [16] Darya Kastsian and Daniel Reznik. “Reduction of local overheating in selective laser melting”. In: *In Proceedings of Simulation of Additive Manufacturing (SIM-AM), Munich, Germany*. Oct. 2017.

- [17] Nils Keller and Vasily Ploshikhin. “New method for fast predictions of residual stress and distortion of AM parts”. In: *Solid Freeform Fabrication Symposium, Austin, Texas*. 2014, pp. 1229–1237.
- [18] Matthijs Langelaar. “An additive manufacturing filter for topology optimization of print-ready designs”. In: *Struct Multidiscip Optim* 55.3 (Mar. 2017), pp. 871–883. ISSN: 1615-1488.
- [19] Matthijs Langelaar. “Topology optimization of 3D self-supporting structures for additive manufacturing”. In: *Additive Manufacturing* 12 (2016), pp. 60–70. ISSN: 2214-8604.
- [20] Richard Leach and Simone Carmignato. *Precision Metal Additive Manufacturing*. CRC Press, Sept. 2020. ISBN: 113834771X.
- [21] Jikai Liu, Andrew T. Gaynor, Shikui Chen, Zhan Kang, Krishnan Suresh, Akihiro Takezawa, Lei Li, Junji Kato, Jinyuan Tang, Charlie C. L. Wang, Lin Cheng, Xuan Liang, and Albert. C. To. “Current and future trends in topology optimization for additive manufacturing”. In: *Struct Multidiscip Optim* 57.6 (June 2018), pp. 2457–2483. ISSN: 1615-1488.
- [22] Kai Liu and Andrés Tovar. “An efficient 3D topology optimization code written in Matlab”. In: *Structural and Multidisciplinary Optimization* 50.6 (Dec. 2014), pp. 1175–1196. ISSN: 1615-1488.
- [23] Aiden A. Martin, Nicholas P. Calta, Saad A. Khairallah, Jenny Wang, Phillip J. Depond, Anthony Y. Fong, Vivek Thampy, Gabe M. Guss, Andrew M. Kiss, Kevin H. Stone, Christopher J. Tassone, Johanna Nelson Weker, Michael F. Toney, Tony van Buuren, and Manyalibo J. Matthews. “Dynamics of pore formation during laser powder bed fusion additive manufacturing”. In: *Nature Communications* 10.1 (Apr. 2019), p. 1987. ISSN: 2041-1723.
- [24] Raya Mertens, Stijn Clijsters, Karolien Kempen, and Jean-Pierre Kruth. “Optimization of Scan Strategies in Selective Laser Melting of Aluminum Parts With Down-facing Areas”. In: *Journal of Manufacturing Science and Engineering* 136(6) (Dec. 2014).
- [25] Gunther Mohr, Simon J. Altenburg, and Kai Hilgenberg. “Effects of inter layer time and build height on resulting properties of 316L stainless steel processed by laser powder bed fusion”. In: *Additive Manufacturing* 32 (2020), p. 101080. ISSN: 2214-8604.
- [26] Gunther Mohr, Simon J. Altenburg, Alexander Ulbricht, Philipp Heinrich, Daniel Baum, Christiane Maierhofer, and Kai Hilgenberg. “In-Situ Defect Detection in Laser Powder Bed Fusion by Using Thermography and Optical Tomography—Comparison to Computed Tomography”. In: *Metals* 10.1 (2020). ISSN: 2075-4701.
- [27] T.P. Moran, D.H. Warner, and N. Phan. “Scan-by-scan part-scale thermal modelling for defect prediction in metal additive manufacturing”. In: *Additive Manufacturing* 37 (2021), p. 101667. ISSN: 2214-8604.

- [28] Shubham Patel, James Mekavibul, Jami Park, Anchit Kolla, Ryan French, Zachary Kersey, and Gregory Lewin. “Using Machine Learning to Analyze Image Data from Advanced Manufacturing Processes”. In: *2019 Systems and Information Engineering Design Symposium (SIEDS), Charlottesville, VA, USA (Apr. 2019)*, pp. 1–5.
- [29] Xiaoping Qian. “Undercut and overhang angle control in topology optimization: a density gradient based integral approach”. In: *International Journal for Numerical Methods in Engineering* 111.3 (2017), pp. 247–272.
- [30] R. Ranjan, C. Ayas, M. Langelaar, and F. van Keulen. “Controlling local overheating in topology optimization for additive manufacturing”. In: *Structural and Multidisciplinary Optimization* 65.6 (May 2022), p. 162. ISSN: 1615-1488.
- [31] Rajit Ranjan, Can Ayas, Matthijs Langelaar, and Fred van Keulen. “Fast Detection of Heat Accumulation in Powder Bed Fusion Using Computationally Efficient Thermal Models”. In: *Materials* 13.20 (2020). ISSN: 1996-1944.
- [32] John Romano, Leila Ladani, and Magda Sadowski. “Thermal Modeling of Laser Based Additive Manufacturing Processes within Common Materials”. In: *Procedia Manufacturing* 1 (2015). 43rd North American Manufacturing Research Conference, NAMRC 43, 8-12 June 2015, UNC Charlotte, North Carolina, United States, pp. 238–250. ISSN: 2351-9789.
- [33] Marleen Rombouts, L. Froyen, A. Gusarov, El Hassane Bentefour, and Christ Gloorieux. “Photopyroelectric measurement of thermal conductivity of metallic powders”. In: *Journal of Applied Physics* 97 (Dec. 2004), p. 24905.
- [34] Maximilian Schniedenharn, Frederik Wiedemann, and Johannes Henrich Schleifenbaum. “Visualization of the shielding gas flow in SLM machines by space-resolved thermal anemometry”. In: *Rapid Prototyping Journal* 24.8 (Jan. 2018), pp. 1296–1304. ISSN: 1355-2546.
- [35] Ole Sigmund. “Morphology-based black and white filters for topology optimization”. English. In: *Structural and Multidisciplinary Optimization* 33.4-5 (2007), pp. 401–424. ISSN: 1615-147X.
- [36] Krister Svanberg. “The method of moving asymptotes—a new method for structural optimization”. In: *Int J Numer Methods Eng* 24.2 (1987), pp. 359–373.
- [37] Emiel van de Ven, Robert Maas, Can Ayas, Matthijs Langelaar, and Fred van Keulen. “Overhang control based on front propagation in 3D topology optimization for additive manufacturing”. In: *Computer Methods in Applied Mechanics and Engineering* 369 (2020), p. 113169. ISSN: 0045-7825.
- [38] F Van Keulen, RT Haftka, and NH Kim. “Review of options for structural design sensitivity analysis. Part 1: Linear systems”. In: *Computer methods in applied mechanics and engineering* 194.30-33 (2005), pp. 3213–3243.
- [39] W. H. WALTON. “Feret’s Statistical Diameter as a Measure of Particle Size”. In: *Nature* 162.4113 (Aug. 1948), pp. 329–330. ISSN: 1476-4687.
- [40] Di Wang, Yongqiang Yang, Ziheng Yi, and Xubin Su. “Research on the fabricating quality optimization of the overhanging surface in SLM process”. In: *Int J Adv Manuf Tech* 65.9 (Apr. 2013), pp. 1471–1484. ISSN: 1433-3015.

- [41] Fengwen Wang, Boyan Lazarov, and Ole Sigmund. “On projection methods, convergence and robust formulations in topology optimization”. In: *Structural and Multidisciplinary Optimization* 43 (June 2011), pp. 767–784.
- [42] Pinku Yadav, Vibhutesh Kumar Singh, Thomas Joffre, Olivier Rigo, Corinne Arvieu, Emilie Le Guen, and Eric Lacoste. “Inline Drift Detection Using Monitoring Systems and Machine Learning in Selective Laser Melting”. In: *Advanced Engineering Materials* 22.12 (2020), p. 2000660.
- [43] Y. Yang, M.F. Knol, F. van Keulen, and C. Ayas. “A semi-analytical thermal modelling approach for selective laser melting”. In: *Additive Manufacturing* 21 (2018), pp. 284–297. ISSN: 2214-8604.
- [44] Guenter Zenzinger, Joachim Bamberg, Alexander Ladewig, Thomas Hess, Benjamin Henkel, and Wilhelm Satzger. “Process monitoring of additive manufacturing by using optical tomography”. In: *AIP Conference Proceedings* 1650.1 (2015), pp. 164–170.
- [45] Wenyong Zhang, Mingming Tong, and Noel M. Harrison. “Resolution, energy and time dependency on layer scaling in finite element modelling of laser beam powder bed fusion additive manufacturing”. In: *Additive Manufacturing* 28 (2019), pp. 610–620. ISSN: 2214-8604.
- [46] Xiaobing Zhang, Bo Cheng, and Charles Tuffile. “Simulation study of the spatter removal process and optimization design of gas flow system in laser powder bed fusion”. In: *Additive Manufacturing* 32 (Mar. 2020), p. 101049.
- [47] Mingdong Zhou, Yichang Liu, and Zhongqin Lin. “Topology optimization of thermal conductive support structures for laser additive manufacturing”. In: *Computer Methods in Applied Mechanics and Engineering* 353 (2019), pp. 24–43. ISSN: 0045-7825.

# 6

## APPLICATIONS

*This chapter presents several additional applications of the the novel TO algorithm presented in Chapter 4 (2D) and Chapter 5 (3D). First, a metallic mould insert, which is to be produced by the Laser Powder Bed Fusion (LPBF) technique, is considered and a topology optimization problem with hotspot constraint is defined. A 50% reduction in mass is achieved while enhancing the manufacturability of the insert. Next, the idea of avoiding overheating is extended for designing efficient support structures whereas the design of the part remains fixed. The modified formulation along with preliminary results are presented which highlight the potential of the novel TO method for efficient support structure designs. A concept of vicinity penalization is introduced which promotes minimization of part-support interface area in order to reduce post-processing costs. The method results in 'tree-like' supports which are expected to provide desired heat evacuation behavior. Finally, conclusions and a discussion on future perspectives are presented.*

---

Parts of this chapter have been published in [Precision Metal Additive Manufacturing, Chapter 2: Topology Optimisation Techniques \(CRC Press, 2020\)](#).

## 6.1. TO OF AN INJECTION MOULD INSERT

The case study has been provided by a manufacturer of consumers goods where TO was performed on a metallic mould insert, which is to be produced by L-PBF out of Maraging 300 steel. The reduction of mass for the purpose of reducing L-PBF production time and material use is considered during the design stage. TO is, therefore, selected as an ideal approach for designing the mould insert. Using the double symmetry of the original mould design, only one quarter of the mould is optimized, and the isometric views of the top and bottom of the quarter mould are shown in Figure 6.1a and b, respectively. The black arrow in Figure 6.1b signifies build direction with the design having a conformal cooling channel running beneath the mould cavities. Here, the yellow regions represent the fixed geometric features, *i.e.* this region has been excluded from the TO design domain and is referred to as non-design domain. The design space, represented in pink, is the domain where the TO could optimize the material layout for the given set of loads, boundary conditions and volume constraint, with the objective of maximizing the stiffness of the mould.

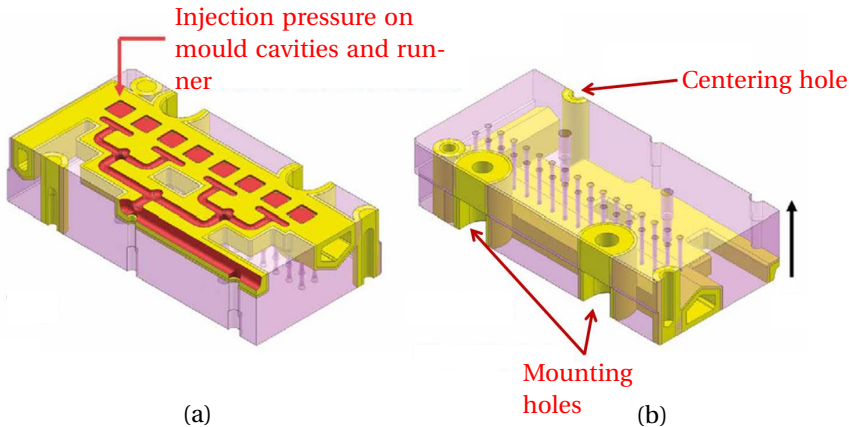


Figure 6.1: Design space for TO of an injection mould shown from (a) top and (b) bottom. The yellow features indicate regions that should remain intact during the TO process, *i.e.*, so-called non-design domain. Pressure due to plastic injection is applied on the runner cavities shown in red. The interfaces for mounting and centering holes with the design domain are considered fixed [12].

The loading condition mimicked the injection pressure load on the runners and mould cavities using the maximum possible pressure multiplied by a safety factor of 1.5. The water pressure in the cooling channel is considered negligible. Mounting holes and centering holes (highlighted in Figure 6.1b) were set as fixed. The mechanical properties of Maraging 300 steel were used. The black arrow in Figure 6.1b represents the build direction. Details on different numerical and physical parameters can be found in Sinico et al. [12].

The optimized designs using standard and hotspot TO are shown in Figure 6.2a and b, respectively. The presented results are shown for half of the mould while only quar-



ter was used for TO. In accordance with the used volume constraint, volume has been reduced to 50% of the initial design for both of the cases. Lastly, Figure 6.3 shows the hotspot fields for both of the designs with a common temperature scale normalized between 0 and maximum value found across both designs. It was found that maximum hotspot temperature was 30% lower in the design using hotspot TO compared to that of standard TO.

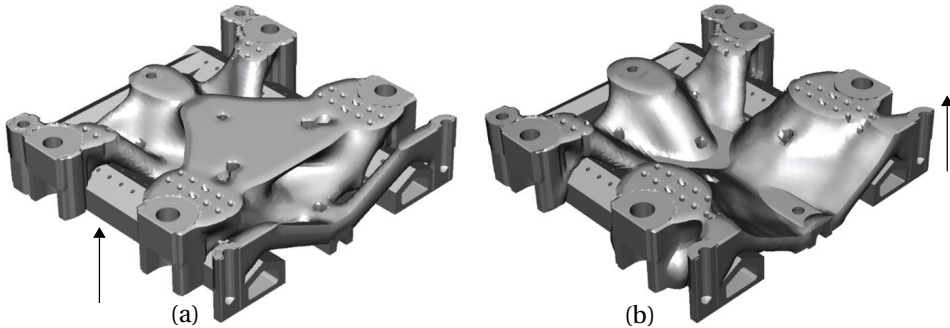


Figure 6.2: (a) Design obtained using standard TO (b) Design obtained using hotspot TO. The black arrows indicate the build direction.

This case study demonstrates that adopting enhanced TO methods at an early design stage can assist in conceptualising efficient, low-mass, easy-to-manufacture designs for precision applications. This can directly lead to savings in cost and time, and can even make the difference between a manufacturable, economically feasible solution or an infeasible one.

## 6.2. TO FOR SUPPORT STRUCTURES FOR EFFICIENT HEAT EVACUATION

In this section, the hotspot TO method is applied to address support structure optimization. In both laser and electron beam based powder bed fusion (PBF) techniques, the manufactured specimens generally consist of the functional part and the sacrificial support structures. The latter are used to facilitate a defect and overheating-free manufacturing.

There are three main purposes associated with these supports. First, they act as heat evacuating members and hence prevent local overheating in the part. LPBF parts remain submerged in the powder, *i.e.* all lateral sides remain in contact with the un-molten powder which has approximately 1% of the thermal conductivity of the bulk material [11]. Consequently, the features which do not allow proper heat evacuation, *e.g.* acute overhangs, funnel-shaped regions and thin connections, are prone to local overheating [8]. **Craeghs** performed in-situ monitoring of the melt pool and showed that significant enlargement of the meltpool occurs when heat is not properly evacuated. It is shown in

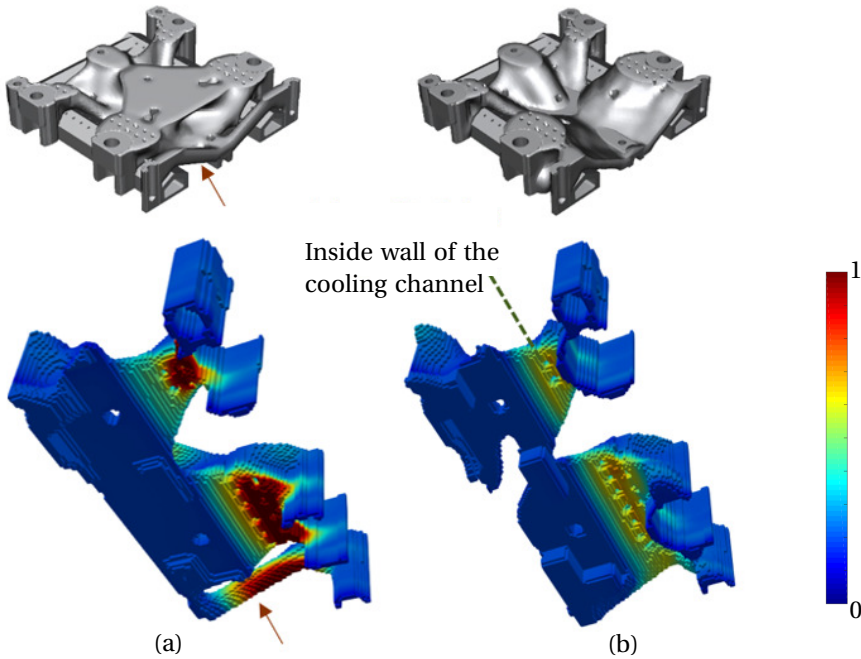


Figure 6.3: Normalized hotspot fields found using localized steady-state AM model *i.e.* hotspot detection from Chapter 4 as a post optimization step for (a) design obtained using standard TO (b) design obtained using hotspot TO. Due to the symmetry in design, temperature fields are shown only for the quarter of the design.

the same study that use of supports results in more uniform temperature distributions, leading to reduced overheating. Moreover, the uneven and cyclic heat distribution contributes to formation of residual stresses which leads to part distortion. Supports also provide stiffness against the distortion and hence, enhance manufacturability. Lastly, due to the nature of layer-by-layer manufacturing, most of the AM processes are unable to print features with long overhangs as they cannot sustain their self-weight. Therefore, supports can provide stiffness for carrying the structural load of the part. On one hand, high support volume will perform better in context of both thermal and structural aspects, but on the other hand, it would increase material waste, printing time and post processing efforts. Therefore, there has been significant research efforts for designing optimal supports that could efficiently dissipate heat and provide structural strength using less material.

Figure 6.4 presents an overview of existing methods commonly used for optimizing supports. Different methodologies can be divided primarily into two groups: manual design and topology optimization based techniques. (Computer-aided) manual support design methods generally use predefined geometries in a repeated pattern to reduce the support volume. Some of the commonly used configurations are based on lattice structures [13] and tree-like shapes [14], shown in Figure 6.4a and Figure 6.4b, respectively.

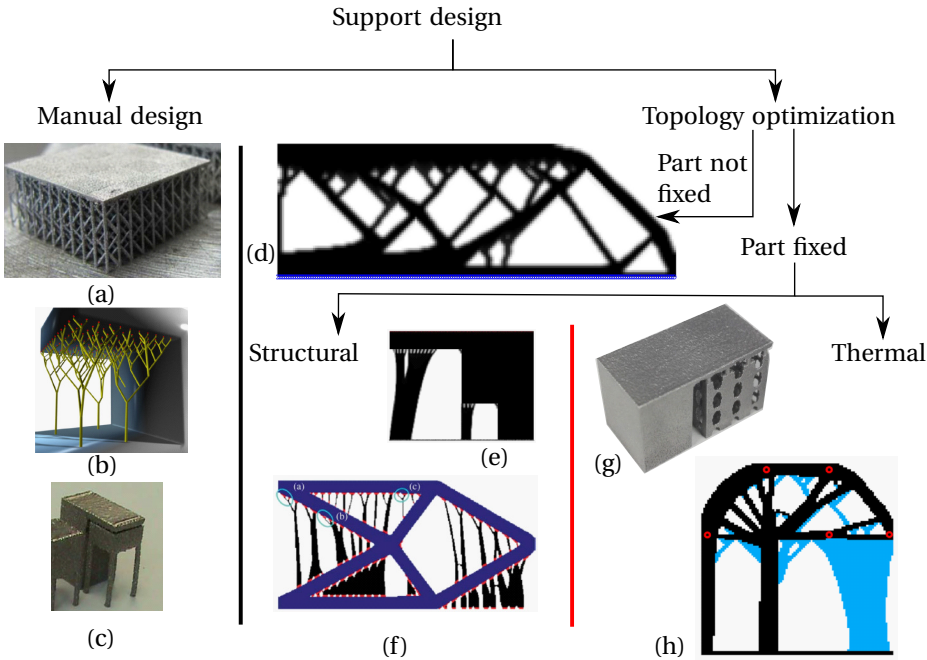


Figure 6.4: A classification of existing literature on support optimization. Supports obtained using manual design techniques: (a) Lattice supports [13] (b) Tree-like supports [14] (c) Contact less supports [2]. Topology optimization based methods: (d) AM filter [6] (e) and (f) supports designed considering structural load of the part [4, 16]. (g) and (h) supports designed considering thermal load of the part. [3, 15]

Another interesting concept, mainly utilized in EB-PBF, is that of contact-less supports [2] shown in Figure 6.4c. Here, a small gap is intentionally provided between part and support which facilitates easy removal of supports while still providing sufficient heat evacuation for the part. The utilization of contact-less supports was shown in the context of LPBF by Paggi et al. [9]. The aforementioned manual design methods depend heavily on the designer's experience and do not provide the optimal supports suited specifically for a particular part design. On the other hand, topology optimization (TO) provides a systematic approach for finding optimized structures aiming for a predefined functionality with operational constraints. Therefore, there has been a significant research interest for developing TO formulations which could address the need, placement and layout of support structures during the design process.

Next, the research in TO for reducing support requirements can be further classified into two groups. The first set of techniques focuses on optimization of parts so that the need for supports is already minimized. A representative example of such technique is the AM filter presented by Langelaar [5]. The method performs a printability check using a geometrical overhang criterion and finds an optimized part design which might not need any supports. An example of such optimized part design is shown in Figure 6.4d where features with acute overhang angles are not allowed during the optimization. Sim-

ilar to this, there are several formulations proposed in the literature which focus on optimizing part design such that support requirements are minimal [7]. However, the quest for finding fully self-supporting designs restrict the design space. Due to this, part performances are generally compromised. In order to address this, researchers have developed TO techniques which focus entirely on support optimization while the part design remains fixed. This is also motivated by the fact that often designs are obtained after many time-consuming iterations and it is not convenient to modify them at a later stage.

The existing TO techniques on support optimization can again be divided into two subgroups. The first subgroup considers a structural load of the part and optimizes support entirely with an objective of carrying this load. Examples of such approaches as shown in Figure 6.4e and f [4, 16]. Such techniques are focused on polymer based AM processes where supports are mainly used for providing stiffness against gravity and heat evacuation is not critical. The other subgroup deals with metal AM processes where operating temperatures are high and the main role of support is to conduct away the excess heat. Since the TO method presented in this chapter is also related with metal AM and focuses on the thermal aspect, a brief summary of such methods is presented below.

6 Huang et al. [3] used a cantilever shape, shown in Figure 6.4g, for which TO was performed with a thermal compliance minimization problem which aims to maximize heat conduction through the supports. A number of localized volume constraints were used which led to a lattice based support design. For comparison, the lattice based TO support was manufactured along with other commonly used support shapes, *i.e.*, pillar, wall and so-called “TY” support which basically resemble an inverted ‘Y’ shape. The warpage of the overhanging surface, which is taken as a measure of heat accumulation, was measured and it was shown that the TO based supports performed better. The method shows the promising potential of the TO method and provides useful experimental observations. However, as the focus of the method is on the heat evacuation capacity of the supports, a validation step using thermal history would have been more useful. Although warpage is an indicative measure of overall quality, it can not be assumed to have an one-on-one co-relation with heat accumulation and other factors such as, residual stresses, recoater time, also contribute significantly to the warpage. Another interesting paper by Zhou, Liu, and Lin [15] integrates a transient AM model with TO with an objective to minimize temperatures at selected points in the part. The supports (shown in blue in Figure 6.4h) are optimized while the part design remains fixed (shown in black). Although promising, the method is reported to be computationally very expensive even with several major simplifying assumptions.

The presented literature review highlights that although, there has been a significant effort towards optimizing support structures, a TO method which can generate support structures for heat evacuation in a computationally efficient manner is still lacking. In this regard, the slab based localized steady-state thermal model developed in Chapter 2 is an ideal candidate for quickly identifying the regions in a given design which are critical from the point of view of heat evacuation. This information can then be used for designing optimal supports. Below, we describe an initial attempt to introduce the benefits

of the computationally inexpensive hotspot analysis to the problem of support structure design.

### 6.2.1. PROBLEM FORMULATION

An L-PBF part  $\Omega$  is assumed to be the starting point for the presented support optimization algorithm. The part  $\Omega$  and its build orientation remain fixed, and support structures are optimized for minimal volume and part-support contact area, while achieving a desired level of heat evacuation. The latter is motivated by the fact that the post-processing efforts are directly proportional to the contact area [10]. Although the method can be applied to any arbitrary part design, here we explain the algorithm using a design of an inverted L shape shown in Figure 6.5a. A brief summary of the entire process is given below while details are provided in subsections:

1. As the first step, the fixed part  $\Omega$  is analyzed using the simplified AM model and the hotspot field  $\mathbf{T}_{HS}(\Omega)$  is obtained.
2. Next, a virtual heat load  $\mathbf{Q}_{vir}$  is calculated which has same the spatial distribution as the hotspot field. A new boundary value problem is defined where this virtual heat flux acts as a heat load while the bottom of the domain, *i.e.*, the baseplate acts as a heat sink. The motivation behind this load definition is that the temperatures are highest in the regions prone to overheating and hence, the heat flux  $\mathbf{Q}_{vir}$  (which is proportional to the temperatures) represents the heat evacuation requirements. Note that this virtual load is not the physical heat flux imposed due to the moving laser. Instead, it is only a measure of relative overheating that features would experience, if manufactured without supports. Also it should be acknowledged that this is one way of defining the heat load for TO and other definitions can also be investigated.
3. The objective of the optimization problem is to minimize support volume. Additionally, a novel vicinity penalization scheme is used where penalty weights for reduction of the part-support contact area are introduced in the objective.
4. The heat evacuation performance of the support structures is quantified by the thermal compliance and controlled using a constraint in the optimization problem. In order to provide for a reference value, the best-case scenario of a design domain fully filled by support material is analyzed and the associated thermal compliance is computed in a pre-optimization step. This facilitates formulation of the thermal compliance constraint.
5. Finally, the TO problem of minimizing support volume and part-support contact area with thermal compliance as a constraint is solved using MMA.

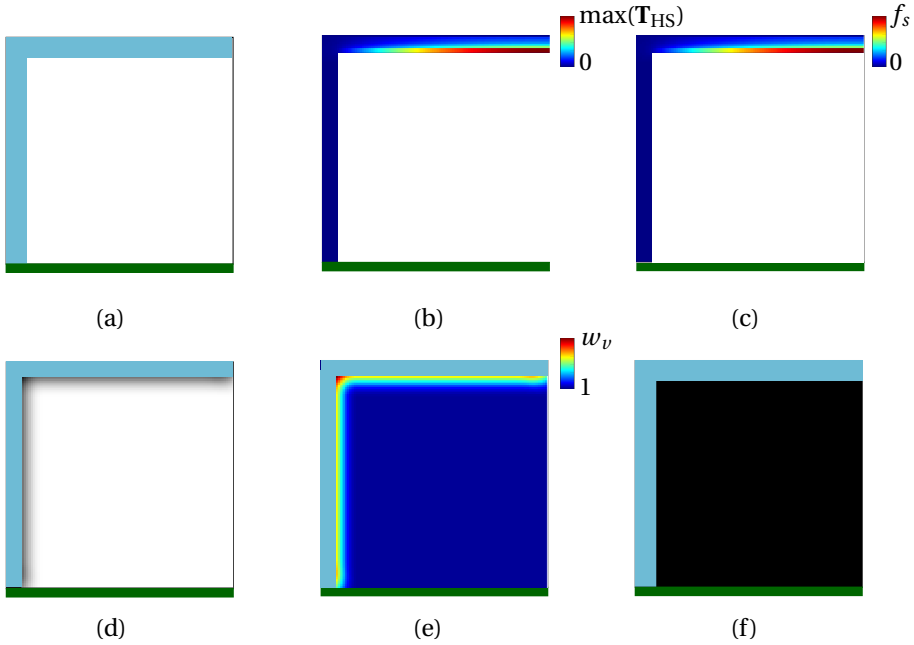


Figure 6.5: (a) Inverted L shape part  $\Omega$  considered for explaining the support optimization algorithm. (b) Hotspot temperature field  $T_{HS}(\Omega)$  obtained using the simplified AM model. (c)  $Q_{vir}$  calculated using the hotspot temperature field with  $f_s$  as the scaling factor such that  $\max(Q_{vir}) = f_s$ . (d) Filtered density field using  $R = 6$  elements. (e) Vicinity penalization field used for minimizing part-support contact area. (f) Part  $\Omega$  with fully solid support used for calculating the reference thermal compliance.

### CALCULATION OF VIRTUAL HEAT LOAD

As discussed, the first step is to subject the design  $\Omega$  to the hotspot analysis to identify critical zones of overheating and a hotspot map  $\mathbf{T}_{\text{HS}}(\Omega)$ <sup>1</sup> is obtained. The hotspot map  $\mathbf{T}_{\text{HS}}(\Omega)$  for the inverted L shape is shown in Figure 6.5b. Recall from Chapter 4 that the hotspot map is found using a series of localized steady-state thermal analyses. The discretization scheme used for support TO is identical as used in Chapter 4 with the array of element densities denoted as  $\tilde{\rho}$ . Next, the hotspot map is used to calculate a virtual heat flux as

$$\mathbf{Q}_{\text{vir}} = f_s \frac{\mathbf{T}_{\text{HS}}}{\max(\mathbf{T}_{\text{HS}})}, \quad (6.1)$$

where  $f_s$  is a scaling factor. The heat flux calculated here contains the magnitudes of nodal heat fluxes. The normalization by  $\max(\mathbf{T}_{\text{HS}})$  controls the magnitude of  $\mathbf{Q}_{\text{vir}}$  such that  $\max(\mathbf{Q}_{\text{vir}}) = f_s$ . As mentioned in Section 6.2.1, the motivation behind this heat load definition is that regions with high hotspot temperatures indicate overheating and require heat evacuation.

### DEFINING THE VICINITY PENALIZATION FIELD

One of the criteria to design efficient supports is to minimize part-support contact area [10]. A large contact area increases post-processing costs during support removal. Moreover, the part-support interface exhibits high surface roughness and hence requires dedicated operations for improving the surface quality. Therefore, in this work, a penalization zone is defined in the vicinity of the part which compels the optimizer to use less material near the part surface while optimizing the heat evacuation performance of the support.

The density filter proposed by Bruns and Tortorelli [1] is used to define the vicinity penalization zone for the given part. Note that this filtering scheme was originally proposed for imposing a length scale and to avoid checker-boarding during topology optimization and the scheme is used for the originally intended purposes in the support TO, formulated later in Section 6.2.2. This scheme essentially operates such that the filtered density for each finite element is defined as a weighted mean of the densities of neighbouring elements located within a distance  $R$  from the centre of the element, with  $R$  referred to as the filter radius. It was identified that the same filtering scheme can be efficiently used for defining a penalization zone near the part and the procedure is explained below.

The density filtering is applied on the discretized representation of the part  $\Omega$  with filtered density field shown in Figure 6.5d, represented as  $\tilde{\Omega}$ . It can be observed that this field decays moving away from the part boundary, with decay distance controlled by filter radius  $R$ . The entire field is multiplied by a weight factor  $w_v$  and unity is added to get the resulting vicinity penalization contours, shown in Figure 6.5e. As intended, the field has a high penalization value near the part while it decays moving away from the

<sup>1</sup>The boldface symbol signifies that  $\mathbf{T}_{\text{HS}}(\Omega)$  is an array.

part with value of 1 far away from the part. Since the intention of this field is to control material distribution only in the support design domain, the penalization field is only considered in the support region and is neglected for the elements belonging to the part. An array  $\mathbf{L}$  is defined containing the vicinity penalization field in the same order as in  $\tilde{\rho}$ . An objective function is defined as  $J = \mathbf{L}^T \tilde{\rho}$  which basically returns a weighted sum of elements' volumes, with weights coming from the constructed vicinity penalization field. Note that the array  $\mathbf{L}$  is determined as a pre-optimization step and remains constant during optimization. The objective function  $J$  is minimized during the optimization which leads to minimization of support volume. In addition to this, support-part contact area is also reduced as higher cost is implied for adding material in the vicinity of the part. The weight factor  $w_v$  provides a parameter for controlling the intensity of this penalization effect and influence of this parameter is discussed later in Section 6.2.3.

### CALCULATION OF REFERENCE COMPLIANCE

While the objective of the optimization remains support volume minimization, the heat evacuation efficiency of supports is controlled using thermal compliance, defined as a constraint. The best-case scenario of fully solid support, shown in Figure 6.5f, is taken as a reference and provides a lower bound value for the thermal compliance. Hence, compliance calculated using fully solid support is referred to as  $c_{\text{ref}}$ . Next, a constraint is formulated such that thermal compliance of the structure  $c$  is allowed to be greater than  $c_{\text{ref}}$  by an efficiency factor  $\eta$  *i.e.*

$$\eta \frac{c}{c_{\text{ref}}} - 1 \leq 0. \quad (6.2)$$

The numerical value of parameter  $\eta$  basically controls the efficiency of supports for heat evacuation with  $\eta = 1$  representing fully solid supports. Moreover, the choice of  $\eta$  has a direct impact on the volume of supports that is needed to achieve the desired efficiency. This aspect is later discussed in Section 6.2.3.

### 6.2.2. SUPPORT OPTIMIZATION

The complete problem of support optimization can now be stated as

$$\min_{\rho} : J(\rho) = \mathbf{L}^T \tilde{\rho}, \quad (6.3a)$$

$$\text{subject to} \quad (6.3b)$$

$$c = \mathbf{Q}_{\text{vir}}^T \mathbf{T}(\tilde{\rho}), \quad (6.3c)$$

$$\eta \frac{c}{c_{\text{ref}}} - 1 \leq 0, \quad (6.3d)$$

$$\mathbf{G}\mathbf{T} = \mathbf{Q}_{\text{vir}} \quad (6.3e)$$

$$\mathbf{0} \leq \rho \leq \mathbf{1}. \quad (6.3f)$$

Here,  $\rho$  is the array of design variables, Eq. (6.3e) represent the discretized version of the heat equation with  $\mathbf{G}$  representing the global conductivity matrix and  $\mathbf{T}$  represents



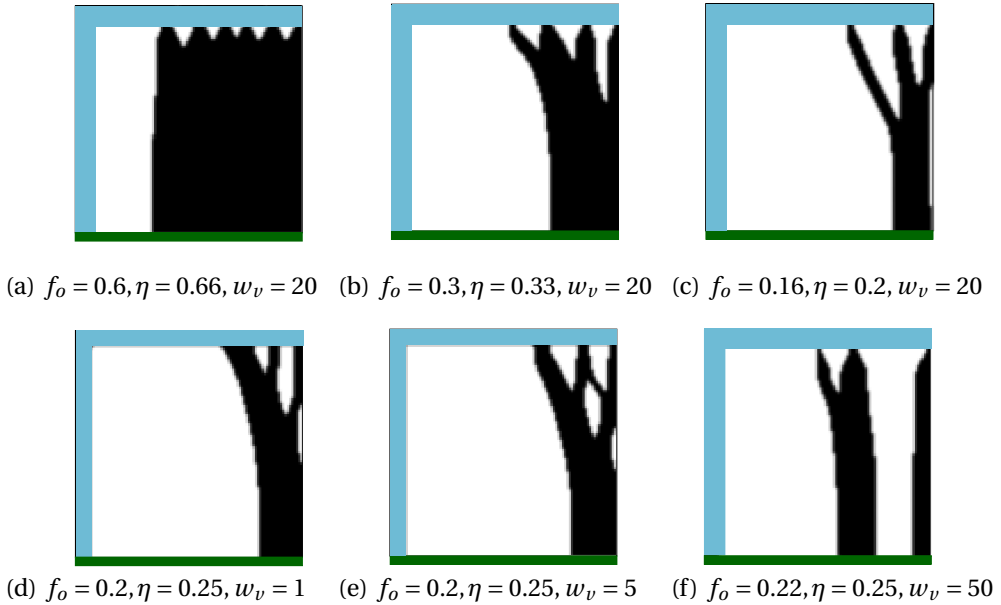


Figure 6.6: Optimized supports for the inverted L shape part. (a)–(c) presents the results for varying efficiency  $\eta$  with a constant vicinity penalization weight  $w_v = 20$ . Volume fraction for supports  $f_o$  is also given for each result. It is evident that more support material is needed to meet the stricter thermal compliance constraint with a higher value of  $\eta$ . (d)–(f) presents the results for varying vicinity penalization weight with a constant value of  $\eta = 4$ . A diminishing part-support contact area can be observed with increasing  $w_v$ .

the nodal temperatures. The definition of thermal compliance is given by Eq. (6.3c). Recall that in addition to defining the vicinity penalization zone, the density filtering scheme described by Bruns and Tortorelli [1] has also been used to impose a length-scale and avoid checker-boarding. It gives the relation between design variables and element densities as

$$\tilde{\rho}_e = \frac{\sum w_{e,i} \rho_i}{\sum w_{e,i}}, \quad (6.4)$$

where,  $\tilde{\rho}_e$  is the density of an element  $e$  centered at position  $\mathbf{r}_e$  and  $w_{e,i}$  is a weight factor at position  $\mathbf{r}_i$ . The weight factor is defined using a linearly decaying distance function:  $w_{e,i} = \max(0, R - \|\mathbf{r}_i - \mathbf{r}_e\|)$  with filter radius  $R$  set as 1.5 times elements' thickness for the presented results.

### 6.2.3. 2D RESULTS

A set of results for the case of inverted L shape is shown in Figure 6.6. As a general observation, the support optimization leads to tree-like structures which connect the most severely heated overhanging region with the baseplate for heat evacuation. The set of designs in Figure 6.6a–c show the effect of efficiency  $\eta$  which controls the level of compromise in thermal compliance as compared to a fully solid support, see Eq. (6.2). Here,

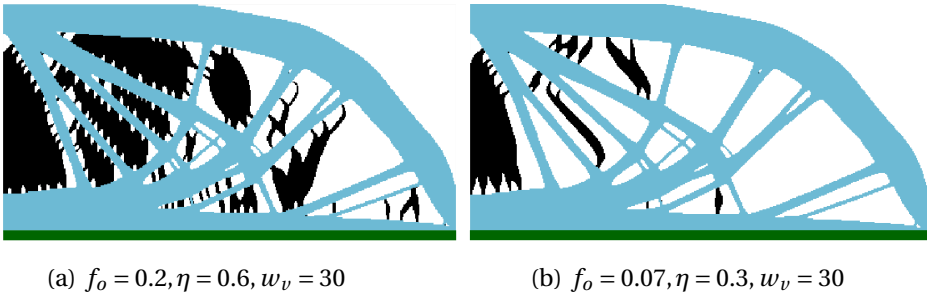


Figure 6.7: Optimized supports for a complex part. As expected, lower  $\eta$  value delivers a lower support volume.

it is visible that thinner structures are generated with decreasing efficiency  $\eta$ . This is also reflected by the decreasing trend of the total support volume with decreasing  $\eta$ . Next, the set of designs in Figure 6.6d–f show the influence of weight  $w_v$  used for controlling the severity of the vicinity penalization field and it is evident that there is a tendency to reduce the part-support interface as  $w_v$  increases.

In order to test the generality and robustness of the proposed algorithm, support optimization is performed on a relatively complex 2D design and the results for  $\eta = 1.6$  and  $\eta = 3$  are shown in Figure 6.7a and b, respectively. Here, again lower support volume is obtained for a lower value of  $\eta$ .

## 6

#### 6.2.4. 3D RESULTS

It remains to demonstrate the developed support optimization method on a realistic 3D part. For this purpose the method is applied on the part shown in Figure 6.8a. The part design is provided by an industrial partner on which the idea of contact-less supports have been investigated and optimized gap between part and support has been identified by experimental trials. Figure 6.8b shows the fixed horizontal disk of contact-less support in red with associated dimensions. This disk serves as a heat evacuating member for the horizontal region of the part which would otherwise manifest overheating during manufacturing, and is separated from the part by a gap of  $500 \mu\text{m}$ . The optimization problem is formulated for generating the supports connecting the horizontal disk of contact-less support and the baseplate. The concept of reducing part-support interface area has not been used here since support detachment from the disk is not needed. Also, only quarter of the disk is simulated, taking the advantage of the symmetry.

The found solution using  $\eta = 0.2$  is shown in Figure 6.8c and an isometric view is shown in Figure 6.8e. The hotspot temperature field for the part alone is shown in Figure 6.8d where the maximum normalized temperature is found to be 121.4 for the overhanging region. Simulating the part together with the contactless support and the actual gap of  $500 \mu\text{m}$  proved difficult in the applied numerical setting. The hotspot fields of part with support are therefore determined with no gap, shown in Figure 6.8f, and with

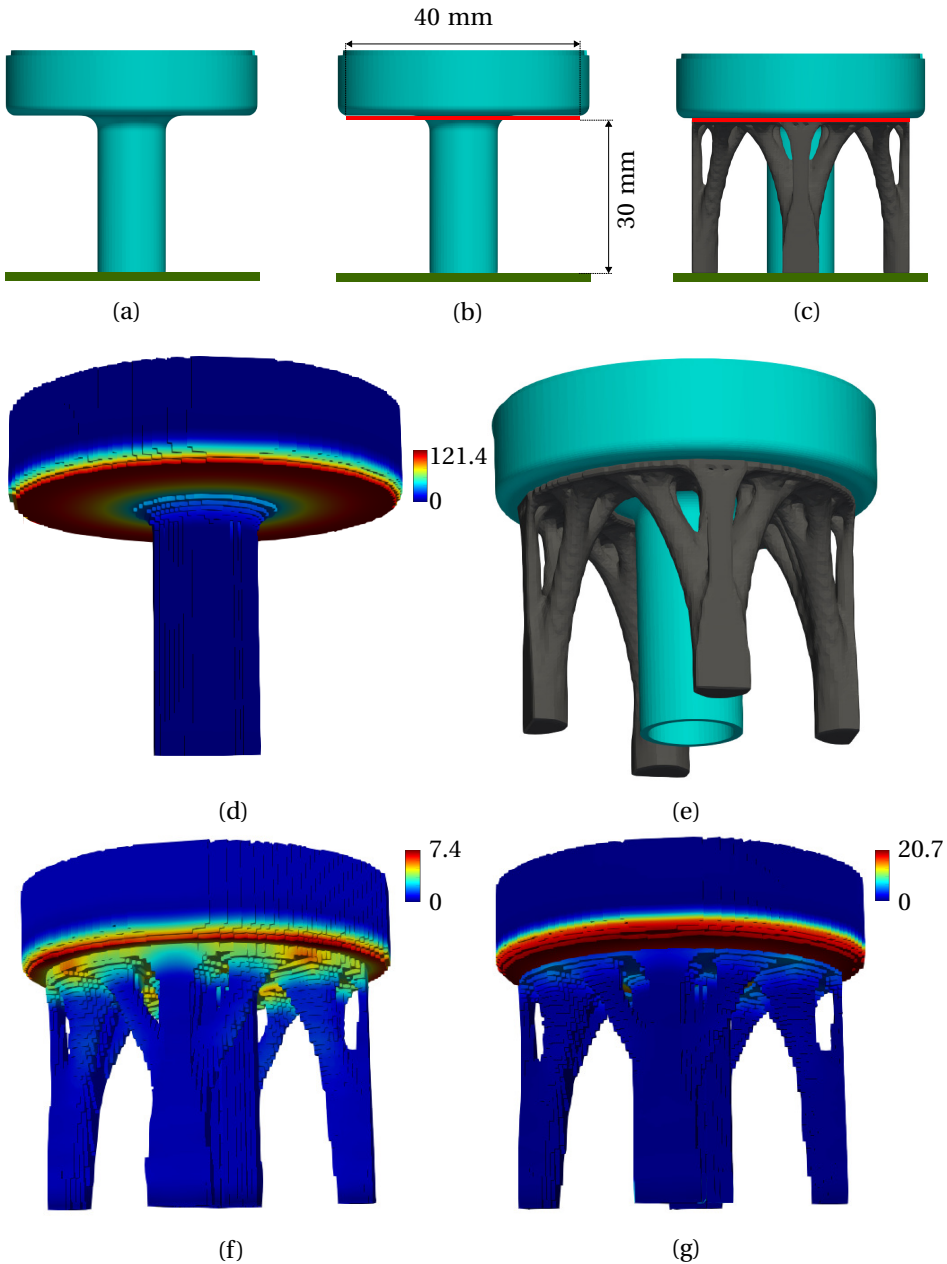


Figure 6.8: Support optimization for a 3D part using contact-less support. (a) The part considered for support optimization. (b) Part and contact-less support disk (red) with dimensions. (c) The optimized support for  $\eta = 0.2$  with  $f_o = 0.15$ . (d) Hotspot field found only considering the part. (e) An isometric view of the optimized supports. (f) Hotspot field found assuming no gap between part and support. (g) Hotspot field found assuming a gap of 1 mm between part and support.

a gap of 1 mm, shown in Figure 6.8g. These cases consider two extremes and the true performance will fall between them. Powder conductivity of 1% as compared to bulk material is considered for performing the hotspot analysis [11]. As expected, the maximum temperatures for both cases are found to be much lower than that found without any supports. Maximum normalized temperatures lie between 7.4 and 20.74, which corresponds to reductions by a factor 6 to 16 compared to the case without support. This case study shows that the algorithm can be easily scaled to a real-size part and deliver supports which can provide efficient heat evacuation while minimizing material waste.

### 6.3. CONCLUSIONS

In this chapter, two applications of the novel hotspot TO method have been presented. Application of hotspot TO on an industrial test case shows promising potential of the presented algorithms for increasing manufacturability of complex real-size AM parts. Furthermore, hotspot TO was utilized for designing efficient support structures for a given part.

Although the support optimization method delivers promising support designs which take heat evacuation into account while minimizing volume and contact area, experimental validation is still needed for establishing the performance of the proposed optimal supports. One way to achieve this is by comparing the manufacturability enhancement they provide against commonly used lattice based supports. The metrics that should be used for evaluating the performance of the support are also yet to be determined. Some possible options are: thermal history of part, surface metrology for observing cross-related issues, post-processing efforts. Next, other options of boundary conditions can also be considered while formulating the optimization problem. For example, in the current formulation  $Q_{vir}$  is determined in an ad-hoc manner from hotspot field  $T_{HS}$ . Alternatively, a Dirichlet boundary condition can also be defined where load temperatures can be directly specified using  $T_{HS}$ . Lastly, supports also provide stiffness to the part against the distortion. This aspect can also be considered while formulating the optimization problem and hence, seen as an avenue of future research.

### REFERENCES

- [1] Tyler E. Bruns and Daniel A. Tortorelli. “Topology optimization of non-linear elastic structures and compliant mechanisms”. In: *Comput Method Appl M* 190.26 (2001), pp. 3443–3459. ISSN: 0045-7825.
- [2] Kenneth Cooper, Phillip Steele, Bo Cheng, and Kevin Chou. “Contact-Free Support Structures for Part Overhangs in Powder-Bed Metal Additive Manufacturing”. In: *Inventions* 3.1 (2018). ISSN: 2411-5134.
- [3] Renkai Huang, Ning Dai, Xiaosheng Cheng, and Lei Wang. “Topology optimization of lattice support structures for heat conduction in selective laser melting”. In: *The*

- International Journal of Advanced Manufacturing Technology* 109.7 (Aug. 2020), pp. 1841–1851. ISSN: 1433-3015.
- [4] Yu-Hsin Kuo, Chih-Chun Cheng, Yang-Shan Lin, and Cheng-Hung San. “Support structure design in additive manufacturing based on topology optimization”. In: *Structural and Multidisciplinary Optimization* 57.1 (Jan. 2018), pp. 183–195. ISSN: 1615-1488.
- [5] Matthijs Langelaar. “An additive manufacturing filter for topology optimization of print-ready designs”. In: *Structural and Multidisciplinary Optimization* (July 2016).
- [6] Matthijs Langelaar. “An additive manufacturing filter for topology optimization of print-ready designs”. In: *Struct Multidiscip Optim* 55.3 (Mar. 2017), pp. 871–883. ISSN: 1615-1488.
- [7] Jikai Liu, Andrew T. Gaynor, Shikui Chen, Zhan Kang, Krishnan Suresh, Akihiro Takezawa, Lei Li, Junji Kato, Jinyuan Tang, Charlie C. L. Wang, Lin Cheng, Xuan Liang, and Albert. C. To. “Current and future trends in topology optimization for additive manufacturing”. In: *Struct Multidiscip Optim* 57.6 (June 2018), pp. 2457–2483. ISSN: 1615-1488.
- [8] Raya Mertens, Stijn Clijsters, Karolien Kempen, and Jean-Pierre Kruth. “Optimization of Scan Strategies in Selective Laser Melting of Aluminum Parts With Down-facing Areas”. In: *Journal of Manufacturing Science and Engineering* 136(6) (Dec. 2014).
- [9] Umberto Paggi, Rajit Ranjan, Lore Thijs, Can Ayas, Matthijs Langelaar, Fred van Keulen, and Brecht van Hooreweder. “New support structures for reduced overheating on downfacing regions of direct metal printed parts”. English. In: *Proceedings of the Annual International Solid Freeform Fabrication Symposium*. 30th Annual International Solid Freeform Fabrication Symposium : An Additive Manufacturing Conference ; Conference date: 12-08-2019 Through 14-08-2019. University of Texas, 2019, pp. 1626–1640.
- [10] Rajit Ranjan, Rutuja Samant, and Sam Anand. “Integration of Design for Manufacturing Methods With Topology Optimization in Additive Manufacturing”. In: *Journal of Manufacturing Science and Engineering* 139.6 (Jan. 2017), pp. 61007–61014. ISSN: 1087-1357.
- [11] Marleen Rombouts, L. Froyen, A. Gusarov, El Hassane Bentefour, and Christ Gloorieux. “Photopyroelectric measurement of thermal conductivity of metallic powders”. In: *Journal of Applied Physics* 97 (Dec. 2004), p. 24905.
- [12] Mirko Sinico, Rajit Ranjan, Mandanà Moshiri, Can Ayas, Matthijs Langelaar, Ann Witvrouw, F Keulen, and Wim Dewulf. “A mold insert case study on topology optimized design for additive manufacturing”. In: *30th Annual International Solid Freeform Fabrication Symposium, SFF* (2019).
- [13] Giovanni Strano, L. Hao, Richard Everson, and Ken Evans. “A new approach to the design and optimisation of support structures in additive manufacturing”. In: *The International Journal of Advanced Manufacturing Technology* 66 (June 2012).

- [14] Juraj Vanek, Jorge Garcia Galicia, and Bedrich Benes. “Clever Support: Efficient Support Structure Generation for Digital Fabrication”. In: *Computer Graphics Forum* 33 (Aug. 2014).
- [15] Mingdong Zhou, Yichang Liu, and Zhongqin Lin. “Topology optimization of thermal conductive support structures for laser additive manufacturing”. In: *Computer Methods in Applied Mechanics and Engineering* 353 (2019), pp. 24–43. ISSN: 0045-7825.
- [16] Mingdong Zhou, Yichang Liu, and Chuang Wei. “Topology optimization of easy-removal support structures for additive manufacturing”. In: *Structural and Multidisciplinary Optimization* 61.6 (June 2020), pp. 2423–2435. ISSN: 1615-1488.

# 7

## CONCLUSIONS AND RECOMMENDATIONS

### 7.1. CONCLUSIONS

This thesis demonstrates the effectiveness of a novel topology optimization (TO) approach for avoiding overheating defects in metal additive manufacturing (AM). Unlike previously presented TO methods in the literature which employ geometry-based considerations, the physics-based TO method presented here incorporates the local thermal characteristics of a part during the printing process. Although the discussion in this thesis remained focused on overheating, the merits associated with a physics-based yet computationally efficient methods have more general implications. This is because a physics-based approach captures the AM process in a more intimate manner compared to a geometrical approach, and hence, it has a high chance of predicting problems in metal AM to enhance manufacturability. In this thesis, numerical and experimental investigations revealed that the physics-based TO method indeed leads to designs with much less overheating, which is not guaranteed by the geometry-based TO approaches.

The first half of the thesis deals with the investigation of commonly used simplifications in part-scale modelling of the metal AM process. In Chapter 2, these simplifications are studied based on the assumed spatial and temporal resolutions for modelling the process. In the spatial regime, material lumping choices are investigated and it is concluded that layer-by-layer models are sufficient for capturing peak temperatures while patch-by-patch models are required for analysing the influence of scan vectors. In the temporal regime, two extremes of defining laser exposure times, *i.e.*, flash and gradual heating schemes are investigated. It is concluded that if peak process temperatures are to be captured, flash heating should be used, but this requires a fine spatial discretization of the part. While gradual heating schemes are suitable for capturing temperatures far away from the layer being deposited, and allow for coarser meshes and hence requiring lower computational effort. In Chapter 3, once again various simplifications are

studied, concentrating on predicting local overheating using simplified LPBF models. Using high-fidelity transient simulations, it is shown that overhang control on geometrical basis does not necessarily guarantee overheating avoidance. Based on this finding, it is concluded that commonly used geometry-based TO methods which simply prohibit acute overhangs are not sufficient for avoiding overheating. Next, it is concluded that a steady-state thermal analysis can predict overheating prone features while providing extremely high computational gains compared to a transient analysis.

The second half of this thesis deals with the second research question: how can topology optimization (TO) be used for designing LPBF parts which are more robust against overheating? This has been thoroughly investigated in Chapter 4 and Chapter 5. It is evident that establishing a sufficiently accurate and computationally efficient simplified LPBF model is instrumental for developing a physics-based TO approach. However, understanding the scope/limitations of simplifications in LPBF modelling becomes especially important. This is because potentially any simplified model can be coupled with TO but a flawed model can be exploited by the optimizer to render optimized designs which will fail in reality. The community should therefore remain prudent about the use of simplified LPBF models and should always verify their range of validity. The balance between accuracy and computational efficiency can be used as a metric to judge the usefulness of a simplified model to be integrated with TO. However, it should also be acknowledged that establishing the validity of a simplified model requires significant numerical/physical experimentation. If the validity of the underlying simplified LPBF model cannot be thoroughly established, at least post-optimization validation studies must be conducted for the TO results.

7

In Chapter 4, the simplified LPBF model based on steady-state thermal responses presented in Chapter 3 has been integrated with the density based TO. Numerical experiments revealed that the use of a robust TO formulation is necessary to obtain printable results. Based on a comparison with a geometry-based TO approach, it is concluded that geometry-based TO methods can be either insufficient or over-restrictive for overheating avoidance. The former finding is highlighted by the observation of significant overheating in geometry-based TO design, numerically in Chapter 4 and experimentally in Chapter 5. The latter finding is evident by presence of benign overhangs in designs generated by physics-based TO, again, demonstrated numerically in Chapter 4 and experimentally in Chapter 5. From the validation experiments presented in Chapter 5, it is found that the novel physics-based TO is capable of effectively limiting thermal problems in an AM part. It is also concluded that hatch patterns significantly influence the thermal behavior and therefore the laser scanning path should also be considered while evaluating overheating. Another important learning is that during the experiments process conditions in the build chamber significantly vary for the parts which extended to the edges and corners of the build plate, leading to noise in optical tomography (OT) data.

It is highlighted in both Chapter 4 and Chapter 5, that the part performance is compromised for TO methods which considered AM-related manufacturability. This can be



undesirable in certain performance critical cases and, as a possible alternative, support optimization can be considered where part design remains intact and supports are optimized for efficient heat evacuation for enhancing manufacturability. A preliminary investigation of this idea is presented in Chapter 6, which next to test problems also included an industrial case study of an injection mould design which showcases the usability of the proposed method. It is demonstrated that the novel TO can potentially create efficient supports designed for maximum heat evacuation from the part. Although useful, the approach also raises new questions that require further investigation, for which recommendations are given in Section 7.2.

While results presented show the successful use of a simplified LPBF models in combination with TO, the method has some shortcomings. Several modelling simplifications were critically discussed in Chapter 3 while developing the most simplified model which was subsequently integrated with TO in Chapter 4. Nevertheless, the transient reference model, which was the starting point in Chapter 3, also assumed layer-by-layer deposition, *i.e.* excluding the influence of hatch patterns. This choice was made in the interest of computational efficiency and it is shown by comparison with experimental observations reported in literature that the reference model is capable of capturing overheating. However, with this simplification the model remains on the conservative side and, when coupled with TO, it might generate over-restrictive optimized designs. This in turn can reduce the performance unnecessarily. Moreover, the significant influence of hatch patterns on overheating behaviour, which was experimentally observed in Chapter 5, also highlights that inclusion of hatch information is important for a fully physics informed TO-for-AM approach. Next, due to the assumption of complete part cooling between subsequent layer depositions, the presented model does not account for the gradual heat accumulation that occurs during the build process. This becomes especially relevant for tall parts built using material with low diffusivity. Additionally, mainly due to the steady-state assumption, the simplified model provides for a qualitative analysis where temperatures do not represent the actual temperature transients. This aspect prohibits the use of the presented models for more detailed analyses, for example, micro-structure predictions.

## 7.2. RECOMMENDATIONS

In this section, recommendations are provided under three themes as a list of prospective ideas for new research directions.

### 7.2.1. THERMAL MODELLING OF AM

#### 1. Laser scanning information in the simplified AM model:

In Chapter 3, the three novel simplifications which provided maximum computational boost were built upon a high fidelity reference model. However, the reference model itself assumed a layer-by-layer material deposition and it was shown that even with this simplification, the model was capable of overheating detection. Nevertheless, it was argued in Chapter 2 that such a model assumes a worst-

case scenario and cannot capture influence of laser scanning strategies. Later, it was also observed through experimental validation in Chapter 5, that the directional effects were indeed influential for overheating. Therefore, there is a need to consider models which resolve the laser scanning and develop simplifications for these types of models. In this regard, the novel simplifications of spatio-temporal decoupling presented in Chapter 3 can already be seen as promising options and should be investigated.

## 2. **Transient thermal model for TO:**

A localized steady-state thermal model was used for the simplified LPBF model which was integrated with TO. In Chapter 3, the model was shown to be capable of providing a qualitative indication of overheating regions. In the same chapter, another simplified model was presented which used localized transient thermal analysis and was shown to provide even good quantitative match as compared to a high fidelity simulation. The localization assumption provided a computational gain of around 150 times compared to the high fidelity analysis and hence, provides for a good balance between accuracy and computational times making it suitable for coupling with TO. However, due to the transient nature of the simulation, integration with TO will require additional efforts and it was not possible to pursue this idea due to time-restrictions. Hence, it is seen as a future research topic with a promising potential. A direct benefit would be that the obtained temperatures would retain their physical meaning.

## 3. **Slab thickness estimation:**

The novel physics-based TO uses a parameter referred to as slab thickness and it determines the size of the local domain in the steady-state analysis. It indicates the thermal interaction distance up to which features influence the thermal behaviour for the newly added topmost layer. In Chapter 3, using an analytical solution to the heat equation, slab thickness was estimated as the characteristic length (also known as the mean conduction length). Although it provides an estimate, more elaborate numerical calibration using transient simulations can be performed for a more accurate prediction for a given set of material and process parameters.

## 4. **Re-thinking boundary conditions:**

The LPBF models presented in this thesis use a heat sink boundary condition (applied as a Dirichlet) at the interface between the baseplate and the part while laser energy is assumed to be deposited at the topmost layer. It is a commonly used assumption in part-scale LPBF modelling, however, other variations, *e.g.*, flux-based BC at the baseplate can also be studied. Moreover, the heat conducted to surrounding powder is considered to be negligible due to significantly lower powder conductivity. This assumption can also be relaxed with applying convection boundary conditions on the lateral surfaces of the part.

## 5. **Explore indicators for overheating detection:**

The issue of local overheating has been studied thoroughly in this thesis. For this purpose, the peak temperature attained by a material point during the simulation was used as an indicator of overheating. There are several related parameters

which have been identified and their relationship with the issue of overheating remains as a prospective topic for future investigations. For example, cooling rates, the gradual build up of heat due to part height, secondary peak temperatures etc. can be studied for developing even deeper understanding of the heat transfer phenomena during the AM process.

### 7.2.2. MECHANICAL ASPECTS

#### 1. **Experimental investigation of overheating influence on mechanical properties:**

The thesis presents an experimental study where in-situ optical tomography data is used for evaluating the overheating behaviour of a design. It is expected that a design which manifests lower overheating will also exhibit better mechanical properties. However, more experimental work is needed to verify this. Surface metrology, computer tomography (CT) and/or microstructural evaluation can be used to examine the specimens and develop more quantitative understanding about the influence of overheating on part quality.

#### 2. **Critical issues other than overheating:**

Local overheating is a critical issue which compromises LPBF part quality and hence, it was the main focus of this thesis. However, there are other major issues that drastically reduce LPBF manufacturability. In this context, the residual stresses and part deformations are the biggest concerns. However, prediction of stresses and deformations normally requires computationally demanding LPBF simulations and suffers from similar challenges as for the case of overheating. Therefore, there is a crucial need for dedicated efforts on developing simplified models and coupled TO methods which could efficiently take residual stresses and deformations into account.

### 7.2.3. EXTENSIONS

#### 1. **Utilizing machine capabilities for improving TO:**

A recent development in LPBF machines enables in-situ regulation of the laser power aiming to avoid overheating issues. This feature is typically referred to as using 'downskin parameters' where the machine switches to a more conservative set of process parameters while scanning acute overhangs. Although these are proprietary algorithms and not yet an established practise, it is presumed that they are based on geometry information. The findings in thesis suggest that these algorithms, if based solely on geometric information, might not be sufficient for overheating avoidance. For this reason, the physics-based approach can also be used for designing control algorithms for wisely regulating the laser power. Alternatively, the laser power regulation capabilities can be taken in account while development of the thermal model. This would enhance the design freedom leading to less conservative higher performance designs.

#### 2. **Improving support TO:**

Finally, the preliminary investigation into a thermal support optimization method presented in Chapter 6 requires further attention. The performance of the optimized supports should be evaluated based on the heat evacuation efficiency and

its impact on the final part quality should be examined. For this purpose, both numerical modelling and experimental research can be insightful. Based on the performance of the optimized supports, alternate formulations may be conceived.

# A

## A NUMERICAL STUDY USING ANALYTICAL SOLUTION FOR 1D HEAT TRANSFER

To capture the temperature transients, adequate mesh resolution is necessary. Therefore, it is crucial to choose the mesh size carefully. A numerical experiment of a simple 1D heat transfer is considered for which the analytical solution is already known to identify the numerical errors.

A one-dimensional domain with length  $L$  is shown in Figure A.1a. The domain is subjected to a heat flux  $Q$  from the top, and the bottom end is assumed to be a heat sink, *i.e.*  $T = T_0$ .<sup>1</sup> The initial temperature of the domain is also assumed to be  $T_0$ . These boundary and initial conditions are reminiscent of the thermal situation experienced by a typical MAM part. The analytical solution representing the evolution of temperature is given as

$$T_h^a(x, t) = T_0 + \frac{Qx}{k} \left[ 1 - 2 \sum_{n=1}^{\infty} \left( \frac{(-1)^{(n+1)}}{\lambda_n^2} \right) \sin\left(\lambda_n \frac{x}{L}\right) e^{-\frac{\lambda_n^2 \alpha t}{L^2}} \right], \quad (\text{A.1})$$

where  $x$  is position and  $\lambda_n = (2n - 1)\pi/2$ . The detailed derivation is given in Appendix B. When the heating regime ends, followed by a cooling period, heat flux is removed *i.e.*  $Q=0$ . The analytical solution during the cooling period is given as

$$T_c^a(x, t) = T_0 + \frac{2Qx}{k} \sum_{n=1}^{\infty} \frac{(-1)^{(n+1)}}{\lambda_n^2} (1 - e^{-\frac{\lambda_n^2 \alpha t_h}{L^2}}) \sin\left(\lambda_n \frac{x}{L}\right) e^{-\frac{\lambda_n^2 \alpha t}{L^2}}, \quad (\text{A.2})$$

where  $T_c^a$  represents temperature variation during the cooling regime.

---

<sup>1</sup>Unlike the 3D case where volumetric heat source was used, here a heat flux boundary condition is defined.

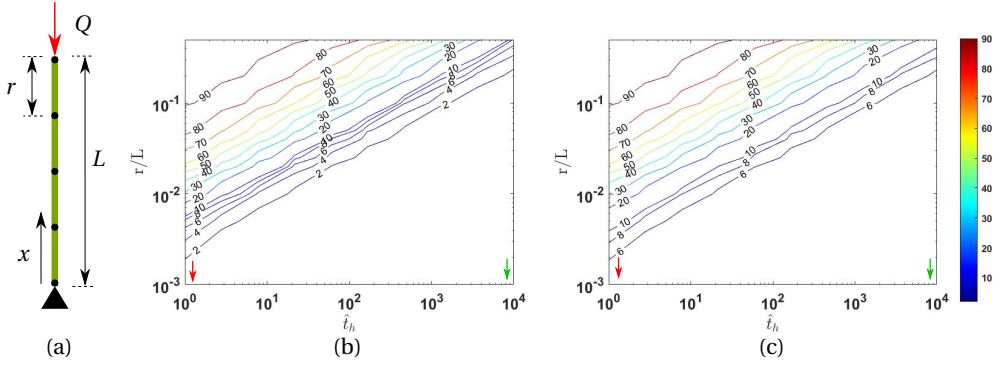


Figure A.1: (a) 1D domain with length  $L$  subjected to heat flux  $Q$  from top while a heat sink boundary condition is assumed at the bottom. The domain is discretised uniformly using linear elements with length  $r$ . Contour plot of percentage error calculated by comparing analytical and numerical solutions for the peak temperatures obtained at  $x = L$  with (b) time step  $\Delta t = t_h/50$  and (c)  $\Delta t = t_h/5$ .

A finite element discretisation scheme is used to solve this boundary value problem numerically. For this purpose, the domain is discretised into linear elements of equal length  $r$  while a time step of  $\Delta t$  is used for the temporal discretisation. An unconditionally stable implicit time integration scheme is used [1]. First, the heating regime is considered and the temperature at the end of the heating step when  $t = t_h$  at  $x = L$  is used for comparing the numerical solution  $T_h^n$  with  $T_h^a$  found using Eq. (A.1). The numerical experiment is repeated for different normalised heating times and mesh sizes. The percentage error between analytical and numerical solutions is calculated as

$$e = \frac{T_h^a - T_h^n}{T_h^a} \times 100\%. \quad (\text{A.3})$$

Figure A.1b shows the contour levels for the error  $e$  found using different  $r$  values while a constant time step  $\Delta t$  of  $\hat{t}_h/50$  is used. Note that the normalised heating time  $\hat{t}_h$  ranges from the flash heating value (indicated by red arrows) to typical values used in a gradual heating regime (indicated by green arrows).

The first observation from the contour plot reveals that for a fixed level of accuracy, flash heating requires much higher spatial refinement as compared to gradual heating, shown by red and green arrows, respectively. This can be understood by the concept of characteristic length given by  $\kappa = \sqrt{\alpha \hat{t}_h}$ , where  $\alpha$  is the thermal diffusivity. This length signifies the zone of influence near the heat source for short heating times, and a fine spatial resolution is required to capture the steep gradients within this small heat affected zone. Next, time step  $\Delta t = \hat{t}_h/5$  is considered for analysing the influence of time stepping on the accuracy, and the contour plot is shown in Figure A.1c. A slightly higher percentage error is found for the same set of  $r$  and  $\hat{t}_h$ . However, this observation holds only until the percentage error is less than 20%, beyond which the contour plots shown in Figure A.1b and c are virtually identical. This suggests that spatial refinement dictates the solution, and even with very fine temporal discretisation, the correct numerical

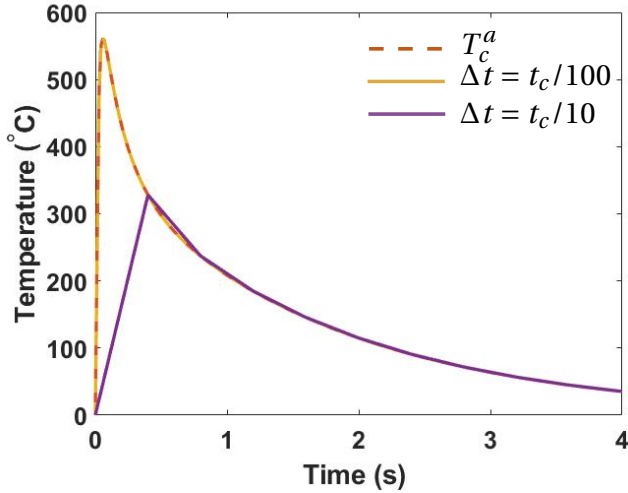


Figure A.2: The temperature evolution at  $x = L/2$  during the cooling period after a heating step with  $\hat{t}_h = 1$ . The thermal history is found using analytical solution using Eq. (A.2) and numerically with  $\Delta t = t_c/100$  and  $t_c/10$ , where  $t_c = 4$  is considered.

solution cannot be found unless spatial mesh is refined.

The next observation is associated with the cooling step and far field temperatures. The 1D domain is flash heated for  $\hat{t}_h = 1$  and the evolution of temperature at  $x = L/2$  is found using both analytical solution (Eq. (A.2)) and numerical computation. The variation is shown in Figure A.2 where numerical temperature are found using two different  $\Delta t$  values. It is found that the numerical solution with larger time steps leads to under-prediction of far-field peak temperatures. Also, it is observed from the analytical solution that there is a significant variation in temperature during the first few seconds of the cooling step, during which peak value is attained. Therefore, it is recommended to have a fine temporal discretisation, especially at the beginning of the cooling step.





# B

## DERIVATION OF ANALYTICAL SOLUTION FOR ONE-DIMENSIONAL HEAT EQ.

We consider the one-dimensional heat equation given by Eq. (3.11). The boundary conditions for the heating regime and the initial condition are given by Eqs. (3.12)–(3.14), respectively. Note that these are non-homogeneous, while the method of separation of variables can be applied only for homogeneous BCs. Therefore, following transformations are introduced

$$\tilde{x} = \frac{x}{L}, \quad (\text{B.1})$$

$$\tilde{t} = \frac{t}{\tau}, \quad (\text{B.2})$$

$$\tilde{T} = T - T_s - T_{ss}\tilde{x}, \quad (\text{B.3})$$

where  $\tau = L^2/\alpha$  and  $T_{ss} = (QL)/k$ . Using Eqs. (B.1–B.3) the heat equation is transformed as

$$\frac{\partial \tilde{T}}{\partial \tilde{t}} = \frac{\partial^2 \tilde{T}}{\partial \tilde{x}^2}, \quad (\text{B.4})$$

while the flux BC becomes

$$\left. \frac{\partial \tilde{T}}{\partial \tilde{x}} \right|_{\tilde{x}=1} = 0. \quad (\text{B.5})$$

The other boundary condition i.e.,  $T = T_s$  at  $x = 0$  and the initial condition given by Eq. (3.14) also gets modified as

$$\tilde{T}(0, \tilde{t}) = 0 \quad \text{for} \quad \hat{t} \geq 0, \quad (\text{B.6})$$

$$\tilde{T}(\tilde{x}, 0) = T_0 - T_s - T_{ss}\tilde{x} = p(\tilde{x}) \quad \text{for } \tilde{x} > 0. \quad (\text{B.7})$$

The boundary conditions are now homogeneous. Hence, method of separation of variable can be used. Using which,  $\tilde{T}$  is assumed to be a combination of two separate functions, i.e.,

$$\tilde{T} = X(\tilde{x})\psi(\tilde{t}), \quad (\text{B.8})$$

where  $X$  and  $\psi$  are functions of  $\tilde{x}$  and  $\tilde{t}$  alone, respectively. Putting Eq. (B.8) in Eq. (B.4), the general solution can be worked out as

$$\tilde{T}(\tilde{x}, \tilde{t}) = (A\sin(\lambda\tilde{x}) + B\cos(\lambda\tilde{x}))(Ce^{-\lambda^2\tilde{t}}), \quad (\text{B.9})$$

where  $A, B$  and  $C$  are constants. Next, we use the boundary conditions for determining the values for these constants. Using boundary condition described by Eq. (B.6) and ignoring trivial solutions, it can be worked out that  $B = 0$ . Putting this in Eq. (B.9), we get

$$\tilde{T}(\tilde{x}, \tilde{t}) = D\sin(\lambda\tilde{x})e^{-\lambda^2\tilde{t}}, \quad (\text{B.10})$$

where  $D = AC$ . Now, we use the other boundary condition described by Eq. (B.5) which yields

$$\left. \frac{\partial \tilde{T}}{\partial \tilde{x}} \right|_{\tilde{x}=1} = D\lambda \cos(\lambda)e^{-\lambda^2\tilde{t}} = 0, \quad (\text{B.11})$$

which gives

$$\lambda_n = \frac{2n-1}{2}\pi \quad \text{for } n = 1, 2, 3, \dots \quad (\text{B.12})$$

Now we apply principle of superposition, which means that if the solution holds true for one  $\lambda$ , then it must be true for a linear combination of all  $\lambda_n$ . Hence,

$$\tilde{T}(\tilde{x}, \tilde{t}) = \sum_{n=1}^{\infty} D_n \sin(\lambda_n \tilde{x}) e^{-\lambda_n^2 \tilde{t}}, \quad (\text{B.13})$$

combines the solutions for all possible  $\lambda$  values. Finally, we utilize the initial condition given by Eq. (B.7) for determining the constant  $D_n$  as

$$\tilde{T}(\tilde{x}, 0) = \sum_{n=1}^{\infty} D_n \sin(\lambda_n \tilde{x}), \quad (\text{B.14})$$

which should be equal to the temperature distribution given by Eq. (B.7). This gives

$$p(\tilde{x}) = \sum_{n=1}^{\infty} D_n \sin(\lambda_n \tilde{x}). \quad (\text{B.15})$$

For determination of  $D_n$ , orthogonality property of the function  $\sin(\lambda_n \tilde{x})$  is utilized. This gives

$$D_n = \frac{\int_0^1 p(\tilde{x}) \sin(\lambda_n \tilde{x}) d\tilde{x}}{\int_0^1 \sin^2(\lambda_n \tilde{x}) d\tilde{x}}, \quad (\text{B.16})$$

or

$$D_n = 2 \int_0^1 p(\tilde{x}) \sin(\lambda_n \tilde{x}) d\tilde{x}, \quad (\text{B.17})$$

as denominator of Eq. (B.16) becomes 1/2. Now, putting the value of  $p(\tilde{x})$  from Eq. (B.7), we get

$$D_n = 2 \int_0^1 (T_0 - T_{ss} \tilde{x} - T_s) \sin(\lambda_n \tilde{x}) d\tilde{x}. \quad (\text{B.18})$$

Integration yields

$$D_n = \frac{2(T_0 - T_s)}{\lambda_n} - \frac{2T_{ss}(-1)^{(n+1)}}{\lambda_n^2}. \quad (\text{B.19})$$

Finally, we substitute  $D_n$  from Eq. (B.19) into Eq. (B.13) and subsequently use Eq. (B.3), to get temperature distribution during the heating regime as

$$T_h(x, t) = T_s + T_{ss} \frac{x}{L} + 2 \sum_{n=1}^{\infty} \left( \frac{(T_0 - T_s)}{\lambda_n} - \frac{T_{ss}(-1)^{(n+1)}}{\lambda_n^2} \right) \sin\left(\lambda_n \frac{x}{L}\right) e^{-\frac{\lambda_n^2 \alpha t}{L^2}}. \quad (\text{B.20})$$

Note that  $T_{ss} = (QL)/k$  is same as the steady-state temperature at  $x = L$  for the heating step, i.e.,  $T_{ss} = T_h(L, \infty)$ .

The derivation for cooling regime remains exactly the same except the initial condition is now prescribed by the temperature distribution at the end of the heating step, i.e.,

$$\tilde{T}(\tilde{x}, 0) = p_h(\tilde{x}) = T_h(\tilde{x}, \tilde{t}_h) \quad \text{for } \hat{x} > 0. \quad (\text{B.21})$$

Therefore, replacing  $p(\tilde{x})$  by  $p_h(\tilde{x})$  in Eq. (B.17), integrating and using Eq. (B.3) leads to the solution for cooling regime as

$$T_c(x, t) = T_s + 2 \sum_{n=1}^{\infty} \left( \frac{T_{ss}(-1)^{(n+1)}}{\lambda_n^2} (1 - e^{-\frac{\lambda_n^2 \alpha t_h}{L^2}}) + \frac{(T_0 - T_s)}{\lambda_n} e^{-\frac{\lambda_n^2 \alpha t_h}{L^2}} \right) \sin\left(\lambda_n \frac{x}{L}\right) e^{-\frac{\lambda_n^2 \alpha t}{L^2}}. \quad (\text{B.22})$$



# C

## APPENDIX: SENSITIVITY ANALYSIS OF THE HOTSPOT CONSTRAINT

The sensitivity of the thermal constraint given by Eq. (4.9) with respect to design variable  $\rho$  is derived using the adjoint method. First, the relation between the temperature for the  $J^{\text{th}}$  slab  $\hat{\mathbf{T}}^{(J)}$  and  $\hat{\mathbf{T}}^\Omega$  is defined as

$$\hat{\mathbf{T}}^\Omega = \sum_{J=1}^m \mathbf{L}^{(J)} \hat{\mathbf{T}}^{(J)}, \quad (\text{C.1})$$

where  $\mathbf{L}^{(J)}$  is a matrix prepared for extracting top node temperatures for the  $J^{\text{th}}$  slab and sequentially place them in  $\hat{\mathbf{T}}^\Omega$ . Next, the constraint given by Eq. (4.9) is written in augmented form as

$$f^* = f + \sum_{J=1}^m (\boldsymbol{\lambda}^{(J)})^T (\mathbf{Q}^{(J)} - \mathbf{G}^{(J)} \mathbf{T}^{(J)}), \quad (\text{C.2})$$

with  $\boldsymbol{\lambda}^{(J)}$  as the Lagrange multiplier vector for the  $J^{\text{th}}$  slab. Differentiating the augmented constraint with respect to element density  $\tilde{\rho}_e$  gives

$$\frac{\partial f^*}{\partial \tilde{\rho}_e} = \frac{\partial f}{\partial \tilde{\rho}_e} + \sum_{J=1}^m (\boldsymbol{\lambda}^{(J)})^T \left( \frac{\partial \mathbf{Q}^{(J)}}{\partial \tilde{\rho}_e} - \mathbf{G}^{(J)} \frac{\partial \mathbf{T}^{(J)}}{\partial \tilde{\rho}_e} - \frac{\partial \mathbf{G}^{(J)}}{\partial \tilde{\rho}_e} \mathbf{T}^{(J)} \right). \quad (\text{C.3})$$

Expansion of the first term in the RHS of Eq. (C.3) gives

$$\frac{\partial f}{\partial \tilde{\rho}_e} = \frac{\left[ \frac{1}{n} \sum_{i=1}^n (\hat{T}_i^\Omega)^P \right]^{\left(\frac{1}{P}\right)-1}}{n T^{\text{cr}} N_c} \left[ (\hat{\mathbf{T}}^\Omega)^{P-1} \right]^T \sum_{J=1}^m \mathbf{L}^{(J)} \frac{\partial \mathbf{T}^{(J)}}{\partial \tilde{\rho}_e}. \quad (\text{C.4})$$

In order to avoid computation of state sensitivities, all the terms with  $\partial \mathbf{T}^{(J)} / \partial \tilde{\rho}_e$  are combined. This leads to the following sensitivity expression:

$$\frac{\partial f^*}{\partial \tilde{\rho}_e} = \sum_{J=1}^m (\boldsymbol{\lambda}^{(J)})^T \left( \frac{\partial \mathbf{Q}^{(J)}}{\partial \tilde{\rho}_e} - \frac{\partial \mathbf{G}^{(J)}}{\partial \tilde{\rho}_e} \mathbf{T}^{(J)} \right). \quad (\text{C.5})$$

Here,  $\boldsymbol{\lambda}^{(J)}$  is the solution of following equation:

$$\frac{\left[ \frac{1}{n} \sum_{i=1}^n (\hat{T}_i^\Omega)^P \right]^{\left(\frac{1}{P}-1\right)}}{n T^{\text{cr}} N_c} \left[ (\hat{\mathbf{T}}^\Omega)^{P-1} \right]^T \mathbf{L}^{(J)} - (\boldsymbol{\lambda}^{(J)})^T \mathbf{G}^{(J)} = 0, \quad (\text{C.6})$$

where  $J = 1, \dots, m$ . Furthermore, expressions for  $\partial \mathbf{G}^{(J)} / \partial \tilde{\rho}_e$  and  $\partial \mathbf{Q}^{(J)} / \partial \tilde{\rho}_e$  can be found by differentiating Eq. (4.5) and Eq. (4.6), respectively. Sensitivities with respect to the design variables are calculated using the chain rule:

$$\frac{\partial f^*}{\partial \rho_e} = \frac{\partial f^*}{\partial \tilde{\rho}_e} \frac{\partial \tilde{\rho}_e}{\partial \rho_e}. \quad (\text{C.7})$$

# LIST OF PUBLICATIONS

## JOURNAL PUBLICATIONS

1. **R. Ranjan**, Z. Chen, C. Ayas, M. Langelaar and F. van Keulen. (2023) *Overheating Control in Additive Manufacturing Using a 3D Topology Optimization Method and Experimental Validation*, [Additive Manufacturing](#) 61, p. 103339. ISSN: 2214-8604.
2. **R. Ranjan**, C. Ayas, M. Langelaar and F. van Keulen. (2022) *Controlling local overheating in topology optimization for additive manufacturing*, [Structural and Multidisciplinary Optimization](#) 65, 162.
3. **R. Ranjan**, C. Ayas, M. Langelaar and F. van Keulen. (2020) *Fast Detection of Heat Accumulation in Powder Bed Fusion Using Computationally Efficient Thermal Models*, [Materials](#) 13.20. ISSN: 1996-1944.
4. **R. Ranjan**, M. Langelaar, F. van Keulen and C. Ayas. *Classification and analysis of common simplifications associated with part-scale modeling of metal additive manufacturing processes*, Submitted to *Advanced Modeling and Simulation in Engineering Sciences*.

## CONFERENCE PUBLICATIONS

1. **R. Ranjan**, M. Bayat, C. Ayas, M. Langelaar and F. van Keulen. (11–15 Jan, 2021) *Reducing computational expenses associated with thermal modeling of additive manufacturing*, [Proceedings of 14th World Congress on Computational Mechanics](#), Online.
2. **R. Ranjan**, C. Ayas, M. Langelaar and F. van Keulen. (11–13 Sep, 2019) *Detecting Heat Accumulation in Additive Manufacturing Parts using Computationally Efficient Thermal Models*, [Proceedings of International conference on Simulation for Additive Manufacturing \(Sim-AM\)](#), Pavia, Italy.
3. **R. Ranjan**, C. Ayas, M. Langelaar and F. van Keulen. (22–25 July, 2018) *Towards design for precision additive manufacturing: A simplified approach for detecting heat accumulation*, [Proceedings of Advancing Precision in Additive Manufacturing](#). Berkeley, USA.
4. **R. Ranjan**, Y. Yang, C. Ayas, M. Langelaar and F. van Keulen. (10–11 Oct, 2017) *Controlling Local Overheating in Topology Optimization for Additive Manufacturing*, [Proceedings of Special Interest Group Meeting: Additive Manufacturing](#), Leuven, Belgium.

## BOOK CHAPTER

1. **R. Ranjan**, C. Ayas, M. Langelaar and F. van Keulen. (2020) *Topology Optimisation Techniques*, in [Precision Metal Additive Manufacturing](#), R. Leach and S. Carmignato, Eds., Boca Raton, London, New York: CRC Press, ch. 2, pp. 11–34.





# ACKNOWLEDGEMENTS

My PhD journey has been eventful. Although long and occasionally tiring, its never been lonely. I would like to thank everyone who inspired me and kept me going on this path.

Firstly, my parents who made me the person I am. My late father, with his never-ending enthusiasm and jovial personality, always had a bit of poetry or anecdote to share whenever I felt low. 'Find a living in things that you enjoy doing' was one of the life mantra he lived by and I wish to continue on the path he showed. It was his conviction to see me graduate and I miss him dearly when I am close to the finish line. I would also like to thank my mother for unconditional love and support she always provided.

Next, I would like to sincerely thank my supervisors: Fred van Keulen, Matthijs Langelaar and Can Ayas. My journey as a researcher has just started and I could not have wished for better mentors. You gave me freedom to explore new ideas, helped me mature them and then nudged me in right directions to take it to publication. Even before the pandemic hit us, I was almost a remote-PhD candidate. However, your supervision helped me maintain focus on my research problem. I am also grateful to the PME support staff for fulfilling my various requests time to time.

A good amount of research presented in this thesis was done in planes, trains, cafes, airports and hotel lobbies since the project required significant travel. Almost always, travel was complemented with pleasant company of the PAM<sup>2</sup> family. My sincere thanks to all the PAM<sup>2</sup> supervisors and fellow PhDs: Amal, Aditi, Amrozia, Jitka, Juliana, Mirko, Markus, Subba, Umberto, Mohamad, David, Mandy, Lokesh and Siwen. We did have a great time together and created many amazing memories. A special shout out to Mohamad, David, Mandy, Lokesh, Dr. Luca and Prof. Jesper for hosting me during my secondments. I would also like to thank Dr. Ann Witvrouw and Kopila Gurung for coordinating the project.

Although PAM<sup>2</sup> kept me on the move but base station remained at Delft. And there were few who made it feel like home. Pleasant discussions with Arnoud, Stijn, Dirk, Max, Emiel, Sanne, Sabiju, Prabhat, Saleh, Jian, Qi and Yong kept the office lively. Evening chats while cooking with the companions of AVS13: Rakesh, Deepak, Ashish, Sumit were relaxing. Vibhas, being both an office colleague and flatmate, tolerated me the most. So thanks to all of you.

Next, I would like to thank Dr. Zhuoer Chen for research collaboration. Also, I would like to thank Dr. Fauzan Adziman for nice discussions and guidance about deployment of research ideas on industrial level.

I would like to thank my sisters and brother-in-laws for taking care of things back home so that I could fully concentrate on my research. Lastly, I would like to thank my wife Rini. Our marriage coincided with arrival of a global pandemic and it did throw some unimaginable challenges at us. But you ensured your support to see me reach the finish line. A very special thanks to you. I know you think that I will perpetually have a code to debug or a paper to write. I am afraid that I can't deny this but at-least, after a really long time, I will not have a thesis to work on (hopefully!).

# CURRICULUM VITÆ

## Rajit RANJAN

18-10-1988 Born in Sitapur, India.

### EDUCATION

- 2017-2022 PhD Candidate  
Delft University of Technology  
*Thesis:* Efficient Thermal Modeling and Topology Optimization for Additive Manufacturing  
*Promotors:* Prof. dr. ir. F. Van Keulen and Dr. ir. M. Langelaar  
*Copromotor:* Dr. ir. C. Ayas
- 2013–2015 Master of Science  
University of Cincinnati, USA  
*Thesis:* Design for Manufacturing and Topology Optimization in Additive Manufacturing  
*Supervisor:* Prof. dr. ir. S. Anand
- 2007–2011 Bachelor of Technology  
National Institute of Technology, Allahabad, India

### WORK EXPERIENCE

- 2022-Present Graduate Engineer in Applied Computational Science and Engineering Alloyed Inc.
- 2016-2017 Production system Engineering  
Boeing Research and Technology.
- 2011-2013 Design Engineering  
Tata-Hitachi construction machinery Pvt. Ltd..

## AWARDS

- 2020                    3D Printing Student Challenge organized by Agoria and Sirris
- 2011                    QuEST Inginium organized by QuEST global